

University of Southampton Research Repository ePrints Soton

Copyright © and Moral Rights for this thesis are retained by the author and/or other copyright owners. A copy can be downloaded for personal non-commercial research or study, without prior permission or charge. This thesis cannot be reproduced or quoted extensively from without first obtaining permission in writing from the copyright holder/s. The content must not be changed in any way or sold commercially in any format or medium without the formal permission of the copyright holders.

When referring to this work, full bibliographic details including the author, title, awarding institution and date of the thesis must be given e.g.

AUTHOR (year of submission) "Full thesis title", University of Southampton, name of the University School or Department, PhD Thesis, pagination

UNIVERSITY OF SOUTHAMPTON
FACULTY OF ENGINEERING AND THE
ENVIRONMENT

School of Engineering Sciences

CORRELATION BETWEEN STRUCTURAL AND MAGNETIC
PROPERTIES IN POWDER AND BULK $\text{Mg}(\text{B}_{1-x}\text{C}_x)_2$
PREPARED USING CARBON CHEMICAL VAPOUR DOPED
BORON AND SILICA COATED BORON

by

Maurizio Paolella

Thesis for the degree of Doctor of Philosophy

July 2015

Ad maiora.

UNIVERSITY OF SOUTHAMPTON

ABSTRACT

FACULTY OF ENGINEERING AND THE ENVIRONMENT

School of Engineering Sciences

Doctor of Philosophy

**CORRELATION BETWEEN STRUCTURAL AND MAGNETIC PROPERTIES IN
POWDER AND BULK $\text{Mg}(\text{B}_{1-x}\text{C}_x)_2$ PREPARED USING CARBON CHEMICAL
VAPOUR DOPED BORON AND SILICA COATED BORON**

by Maurizio Paoella

The research project has been focused on the preparation and characterization of $\text{Mg}(\text{B}_{1-x}\text{C}_x)_2$ powder and bulk samples using chemical vapour coated boron and silica coated boron by sol-gel method. The chemical vapour deposition of carbon on boron powder was achieved by reacting ethylene gas on high purity nano-sized boron particles (20-100 nm diameter) with varying deposition temperatures and partial pressures. Undoped and carbon doped boron was then reacted with magnesium rod to produce both $\text{Mg}(\text{B}_{1-x}\text{C}_x)_2$ powder and bulk samples. Transmission electron microscopy showed that the chemical vapour deposition achieved a uniformly thick carbon-rich layer on each particle, regardless of particle size. In addition, the analysis of the diffraction peaks and the characterization of the magnetisation has evidenced the coexistence of phases with different levels of carbon resulting in multiple current paths within the $\text{Mg}(\text{B}_{1-x}\text{C}_x)_2$ samples. The study of the preparation process for bulk $\text{Mg}(\text{B}_{1-x}\text{C}_x)_2$ samples has evidenced that reducing the difference between the time constant of reaction and the time constant of diffusion is crucial to obtain well-sintered samples devoid of cracks. Doping with carbon has shown significant improvements in the field dependence of J_c for the $\text{Mg}(\text{B}_{1-x}\text{C}_x)_2$ bulk samples reaching values comparable with the best literature-reported data for bulk samples. However, the J_c values of the $\text{Mg}(\text{B}_{1-x}\text{C}_x)_2$ bulk samples were observed to be noticeably lower when compared with the best literature-reported data for wires and tapes, owing to the greater density achievable in the latter. In contrast to the carbon doping, the coating with silica via sol-gel process was found to impair the in-field J_c properties of $\text{Mg}(\text{B}_{1-x}\text{C}_x)_2$ bulk samples, presumably due to the huge amount of silica loaded onto the boron powder and to the formation of carbonate and silicate impurities within their reacted microstructure.

List of contents

<i>Abstract</i>	V
<i>List of contents</i>	VII
<i>Declaration of authorship</i>	XIII
<i>Acknowledgements</i>	XV
<i>Definitions and abbreviations</i>	XVII
1 Fundamentals on superconductivity	1
1.1 Introduction to superconductivity	1
1.2 Zero field cooling and field cooling.....	5
1.3 Shielding currents and transport currents.....	7
1.4 Penetration depth and coherence length.....	10
1.5 The vortex state.....	13
1.6 Bean critical state model.....	20
1.7 Historical review of superconducting materials.....	24
1.8 Introduction to MgB ₂	29
1.9 Chemical doping of MgB ₂	30
1.9.1 Chemical doping of MgB ₂ : substitution and addition effects..	30
1.9.2 Literature review on the chemical doping of MgB ₂ bulk samples.....	32

1.9.3 Literature review on the chemical doping of MgB ₂ tapes and wires.....	38
2 Doping methods of MgB₂ superconductor and characterisation techniques: experimental details.....	47
2.1 Carbon Chemical vapour deposition method.....	47
2.1.1 Overview of the Carbon Chemical vapour deposition method.....	47
2.1.2 Chemical vapour deposition of carbon on to the boron precursor powder.....	49
2.2 Sol-gel method.....	51
2.2.1 Overview of the sol-gel method.....	51
2.2.2 Sol-gel method stages.....	52
2.2.2.1 Solution of precursors.....	52
2.2.2.2 Sol-gel transformation.....	52
2.2.2.3 The ageing of the gel.....	54
2.2.2.4 Drying.....	55
2.2.2.3 Densification (Sintering).....	55
2.2.3 Preparation of SiO ₂ -doped Mg(B _{1-x} C _x) ₂ using silica by Sol-Gel method and C-CVD coated boron.....	56
2.3 X-ray diffraction (XRD).....	57
2.3.1 X-ray diffraction (XRD): basic principles.....	57
2.3.2 X-Ray Diffraction of MgB ₂	58
2.4 Transmission electron microscopy (TEM).....	62

2.4.1	Transmission electron microscopy: basic principles.....	62
2.4.2	Transmission electron microscope: main components & features.....	63
2.4.3	Transmission electron microscopy analysis of MgB ₂	64
2.5	Scanning electron microscopy	65
2.5.1	Scanning electron microscopy: basic principles	65
2.5.2	Scanning electron microscope: main components & features.....	67
2.5.3	Scanning electron microscopy analysis of MgB ₂	68
2.6	Magnetization measurements	70
2.6.1	Vibrating Sample Magnetometer (VSM): main components & features	70
2.6.2	Magnetisation measurements of MgB ₂ using VSM: calculation of J_c and description of the main effects causing a deviation from the reported magnetic field.....	72
3	Preparation and properties of Mg(B_{1-x}C_x)₂ powder samples using carbon chemical vapour doped boron	75
3.1	Synthesis procedures of undoped and C-CVD doped MgB ₂ powder samples.....	75
3.2	XRD characterization and temperature-dependent magnetization measurements.....	78
3.3	TEM image analysis.....	88
3.4	Conclusion.....	92
4	Preparation and properties of Mg(B_{1-x}C_x)₂ bulk samples using carbon chemical vapour doped boron and SiO₂ coated boron.....	93

4.1 Methods of preparing MgB ₂ bulk samples and related issues.....	93
4.1.1 Background to in-situ challenges.....	93
4.1.2 Sample preparation.....	95
4.1.3 Study and optimization of preparation process.....	97
4.1.3.1 Experimental details.....	97
4.1.3.1 Crack issue.....	107
4.2 Characterisation of undoped MgB ₂	112
4.2.1 Experimental details	112
4.2.2 Structural analysis and critical current density properties..	112
4.3 Preparation and characterisation of Mg(B _{1-x} C _x) ₂ using Carbon Chemical Vapour Coated Boron.....	126
4.3.1 Experimental details	126
4.3.2 Structural analysis and critical current density properties..	126
4.4 Preparation and characterisation of SiO ₂ doped Mg(B _{1-x} C _x) ₂ using Silica Sol-Gel and Carbon Chemical Vapour Coated Boron.....	140
4.4.1 Experimental details	140
4.4.2 TEM image analysis of SiO ₂ -coated boron powder and characterisation of the structural and critical current density properties of reacted bulk samples.....	141
4.5 Comparison of $J_c(B)$ between Mg(B _{0.98} C _{0.02}) ₂ and literature- reported data for doped MgB ₂ bulk samples, and MgB ₂ wires and tapes.....	156

4.5.1 Comparison of $J_c(B)$ between $\text{Mg}(\text{B}_{0.98}\text{C}_{0.02})_2$ and literature-reported data for doped MgB_2 bulk samples.....	156
4.5.2 Comparison of $J_c(B)$ between $\text{Mg}(\text{B}_{0.98}\text{C}_{0.02})_2$ and literature-reported data for doped MgB_2 wires and tapes	161
5 Conclusion and future work.....	165
References.....	169
Appendix.....	179

DECLARATION OF AUTHORSHIP

I, MAURIZIO PAOLELLA, declare that this thesis and the work presented in it are my own and has been generated by me as the result of my own original research.

Title of thesis: CORRELATION BETWEEN STRUCTURAL AND MAGNETIC PROPERTIES IN POWDER AND BULK $Mg(B_{1-x}C_x)_2$ PREPARED USING CARBON CHEMICAL VAPOUR DOPED BORON AND SILICA COATED BORON

I confirm that:

1. This work was done wholly or mainly while in candidature for a research degree at this University;
2. Where any part of this thesis has previously been submitted for a degree or any other qualification at this University or any other institution, this has been clearly stated;
3. Where I have consulted the published work of others, this is always clearly attributed;
4. Where I have quoted from the work of others, the source is always given. With the exception of such quotations, this thesis is entirely my own work;
5. I have acknowledged all main sources of help;
6. Where the thesis is based on work done by myself jointly with others, I have made clear exactly what was done by others and what I have contributed myself;
7. Parts of this work have been published before submission, and these publications are included in Appendix.

Signed:.....

Date:.....

Acknowledgements

First and foremost, I would like to thank Dr Edward Young for having introduced me to the science and technology of superconductivity, for his advice and encouragement, both throughout the stages of this work, from the experimental activity in the laboratory to its writing up.

I am also indebted to Prof Yifeng Yang and Prof Carlo Beduz, for their precious suggestions, both in the design of experiments and in the interpretation of the data, and to Dr. Dmitry Bavykin, for having contributed to this work with his experiments of coating boron with silica by the sol-gel method.

I would also like to express my gratitude to Mike Webb, Robert Loades and Wendell Bailey, both for their tips that have contributed to improving the quality of my work in the laboratory, and for their amiable discussions about football. A big thank you also to Iole, Jessica and Jorge, for having made my everyday experience in the laboratory more pleasant, by joking with me and answering my numerous questions.

I would like to express a warm thank you to Dr Stavros Syngellakis, for his willingness to discuss problems pertinent to structural mechanics, both related to this work, and also beyond this; and to my friend Foundit, for having provided me with suggestions about the use of the English language, which were revealed to be precious in the writing of this work, and also for satisfying my language curiosity.

My biggest thank you is for my family, for always providing me with incessant, and unwavering support and encouragement.

Definitions and Abbreviations

CHEMICAL SYMBOLS

Ag	silver
B	boron
B ₄ C	tetra boron carbide
C	carbon
CNT	carbon nanotubes
Cu	copper
Fe	iron
Gd	gadolinium
Mg	magnesium
MgB ₂	magnesium diboride
MgH ₂	magnesium hydride
Nb	niobium
O	oxygen
SiC	silicon carbide
SiO ₂	silica
Ta	tantalum
Ti	titanium
Tl	thallium
Y	yttrium

SYMBOLS FOR PHYSICAL QUANTITIES

A	vector potential (Wb/m)
\vec{B}	magnetic field (T)
D	electric displacement field (C/m ²)
e	electric charge (C)
E_{bound}	energy density per unit area of the boundary layer (J/cm ²)
F_L (or F)	Lorentz force (N)
H	applied magnetic field
H_c	critical magnetic field (T)
H_{c1}	lower critical magnetic field (T)
H_{c2}	upper critical magnetic field (T)
H_{irr}	irreversibility field (T)
I_c	critical current (A)
J_c	critical current density (A/cm ²)
J_{sh}	shielding current density (A/cm ²)
κ	Ginsburg–Landau ratio
l	mean free path (nm)
λ_L	London penetration depth (nm)
m	mass (Kg)
M	magnetisation (A/m or emu)
μ	permeability (H/m or N/A ²)
μ_0	vacuum permeability (H/m or N/A ²)
n_s	density of super electrons (cm ⁻³)
ξ	coherence length (nm)
r (or a)	radius (cm)
ρ	resistivity (Ω/cm)

ρ_0	residual resistivity (Ω/cm)
T_c	critical temperature (K)
T_{irr}	irreversibility temperature (K)
Φ	magnetic flux (Wb or V/s)
χ	susceptibility
Ψ	order parameter

OTHER ABBREVIATIONS

C-CVD	carbon chemical vapour deposition
CVD	chemical vapour deposition
FC	field cooled
HTS	high-temperature superconductors
IMD	internal magnesium diffusion
LTS	low-temperature superconductors
PICT	powder-in-closed tube method
PIT	powder-in-tube method
ZFC	zero field cooled

Chapter 1

Fundamentals of superconductivity

This chapter presents the key aspects and properties characteristic of superconductivity, focusing on the definition of the vortex state and the Bean critical state model, which is one of the most widely used models for describing the field and current distribution in a superconductor. Moreover, the main features of the MgB_2 , the material object of this research project, are described, providing a detailed literature review of the main results achieved in the field of the chemical doping of MgB_2 bulk samples and MgB_2 wires and tapes.

1.1 Introduction to superconductivity

A perfect superconductor is a material that exhibits two peculiar properties, namely perfect electrical conductivity, i.e. zero resistivity ($\rho = 0$) and perfect diamagnetism ($\vec{B} = 0$), when it is cooled below a characteristic temperature T_c , called the critical temperature. At higher temperatures it is a normal material, and ordinarily is not a good conductor. For example, lead, tantalum, and tin become superconductors, while copper, silver, and gold, which are much better conductors, do not.

According to Matthiessen's rule, electrical resistivity is composed of two terms: ρ_0 , which is a temperature-independent contributions arising from the scattering of the conduction electrons associated with impurity atoms and ρ_{ph} , i.e. phonon contribution to the electrical resistivity of a normal metal. Since the former term is negligible at room temperature, the resistivity of a typical conductor depends linearly on temperature at high

T whereas it obeys the T^5 Bloch law when T is sufficiently below the Debye temperature.

In the case of a superconductor, this description is valid down to the critical temperature, T_c , at which resistivity goes to zero. The discovery of this phenomenon is due to Onnes [1], who in 1911 measured the electrical resistance of mercury and was the first to become aware of the behaviour. However, apart from zero resistivity there is another property that is characteristic of superconductors and distinguishes them from ideal conductors: perfect diamagnetism.

Perfect diamagnetism means that in the equation:

$$\vec{B} = \mu_0 \vec{H}(1 + \chi) = \mu_0 (\vec{H} + \vec{M}) \quad (1.1),$$

where μ_0 is the permeability of vacuum, the susceptibility $\chi = -1$, which, given the relation $\chi = \vec{M}/\vec{H}$ between the magnetisation \vec{M} and the magnetic field H , is equivalent to $\vec{M} = -\vec{H}$, i.e. the internal magnetic field \vec{B} is equal to zero [2]. Physically, it means that when a superconductor is placed between the pole pieces of a magnet, the \vec{B} field lines from the magnet go around it instead of entering, and its own internal field remains zero, as shown in fig.(1.1).

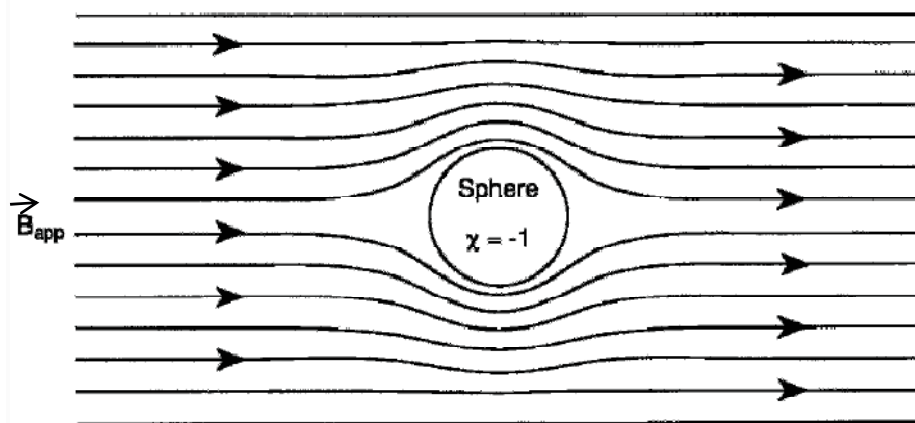


Figure 1.1: Distorted magnetic field lines around a superconductor in a constant applied field [2].

The perfect diamagnetism can lead to one of two different effects depending on whether the material is zero field cooled (ZFC) or non-zero field cooled (FC). In the first case, flux exclusion will be observed, in which the field is excluded from the superconductor when the material is cooled below T_c without any magnetic field present and subsequently placed in an external magnetic field. Alternatively, if the test material is cooled below T_c in the presence of a magnetic field, the field will be expelled from the material as T_c is reached (a phenomenon known as the Meissner effect).

However, there is an upper limit to the magnetic field that the Meissner effect can expel. This critical field, known as the critical magnetic field and denoted by $H_c(T)$, decreases with temperature and become zero at T_c . Moreover, in virtue of the relationship between current and magnetic field ($H = I/2\pi a$ for a wire of radius a carrying current I), there will be a limiting value of the critical current corresponding to:

$$I_c = 2\pi H_c a \quad (1.2)$$

and

$$J_c = \frac{2H_c}{a}. \quad (1.3)$$

Those superconductors that totally exclude an applied magnetic flux are known as Type I superconductors [3]. This class of superconductors exhibits perfect diamagnetism below H_c and admits magnetic field magnetic fields without hindrance when H exceeds H_c as shown in fig.(1.2a).

Other superconductors, called Type II superconductors, totally exclude magnetic flux up to the lower critical field, H_{c1} . Then the magnetic field starts penetrating into the material until at the upper critical field H_{c2} the

material is fully penetrated and the material return to the normal state [3]. Fig.(1.2b) shows this behaviour, in which M rises to a negative maximum at H_{c1} but then M retreats as flux lines start to penetrate into the sample. Therefore the cancellation of H by M is no longer perfect, and the value of B becomes finite within the superconductor.

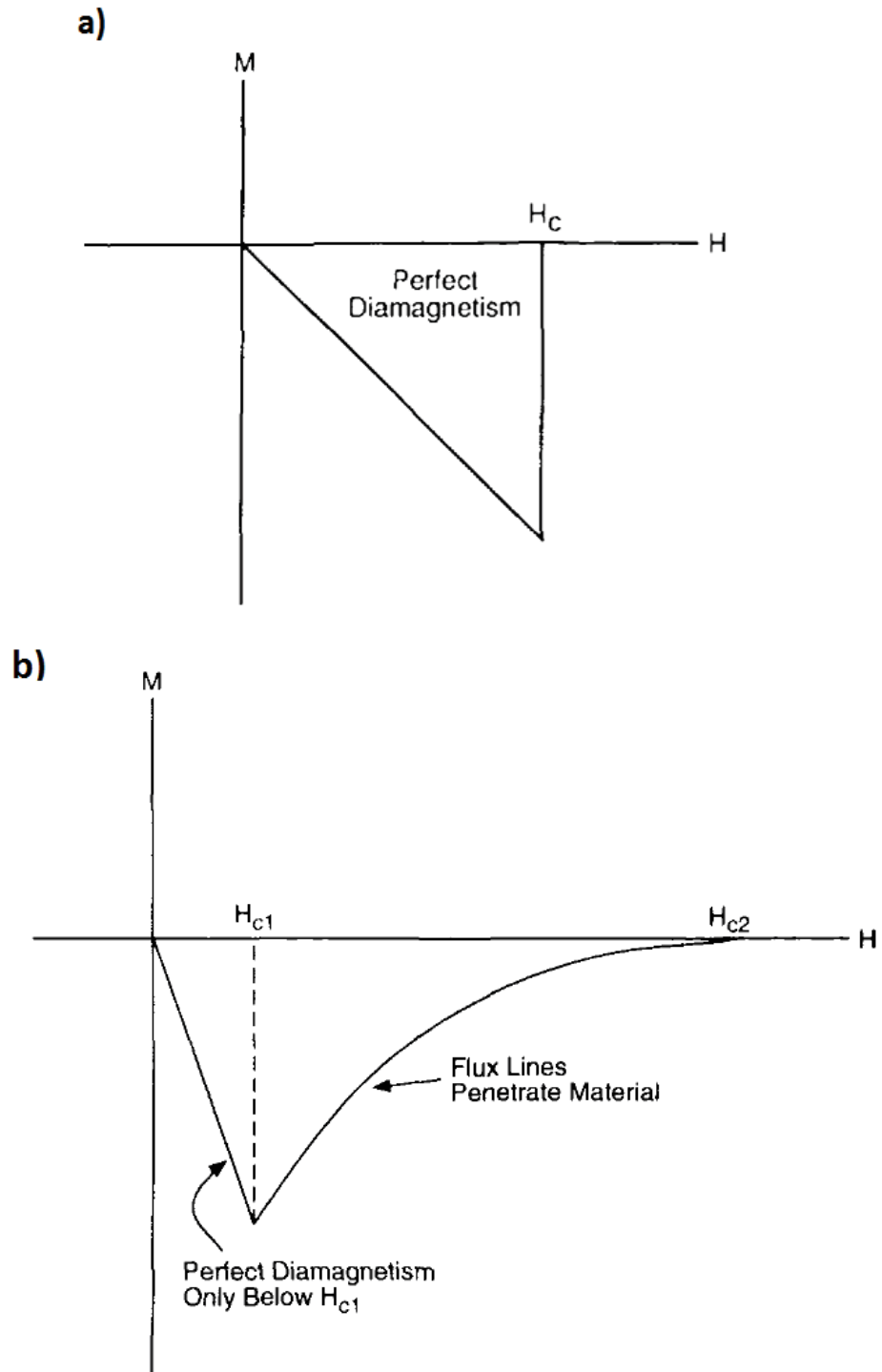


Figure 1.2: Magnetization as a function of applied field for a type I (a) and a type II (b) superconductors [3].

1.2 Zero field cooling and field cooling

An example of how ZFC and FC can result into two distinct final states is given by the case of a hole inside a superconductor. In particular, two different cases can result depending on whether the hole is open (i.e. open to the outside at both ends) or closed. In the first case, if the sample is zero-field-cooled below T_c , a magnetic field applied after cooling will be excluded by both the superconducting region and the hole, in other words, both behave as perfect diamagnetic materials. If, on the other hand, the same sample is field cooled, once it reaches the superconducting state, the magnetic flux will be expelled from the superconducting material, but will remain in the hole. This different behaviour is due to the presence of surface currents that in the former case shield the entire sample (including the hole) from the effects of the external magnetic field, while in the latter case, these same shielding currents are cancelled by the reverse-direction current flowing around the walls of the open hole as shown in fig.(1.3), [2].

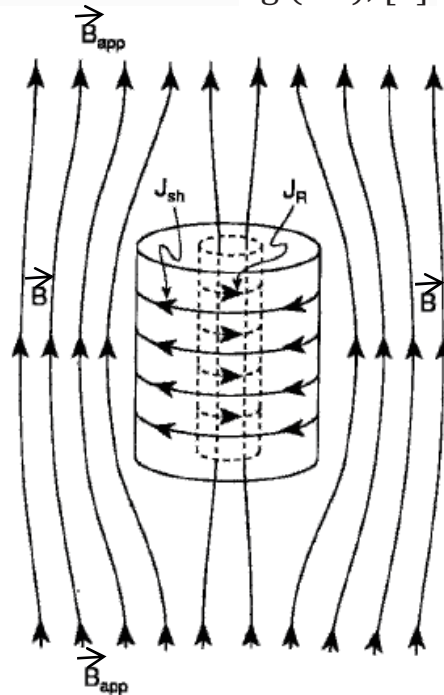


Figure 1.3: Shielding current flow J_{sh} on the outside surface and reverse-direction shielding current flow J_R on the inside surface of a superconducting tube [2].

In the case, instead, of a closed cavity (or hole) this difference in magnetic susceptibility between ZFC and FC samples is not found. In fact, as is easily understood, the magnetic flux is excluded from the closed hole, as it was from the open one. But, in this case, the field also will be excluded for (non-zero) field cooling, fig.(1.4). The reason for this behaviour is that the \vec{B} field lines do not have the opportunity to leave a closed cavity to connect with the external field, because the cavity is completely surrounded by superconducting material. Accordingly, a superconductor with an internal cavity will exhibit $\chi = -1$, behaving much like a solid superconductor (except that the magnetization is present in the superconductor, but not in the cavity).

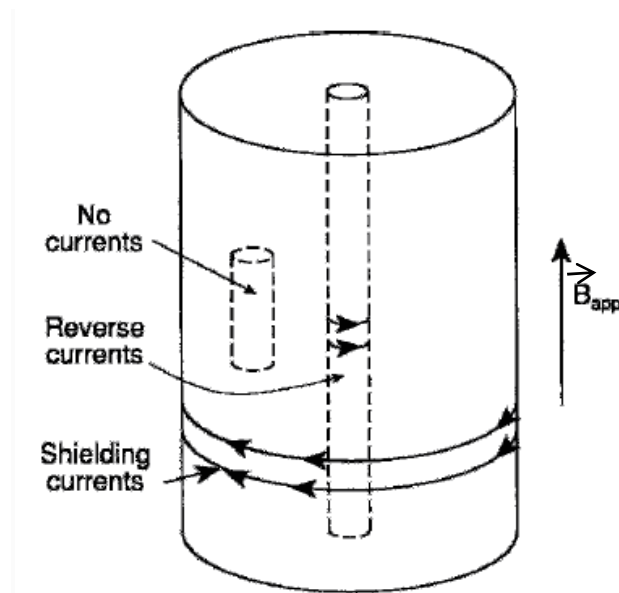


Figure 1.4: Shielding current flow, J_{sh} , on the outside surface and reverse-direction shielding current [2].

Experimentally, since samples are a mixture of a superconducting and non-superconducting material (i.e. fraction of sample volume taken up by holes, intergranular spaces and normal material), values of χ_{zfc} and χ_{fc} are less negative than -1. In particular, in the case of a sample of total volume V_T containing a superconducting material of volume V_s , a hole volume of V_h and an enclosed cavity of volume V_c , the ratio of FC to ZFC magnetization will be given by $\mu_{fc}/\mu_{zfc} = M_{fc}/M_{zfc} = \chi_{fc}/\chi_{zfc} = V_s + V_c / V_s + V_h + V_c$.

Therefore, the overall sample can exclude more flux when it is zero field cooled than it can expel when it is field cooled. The difference between the amount of excluded flux and that of expelled flux is defined as trapped flux. The trapped flux subtracts from the diamagnetic response to make the magnetization less negative in the case of Meissner effect (FC) than in that of shielding current (ZFC) as shown in fig.(1.5) for a Rb_3C_{60} powder sample [4].

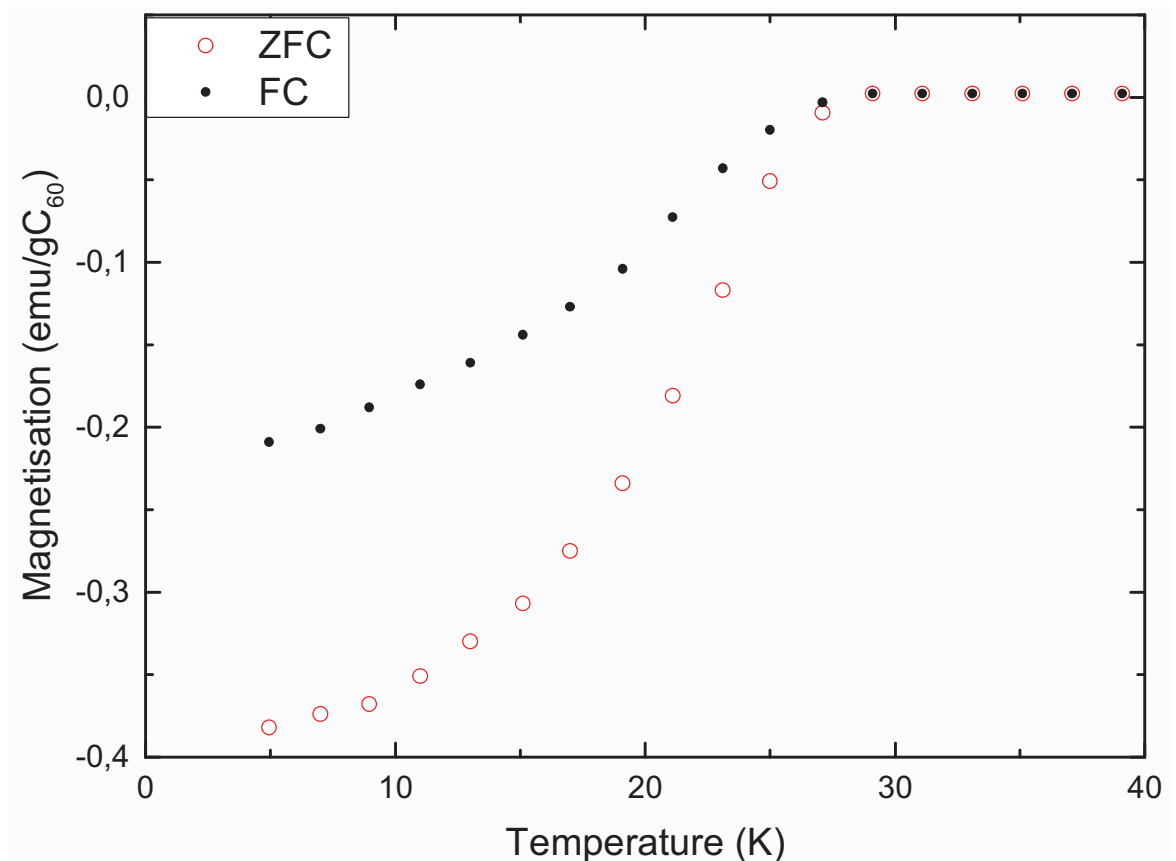


Figure 1.5: Comparison between zero-field-cooled magnetic susceptibility and its field-cooled counterpart for a powder sample Rb_3C_{60} . The data were taken from [4].

1.3 Shielding currents and transport currents

In the previous section the reaction of a superconductor in an applied field has been discussed showing how the presence of a magnetic field generates shielding currents that, flowing around the outside surface of

the superconducting material, cancel out the interior \vec{B} field. In order to provide a more rigorous mathematical description of the phenomenon, it is convenient to start with Maxwell's equation:

$$\nabla \times \vec{B} = \mu_0(\vec{J} + \nabla \times \vec{M}) + \mu_0 \frac{\partial D}{\partial t} \quad (1.4)$$

which, when setting $J = 0$ and $\frac{\partial D}{\partial t} = 0$, where D is the electric field displacement, gives the relationship:

$$\nabla \times \vec{B}_{\text{in}} = \mu_0 \vec{J}_{\text{sh}} \quad (1.5)$$

where J_{sh} is defined the shielding current and is given by $J_{\text{sh}} = \nabla \times M$. This relation, which, when setting $B_{\text{app}} = \mu_0 \lambda J_0$, is equivalent to

$$\vec{J}_{\text{sh}}(r) = -\vec{J}_0 \exp\left[-\frac{R-r}{\lambda}\right], \quad (1.6)$$

demonstrates that the vectors \vec{B} and J , which are mutually orthogonal, can only exist in a surface layer and not in the bulk of the superconductor. The dimensions of this transition layer are characterized by the length scale λ_L , called the London penetration depth, and defined as

$$\lambda_L = \left(\frac{m}{\mu_0 n_s e^2}\right)^{1/2}, \quad (1.7)$$

where m is the mass of charge carriers, n_s is the density of superconducting electrons and e is the charge on the electron. This parameter defines the thickness, within the surface of the superconductor, in which the field B (which has only a z component) falls to $1/e$ of the B_{app} on the outside of the sample, according to the relation:

$$B(r) = B_{\text{app}} \exp\left[-\frac{R-r}{\lambda}\right]. \quad (1.8)$$

It is possible to demonstrate that a similar relationship may be obtained when a current, called transport current, is applied along the axis of a cylindrical wire; and, therefore, there is no essential difference between the behaviour of a shielding current and that of a transport current. When a current is applied by an external source and made to flow along the axis of a superconducting wire of radius R , since the magnetic field is excluded from inside a superconducting wire, the current density cannot be uniform across its cross section. In order to maintain $B = 0$ inside, the transport density must, therefore, flow in a surface layer of thickness λ , as illustrated in fig.(1.6), exhibiting an exponential dependence on distance, similar to that for the shielding current, i.e.

$$J(r) = \frac{B_{surf}}{\mu_0 \lambda} \exp \left[-\frac{(R - r)}{\lambda} \right]. \quad (1.9)$$

Using the eq.(1.5), it is possible to find an expression for the magnetic field inside the wire which is equivalent to the eq.(1.9) for the shielding current. This analogous behaviour shows that it is equivalent to ejecting a current in a superconductor, which induces a magnetic field, and to place a superconductor in an external magnetic field (which will produce demagnetization current), in that the current-field relationship will be the same.

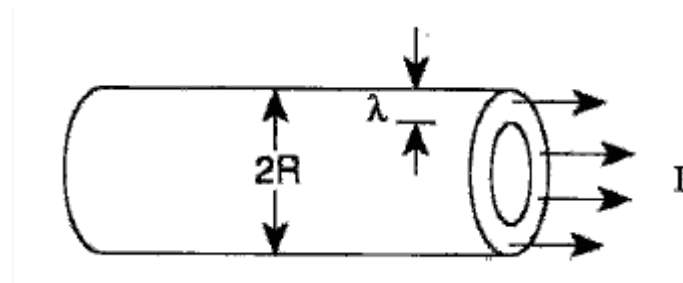


Figure 1.6. Shielding current flow J_{sh} on the outside surface and reverse-direction shielding current [1].

1.4 Penetration depth and coherence length

The two fundamental length scales associated with superconductivity are the penetration depth, λ , and the coherence length, ξ . We have already introduced the former in the previous section, defining it as the mean distance over which an external magnetic field falls off exponentially inside a superconductor. In this section the London equation is presented and the penetration depth, λ , is defined by calculating a solution to the London equation. Moreover, the meaning of the second characteristic length parameter, the coherence length, ξ , is investigated, and a description is provided of how the relationship between these two parameters forms the basis of the definition of the classes of superconductors, type I and type II.

In order to explain the phenomenon of superconductivity, the London brothers put forth an hypothesis [5]: the current density is linear proportional to a vector potential, \vec{A} , according to the equation:

$$\vec{J} = -\frac{-1}{\mu_0 \lambda_L^2} \vec{A}. \quad (1.10)$$

Recalling that the magnetic field \vec{B} is related to the vector potential A by

$$\vec{B} = \nabla \times \vec{A} \quad (1.11)$$

the eq.(1.10) becomes, by taking the curl of both sides,:

$$\nabla \times \vec{J} = -\frac{-1}{\mu_0 \lambda_L^2} \vec{B}. \quad (1.12)$$

If we now consider Maxwell's equation, eq.(1.4), and take the curl of that, the following equation is obtained:

$$-\nabla^2 B = \mu_0 \nabla \times J. \quad (1.13)$$

If the eq.(1.13) is substituted in (1.14), this yields:

$$-\nabla^2 \vec{B} = \frac{-1}{\lambda_L^2} \vec{B} \quad (1.14)$$

which has the variable solution represented by,

$$B(x) = B_0 \exp\left(-\frac{x}{\lambda_L}\right) \quad (1.15)$$

The eq.(1.18), which has the same form as eq.(1.7), provides the mathematical definition of penetration depth: it is a constant expressing the length scale in which the external magnetic field decays exponentially inside the superconductor.

In order to define the second of the two fundamental length scales of superconductivity, the coherence length, ξ , first it is appropriate to provide an overview of the theory of Bardeen, Cooper e Schriffer (BCS), which is a cornerstone of superconductivity, and provides the framework for defining the above-mentioned parameter. When an electron passes in the vicinity of an ion in the crystal lattice, an interaction of attraction is manifested between the two particles due to the opposite sign of the electrical charges of the respective particles. The ion, which in equilibrium is equidistant from the neighbouring ions in the crystal, is displaced toward and approaches some neighbouring ions due to the force of attraction for the electron. A zone of higher positive charge density is thus created that moves like an elastic wave through the lattice. Another electron that passes in the vicinity of the excess of positive charge is subjected, in turn, to an attractive force. Overall, the two electrons are subjected to an attractive force, mediated by their interaction with the crystal lattice, which competes with the electrostatic repulsive force. Moreover, since ions move more slowly than electrons, the comparatively longer residence time of ions in non-equilibrium

positions facilitates the attraction phenomenon and, consequently, the local charge inhomogeneity. The behaviour is increasingly marked as the temperature decreases, because of the limited thermal agitation. In particular, at the critical temperature, attractive forces exceed the repulsive ones, creating a bound state between pairs of electrons (called Cooper's couples) which behave as superelectrons.

The electrons interact only if the mutual distance is below a certain parameter (characteristic of each superconductor) which is called coherence length, ξ . More precisely, ξ is the length scale over which the density of super electrons n_s , a characteristic of the superconducting state, increases from zero at the interface with a normal material to constant value inside the superconductor. The actual coherence length is defined as:

$$\frac{1}{\xi} = \frac{-1}{\xi_0} + \frac{1}{l} \quad (1.16)$$

where ξ_0 is the intrinsic coherence length, whilst l is the mean free path, which expresses the average distance an electron travels between collisions.

The two characteristic length parameters, the penetration depth λ and the coherence length ξ , are linked through the Ginsburg–Landau ratio, κ , defined as $\kappa = \lambda / \xi$. The difference between Type I and Type II superconductors can be expressed in terms of κ , as illustrated in fig.(1.7), [6]. In Type I superconductors $\kappa < 1$, fig.(1.7a), i.e., the coherence length is larger than the penetration depth and it is maintained over relatively large distances within the samples, without being disturbed by the presence of external magnetic fields. Therefore, they exhibit zero resistance and perfect diamagnetism below the critical field H_c , whilst they become normal in higher applied fields. In Type II superconductors fig.(1.30b), by contrast, where $\kappa > 1$, i.e. the coherence length is short

compared to the penetration depth, superconductivity is confined within such a short coherence length that it can still exist with a nearby magnetic field that has penetrated deeply into the sample, for fields with values between the H_{c1} and H_{c2} , as shown in fig.(1.7b). In the next section, a more rigorous definition of Type II superconductors is provided, by discussing it within the framework of the mixed, or vortex, state theory, which is outlined. In fig.(1.7), it is also shown the behaviour of the order parameter $\Psi(x)$ which is a complex scalar usually normalized so that $|\Psi(r)|^2$ gives the number density of Cooper pairs at a point r:

$$|\Psi(r)|^2 = \Psi^*(r)\Psi(r) = n_s \quad (1.17)$$

where $\Psi^*(r)$ is the complex conjugate of $\Psi(r)$, n_s is the number of superconducting electrons and $n_s = n - n_n$, where n is the total number of free electrons, and n_n is the number of non-superconducting electrons.

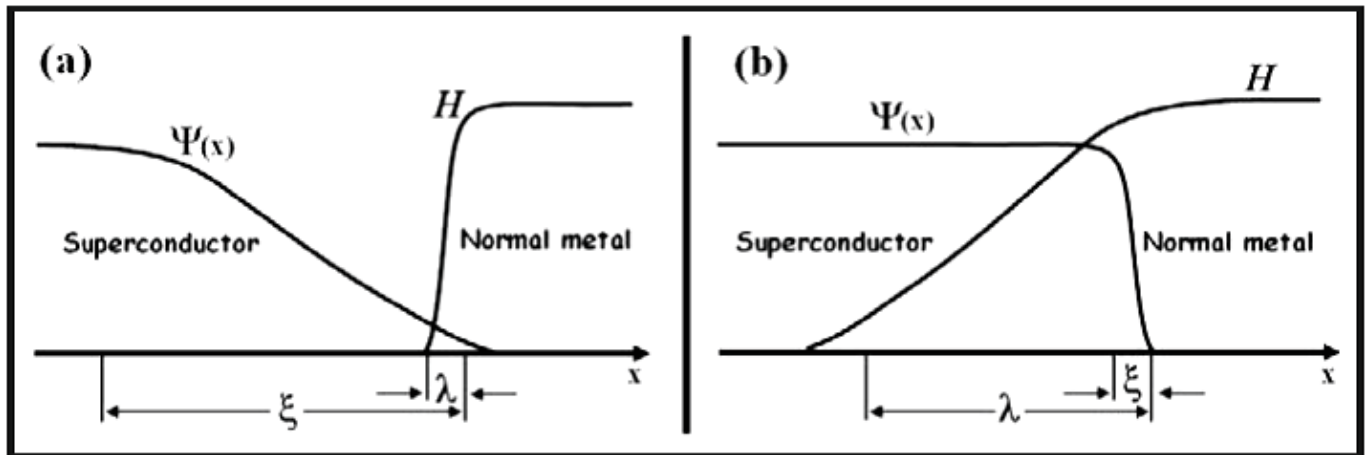


Figure 1.7. Definition of Type I (a) superconductor and Type II (b) superconductor in terms of coherence length ξ and penetration depth λ [6].

1.5 The vortex state

The concepts of the critical magnetic field H_c , lower critical field H_{c1} , and upper critical field H_{c2} can be better understood by observing the mean field phase diagram of fig.(1.8a and b) of the magnetic field versus temperature for type I and type II superconductor [7]. A type I

superconductor expels magnetic flux completely from its interior below the critical field H_c , whilst admitting magnetic fields when H exceeds H_c . A type II superconductor completely expels the field below the lower critical field H_{c1} - this is the Meissner-Ochsenfeld effect. In the intermediate field regime $H_{c1} < H < H_{c2}$ the magnetic field penetrates the sample via flux lines or vortices: this is the Shubnikov phase with vortices arranged in a triangular Abrikosov lattice. Above the upper critical field H_{c2} superconductivity is destroyed, the material is fully penetrated and the normal state is restored. The region in the phase diagram of fig.(1.8b) wherein the applied field is between H_{c1} and H_{c2} is known as the mixed state [7], [8], [9].

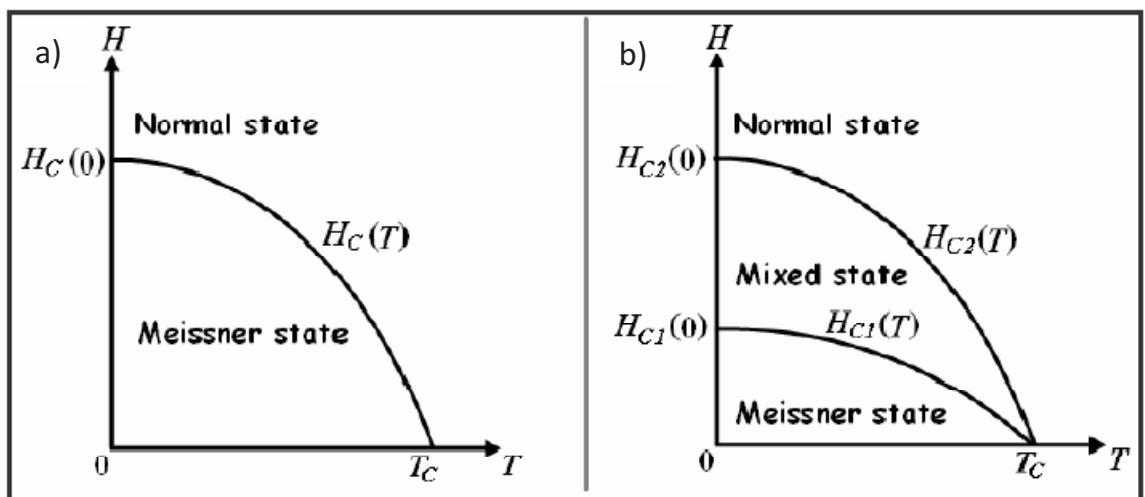


Figure 1.8. Phase diagram of the applied magnetic field versus temperature for (a) type I and (b) type II superconductor [7].

Referring back to the M vs. H curve of fig.(1.2), in an ideal type II superconductor, the magnetisation M rises to a negative maximum at H_{c1} , thereafter it retreats up to zero when the applied magnetic field H is increased up to H_{c2} , and then it exactly retraces its path when H is reduced.

However, no real superconductor gives the exact retracing as described by the ideal curve. In fact, the decreasing- H path of M , which at first retraces the forward path (since the magnetisation is reversible), in

correspondence of a field value, known as the irreversibility field H_{irr} , deviates from the upward curve, and therefore results in M no longer being a single-valued function of H , as shown in fig.(1.9) [10]. The irreversibility line $B_{irr}(T)$, as plotted in the graph of fig.(1.10) for a high temperature superconductor [11], separates the “vortex lattice” phase with vortices pinned or otherwise held in place from the “vortex liquid” with many vortices unpinned or free to move reversibly, but with dissipation. An outstanding feature of the phase diagram of fig.(1.10) is that the irreversibility line represents the boundary between the magnetically irreversible region with nonzero J_c and the reversible region with zero J_c in the field(B)-temperature(T) plane. The concepts of critical current and irreversibility field are closely related in that, in practical superconductors, the goal of maximizing the current which can flow without dissipation is generally pursued by raising H_{irr} as high as possible. In fact, whilst in the region between H_{irr} and H_{c2} energy is dissipated by the freely moving unpinned flux lines, below H_{irr} flux pinning takes place and a finite critical current can flow. The methods which have been proven to be effective in improving pinning properties, both in LTS and HTS compounds and, in particular, in MgB_2 , are described later in the chapter.

In fig.(1.10), it is also indicated that the order parameter $|\psi|$ is equal to zero in the normal state region, whilst it is bigger than zero both in “vortex liquid” and “vortex liquid” regions.

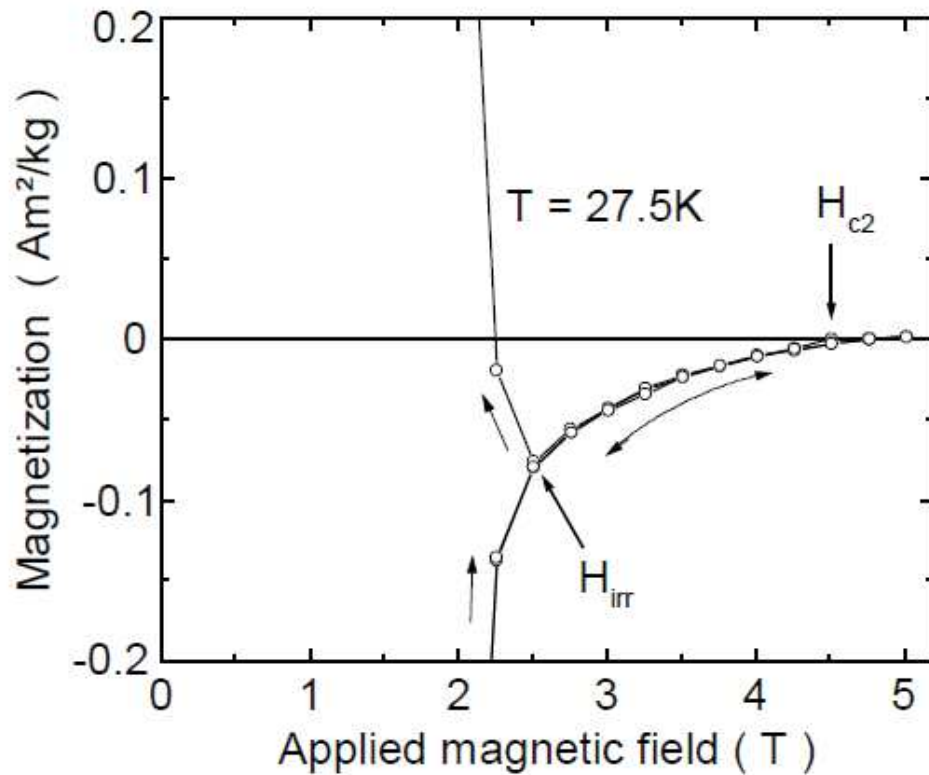


Figure 1.9. Expanded view of magnetization vs. applied field at $T = 27.5$ K of a MgB_2 sample [10]. Arrows mark the upper critical field H_{c2} and the irreversibility field H_{irr} . Arrows are also used to show how the applied field was changed in the different branches of the magnetization loop.

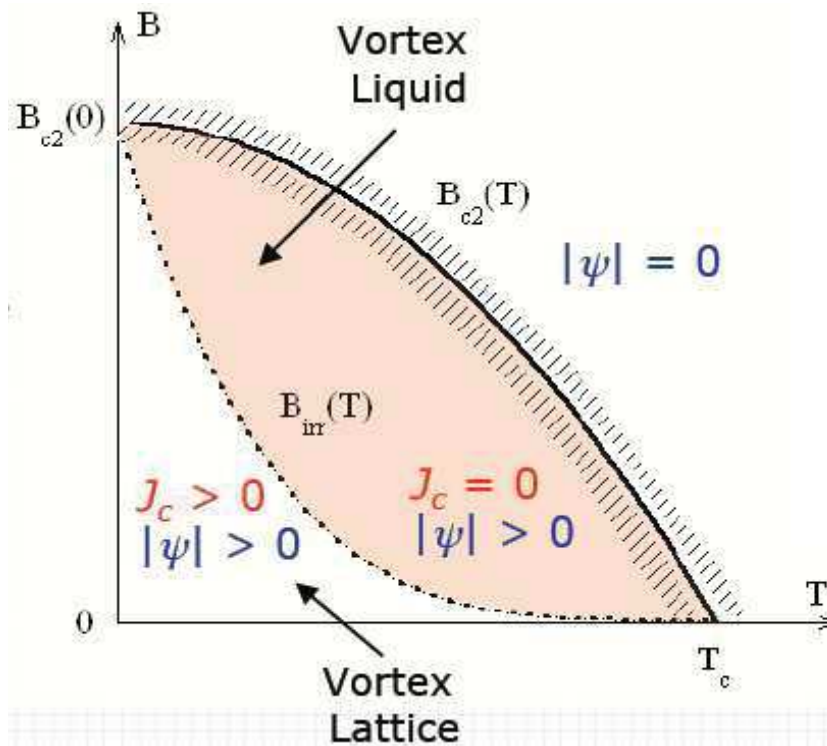


Figure 1.10. Phase diagram of a high temperature superconductor showing the vortex lattice and the vortex liquid separated by the irreversibility line $B_{irr}(T)$ [11]. In the same plot the values of J_c and $|\psi|$ are indicated.

When a magnetic field is first applied to any type of superconductor, the Meissner effect will try to expel that field. Obviously, as the field is increased, it costs more energy to expel it, and the free energy difference between normal and superconducting states decreases. In the case of a Type I superconductor, in the mixed state, there will be the formation of domains of normal material with $\chi \approx 0$ embedded in pure superconducting regions with $\chi = -1$. The boundary between these regions will have a value of energy density per unit area, E_{bound} , of the boundary layer expressed by:

$$E_{\text{bound}} = -\frac{B_c}{2\mu_0} d_{\text{bound}} \quad (1.18)$$

where d_{bound} is equal to:

$$d_{\text{bound}} \approx (\xi - \lambda). \quad (1.19)$$

Since ξ exceeds λ in a Type I superconductor, the resultant boundary energy is positive, so it is not energetically favourable for boundaries to form between their normal and superconducting phases.

In contrast, for a Type II superconductor, the coherence length is short compared to the penetration depth, i.e. d_{bound} is negative, so it becomes energetically favourable for domain walls to form between the superconducting and normal regions. The crossover between the positive and negative boundary energies occurs at $\kappa = 1 / \sqrt{2}$, therefore the domain formation becomes energetically favourable for values of $\kappa > 1 / \sqrt{2}$. These domains, called vortices, are tubular regions of confined magnetic flux having a core radius equal to the coherence length ξ and a surrounding outer region with radius equal to the penetration depth λ , as illustrated in fig.(1.11), [8, 12]. Therefore, for a type II superconductor, λ represents the effective radius of the vortices beyond which the magnetic field decays exponentially to zero, whilst the coherence length ξ can be defined as the distance over which the super

electron density rises from $n_s = 0$ (and $\psi = 0$) at the center of the vortex to its full bulk value.

Mathematically [3], at H_{c1} , in correspondence of which the first penetration of flux lines occurs, a single flux quantum Φ_0 , which, as explained, occupies a core of radius approximately equal to the coherence length, ξ is described by:

$$\Phi_0 = H_{c1}\pi\lambda^2 \quad (1.20)$$

where the spacing between flux lines is equal to the penetration depth, λ .

At H_{c2} the maximum number of flux lines has penetrated the material, the cores are packed tightly, and spaced ξ from each other. Hence, flux quantum will take the following form:

$$\Phi_0 = H_{c2}\pi\xi^2 \quad (1.21)$$

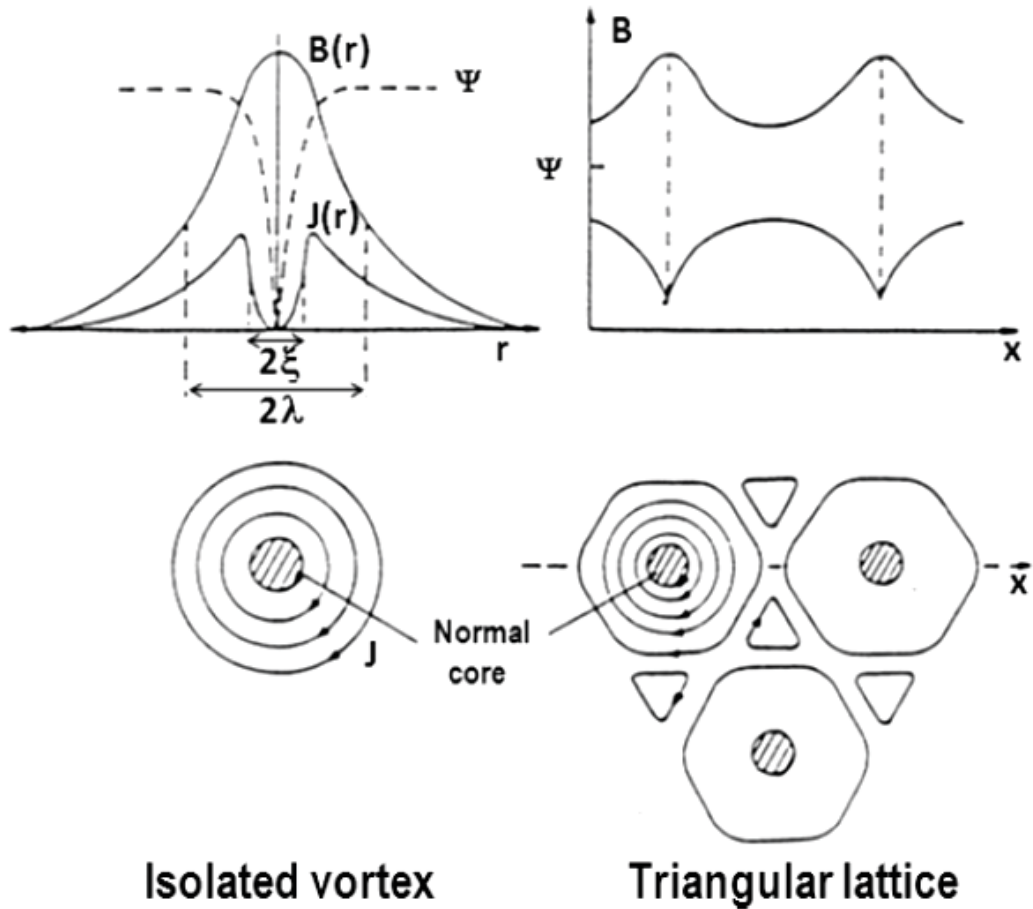


Figure 1.11. Schematical representation of an isolated vortex and a triangular vortex array. In the same figure, shown are also the distribution of the magnetic field B , the order parameter ψ , and the current circulating J around the normal cores [8, 12].

There is, however, a natural tendency for a disruption of such a lattice of flux vortices to occur. In fact, when, between H_{c1} and H_{c2} , a transport current of density J flows through a Type II superconductor, located in a transverse magnetic field, it exerts a force on the vortices, called the Lorentz force, which causes them to move from one side of the sample to the other, according to $F=J \times \Phi_0$, as shown in fig.(1.12), [13]. This flux flow, by Faraday's Law, produces a voltage drop in the superconductor along the direction of the current flow, generating resistivity phenomena which provide the mechanism for heat dissipation. This motion of flux lines can be stopped by impediments such as grain boundaries and impurities, which pin the flux lines, allowing the current to flow without dissipation.

The pinning must be strong enough to maintain the gradient given by:

$$\Phi_0 \frac{d}{dx} n(x) = -\mu_0 J_y(x) \quad (1.22)$$

which has been obtained starting from Maxwell's equation, eq.(1.4), expressing the internal magnetic field $B_z(x)$ as equal to the product $n(x)\Phi_0$, that is, the number of vortices per unit area, $n(x)$, times the flux per vortex Φ_0 . Therefore, the stronger the pinning is, the greater the magnitude of the gradient that can be maintained, and hence, from Eq. (1.22) the greater the current density that can flow without dissipation. In the manufacturing process of superconductors (which constitutes one of the principal matters of the present work) this goal is pursued by introducing many defects into the material in order to offer an abundance of pinning sites for achieving high current densities.

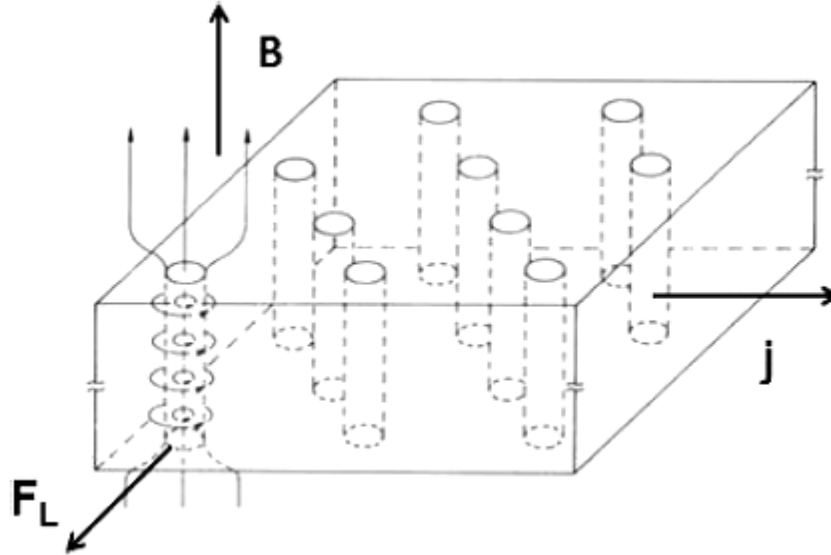


Figure 1.12. Flux lines in a type II superconductor in the mixed state. The Lorentz force F_L acts on each flux line. [13].

1.6 Bean critical state model

In the previous chapter, it has been explained that, in a type II superconductor, the individual lines of magnetic flux penetrating the superconductor behave as small independent vortices, forming a cylindrical region of normal material. In spite of the quantization of the magnetic flux, it is opportune, in order to provide a description of the current density distribution within a superconductor, to adopt a more macroscopic view of the phenomenon and treat it classically.

In a wire, in which the current flows in the z -direction, i.e. $J = (0,0,J_z)$, by virtue of Maxwell's equation, eq.(1.16), the magnetic field \vec{B} must be perpendicular to J whilst the radial component of \vec{B} must be zero. It follows that there will be only a single component of \vec{B} , namely B_θ , and therefore the above-mentioned Maxwell equation reduces to:

$$\frac{dB_\theta(x)}{dx} = \mu_0 J_z(x). \quad (1.23)$$

This relationship means that the field and current density depend only on x , and, in particular, the magnitude of B_θ inside a superconductor decreases with distance from the surface. The current flows where the magnetic field is present, i.e. preferentially near the outer surface of the sample which is said to be in a so-called “critical state”, whilst the interior is shielded from these currents and fields. When the applied field increases in magnitude, the internal field and current densities penetrate inward and, for sufficiently high values of fields, are present throughout the sample. Several models have been proposed for describing the field and current distribution in a superconductor. One of the most widely used of the critical-state models is the Bean critical state model, which has also been employed to calculate J_c via magnetic measurements in this work and is described in this section.

The Bean model states that whenever a current flows in a superconducting wire, it assumes the constant value J_c in the critical state. In the low-field case, in which there is a field- and current-free region near the centre, the internal field at the surface, $x = \pm a$, is equal to the applied field, B_0 , whilst there is a depth, $x = \pm a'$, inside the superconductor at which the internal field drops to zero. The differential equation, obtained by substituting $J_y(x) = J_c$ in eq.(1.28), gives a linear relationship between $B_z(x)$ and x :

$$B_z(x) = B_0 \left(\frac{x - a'}{a - a'} \right) \quad a' \leq x \leq a \quad (1.24)$$

$$B_z(x) = 0 \quad -a' \leq x \leq a' \quad (1.25)$$

$$B_z(x) = B_0 \left(\frac{a' + x}{a' - a} \right) \quad -a \leq x \leq -a' \quad (1.26)$$

The distribution of internal magnetic field, $B_z(x)$, and current density, $J_y(x)$, has been plotted in fig.(1.13a and b). These results imply that only the fraction of the wire needed to carry the current density J_c transports

a current with a value different from zero, and that, when the total current I_0 increases, this thin layer thickens, always carrying J_c . In the high field case, in which the fields and currents exist throughout the superconductor, the internal magnetic field distribution is given by:

$$B_z(x) = B_0 + B^* \left(\frac{x - a}{a} \right) \quad 0 \leq x \leq a \quad (1.27)$$

$$B_z(x) = B_0 - B^* \left(\frac{x + a}{a} \right) \quad -a \leq x \leq 0 \quad (1.28)$$

where B^* is the characteristic field for which the field and current reach the centre of the wire. In fig.(1.13b and c), the distribution of internal magnetic field, $B_z(x)$, and current density, $J_y(x)$, has been plotted, for $B_0 = B^*$ and $B_0 = 2B^*$, respectively.

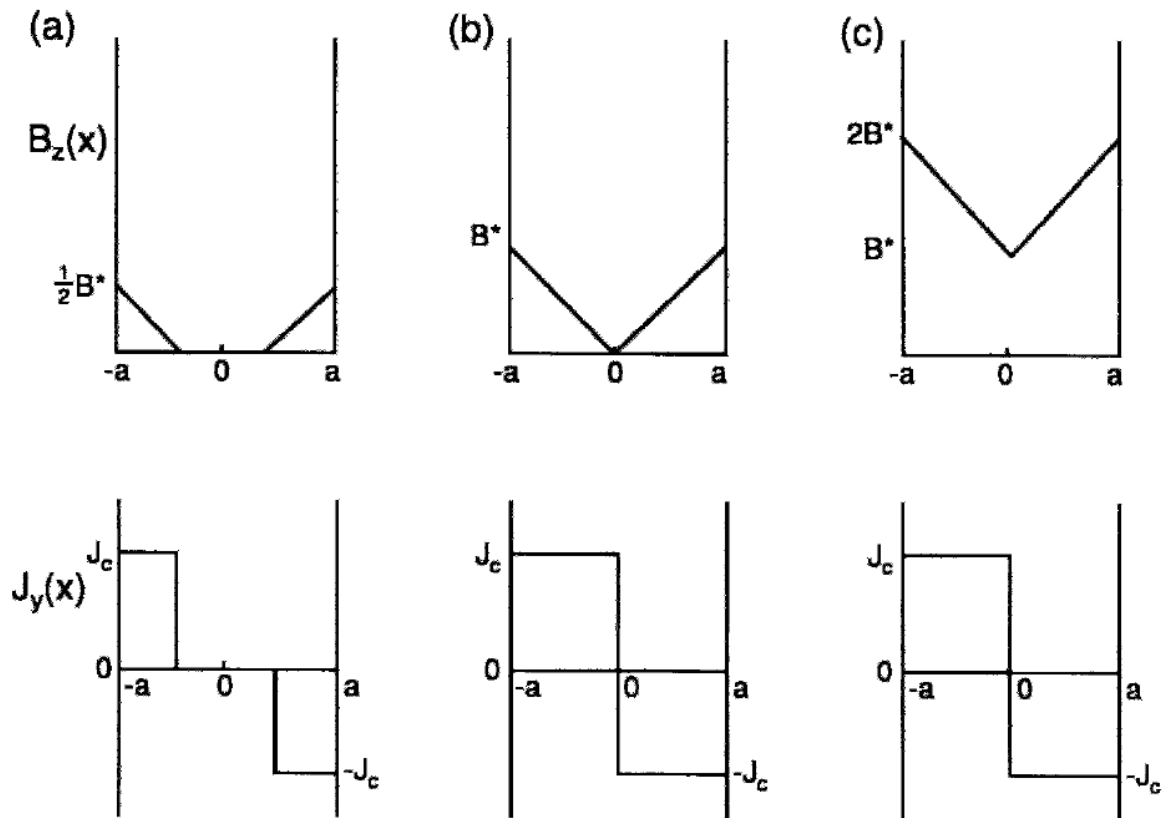


Figure 1.13. Magnetic field and current distribution according to the Bean critical state model in a Type II superconductor. The plots are shown for normalized applied fields given by (a) $B_0/\mu_0 J_c a = 1/2$, (b) $B_0/\mu_0 J_c a = 1$ and (c) $B_0/\mu_0 J_c a = 2$ [1].

J_c values can be derived from M - H hysteresis loop. In order to derive J_c values from the experimentally measured magnetization ones, the Bean

critical state model is used. As described above, this model assumes that critical current flows where the field is present, in accordance with the Maxwell equation (1.3) (this is called a *critical state*), and that, wherever the current flows, it always has the magnitude given by J_c . Therefore, when an external magnetic field H is applied to a superconductor of characteristic dimension t , the relation between the internal field B and the critical current density J_c , as expressed by eq.(1.13), becomes:

$$B = \mu_0 J_c t \quad (1.29)$$

For a rectangular slab (which is the typical cross-section of the samples produced and characterised in this study), the critical current density is determined using the following relation:

$$J_c = \frac{20\Delta M}{t} \quad (1.30)$$

where ΔM is the difference between the two branches of the volume magnetisation hysteresis loop -as shown in fig.(1.14)-, and J_c is expressed in A/cm².

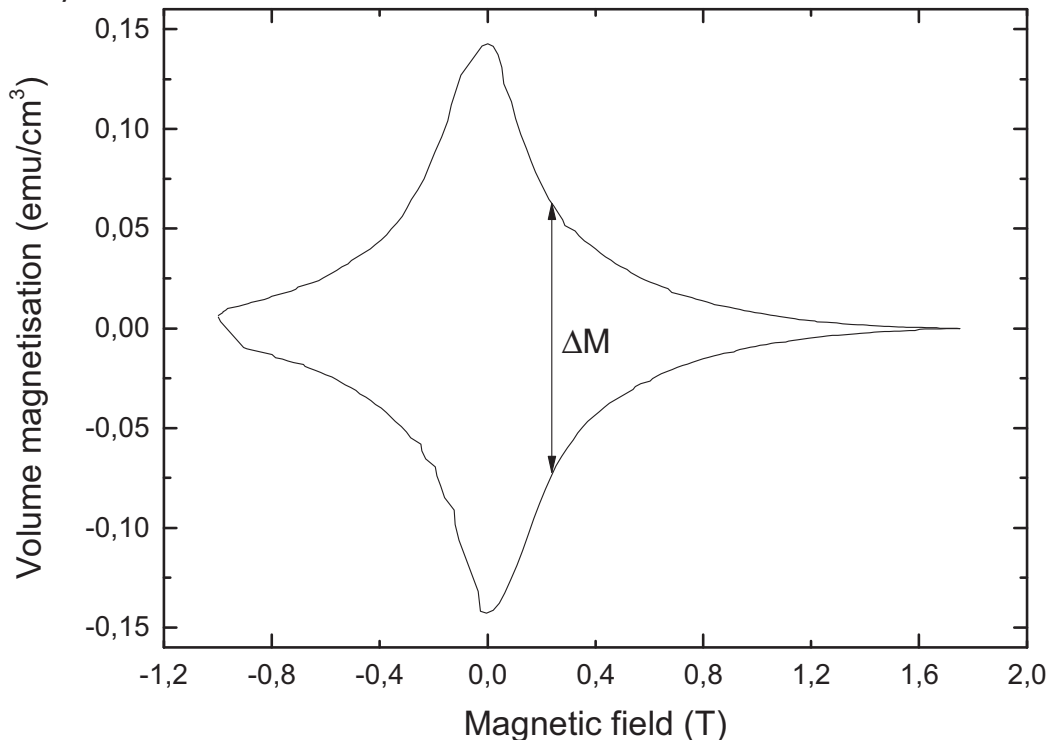


Figure 1.14. Volume magnetisation hysteresis loop used to determine the critical current J_c density as described in the text.

1.7 Historical review of superconducting materials

As mentioned in Chapter 1.1, Hg became the first known superconductor, when Onnes [1] found that below 4.15 K of the dc resistance of mercury dropped to zero. In the first decades after the discovery of superconductivity in Hg, researchers focused their studies on pure elements. In 1913, lead was found to be superconducting at 7 K, while in 1930 niobium was discovered to be a superconductor with a T_c of 9.2 K. A further increase in the superconducting transition temperature was achieved with the discovery of superconductivity in the brittle compounds NbN ($T_c \sim 15$ K) in 1941 [14], and thereafter in Nb₃Sn ($T_c \sim 18$ K) in 1954 [15]. Both materials were type-II superconductors with the upper critical field B_{c2} (25 T for Nb₃Sn) well above those of pure metals. It is also worth noting the discovery of two other interesting niobium compounds, namely NbTi ($T_c \sim 10$ K, $B_{c2} = 10$ T) in 1961, [16], and Nb₃Ge ($T_c \sim 23.2$ K, $B_{c2} = 10$ T) in 1973, [17]. In particular, the latter compound held the record for the highest T_c until 1986, when the observation of superconductivity in Ba-La-Cu-O system initiated the era of high-temperature superconductivity [18]. This definition was introduced to distinguish the new discovered material which, with 35 K, exceeded the critical temperature of 30 K which had theoretically been predicted to be the ceiling for superconductivity from the previously known materials, classified as low temperature superconductors, which all had a T_c of below 30 K. This discovery also unveiled the potential of Copper Oxide systems which, since then, have become subjects of an intense study by researchers. In 1987 the incredible T_c of 93 K was achieved in YBa₂Cu₃O₇ (generally referred to as YBCO), [19] - a big achievement also from an engineering point of view considering that

liquid nitrogen (which is much cheaper than helium) is sufficient to cool YBCO into its superconducting range. In 1988 superconductivity reached 110 K with the discovery of $\text{Bi}_2\text{Sr}_2\text{Ca}_2\text{Cu}_3\text{O}_{10}$ [20], which was synthesized by adding Ca to $\text{Bi}_2\text{Sr}_2\text{CuO}_6$ (known as Bi-2201). The study of the Tl based systems boosted the T_c up to 125 K with the discovery of $\text{Tl}_2\text{Ba}_2\text{Ca}_2\text{Cu}_3\text{O}_{10}$ (Tl-2223) in 1988, [21], a record which was further increased by Berkley *et al.* [22] who reported a T_c for $\text{Tl}_2\text{Ba}_2\text{Ca}_2\text{Cu}_3\text{O}_{10-x}$ under a pressure of 7 GPa. In the nineties the researchers focused their attention to studying the mercury compounds achieving the highest reliable T_c ever measured till date, 164 K, in the $\text{HgBa}_2\text{Ca}_2\text{Cu}_3\text{O}_8$ system under 30 GPa pressure [23]. The discovery of superconductivity at 39 K in MgB_2 in 2001 by Nagamatsu *et al.* [24] opened a new frontier in the application of superconductors. In fact, its transition temperature, which is intermediate between the T_c of LTS and those of HTS, offers the possibility of wide engineering applications in a temperature range of 20–30 K, where the conventional metallic superconductors, such as Nb_3Sn and NbTi , cannot play any role due to their low T_c . In the last fifteen years, great effort has been made to improve the material properties of MgB_2 to meet the performance required for practical applications, and the results of this intense research work will be presented in the following sections.

It is also worth noting the discovery of superconductivity in oxypnictides in 2008 by Y. Kamihara *et al.*, who found $\text{LaFeAsO}_{0.89}\text{F}_{0.11}$ to be superconducting at 26 K [25]. The T_c of this material was further raised by C. Wang *et al.* [26] to 56 K at ambient pressure by replacing La with other rare earth ions of smaller radius, such as Gd, achieving a value of T_c that is second only to the high T_c cuprates.

Fig.(1.15) shows a plot, provided by [27], comparing critical current density performance as a function of magnetic field for the best

literature-reported superconductors. The best J_c performance was reported for metal-organic chemical vapor deposition (MOCVD) grown YBCO double layer tape which achieved the outstanding value of over 10^7 A/cm² at 4.2 K in 20 T when the applied field is parallel to the tape plane [28]. For a better comparison between superconductors, a comparative T - H phase diagram for different superconducting materials is shown in fig.(1.16) [29].

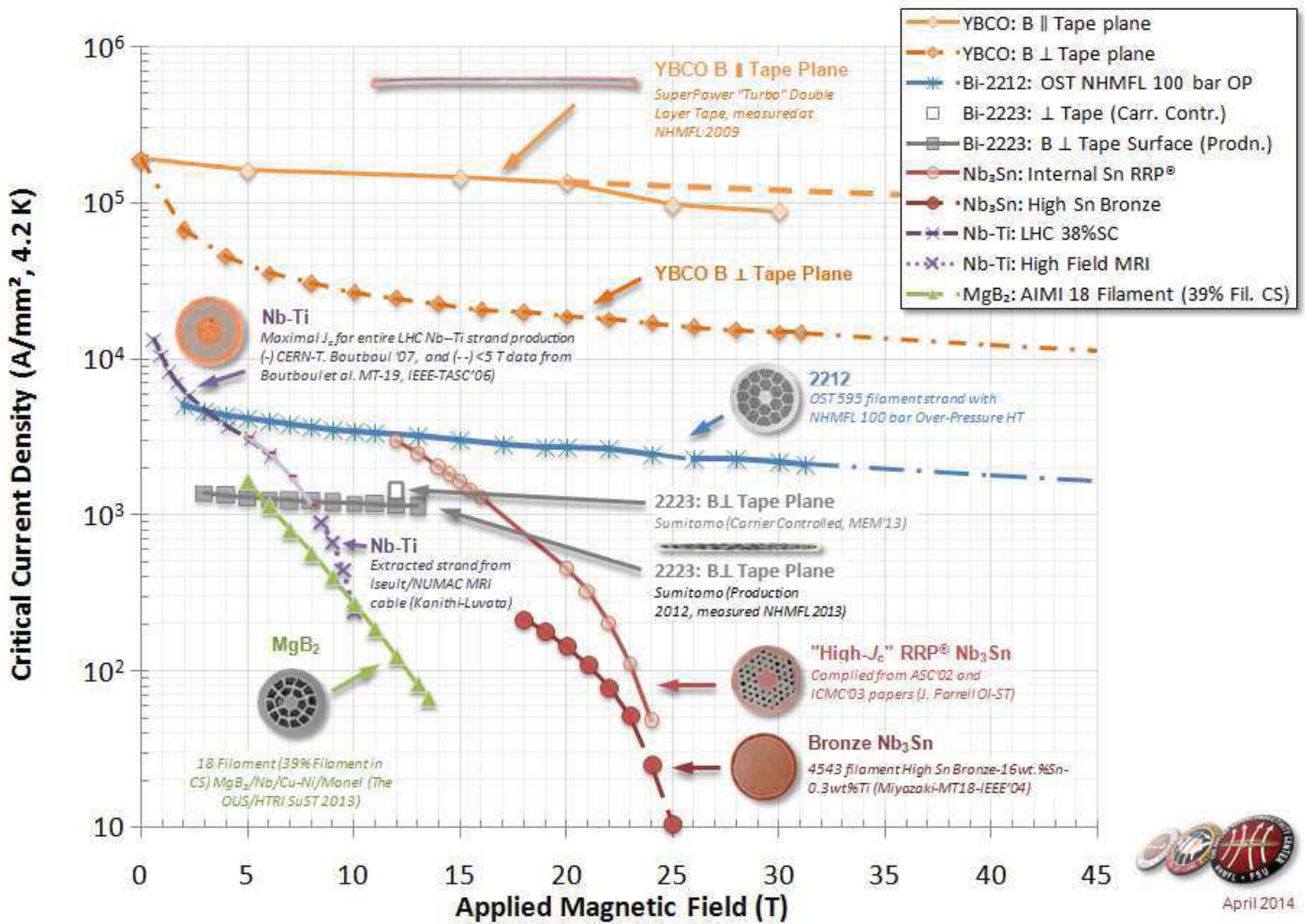


Figure 1.15. Critical current density vs. applied magnetic field for some of the best literature-reported superconductors (the plot is provided by [27]).

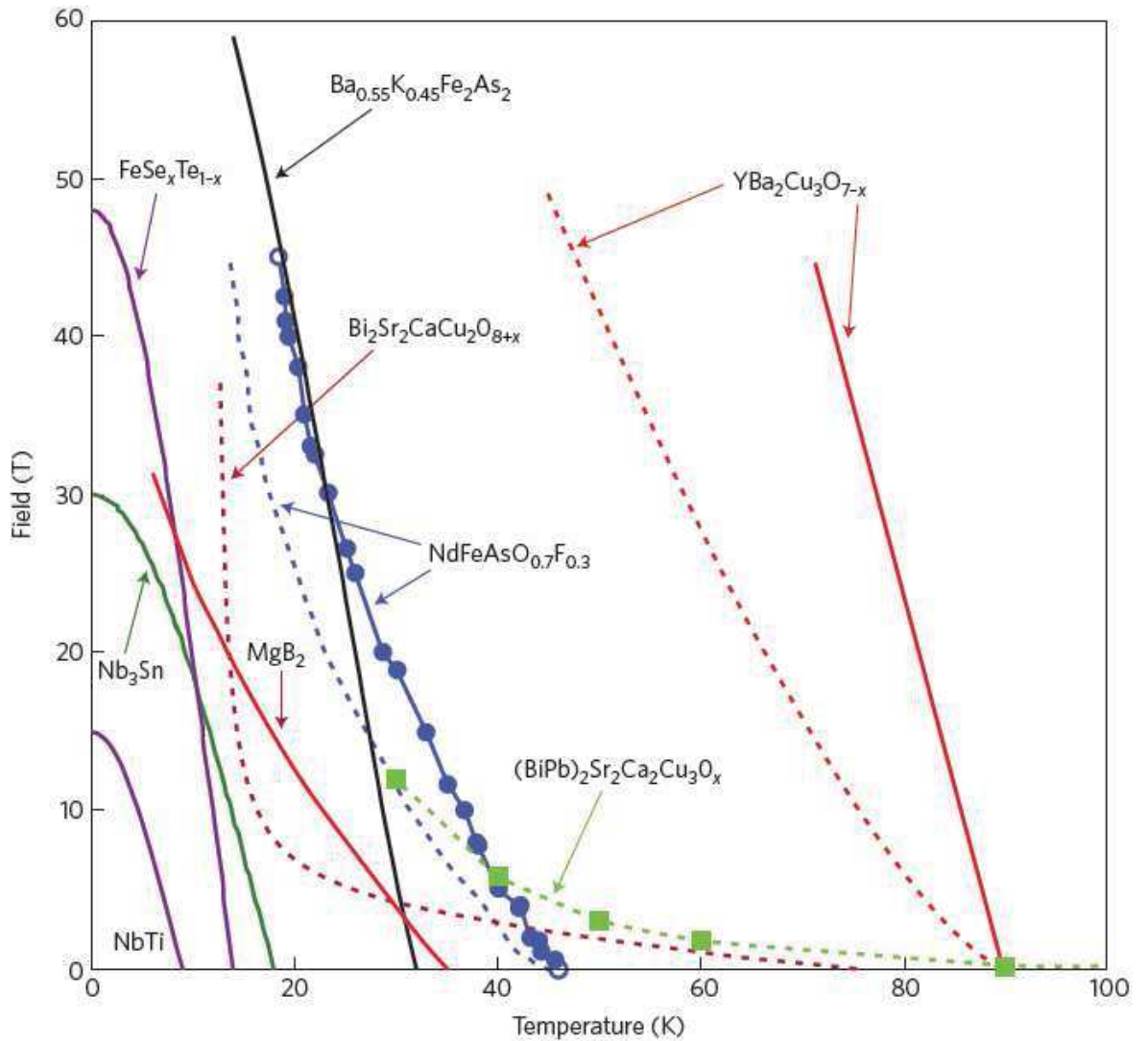


Figure 1.16. Comparative T - H phase diagram for different superconducting materials. The solid and dashed lines show the upper critical fields $H_{c2}(T)$ and the irreversibility fields $H^*(T)$, respectively for H_{c2} , [29].

In order to maximise the pinning strength, thus enhancing J_c , intensive research has been conducted in the field of materials science, attempting to introduce defects into the superconducting materials to offer plentiful pinning sites.

In LTS compounds, the pinning strength was observed to be strongly related to the conditions at grain boundaries. This behaviour was first demonstrated in Nb_3Sn by Schauer and Schelb [30], who found that the pinning force increases inversely to the grain size. This result was then extended to other materials, including MgB_2 , in which reaction at high temperature was found to be detrimental in that it leads to larger grains

and thus to a reduced pinning force. This behaviour can be explained considering that at grain boundaries the periodicity of the lattice is broken, which favours the formation of dislocation and defects that create the condition for a greater number of vortices in that region. The main challenge in these systems is, therefore, reducing the grain size as much as possible in order to achieve the maximum pinning force.

In contrast to LTS compounds, the dominant effect for the pinning behavior in HTS compounds is not the grain boundary type, but the vortex dynamics inside the grains play a decisive role. One of the most successful route to improving the pinning behaviour in HTS compounds is the inclusion of nanoparticles. These additives were seen to enhance the pinning force and, consequently, J_c of REBa₂Cu₃O_y (RE: rare earth elements, RE123) coated conductor tapes using nanoparticles [31]. The addition of RE₂O₃ nanoparticles was also found to be beneficial to the reduction of anisotropy in [32]. Another successful way to create pinning sites is that developed by Civale *et al* who irradiated YBCO with heavy ions, such as tin, in order to produce damaged tracks that serve as containers for flux lines [33]. In particular, they managed to calibrate the irradiation dose corresponding to the expected number of flux lines, so that there was one columnar defect with which to confine each vortex. Such a microstructure, which consists of very long columns of highly defected material, was observed to be capable of enhancing flux pinning, enabling a considerable enlargement of the irreversibility region in the H-T plane.

1.8 Introduction to MgB₂

Our research activity has been focused on the improvement in transport properties of MgB₂ bulk and powder by the optimization of sintering conditions. Since the discovery of superconductivity in magnesium diboride by Nagamatsu *et al.* in early 2001 [24], magnesium diboride has been one of the most widely studied superconductors due to both scientific and engineering characteristics and economic reasons, which will be discussed in more detail in the following sections.

First of all, the critical temperature of about 39 K is intermediate between those of LTS, such as NbTi ($T_c = 9$ K) and Nb₃Sn ($T_c = 18$ K), and those of HTS, such as Bi₂Sr₂CaCu₂O_{8-x} ($T_c \sim 90$ K) and (Bi, Pb)₂Sr₂Ca₂Cu₃O_{10-x} ($T_c \sim 110$ K). This T_c value allows readily available, inexpensive closed-cycle refrigerators to be used rather than the expensive Liquid He cooling system. MgB₂ has also demonstrated to have interesting J_c properties and strong grain coupling due to the long coherence length. These outstanding properties have been explained on the basis of the electronic structure of MgB₂ that is similar to that of graphite, since it is comprised of honeycomb boron layers separated by magnesium layers, as shown in fig.(1.17), [34]. In particular, its electronic structure can be described by an effective two-band model, or better as two coupled (single-band) model superconductors characterized by a strong interband coupling that reduces the large gap and the corresponding transition temperature. The finite interband coupling causes superconductivity to appear always in both bands simultaneously, that means at the same transition temperature. The upper critical field, H_{c2} , which is relatively low in pristine MgB₂ samples, due to the long coherence length ξ and poor flux pinning strength [35], can be significantly enhanced by C doping, neutron irradiation, etc. In particular,

outstanding values of $H_{c2}^{\perp}(4.2) \approx 35$ T and $H_{c2}^{\parallel}(4.2) \approx 51$ T were measured perpendicular and parallel to the ab plane in C-alloyed films [36].

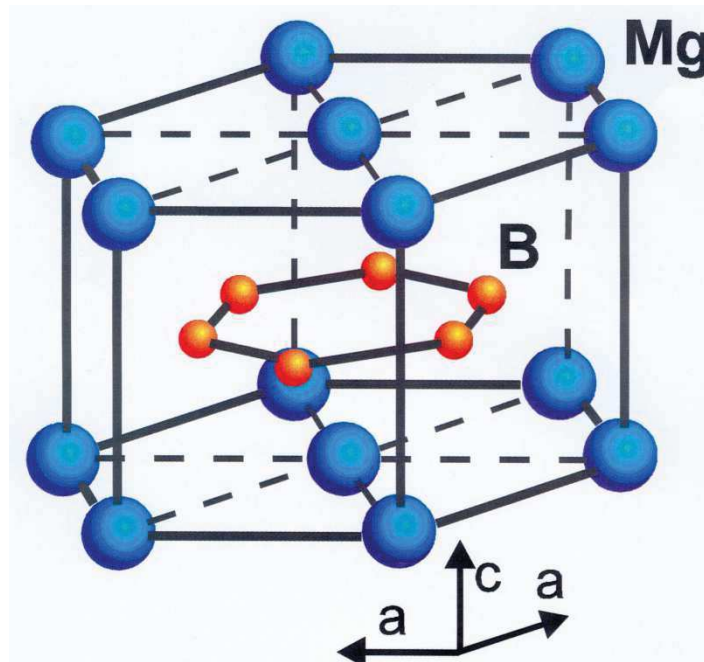


Figure 1.17: Crystal structure of MgB₂: hexagonal layers of boron atoms (orange spheres) are interleaved by layers of magnesium (blue spheres) centred on the hexagons. The lattice constants of the hexagonal unit cell are $a=0.3086$ nm, $b=0.3524$ nm [29].

1.9 Chemical doping of MgB₂

1.9.1 Chemical doping of MgB₂: substitution and addition effects

Of all the approaches targeted for the enhancement of transport properties in MgB₂ bulk samples, one of the methods proven most successful is chemical doping, by virtue of the beneficial effects that addition and/or substitution of chemical elements to the MgB₂ lattice entails.

In the next section, a literature review of the main results achieved in the field of the chemical doping of MgB₂ bulk samples and MgB₂ wires and tapes will be presented. In the present session the mechanisms that lead

to the enhancement of the critical properties of MgB₂ are elucidated by analysing the effects that the improvement of the microstructure by means of chemical doping in particular has on J_c and H_{c2} of MgB₂.

There are basically two kinds of doping effects: substitution and addition effects [37]. With regard to the substitution effect, the dopant substitutes into the B or the Mg crystal site, thus providing impurity scattering of charge carriers and results in changes of the electronic state, lattice distortions, and crystallinity. This will drive MgB₂ to the “dirty limit” and hence enhance the H_{c2} and H_{irr} .

In the case of magnesium diboride, the effects of substituting carbon for boron proved by far the most effective and interesting from the perspective of industrial applications of the material in the area of high currents and high fields, generating great interest in the research community. The substitution of carbon for boron has been found to have a profound impact on the carrier density and impurity scattering. This behaviour has been explained by virtue of the two-gap structure of MgB₂. Carbon, which has one more electron than boron, donates electrons to the σ band resulting in an enhancement of charge carrier scattering occurring on C-substituted sites and Mg vacancies within the two energy bands in MgB₂. This scattering has been thought [38] to be responsible for the considerable upper critical field increase. Gurevich *et al.* have, in fact, pointed out that H_{c2} can only be affected by disorder on a scale smaller than the clean limit coherence length GL , ξ_σ , which is about 8-10 nm, and the increase in H_{c2} therefore indicates a strong scattering on the atomic scale (10 nm) that is most likely due to the C impurities on the B planes.

Instead, the particles doped by addition will remain between the grains only, producing a substantial effect on the grain growth and grain

connectivity, while also having a role in grain boundary flux pinning. With regard to magnesium diboride, the addition of Ti has proved to be very effective in improving the $J_c(H)$ behaviour [39]. Ti does not enter the lattice of MgB_2 , and thus has almost no effect on T_c and H_{c2} . By improving the microstructure, doping with Ti, though, enhances grain boundary pinning in MgB_2 ; consequently, this improves J_c , in particular at low fields. Because the H_{c2} of MgB_2 is relatively low and the improvement of H_{irr} by doping with Ti is very limited, the resulting critical current density performance at high field is quite modest. Moreover, the addition of Ti eliminates the porosity present in the carbon-doped MgB_2 pellets, resulting in an improved intergrain connectivity and an increase of effective current pass.

1.9.2 Literature review on the chemical doping of MgB_2 bulk samples

In recent years, various kinds of chemical doping of MgB_2 bulk samples, including single elements (metal and non-metal), silicates, various carbon sources, and other compounds have been investigated and reported. In particular, doping by carbon and silicon-containing compounds such as carbon nanotubes (CNT), B_4C , SiC , carbohydrate, Si and SiO_2 has attracted the interest of researchers and is generally regarded as the most promising route to higher J_c performance superconductors. In this section, the progress of experimental efforts in the doping of bulk MgB_2 using these doping sources, and also titanium and yttrium, and the effects of these kinds of doping on J_c and H_c will be reviewed.

Promising results on the physical and magnetic properties of MgB_2 bulk made from carbon doped boron powder have been presented by Young

et al [40]. The authors developed a method of intrinsically homogeneous carbon loading by chemical vapour deposition (CVD) of C on to the B precursor powder by using ethylene gas. They have found that CVD coating of boron powder is capable of achieving full carbon substitution at the nominal doping level up to 7%. Moreover, the 4% C-doped sample exhibited significantly high critical current density performance, reaching values as high as 16.5×10^4 A/cm² at 20 K in 2 T, and 5.4×10^4 A/cm² at 5 K in 5 T.

Yeoh *et al* [41] have showed that carbon nanotube-doped (CNT-doped) samples exhibit optimum J_c , in particular at high sintering temperatures ($\geq 900^\circ\text{C}$) at which carbon substitution for boron becomes the preferred process. The same authors have found that the use of ultrasonication favours a more homogenous mixing of CNTs with the precursor powder and improves reaction between the dopant and MgB₂ matrix resulting in a significant enhancement in the field dependence of the critical current density [42]. The reported values are 8.6×10^4 A/cm² at 20 K in 2 T, and 7.2×10^4 A/cm² at 5 K in 5 T, for samples at the 10% CNT doping level.

A comparative study of Yamamoto *et al.* [43] on the doping effects of SiC and B₄C on the superconducting properties of MgB₂ has shown that, although both are effective dopants for improving J_c , the former is preferable in that it provides moderate amounts of carbon even at low temperatures ($\approx 600^\circ\text{C}$). In fact, whilst the magnetic field dependence of critical current density for the B₄C doped samples is significant only for treatment at temperatures of 850°C (J_c reached as high as 4.3×10^4 A/cm² at 20 K in 2 T, and 4.9×10^4 A/cm² at 5 K in 4.7 T), SiC doped samples showed significant J_c properties (the reported values are of 3.7×10^4 A/cm² at 20 K in 2 T, and 3.1×10^4 A/cm² at 5 K in 4.8 T) even in the low-temperature synthesis performed at 600°C . This behaviour, for SiC doping, has been explained by Dou *et al* in their dual reaction model [44],

wherein the fresh reactive C released from SiC at low temperature ($\approx 600^\circ\text{C}$) -at which SiC reacts with Mg to form Mg_2Si - can be easily incorporated into the lattice of the MgB_2 . The possibility of attaining moderate carbon substitution with the low temperature synthesis, combined with the enhancement of grain boundary pinning due to comparatively small grain size and poor crystallinity, is considered to be responsible for the improvement of H_{c2} and, consequently, of J_c at high field for the SiC-doped samples sintered at 600°C .

Wang *et al.* [45] have explored this approach, preparing nano-SiC doped samples by using the hot-isostatic pressing method, and nano-Si and nano-C doped samples, which were used as comparative benchmark. The best J_c performance was measured for the 10 wt% SiC doped sample, which exhibited values as high as $30.3 \times 10^4 \text{ A/cm}^2$ at 20 K in 2 T, and $15.4 \times 10^4 \text{ A/cm}^2$ at 5 K in 5 T. The same authors also observed that the particle size significantly affected pinning, and that the smaller the particles were, the smaller the dimensions of the Mg_2Si impurities phase formed, and the stronger the flux pinning. They claimed that the larger grain sizes of Si and C (40-60 nm), as compared to that of SiC (20 nm), explained the difference in J_c performance in favour of the SiC doped samples.

Excellent $J_c(H)$, particularly at high fields and low temperatures (the reported values were $17.3 \times 10^4 \text{ A/cm}^2$ at 5 K in 5 T), have been achieved by B J Senkowicz *et al.* [46] for pre-reacted MgB_2 doped with C by high-energy ball milling of powdered graphite. The combined effects of carbon doping and grain refinement, which results in a high grain boundary density, are believed to be responsible for both the excess electron scattering, lowering T_c , and the large flux pinning force, enabling high J_c . The authors also found that carbon concentrations higher than 7% depress J_c properties due to connectivity breakdown, resulting in well

connected “islands” in a poorly connected “matrix”, suggesting that excess carbon constitutes a barrier to sintering.

Interesting J_c performance have been reported [47] for MgB₂ samples prepared from 2 h milled and glycerin-treated boron powder which was mixed with magnesium powder and heat-treated at 900°C. The reported critical current density values were as high as 3.7×10^4 A/cm² at 20 K in 2 T, and 5.7×10^4 A/cm² at 5 K in 5 T. These results have been attributed to the enhancement of H_{c2} and J_c due to both the decrease of the grain size and the deterioration of the crystallinity caused by the ball milling of the B powder, and a lattice distortion or strain due to C substitution for B achieved by glycerin addition.

With regard to Si and silicides, it was reported [45] that samples doped with nano-sized (<100 nm) Si powder showed a significantly improved J_c field dependence over a wide temperature range compared to both undoped samples and coarse (44 μm) Si-doped samples. Rui *et al* [48] have successfully synthesised bulk MgB₂ with SiO₂ nanoparticles added. The best J_c performance was obtained for the 7% SiO₂-supplemented sample, reaching 8.2×10^4 A/cm² at 20 K in 2 T, and 4.9×10^4 A/cm² at 5 K in 4.7 T. The addition of SiO₂ nanoparticles was observed to be capable of enhancing J_c at low fields without causing a huge drop in T_c . However, it was ineffective in producing as significant an improvement of J_c at high fields as was produced in low fields, achieved by other dopants such as nanodiamond powder [49]. This discrepancy has been attributed by the authors to the comparatively low pinning efficiency of MgSi₂ inclusions due to their excessively large size (50 nm) as related to the *ab* plane coherence length of MgB₂, which is about 6–7 nm.

Shen *et al* [39] have investigated the doping effects of carbon and titanium on the critical current density of MgB₂. The samples were

prepared by a solid state reaction at ambient pressure using, as starting materials, B powder and Mg powder which were mixed with graphite and/or Ti powders, ground and sintered at 800°C. The results of their XRD analysis and magnetization measurements showed that, on the one hand, Ti does not enter the lattice of MgB₂, and therefore it has no significant effect on T_c and H_{c2} , and limited effect on H_{irr} , resulting in a significant improvement of J_c , mainly at low fields, due to a strongly grain-connected and highly dense structure. On the other hand, C introduces impurity scattering centres in the MgB₂ lattice, leading to a decrease of T_c , but an increase of H_{c2} and H_{irr} , creating a slight reduction of J_c at low fields, but a significant improvement at high fields. The addition of both C and Ti was found to be largely cooperative in improving the superconducting properties of the MgB₂ throughout the whole field range. The authors found that the C-Ti-doped sample has the largest value of the flux pinning force, F_p , for field values above 2 T, which results in the best J_c performance in the range between 2 T and 5 T. Below 2 T, the F_p and J_c values, although slightly lower than those of the Ti-doped sample, are significantly improved when compared to those for undoped and C-doped MgB₂ samples.

Wang *et al* [50] have also studied the superconducting properties of MgB₂ samples doped by addition of Y₂O₃ nanoparticles. The samples were prepared from boron powder, Y₂O₃ nanoparticles and magnesium powder by mixing and sintering them at 900°C. The best J_c performance was measured for the 10 wt.% Y₂O₃ doped sample with values as high as 8.2×10^4 A/cm² at 20 K in 2 T, and 2.7×10^4 A/cm² at 5 K in 5 T. The formation of MgB₂ with a uniform dispersion of YB₄ nanoprecipitates of 3–5 nm size, with larger 10 nm precipitates occurring at grain boundaries, was believed to be responsible of the significantly high irreversibility field and critical current density up to 4-5 T. Above that

field range, the presence of additional phases was observed to impair the superconducting properties of the doped samples.

Listed below in Table 1.1 are the literature-reported values of J_c at 5 and 20 K for the MgB₂ bulk samples doped employing the methods described above.

METHOD	J_c at 5 K	J_c at 20 K
Mg(B _{0.96} C _{0.04}) ₂ prepared with C-CVD doped boron [40]	5.29×10 ⁵ A/cm ² in 2 T 5.4×10 ⁴ A/cm ² in 5 T	4.9×10 ⁵ A/cm ² in 1 T 1.93×10 ³ A/cm ² in 5 T
MgB _{1.80} (SiC) _{0.10} by PICT method [43]	1.17×10 ⁵ A/cm ² in 2 T 3.1×10 ⁴ A/cm ² in 4.8 T	8.14×10 ⁴ A/cm ² in 1 T 2.15×10 ³ A/cm ² in 5 T
MgB _{1.5} (B ₄ C) _{0.10} by PICT method [43]	1.66×10 ⁵ A/cm ² in 2 T 4.9×10 ⁴ A/cm ² in 4.7 T	1.12×10 ⁵ A/cm ² in 1 T 0.9×10 ³ A/cm ² in 5 T
MgB ₂ +10% SiC made by HIP [45]	4.56×10 ⁵ A/cm ² in 2 T 15.4×10 ⁴ A/cm ² in 5 T	5.72×10 ⁵ A/cm ² in 1 T 10.3×10 ³ A/cm ² in 1 T
Mechanically alloyed Mg(B _{0.93} C _{0.07}) ₂ [46]	5.32×10 ⁵ A/cm ² in 2 T 17.3×10 ⁴ A/cm ² in 5 T	
2h milled+glycerin added MgB ₂ [47]	1.61×10 ⁵ A/cm ² in 2.7 T 5.7×10 ⁴ A/cm ² in 5 T	1.03×10 ⁵ A/cm ² in 1 T 0.26×10 ³ A/cm ² in 5 T
7% SiO ₂ -supplemented MgB ₂ [48]		2.9×10 ⁵ A/cm ² in 1 T 0.4×10 ³ A/cm ² in 4.6 T
Mg _{0.95} Ti _{0.05} B _{1.95} C _{0.05} by solid state reaction of mixtures of B, Mg, graphite and Ti powders[39]		1.11×10 ⁵ A/cm ² in 1 T 0.11×10 ³ A/cm ² in 5 T
10 wt% Y ₂ O ₃ doped MgB ₂ [50]	2.19×10 ⁵ A/cm ² in 2.7 T 2.7×10 ⁴ A/cm ² in 5 T	2.07×10 ⁵ A/cm ² in 1 T 0.6×10 ³ A/cm ² in 5 T

Table 1.1: Literature-reported values of J_c at 5 and 20 K for the MgB₂ bulk samples doped as described in Chapter 1.9.2.

1.9.3 Literature review on the chemical doping of MgB₂ tapes and wires

In the previous section, the main results from the literature on the doping of bulk MgB₂ using different types of doping sources have been reviewed and the effects on the superconducting properties of the sintered samples have been described. In this section, in order to provide a more complete picture of doping sources and synthesis methods for MgB₂, as well as to highlight the differences existing with respect to bulk samples, the most successful attempts to dope MgB₂ wires and tapes are reviewed.

Kim *et al.* [51] have investigated the doping effects of single-walled carbon nanotubes (SWCNTs) and multi-walled carbon nanotubes (MWCNTs) on the superconducting properties of MgB₂/Fe wires. The wires were prepared by mixing powders of magnesium, boron, and SWCNT or MWCNTs. With regard to multi-walled carbon nanotubes, two different batches were used with the respective lengths of 0.5 μm in length (MW_{short}CNT), and between 0.5 and 200 μm in length (MW_{long}CNT). The mixed powders were then packed into iron tubes which were drawn to 1.42 mm diameter wires and sintered at 800-900°C. The best J_c performance was observed for the SWCNT doped wire sintered at 900°C, with values as high as 1.04×10^4 A/cm² at 5 K in 10 T. This enhancement of in-field J_c was more significant than that achieved by the MW_{short}CNT doping and much more than that by the MW_{long}CNT doping, and this behaviour was attributed to a comparatively high level of C substitutions into the B sites. These results were consistent with those of T_c , the value of which was estimated to be 35.5 K for the SWCNT doped wire, which is lower than that for either the MW_{short}CNT sample (36.4 K) or for MW_{long}CNT one (37.7 K).

The same author [52] has also investigated the microscopic origin of the increased scattering rate observed in the case of doping with carbon, and

the reasons behind the low-field properties of C doped samples, by undertaking malic acid doping of MgB₂. The wires were obtained using composite powders, prepared by mixing boron powder, toluene and malic acid, drying them out, and then milling them with magnesium powder. The following steps involved putting them into Nb/Monel cladding, drawing them to a final outer diameter of 0.864 mm and sintering at 650°C. The samples exhibited significant J_c properties, and the malic acid was observed to improve both high-field and low-field critical current density (J_c reached as high as 4.42×10^4 A/cm² at 20 K in 3.7 T, and 2.19×10^4 A/cm² at 5 K in 10 T). They found that the microscopic origin of the improved high-field properties is due to boron vacancies. In fact, their analysis showed that boron vacancies generate intrinsic stacking faults within the MgB₂ grains, which causes lattice distortion, and these structural defects were considered to be responsible for the observed increase in the impurity scattering, and therefore for the enhanced upper critical field. Moreover, the inclusion of malic acid leads to boron encapsulation by carbon, which prevents agglomeration during heat treatment, yielding denser packing and a reduction in the percentage of voids from 50% to 40%.

As for doped MgB₂ bulk samples, one of the most promising doping sources is SiC. Matsumoto *et al.* [53] fabricated nanometre-scale SiC-doped MgB₂ tapes by using two precursor powders, MgH₂+B and Mg+B, as starting materials, each of which was mixed with SiC powder of ≈ 30 nm in size. The two resulting mixed powders were then packed into pure iron tubes which were cold rolled into tapes and heat treated at 600°C for 1 h. SiC doping was observed to decrease the sensitivity of J_c to magnetic field and, therefore, to enhance the critical current density properties in samples prepared both from Mg+B powder, and MgH₂+B powder. The best J_c performance (1.52×10^4 A/cm² at 5 K in 10 T) was

obtained for the tape prepared using MgH₂+B powder with a SiC doping level of 10 at%, whilst the tape with M+B powder reached values as high as 0.44×10^4 A/cm² at 5 K in 10 T with a doping rate of 5 at%. The higher value for the MgH₂+B powder has been attributed to the promotion of reaction of Mg and B and the higher density of MgB₂ achievable by using MgH₂+B powder as starting material and to its ability to avoid the oxidation of reacted MgB₂.

The effects of SiC doping on the transport and magnetic properties of MgB₂ wires have also extensively been studied by Kováč *et al.* [54]. They manufactured and characterised four-filamentary MgB₂ wires made by the rectangular wire-in-tube technique (RWIT) and prepared from different initial powders (*ex situ*, *in situ*, *ex situ/in situ* mixture and mechanically alloyed) and sheath materials (Fe, Nb/AgMg, Ti/Cu/Inconel and Ti/Cu/Monel). Ti/Cu/Monel sheathed MgB₂ wires made from mechanically alloyed SiC-doped powder were observed to achieve the best $J_c(B)$ performance at both 4.2 K (2.3×10^4 A/cm² in 10 T) and 20 K (2.37×10^3 A/cm² in 5 T). These results have been attributed to the combined effect of a more pronounced carbon substitution and finer grain structure, which was thought to enhance the grain boundary pinning.

A strong enhancement of J_c , over the whole field range, has been reported by Flükiger *et al.* [55] in *in situ* MgB₂ wires with malic acid (C₄H₆O₅) obtained by Cold High Pressure Densification (CHPD). The C₄H₆O₅ added wires exhibited J_c values enhanced by a factor of 2.1 at 4.2 K (reaching values of 5.1×10^4 A/cm² in 10 T), and even stronger at 20 K (1.12×10^4 A/cm² in 6 T), when processed by CHPD. This room temperature technique was observed to have the effect of both enhancing the mass density of the unreacted Mg + B filament, and to lead to a higher

C content in monofilamentary malic acid ($C_4H_6O_5$) added MgB_2 wires. These densification effects resulted in a higher homogeneity due to enhanced connectivity and were believed to be responsible for the observed enhancement of B_{irr} by more than 1 T, up to 11 T at 20 K.

Li *et al.* [56, 57] have investigated an interesting variant of the *in situ* PIT route, known as the “internal Mg diffusion” (IMD) process, as described by Giunchi *et al.* [58], in which a Mg rod embedded axially in a B-filled tube is subjected to wire drawing and then heat treated. Using fine boron powders *in situ* doped with C from the reduction of CH_4 , they manufactured MgB_2 wires exhibiting both optimum connectivity and high fill factors. The IMD process was observed to eliminate porosity which, on the other hand, develops at the Mg powder sites during heat treatment in PIT MgB_2 wire. These improved structural properties resulted in the enhancement of both critical current density, J_c , and engineering critical current density, J_e , which, in the case of their best sample, a full reacted monofilamentary 2 mol% C doped strand produced by using a reduced diameter of 0.55 mm to obtain full reacted wires, reached the values of 1.07×10^5 A/cm² and 1.67×10^4 A/cm² at 4.2 K in 10 T, respectively. The authors also produced and characterised strands having higher C doping percentages (3 and 4 mol% C). Although the MgB_2 layer J_c was higher for the 3 mol% C sample, the suppression of the MgB_2 layer growth, caused by the increased C concentration, produced a reduction of the non-barrier J_c (defined by taking into account both the area of MgB_2 and the area of the non-superconducting B-rich region) compared to that of the full reacted wires.

Matsumoto *et al.* [53] have also investigated the effect of SiO_2 nanopowder doping for the powder-in-tube processed MgB_2 tapes. They observed that the highest J_c value was obtained by adding 2.5 at% SiO_2

(1.52×10^4 A/cm² at 5 K in 10 T), but higher percentages of doping were observed to have a detrimental effect on the superconducting properties. The SiO₂-doping exhibited a substantial enhancement of the critical current performance at low magnetic fields as compared to undoped samples, however, it did not improve the field dependence of J_c . This behaviour has been attributed to the improvement of the packing density of MgB₂ and of the connectivity of the MgB₂ grains, caused by doping with SiO₂, whilst flux pinning properties were not improved. Unlike SiC, the SiO₂-doping of the tape prepared with MgH₂+B powder exhibited a degradation of J_c with magnetic field, even greater than that of a non-doped tape. The reason for that is thought to be the degradation of MgB₂ core by H₂O which derives from the deoxidation of SiO₂ by H₂ released from the decomposition of MgH₂.

Apart from C and Si, other doping sources, such as Ti and Ni, have proved to be successful in enhancing in-field current density of MgB₂ wires and tapes. Fang *et al.* [59] have fabricated Fe-sheathed Ti-doped wires by stoichiometrically mixing Mg, B, and Ti powders according to Mg_{0.9}Ti_{0.1}B₂. The resulting mixture has been milled in a ball milling for 2 hours, filled in a tube that has been rolled into a square wire first and then flat rolled into a 2.5 mm by 0.2 mm tape, and finally heat treated between 600 and 900°C. They noticed that the field dependence of Ti doped MgB₂ tape was better than that of the undoped sample above 1.5 T (J_c reached as high as 5.8×10^4 A/cm² at 20 K in 2 T), whilst being slightly worse below this field value. This enhanced current carrying capability is thought to be due to the formation of TiB₂ phase within the MgB₂ matrix.

Novosel *et al.* [60] have investigated the structural and transport properties of pure iron-sheathed MgB₂ wires doped with about 1.3 and 2.52 wt% of carbon protected nickel nanoparticles. They observed that, although neither substitution of C for B nor that of Ni for Mg occurred,

doping of MgB₂ with nickel nanoparticles resulted in significant enhancement of J_c at low temperature and high field. The best J_c performance was measured for MgB₂+Ni/C 1.3 wt%, which reached values equal to 1.56×10^4 A/cm² at 20 K in 4 T, and 0.32×10^4 A/cm² at 5 K in 10 T. These results suggested an enhancement of the vortex pinning in doped samples, and the type of pinning mechanisms involved was found to be the same both for undoped and doped samples, namely, the grain boundary pinning. In contrast, no improvement of the critical current density performance at low fields was observed for the wire doped with 2.52 wt% of nanoparticles as compared to the undoped wire. Therefore, there is no evidence for magnetic pinning of vortices by Ni nanoparticles, as instead predicted [61] and observed [62] for MgB₂ samples doped with magnetic nanoparticles.

In addition to the *in situ* route, a different approach, defined *ex situ* technique, has been explored by several research groups to manufacture MgB₂ wires and tapes. Although both fabrication processes are based on the Powder in Tube (PIT) method, the *ex situ* technique differs from the *in situ* one in that the former uses pre-reacted MgB₂, whilst the latter starts from a mixture of unreacted Mg and B. The *in situ* route presents advantages in terms of lower manufacturing cost and reaction process temperature, higher fill factor, and ease in doping the material, all resulting in better J_c performance. On the other hand, the *ex situ* technique has proved to be capable of achieving better homogeneity over long lengths and superior control of the powder granulometry and purity as compared to the *in situ* way: these characteristics have, in recent years, encouraged extensive research activity on the optimisation of the transport and magnetic properties of *ex situ* processed magnesium diboride.

Braccini *et al.* have achieved significant results in the development of MgB₂ mono- and multifilamentary tapes [63, 64] which have successfully been employed in the development of large-scale application devices. In particular, they investigated the effects of the addition of SiC and C and high-energy ball milling of MgB₂ powders on the in-field properties of MgB₂ tapes fabricated by the *ex situ* route of the PIT method. Ball milling was found to both improve the magnetic field behaviour and completely suppress the anisotropy of the critical current at the longest milling time. These effects were enhanced in samples prepared through ball milling of the powders with SiC nanoparticles or carbon, reaching the outstanding value of 10⁴ A/cm² at 13 T in the case of C-doped sample.

The effect of ball milling on J_c and H_{c2} was further investigated by A. Malagoli *et al.* in undoped MgB₂ samples *ex situ* tapes [65]. They found that particle refinement as a result of ball milling decreased the crystallite sizes to a value (estimated at 18 nm) comparable to the mean free path. The resultant density increase of grain boundaries enhanced both the flux pinning force (no additional pinning mechanisms were introduced by the milling) and the upper critical field, H_{c2} (reaching values as high as 9 T at 25 K). This doubly positive effect resulted in J_c reaching 10⁴ A/cm² at 4.2°K in 10 T with H_{irr} values of up to 14 T at 4.2 K in the case of *ex situ* tapes prepared from ball-milled powders. On the other hand, the powder milling process was observed to decrease the connectivity from 12% to 8%, while suppressing both J_c and H_{c2} anisotropy. However, the overall improved J_c performance suggested that the enhanced grain boundary vortex pinning and electron scattering overrode the effect of poorer connectivity in *ex situ* tapes prepared with ball-milled powders.

A. Kario *et al.* have investigated rolled undoped and doped MgB₂ tapes prepared by using high energy milled commercial *ex situ* MgB₂ powder,

[66, 67]. High energy milling was found to reduce J_c anisotropy, as evidenced by the low texture observed in rolled undoped MgB₂ tapes. Carbon doping was seen to further improve J_c isotropy, owing to the reduction of γ , and to enhance J_c in high magnetic fields, explained by the comparatively high values of the temperature dependence of upper critical field, $-\partial\mu H_{c2} / \partial T$. The highest J_c performance was achieved in the C doped tapes heat treated at 800°C/1 h, with values as high as 3.5×10^4 A/cm² at 4.2°K in 9 T, being comparable to the best *in situ* tapes.

The combination of mechanically alloyed precursor powders with nanostructured carbon and PIT tape preparation has been extensively studied by W. Häßler *et al.* [68]. This research group investigated CuNi/Ni sheathed MgB₂ tapes prepared by mechanical alloying of Mg, B and nanocarbon powder. They found that the use of a double sheath, (consisting of an inert inner Nb sheath and an outer Cu₇₀Ni₃₀ sheath), inhibited the formation of a reaction layer. By contrast, the reaction of Fe with B in Fe-sheathed monofilamentary tapes resulted in an interfering Fe₂B layer between the sheath and core material [69]. Since the presence of the Fe₂B reaction layer was believed to hinder current flow into the superconducting core in the case of Fe-sheathed monofilament tapes, the improvements in both the magnetic field dependence of J_c (10^4 A/cm² in 16.4 T at 4.2 K), and the higher values of B_{c2} (12 T at 10 K) and B_{irr} (10.5 T at 10 K) were attributed to the absence of a reaction layer in the CuNi/Ni sheathed MgB₂ tapes.

Listed below in table 1.2 are the literature-reported values of J_c at 5 and 20 K for the MgB₂ wires and tapes doped employing the methods described above.

METHOD	J_c at 5 K	J_c at 20 K
Single-walled carbon nanotubes doped MgB ₂ /Fe wires [51]	1.04×10 ⁴ A/cm ² in 10 T	
Malic acid-doped MgB ₂ wires [52]	2.19×10 ⁴ A/cm ² in 10 T	1.28×10 ⁴ A/cm ² in 5 T
MgH ₂ +B+10% SiC tape [53]	1.52×10 ⁴ A/cm ² in 10 T	
5 wt% SiC mechanically alloyed MgB ₂ wire made by rectangular wire-in-tube technique [54]	2.3×10 ⁴ A/cm ² in 10 T	2.37×10 ³ A/cm ² in 5 T
CHPD processed MgB ₂ wire with malic acid additives [55]	5.1×10 ⁴ A/cm ² in 10 T	1.12×10 ⁴ A/cm ² in 6 T
2% C doped MgB ₂ wire by IMD process [56]	8.9×10 ⁴ A/cm ² in 10 T	
MgB ₂ +2.5% SiO ₂ tapes [53]	2.56×10 ³ A/cm ² in 10 T	
Ti doped MgB ₂ tape [59]		1.36×10 ⁴ A/cm ² in 3.5 T
1.3 wt% Ni/C NPs doped MgB ₂ wire [60]	3.15×10 ³ A/cm ² in 10 T	4.15×10 ³ A/cm ² in 5 T
MgB ₂ <i>ex situ</i> tapes prepared with ball-milled powders with C [63]	2.8×10 ⁴ A/cm ² in 10 T	
MgB ₂ <i>ex situ</i> tapes with 5% C addition [66]	3.44×10 ⁴ A/cm ² in 8.5 T	
CuNi/Nb sheathed tapes with nanocarbon-doped MgB ₂ [68]	6.2×10 ⁴ A/cm ² in 10 T	

Table 1.2: Literature-reported values of J_c at 5 and 20 K for the MgB₂ wires and tapes doped as described in Chapter 1.9.3.

Chapter 2

Doping and coating methods of MgB₂ superconductor and characterisation techniques: experimental details

In this chapter, the technique of chemical vapour deposition of carbon on boron powder and the sol-gel method of coating boron powder by silica are described. Moreover, presented here are the characterisation techniques of x-ray diffraction (XRD), transmission electron microscopy (TEM), scanning electron microscope (SEM), and vibrating sample magnetometer (VSM), that were employed to investigate the physical and magnetic properties of both powder and bulk samples.

2.1 Carbon Chemical vapour deposition method

2.1.1 Overview of the Chemical vapour deposition method

The Chemical Vapour Deposition (CVD) method, as schematically illustrated in fig.(2.1), involves the dissociation and/or chemical reactions of gaseous reactants in a variously activated environment (by heating, light or plasma), followed by the formation of a stable solid product. The deposition involves homogeneous gas phase reactions, which occur in the gas phase, and/or heterogeneous chemical reactions which take place in the proximity of a heated surface, leading to the formation of powders or films.

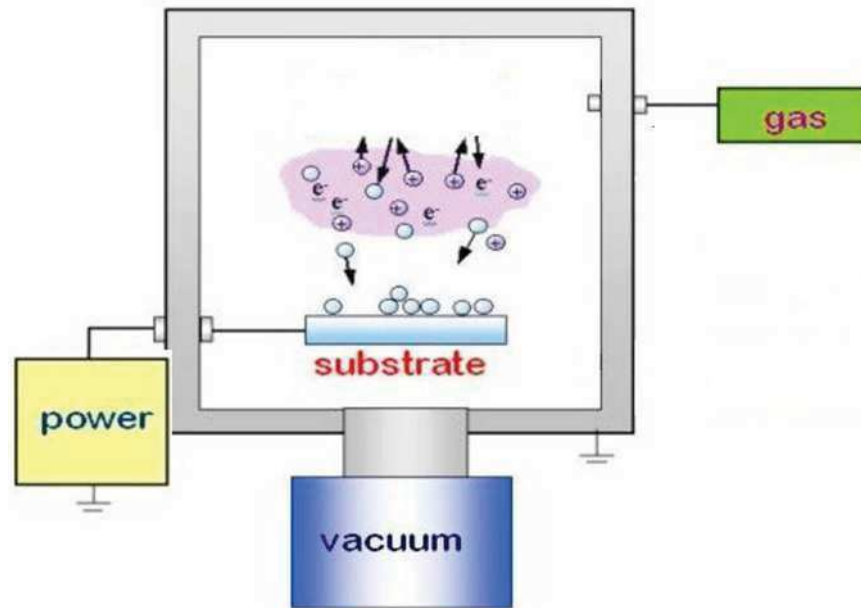


Figure 2.1 Schematic view of the chemical vapour deposition process.

The CVD process consists of three basic steps: (a) the generation of the volatile carrier compound, (b) the transport of volatile compound to the deposition zone, and (c) the chemical reaction to form a solid product. These three distinct steps can be easily identified, for example, in the process of coating metallic tantalum on steel components [70]. The tantalum pentachloride, generated by flowing chlorine over heated tantalum powder, is swept along in a stream of argon and mixed with hydrogen. As the mixture enters a deposition chamber, which has been pre-heated at 1000°C, the $TaCl_5$, is reduced by the hydrogen to form a coating of metallic tantalum on the target surface. In some cases, the preliminary step of generating the volatile species is unnecessary because it is readily available as a gas. For example, this is what happens in the deposition of carbon from ethylene gas, the process which was used in this research project to coat boron particles. In other cases, such as the “pack” processes for aluminising steel or nickel surfaces source, sample and carrier are all mixed together. When the whole pack (a mixture of powdered aluminum, ammonium chloride and powdered alumina) is heated the ammonium chloride decomposes to generate

hydrogen chloride and, then, aluminum monochloride after having reacted with aluminum. The reaction of aluminum monochloride, at the surface of steel and nickel parts, leads to the formation of iron or nickel aluminide.

The formation of a CVD layer is controlled by nucleation on the substrate surface. Growth is observed to start at specific nuclei and then to spread outwards from these nuclei until a complete layer is obtained. This type of growth tends to generate well-ordered structures which are usually porosity-free and have density close to the theoretical values of the final reaction products. The thickness of deposits is limited by the stress incorporated in the deposit, which is caused by the competition between neighbouring growth centres, and that generated by the difference in thermal expansion coefficients between the coating and the substrate. Moreover, the nature of the mechanism involved determines the extent to which the coating bonds to the substrate.

Interdiffusion is probably the most powerful bonding factor with CVD coatings but, in order to develop a sufficiently strong bond, high deposition temperatures and some interaction between coating and substrate are required (as happens between titanium carbide and sintered tungsten carbide at 1000°C). At lower deposition temperatures, bonding is best achieved with rough surfaces which give a mechanical key and by removing any interfering oxide or halide layers.

2.1.2 Chemical vapour deposition of carbon on to the boron precursor powder

As mentioned earlier, the carbon doping of boron precursor powder was achieved by chemical vapor deposition (CVD) method using ethylene gas. The nano boron powder supplied by Specialty Materials Inc, with a grain size of 20-100 nm and a purity of 99%, was placed inside a titanium foil

in a dedicated stainless steel tube furnace (previously evacuated using a rotary pump). It was then treated with ethylene gas supplied by BOC with a purity of 99.92% at various pressures and for different dwell times. The process conditions (gas partial pressure, dwell temperature and duration of the process) have been determined based on the targeted amounts of C doping and will be detailed in the discussion of carbon-doped magnesium diboride powder and bulk samples in the following chapters. The proposed mechanism for the reaction of C-CVD coating of boron powder is as follows:



The chemistry of this process was previously investigated for thermal decomposition of ethylene on Pd [71]. The results reported have shown evidence of how ethylene thermally decomposes at a temperature that depends on the presence of a catalyst, first into ethynyl (CCH), a stable intermediate in the ethylene dehydrogenation. In the second stage of the reaction, raising the temperature brings the decomposition of CCH to completion, and carbon adatoms form on the Pd (110) surface. In order to verify whether in the case of boron an absorption of carbon species occurs, it would be necessary to investigate the process at reaction temperatures sufficiently low so that only the ethynyl species is present.

The C doped boron powder was then reacted with magnesium rod supplied by Sigma-Aldrich with a purity of 99.9% to prepare C doped MgB₂ powder and bulk samples.

2.2 Sol-gel method

2.2.1 Overview of the sol-gel method

The first studies of the sol-gel method are attributed to Ebelmen and Grahan who studied the formation of silica gel starting from silicon alkoxides in 1846. Interest in this synthesis methodology, however, has greatly increased in recent decades in response to the rising demand for innovative materials and alternative techniques for their synthesis. Through the sol-gel method it is possible to synthesize inorganic materials (oxides, glassy materials) in the amorphous polycrystalline state as well as hybrid materials. The method, owing to the numerous adjustable parameters, enables the production of materials with a high degree of homogeneity and purity in either bulk form or in the form of thin layers.

The sol-gel method is classified as a "soft chemistry" synthesis methodology, in that the solid state is obtained starting from low temperatures, operating in particularly mild experimental conditions, unlike other techniques which require more severe operating conditions.

From a chemistry point of view, the process involves a series of hydrolysis and condensation reactions, the first stage of which involves a "sol" or colloidal suspension; the next step involves the formation of the "gel", which consists of a rigid grid still immersed in the liquid. Depending on the subsequent processing of the gel, it is possible to obtain materials in bulk form, thin films, powders, or fibres.

The precursors generally used within the sol-gel method can be alkoxides, acetates or inorganic salts like chlorides and nitrates. Alkoxides are the most commonly used precursors (in the sol-gel process), both because of the existing M-O bond, and because the chemical-physical characteristics

vary according to the nature of the M and the alkoxide groups to which they are bound. In general, the reactivity to hydrolysis is particularly strong for transition metal alkoxides due to the fact that the metallic centre is susceptible to nucleophile attack and can increase its coordination number. In the case of silicon the reactivity is less pronounced because the Si-O bond is less polarized than the M-O one.

2.2.2 Sol-gel method stages

The sol-gel process involves four principle stages, represented schematically in fig.(2.2) below [72].

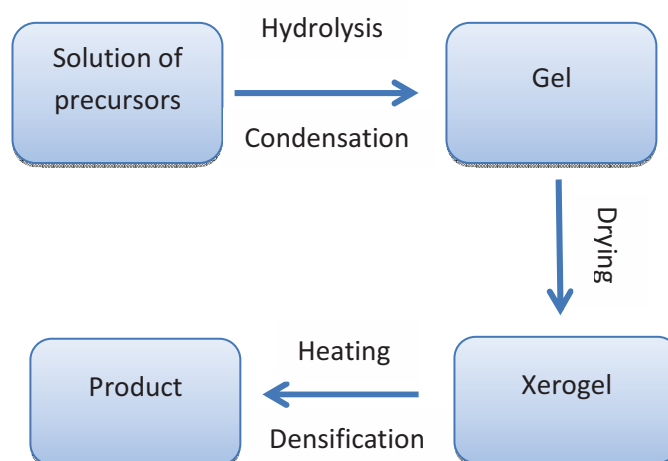


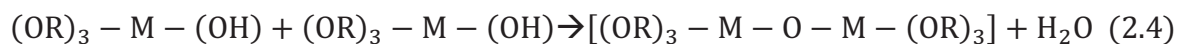
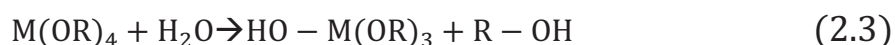
Figure 2.2: Sol-gel method stages.

2.2.2.1 Solution of precursors

The preparation of the precursor solution requires the mixing of different agents: the precursor(s), the organic solvent, water for hydrolysis reactions and, if needed, the catalyst.

2.2.2.2 Sol-gel transformation

As mentioned previously, the reactions that determine the transition from sol to gel are, in the case of alkoxides, of two types:



The above are competing reactions of hydrolysis and condensation, respectively, that are triggered when preparing the solution of the precursors; it is difficult to study them separately.

Such reactions lead to the formation of a gel, a structure partially solidified in the lattice containing one part solvent and a certain amount of water that is not used in the hydrolysis as well as the water produced following the condensation of the hydrolysed species. If the condensation reactions take place before the hydrolysis is complete, it causes premature gel formation and the resulting gel still contains organic groups. This effect may be more or less marked depending on the operating conditions.

The parameters that most affect the course of the reaction and the properties of the final material are the nature of the catalyst and the pH of the solution; they influence, in fact, both the speed of the various processes and the structure of the material. In the case of acid catalysis, the rate of hydrolysis decreases as the reaction progresses so that the polycondensation starts before the hydrolysis is complete. In this case, the structures formed are of the linear type, with few branches. The gel obtained is solid and has high density. The opposite occurs in the case of basic catalysis, in which the polymers that are formed are much more extended and branched but not interconnected. A progressive cross-linking occurs, joining the various cells in the course gel formation. After drying, a low density gel in particulate form is obtained, which is more porous than the previous form. The gelation of the solution is evidenced by a sharp increase of system viscosity (gel point). The time needed to complete this transformation depends on the working conditions.

2.2.2.3 The ageing of gel

The gelation time depends on the composition of the starting solution, the nature of the precursors and the temperature at which the process takes place. Furthermore, the type of catalyst is fundamentally important. As mentioned above, it influences the microstructure of the gel. From this moment onwards, the properties and the structure of the gel continue to evolve, during an aging process during which numerous phenomena occur. Among these, the most important may be classified as [73]:

- Polymerisation: due to the condensation reaction which occurs after the gel point and which leads to the formation of new M-O-M bonds.
- Syneresis: owing to the spontaneous shrinkage of the system following an increase in number of M-O-M bonds formed by condensation and by the movement of strands of solid phase, fig.(2.3). This shrinkage and expulsion of liquids from pores proceeds until the system remains flexible.
- Segregation: due to the gel aging phenomena of phase separation and crystallization can occur, which cause the formation of inhomogeneities within the system. Many hydrated oxide-based gels are amorphous when freshly formed, but gel aging allows a reorganization of the structure by dissolution and re-precipitation, thus giving rise to a crystalline product.

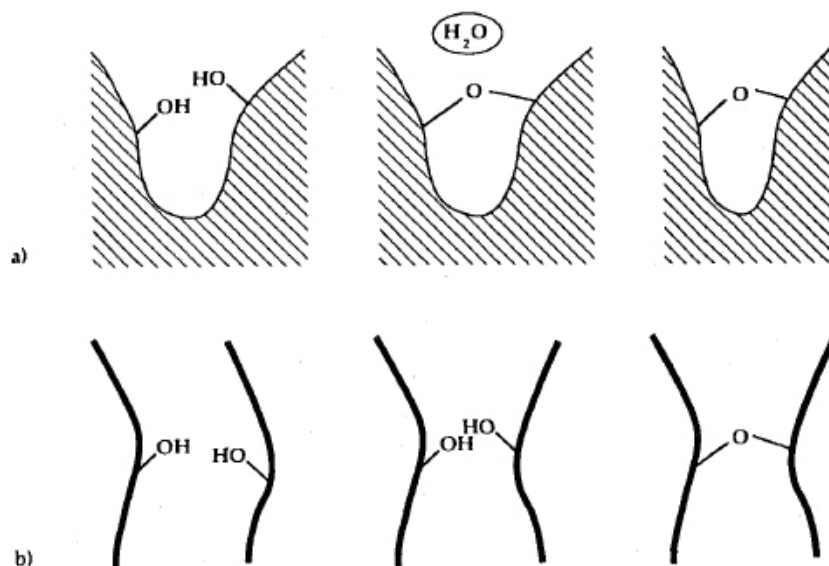


Figure 2.3 Bond formation produces shrinkage due to the condensation between two neighbouring group (a) and to the movement of flexible chains (b), [73].

2.2.2.4 Drying

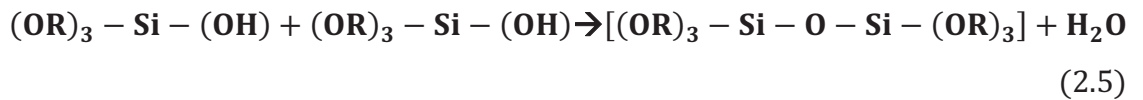
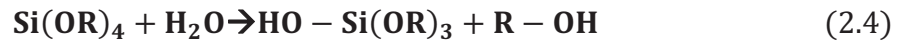
The next phase(drying), which is accomplished by subjecting the gel to a temperature slightly above ambient (50-60°C),is intended to remove the solvent and the water present in the solid formation. In this way, a marked reduction in the system volume occurs as well as a densification of the *xerogel* formation.

2.2.2.5 Densification (Sintering)

The last phase of the process is densification (sintering). In this phase, the xerogel is heated to a high temperature to obtain a compact structure with glassy and polycrystalline characteristics. The temperature of the reheating process depends on the characteristics desired in the finished product. In general, because of the gradual increase in temperature, the xerogel shrinks with a concomitant loss of weight due to the removal of residual organics and driving off the remaining water. Additional treatment at elevated temperatures (>500°C) can induce sintering phenomena or a phase transition.

2.2.3 Preparation of SiO₂-doped Mg(B_{1-x}C_x)₂ using Silica by Sol-Gel method and C-CVD coated Boron

The coating of nano-sized boron powder with silica has been performed by using the sol-gel method. This versatile technique involves two competitive hydrolysis and condensation reactions as follows:



where R=CH₂-CH₃.

The reagents ethanol, tetraethyl orthosilicate (TEOS) and aqueous ammonia (38 wt%) (NH₃), pure grade, were all obtained from Aldrich and were used without further purification.

0.5 g of boron was mixed with 500 cm³ of ethanol and sonicated in ultrasound bath for 5 minutes to achieve good dispersion. 53 cm³ of ethanol, 1.2 cm³ of precursor TEOS, Si(OC₂H₅)₄, and 3.5 cm³ of aqueous NH₃ (catalyst) was slowly added to the suspension of boron at room temperature under vigorous stirring. The solutions were allowed to react for 12 hours under stirring followed by separation of a dark brown precipitate using filtration. The solid sample was thoroughly washed with ethanol, filtered and dried at room temperature. The resultant percentage of silica included into boron powder was 16 wt%. Silica-coated boron was also subsequently coated with carbon using the CVD technique detailed in the Section 2.1.

2.3 X-ray diffraction (XRD)

2.3.1 X-ray diffraction (XRD): basic principles

In general, diffraction occurs when a wave scatters from a set of regularly spaced surfaces that are separated by a distance which is of the same order of magnitude as the wavelength of the wave. On the other hand, given the nature and characteristics of the lattice, reflection is not always possible, even when the above conditions are satisfied, but it is also subject to some special angular relationships between the incident direction and the plane involved. There will be constructive interference if the path length of each wave is equal to an integral multiple of the wavelength, that is, if it satisfies Bragg's Law:

$$n\lambda = 2d \sin \theta \quad (2.6)$$

as shown in fig.(2.4).

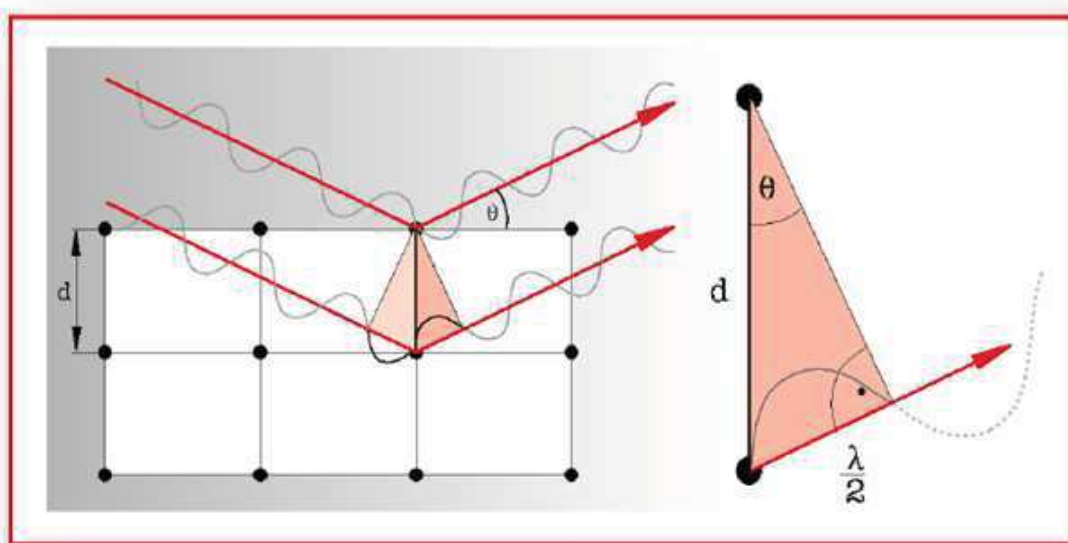


Figure 2.4: Fundamental Principle of X-Ray Diffraction Analysis (XRD).

This is accomplished using a diffractometer designed according to the Bragg-Brentano geometry, fig.(2.5), i.e. by placing the disk containing the sample in the form of powder or bulk in the direction of the incident beam and tilted by an angle θ while a detector rotates around to it on an

arm at twice this angle. The X-ray source consists of a Coolidge tube while the detector is a CCD camera that captures the detected diffraction image.

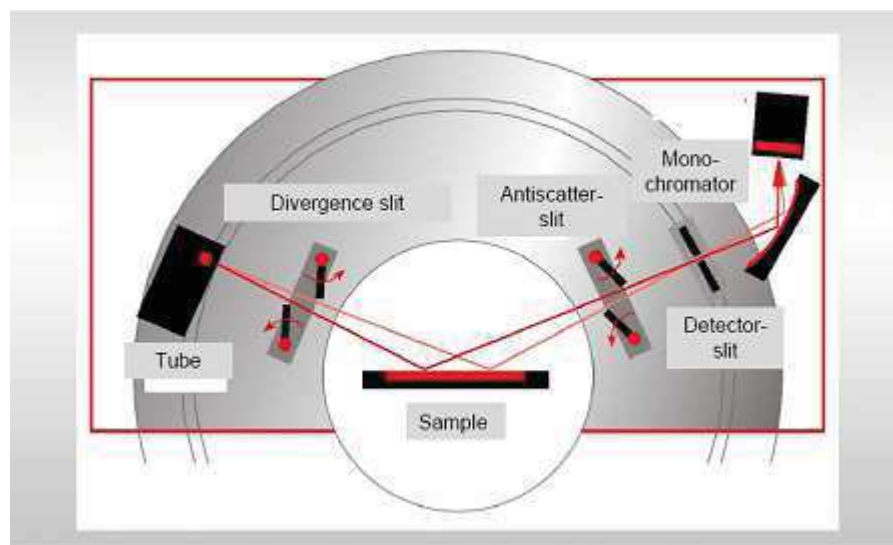


Figure 2.5.: Bragg-Brentano geometry.

The diffraction spectrum, in which the intensity data is represented as a function of the diffraction angle, represents the projection of the reciprocal lattice in the 2θ -monodimensional space.

The XRD is a very powerful non-destructive technique since it is capable of performing different types of analysis by comparing the diffraction pattern with a known standard diffraction pattern or to a database. The most widespread and also the uses most related to our research activity are the identification and characterization of materials, in order to identify the constituent phases, the degree of crystallinity and the quantitative analysis of lattice parameters, in as much as the latter two are an indicator of the level and homogeneity of carbon doping.

2.3.2 X-Ray Diffraction of MgB_2

The structural properties of MgB_2 were investigated using a Bruker D2 PHASER diffractometer. In particular, X-ray diffraction allows us to estimate the amount of carbon included (defined as the actual carbon

content) in the magnesium diboride lattice. Carbon doping of MgB_2 , in fact, results in highly anisotropic lattice contractions: the in-plane a -axis dimension is sharply reduced, while the interplane c -axis is unaffected, as shown in fig.(2.6) (a) and (b), [74].

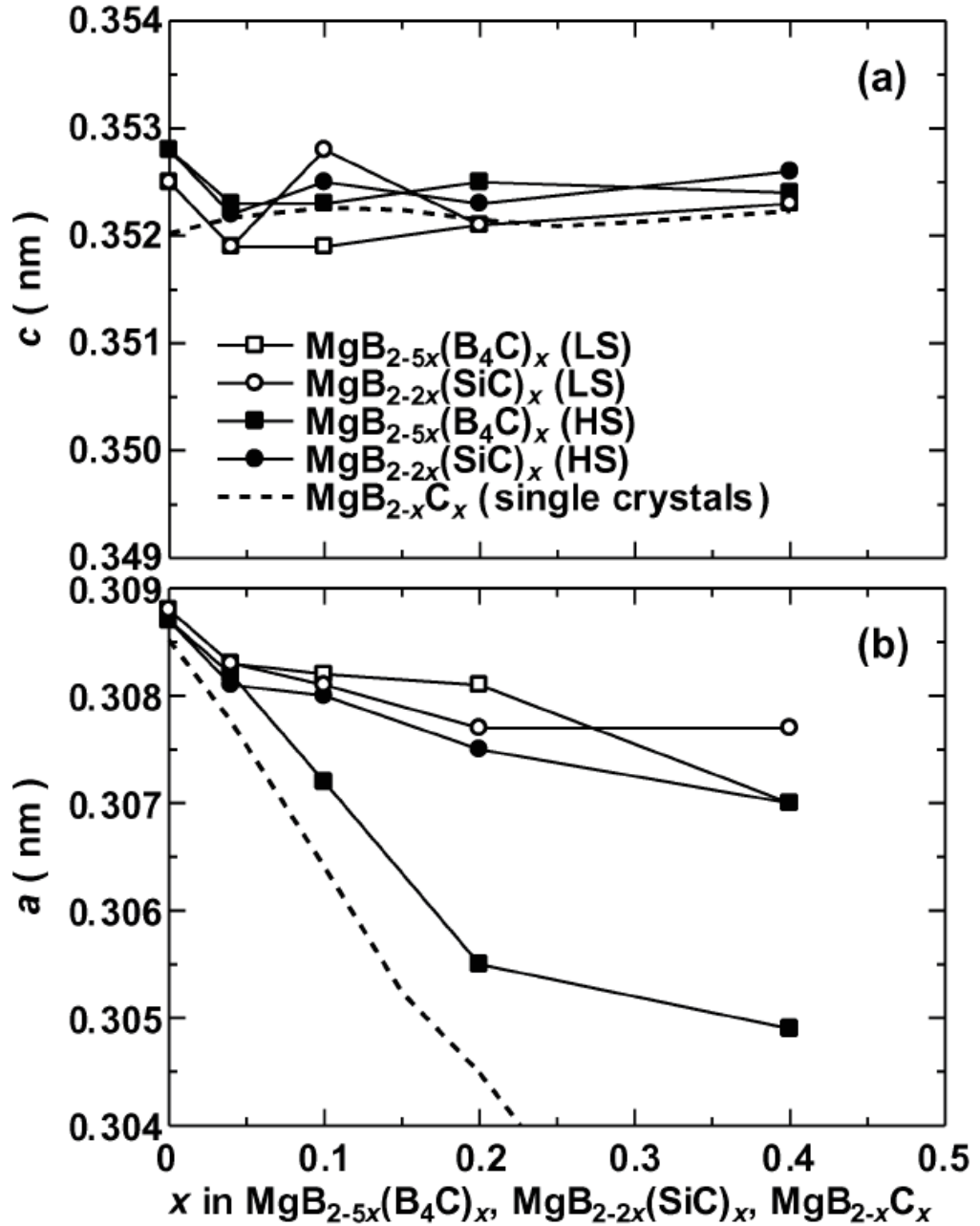


Figure 2.6. Lattice parameters c and a as a function of the nominal carbon content x in the B_4C doped $\text{MgB}_{2-5x}(\text{B}_4\text{C})_x$, SiC doped $\text{MgB}_{2-2x}(\text{SiC})_x$ bulks and carbon substituted $\text{MgB}_{2-x}\text{C}_x$ single crystals. LS=650°C, HS=850°C. The c lattice, shown in (a) remains unaffected, but the a lattice shown in (b) contracts with increasing x [74].

In order to estimate the carbon content, x , of samples, $\text{Mg}(\text{B}_{1-x}\text{C}_x)_2$, an empirical result obtained through synthesis and structural analysis of

single crystal, [75], was used as a calibration. The data for the single crystals, plotted as the shift in the a -axis against x , is shown in fig.(2.7) together with a linear fit.

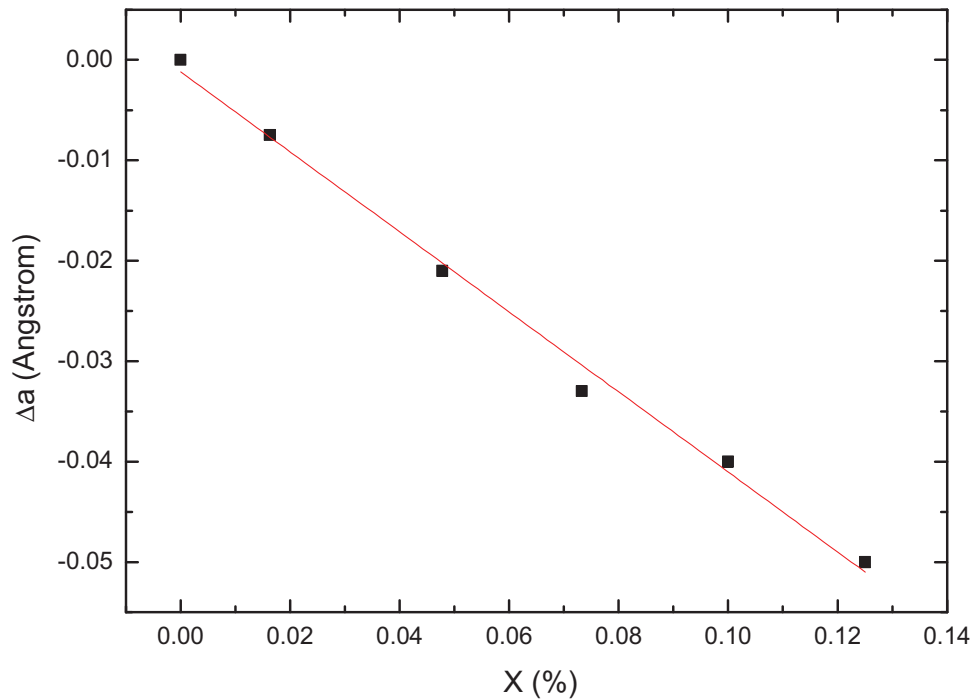


Figure 2.7: Interpolated curve showing the variation of lattice constants (Δa) vs carbon content (x) in $\text{Mg}(\text{B}_{1-x}\text{C})_2$ single crystal.

The change in the a -axis lattice parameter was calculated from the angular shift of the (100) reflection which, when inserted in Bragg's equation, gives the spacing between the planes in the atomic lattice (d). The a -axis lattice parameter was then calculated, considering that MgB_2 adopts a hexagonal structure, fig.(2.8), with the following relation:

$$a = \frac{d}{\cos(30^\circ)} \quad (2.3).$$

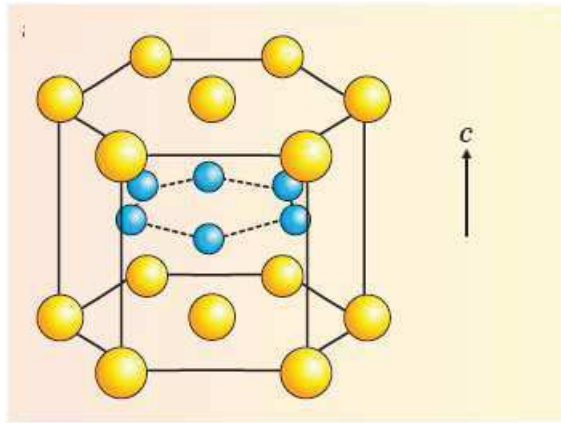


Figure 2.8: Crystal structure of MgB₂: hexagonal planes of magnesium (yellow) interleaved with honeycomb layers of boron (blue).

To correct for the possible error in the positioning of the Mg(B_{1-x}C_x)₂ bulk sample in the holder when determining the carbon content, x , a bar-shaped piece of alumina, used as a reference [76] for calibrating the XRD peak positions, was placed alongside the sample, so that both top surfaces were at exactly the same level, as shown in fig.(2.9).

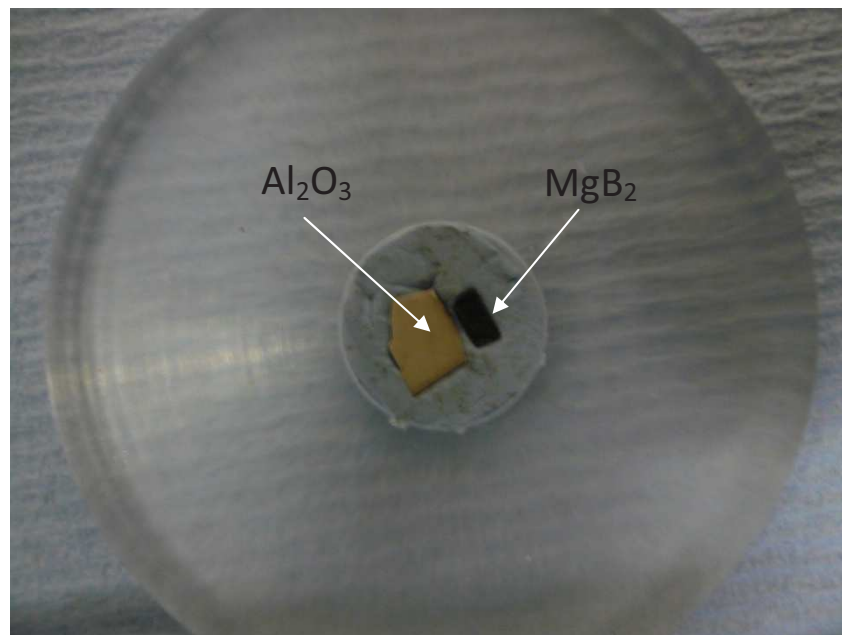


Figure 2.9: Sample holder for XRD measurements with the MgB₂ sample and a piece of Al₂O₃, used as a reference, mounted so that both top surfaces were at the same level.

2.4 Transmission electron microscopy (TEM)

2.4.1 Transmission electron microscopy: basic principles

Transmission electron microscopy (TEM) is a technique in which a beam of electrons is transmitted through an ultra-thin specimen, interacting with the specimen as it passes through. In TEM, the object is bombarded by a beam of electrons, the so-called primary electrons, fig.(2.10). In areas occupied by the object where these electrons encounter atoms with large (heavy) atomic nuclei, they tend to rebound. Electrons can be also repulsed (or absorbed) in areas where the material is relatively dense or thick. However, in regions where the material consists of lighter atoms or where the specimen is thinner or less concentrated, the electrons are able to pass through. Eventually the traversing electrons (transmission) reach the scintillator plate at the base of the column of the microscope. The scintillator contains material (e.g. phosphor compounds) that can absorb the energy of the incoming electrons and convert it to light flashes. The contrast image that is formed on this plate corresponds to the selective pattern of reflection or transmission of electrons, depending on the local properties of the object.

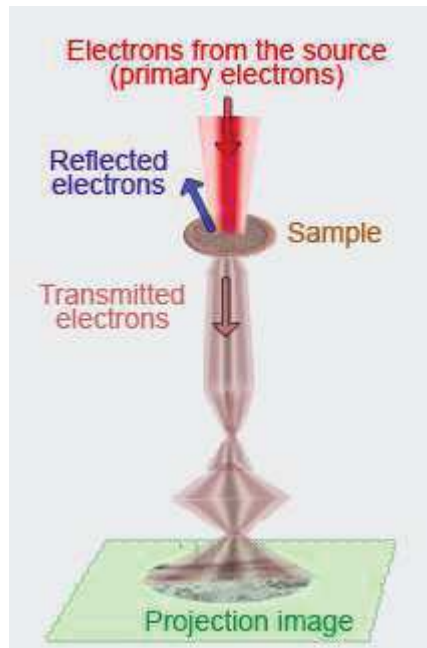


Figure 2.10: Functional principle of transmission electron microscopy.

2.4.2 Transmission electron microscope: main components & features

An electron gun, generally thermionic, is placed at the top of the instrument to accelerate electrons using a potential difference of between 40 and 200 kV. The gun's electron beam is, then, demagnified by a set of condenser lenses, to enable the operator to focus the beam onto the specimen area, which is allocated in the specimen chamber. The remaining components are the objective chamber, located at the bottom of the specimen chamber, the function of which is to produce an intermediate image subsequently magnified by the projector lenses, and the image record system for direct image observation by the operator. The use of electrons, in place of photons, allows the TEM to achieve a resolution of 0.2 nm which is much higher than the one achievable by optical microscopes since the wavelength of electrons is far shorter than that of photons. Another design feature of the TEM worth mentioning is the capability of using the mass-thickness contrast to detect areas of the sample that are thicker, or with a higher atomic number (as in our case,

in which C is heavier than B) which will appear dark (since they scatter more strongly) whilst regions without a sample will appear bright – hence the term "bright field".

On the other hand, the TEM can also be used in the dark field mode. This is useful for crystalline samples in which the objective aperture can be adjusted to select a particular diffracted beam. In this case, since the reflections that are selected do not include the unscattered beam, the image will appear dark, giving rise to the name "dark field." This mode of operation is used, for example, for the identification of lattice defects in crystals, such as dislocations or stacking faults. In particular, if a sample is slightly tilted from the Bragg angle, any defect which locally tilts the plane to the Bragg angle will produce particularly strong contrast variation making the tilt produced by the defect quite readily visible (i.e. the diffraction tilt produced by the local variation in the orientation of the planes).

2.4.3 Transmission electron microscopy analysis of MgB₂

Boron and MgB₂ powder samples were examined using a JEOL JEM-3010 transmission electron microscope. In fig.(2.11a and b), [77], two TEM pictures of sintered MgB₂ samples, made from powder milled, are shown. TEM is widely used to verify the average size of the grains and their distribution across the sample. Moreover, taking advantage of the enhanced contrast furnished by the bright-field images as in fig.(2.11b), it is possible to identify the presence and the extension of porosity, amorphous regions, and other second phases (bright regions) as well as of heavy phase and inclusions (dark regions).

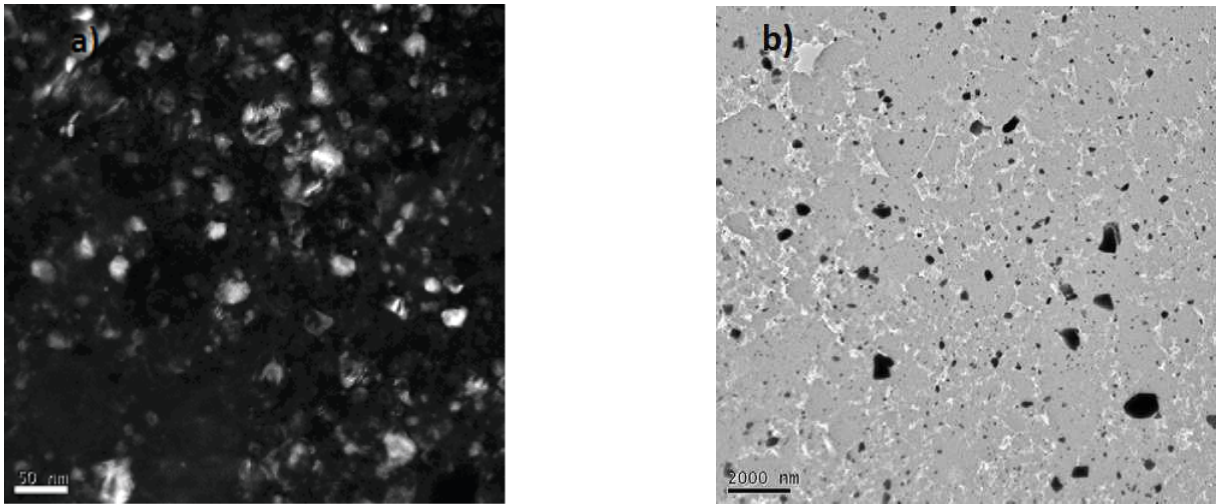


Figure 2.11: Dark field (a) and bright field (b)TEM images showing grain-related diffraction contrast in sintered MgB_2 samples[77].

The mass-thickness contrast is also used to assess the level of carbon deposited in relation to the cross section and the volume of the boron grains in carbon coated boron samples, fig.(2.12). Carbon, which is less dense than central boron+carbon region, appears brighter and was observed to form an annular-shaped layer on the boron particles.

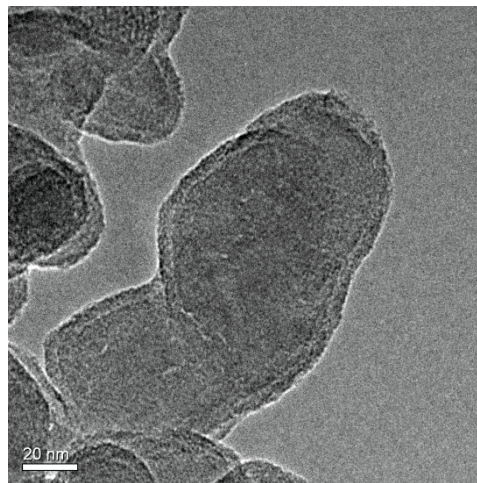


Figure 2.12: TEM images for carbon coated boron powder.

2.5 Scanning electron microscopy

2.5.1 Scanning electron microscopy: basic principles

Scanning electron microscope (SEM) is a type of microscope that produces images of a sample by scanning it with a focused beam of

electrons, fig.(2.13). In SEM the object is bombarded by primary electrons from the source according to a scanning pattern. These striking electrons can cause the emission of secondary electrons. The number of generated secondary electrons per time unit and the velocity of those electrons are affected by the height and slope of the surface of the object in a particular area. The secondary electrons, accelerated by applying a bias voltage of $\sim +10$ keV, strike a scintillator disc which, like in the TEM, contains substances which can convert the energy of the striking electrons into photons (light). The more secondary electrons reach the scintillator, the brighter the signal is at that point. This light is then transmitted into a photomultiplier tube which converts the photons into pulses of electrons which may then amplified and used to modulate the intensity of a CRT. With regard to the backscattered electrons, dedicated multi-element detectors either of scintillator or of semiconductor types are preferably used. This mode of operation is capable of achieving a strong topographic contrast by collecting signals from elements located on opposite side of the optic axis and then subtracting from each other so that contrast from any topographic features will be enhanced.

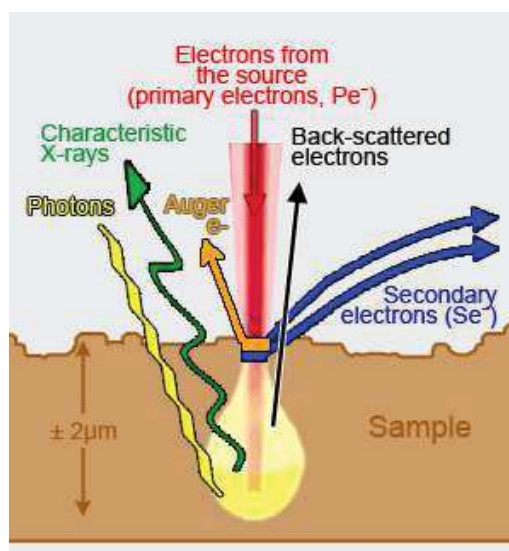
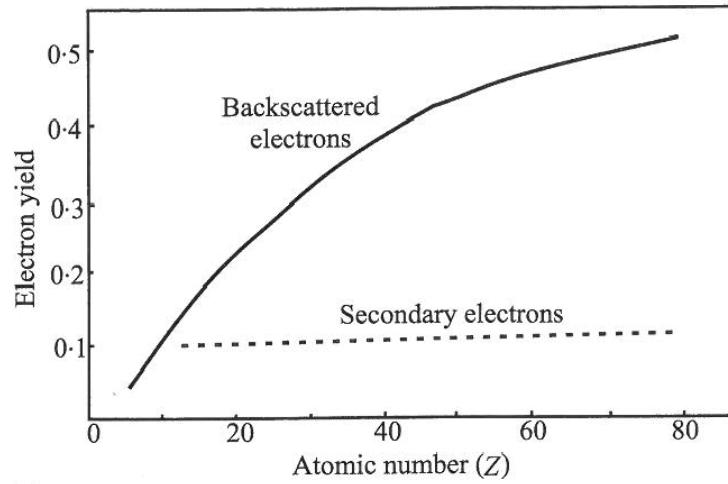


Figure 2.13: Scanning electron microscopy.

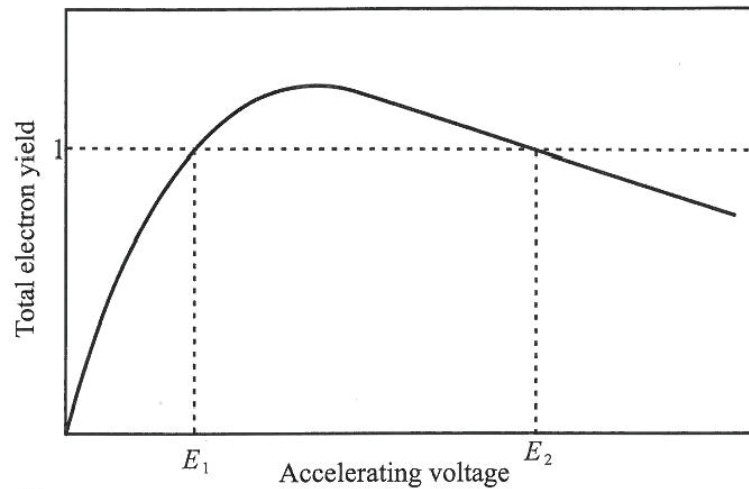
2.5.2 Scanning electron microscope: main components & features

In principle, any radiation that is a result of inelastic scattering with the specimen (and consequently any change in radiation resulting from a measurable change in the specimen) can be used to provide a signal to modulate the CRT and thus provide contrast in the image. However among all the radiation sources illustrated in fig.(2.13), [78], the most interesting and those detectable by virtually every SEM are: secondary electrons and backscattered electrons.

Backscattered electrons, which are the primary electrons that leave the surface before yielding all their energy, originate from a region of the sample (known as *sampling volume*) that is smaller than one micrometre. Therefore, although they are not so numerous as secondary electrons, they are very energetic. Secondary electrons, on the other hand, are those electrons that escape from the specimen with energies below 50eV. Generally, they are likely to be electrons generated mainly by the primary electrons penetrating the specimen and to which, within a short distance of the surface, a certain amount of energy has been transferred. They give the best spatial resolution because they have the smallest sampling volume. As shown in fig.(2.14(a)), the number of backscattered electrons emitted from the specimen for each incident electron (known as backscattered electron coefficient, η) is strongly dependent on the atomic number while the corresponding secondary electron coefficient (δ) is not. The total electron yield is a complex function of the accelerating voltage, which exhibits the maximum electron energy between 1 eV and 5 keV, fig.(2.13(b)). This behaviour is a consequence of the voltage dependence of δ , since η does not vary with voltage.



(a)



(b)

Figure 2.14: (a) The effect of atomic number on the yield of backscattered electrons (η) and secondary electrons (δ) (b) The effect of accelerating voltage on the total yield ($\eta+\delta$), [78].

2.5.3 Scanning electron microscopy analysis of MgB_2

The microstructure of the MgB_2 samples was studied with a JEOL JSM-6500F scanning electron microscope. Topographic contrast is generally exploited in the characterization of MgB_2 , using either secondary electrons or backscattered electrons in a SEM. Fig.(2.15) presents secondary electron images of a C doped MgB_2 , with a nominal doping fraction of 10%, [46]. The morphology of the samples is characterised by the presence of a porous matrix, which appears bright due to high density of edges within the microstructure, and dense and darker islands which are devoid of pore spaces. Since the contrast between the two areas changes with the doping fraction, it is possible to assess the

composition and to study the connectivity of doped MgB_2 . However, as the magnitude of the atomic number contrast is weak for adjacent elements (such as B and C), compositional differences cannot be satisfactorily investigated using only SEM, but it would be better to perform analysis by EDX (which is available in SEMs equipped with a X-ray detectors) to achieve a full understanding of the composition of specimens.

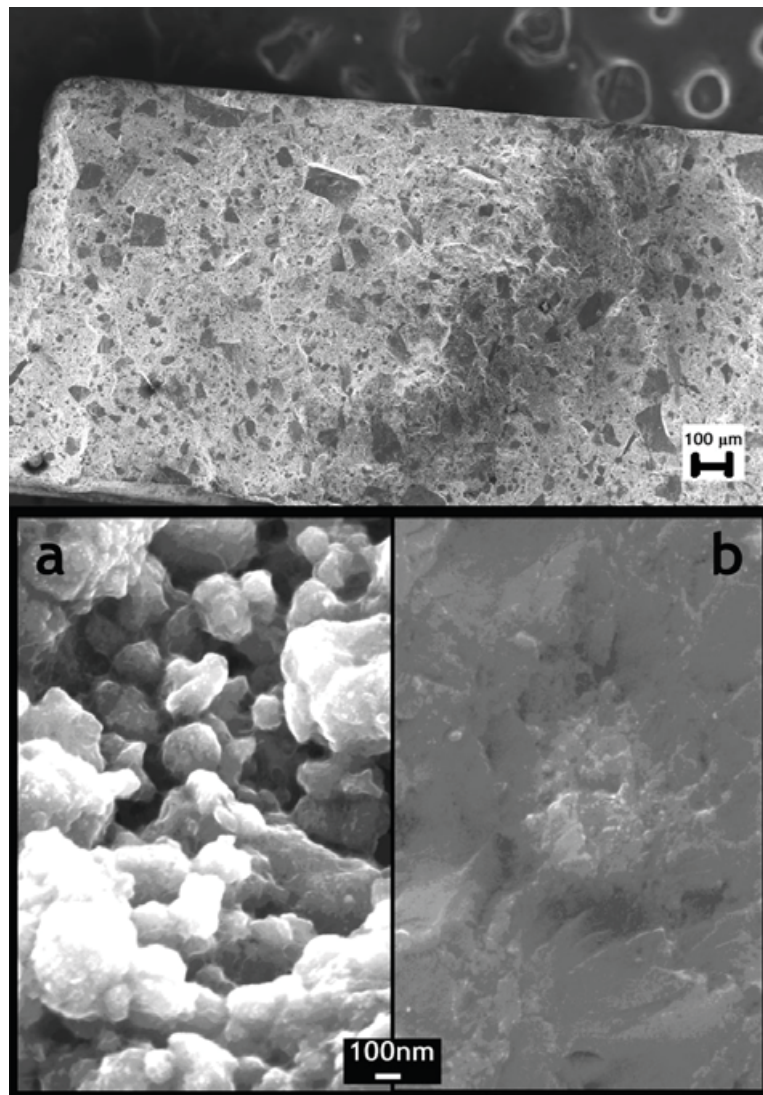


Figure 2.15. Scanning electron images of C doped MgB_2 (porous matrix is shown in (a), dense island in (b))[46].

2.6 Magnetization measurements

2.6.1 Vibrating Sample Magnetometer (VSM): main components & features

Magnetic measurements allow the equilibrium value of the magnetization in a sample to be determined. The sample is magnetised by an applied magnetic field and the magnetic moment of the sample is measured, producing the characteristic magnetization curve $M(H)$.

In this study, we have performed magnetization measurements using a Vibrating Sample Magnetometer (VSM) in a *Quantum Design Physical Property Measurement System* operating up to 9 T. A typical experimental set-up for this type of magnetization measurements is illustrated in fig.(2.16), [79]. The Vibrating Sample Magnetometer is equipped with a linear motor transport (head) for vibrating the sample, a coilset puck for detection, electronics for driving the linear motor transport and detecting the response from the pickup coils. The sample is attached to the end of a sample rod that is driven sinusoidally. The centre of oscillation is positioned at the vertical centre of a gradiometer pickup coil. The voltage induced in the pickup coil is amplified and lock-in detected in the VSM detection module. The VSM measurement is performed by oscillating the sample near a detection (pickup) coil and synchronously detecting the voltage induced. The principle of operation for a vibrating sample magnetometer is that a changing magnetic flux will induce a voltage in a pickup coil (Faraday's Law). The time dependent induced voltage is given by the following equation:

$$V_{coil} = \frac{d\Phi}{dT} = (d\Phi/dz)\left(\frac{dz}{dT}\right) \quad (2.7)$$

where Φ is the magnetic flux (expressed in Wb), z is the vertical position of the sample with respect to the coil (measured in m) and t is time (s).

The voltage is given by:

$$V_{coil} = 2\pi f C m A \sin(2\pi f t) \quad (2.8)$$

where C is a coupling constant, m (A/cm) is the DC magnetic moment of the sample, A is the amplitude of oscillation, and f (Hz) is the frequency of oscillation. Therefore, the magnetization measurement involves measuring the coefficient of the sinusoidal voltage response from the detection coil.

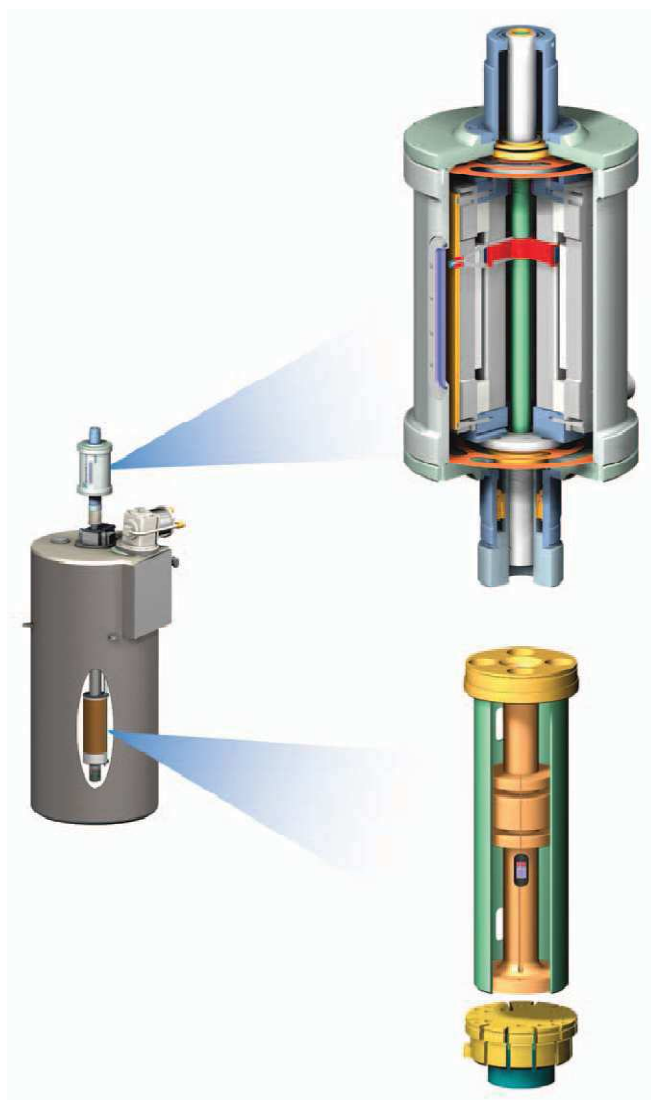


Figure 2.16. Vibrating sample magnetometer (VSM) used to perform magnetisation measurements, [79].

2.6.2 Magnetisation measurements of MgB₂ using VSM: calculation of J_c and description of the main effects causing a deviation from the reported magnetic field

There are some physical phenomena that cause the PPMS reported magnetic field to differ from the actual magnetic field at the sample location [80]. In the processing and analysis of magnetization data, we have considered, in particular, two effects: magnetic remanence and paramagnetic contribution.

Magnetic remanence is the magnetization of a superconductor that remains after the previously applied magnetic field has been removed. This phenomenon typically occurs when the magnetic field is set back to zero from a high value. Some pinned flux lines remain, and create a small residual magnetic field.

In order to eliminate this artefact, the following procedure, illustrated in fig.(2.17), has been adopted. First, the equation of the line passing through the maximum value of magnetization and the origin of axes has been calculated. Then, the equation data has been used to generate a correction for the PPMS reported magnetic field. A similar procedure has been used to subtract the paramagnetic contribution from the PPMS reported magnetisation data, which causes a positive deviation of the data in correspondence of the maximum applied magnetic field. The corrected magnetisation loop, plotted with a solid red line in the same figure, has then been used to derive the magnetic J_c using the Bean's model as described above.

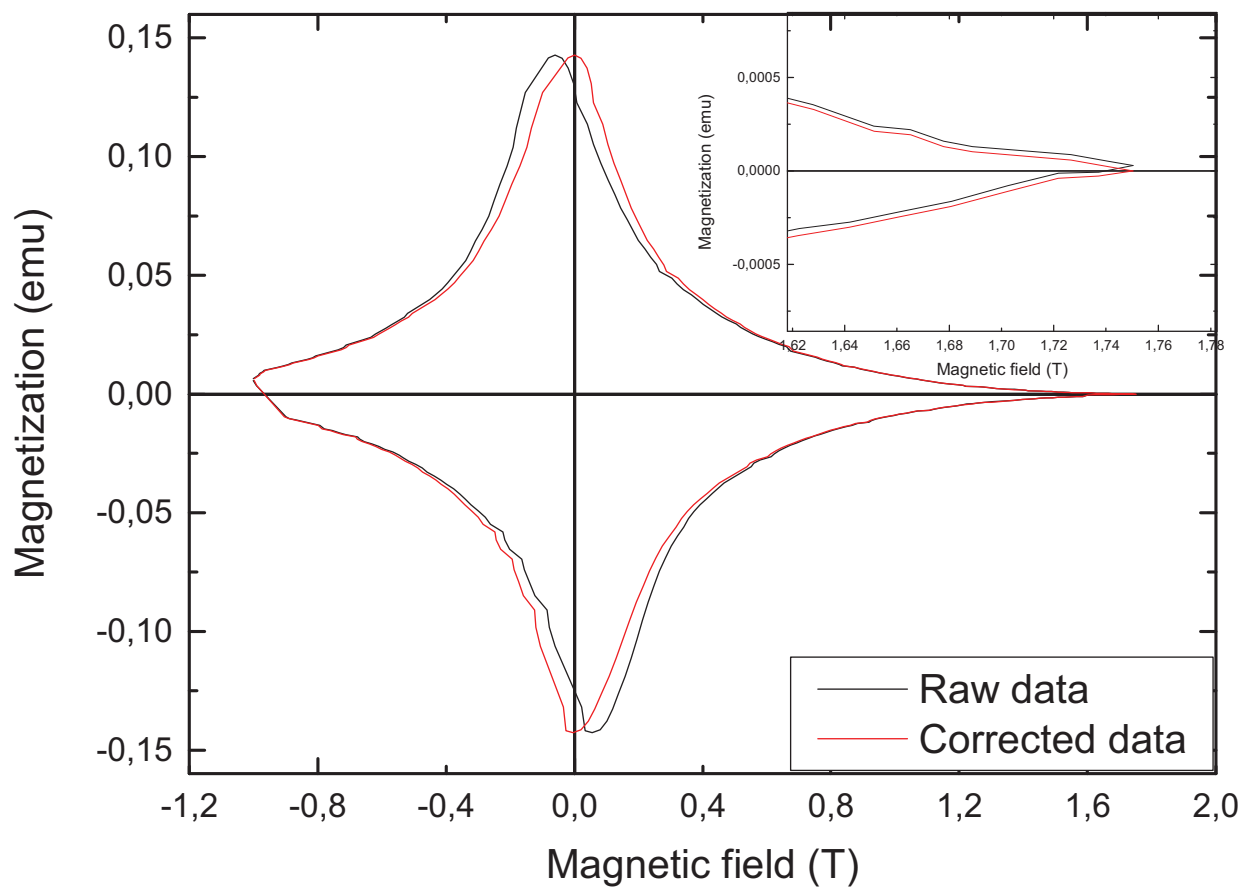


Figure 2.17. Graph showing the original magnetisation loop (solid black line) and the corrected loop (solid red line) obtained after removing the magnetic remanence and paramagnetic contribution (The inset shows the enlarged view of the field-dependent magnetisation for both the original magnetisation loop and the corrected loop in correspondence of the maximum applied magnetic field).

Chapter 3

Preparation and properties of $\text{MgB}_2(\text{C} - x\%)$ powder samples using carbon chemical vapour doped boron

$\text{MgB}_2(\text{C} - x\%)$ powder samples were prepared by reacting Mg with carbon-doped boron powder at 900°C . Carbon doped boron powder was obtained by chemical vapor deposition using ethylene gas on nano-sized boron particles (20-100 nm diameter) with varying deposition temperatures and gas partial pressures. Analysis through x-ray diffraction, transmission electron microscopy and the characterization of the temperature-dependence of magnetisation was employed to estimate the level of the carbon doping and evaluate the homogeneity and effectiveness of the method in enhancing the critical current density performance.

3.1 Synthesis procedures of undoped and C-CVD doped MgB_2 powder samples

The preparation of the undoped and doped MgB_2 was carried out by using nano-particle boron powder with diameters between 20-100nm. The powder was wrapped in tantalum foil along with 20% excess of the stoichiometric amount of Mg either in the form of ribbon or rod and placed inside a stainless steel tube as shown in fig.(3.1). Then the tube, sealed by applying uniaxial pressure on both ends (one before and the other after inserting the powder), was placed in a furnace, which was evacuated, and was heated up to 900°C for 6 hours in an argon

atmosphere at a pressure of 0.3 bar, and finally allowed to cool to room temperature.

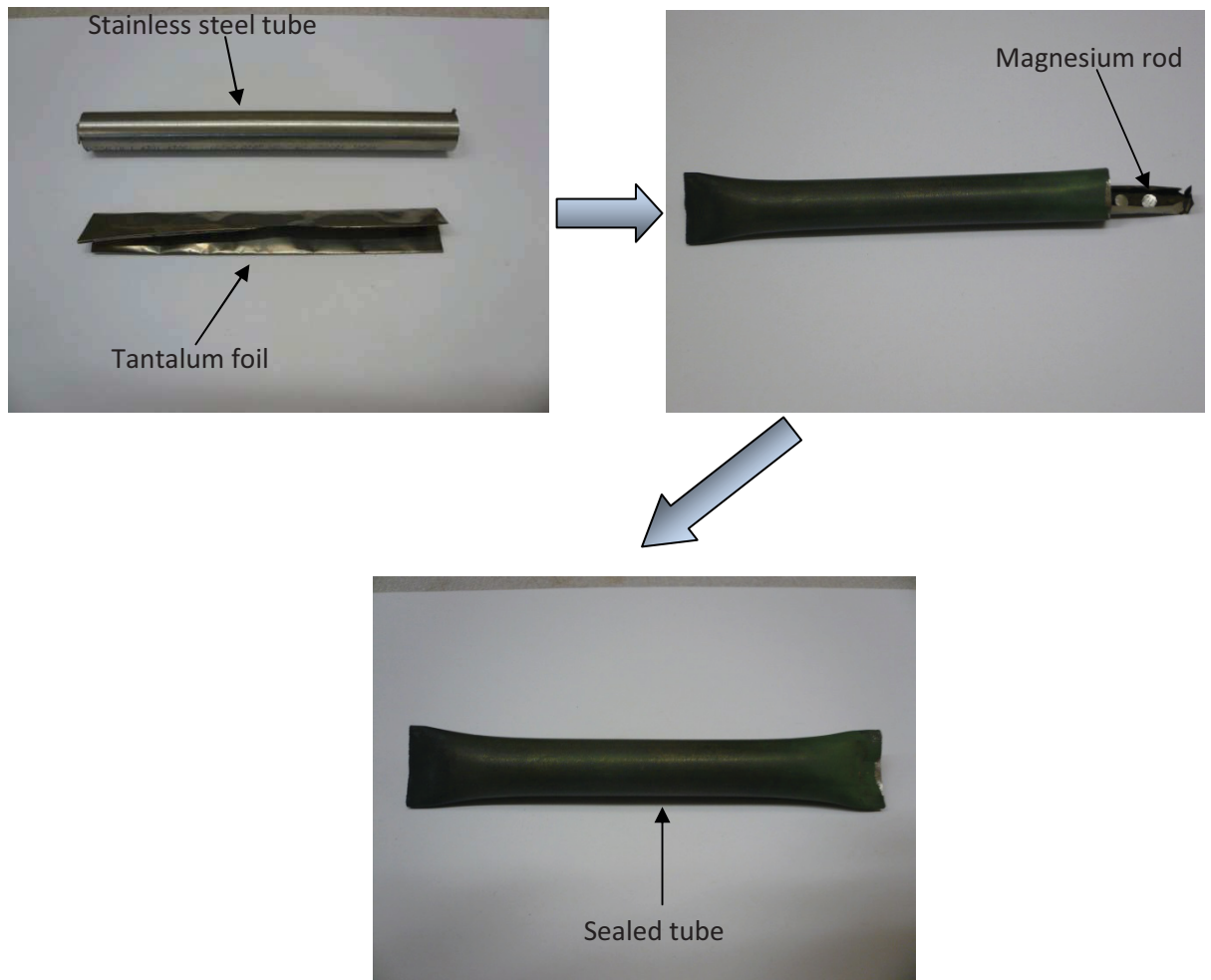


Figure 3.1: Preparation process of MgB₂ powder samples.

The methodology for preparing samples has been the result of modifications that have over time affected the entire process, just described, with the aim of optimizing it, and speeding it up. Argon, for example, was used to prevent any leaks in the system from enabling air to penetrate inside the oven, which would result in a probable oxidation of the precursor with obvious deleterious effects on the transport properties, which constitute the scope of this research. This precaution was very effective, as confirmed by the XRD results presented in the

following section, and allowed us also to eliminate the delicate and time-consuming task of welding the pipe ends to provide the seal.

Using the methodology just described, we prepared samples of undoped magnesium diboride treated at 900°C for six hours using the tube furnace shown in fig.(3.2). The reaction temperature of 900°C and the dwell time of six hours were chosen because they allowed to obtain fully reacted powder samples. Lower reaction temperatures and/or shorter dwell times were observed to not be capable of achieving completely reacted powders, resulting in samples containing significant amounts of MgB_x phases with $x=4,6,12$. The phases were identified by matching the XRD patterns of the produced samples and the literature-reported patterns for Mg-deficient compounds.

In order to assess the effect of chemical dopants on electron transport properties, in addition and in parallel with those samples, the first experiments in carbon doping magnesium diboride by chemical vapour deposition (CVD) were performed. This operation was carried out by treating boron powder, which had been placed inside either tantalum or titanium foil in a stainless steel tube furnace (evacuated using a rotary pump), with ethylene gas for 2 hours at 0.1-1.5 bars. The doping was performed using both ^{12}C and ^{13}C , in order to verify if the use of different isotopes of C produced any effect on the microstructural and magnetic properties of final samples, in particular in terms of phase homogeneity.

The amount of deposited carbon, estimated from the mass increase (determined by measuring the mass of boron powder before and after the deposition), allowed us to identify which process conditions (gas partial pressure and duration of the process) produced certain nominal values of carbon doping.

The precursor boron powder, coated with carbon using CVD, was then used to prepare carbon-doped magnesium diboride powder samples, referred to as C-CVD MgB_2 , with the same method and process parameters used to make undoped MgB_2 . Detailed in Table 3.1 are the $\text{MgB}_2(\text{C} - x\%)$ samples produced along with the respective nominal and actual carbon content and doping temperatures. The C doping temperatures for all precursor boron powders were set to 650°C , except for $\text{MgB}_2(\text{C} - 4.4\%)$, which was treated at 900°C in order to evaluate if and to what extent the higher doping temperature would influence the microstructure and the transport properties of the final samples.



Figure 3.2: Tube furnace used to react MgB_2 powder samples.

3.2 XRD characterization and temperature-dependent magnetization measurements

The undoped and C-CVD MgB_2 samples were characterized by XRD measurements. The purpose of this type of analysis was both to identify the oxygen-containing compounds that disrupt the transport properties

of superconductors and also to effect a qualitative and quantitative analysis of the constituent phases of the C-CVD MgB_2 samples produced.

The XRD analysis of undoped MgB_2 , shown in fig.(3.3), was conducted over a rather wide range of angles (10-70 degrees) and resulted in an absence of peaks that would indicate the presence of oxygen (which is an indirect confirmation that the system used for reacting the powder was vacuum-tight).

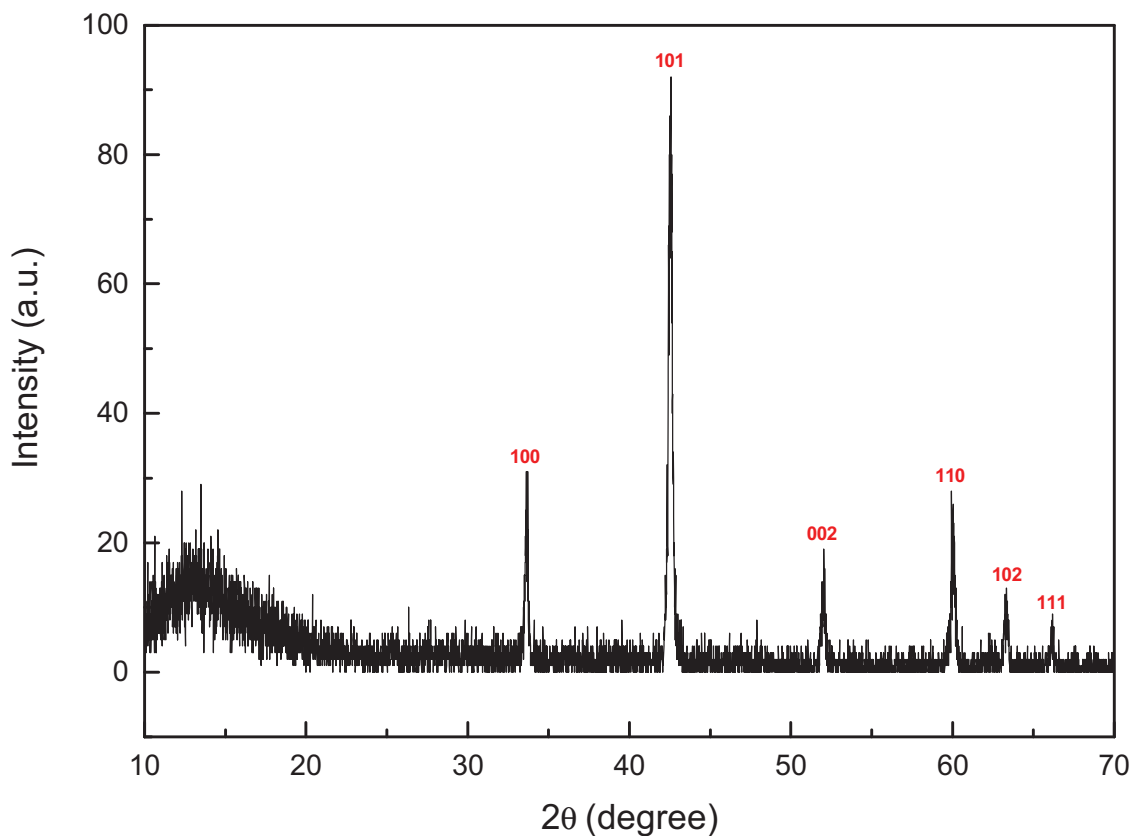


Figure 3.3: Powder XRD pattern for the undoped MgB_2 . The different crystallographic reflections are indicated in red.

Fig.(3.4) shows the (100) reflection for the undoped MgB_2 and C-CVD doped MgB_2 samples. The graph indicates that the (100) peaks in the doped samples were shifted to larger angles with increasing nominal doping percentages of carbon. This behaviour has previously been explained by the shrinkage in a -axis lattice parameters caused by carbon substitution for boron in MgB_2 [75]. The actual doping fractions have been estimated using the empirical calibration curve described in

Chapter 2.3 using Al_2O_3 as a reference [76]. The results obtained, indicated as $\text{MgB}_2(\text{C} - x\%)$ in Table 3.1 and in the rest of this chapter, evidence that only part of the carbon deposited on the boron powder was replaced in the MgB_2 lattice. Furthermore, the data suggest that the increase of dwell temperature from 650°C to 900°C did not seem to significantly affect the amount of carbon substituted in the MgB_2 lattice.

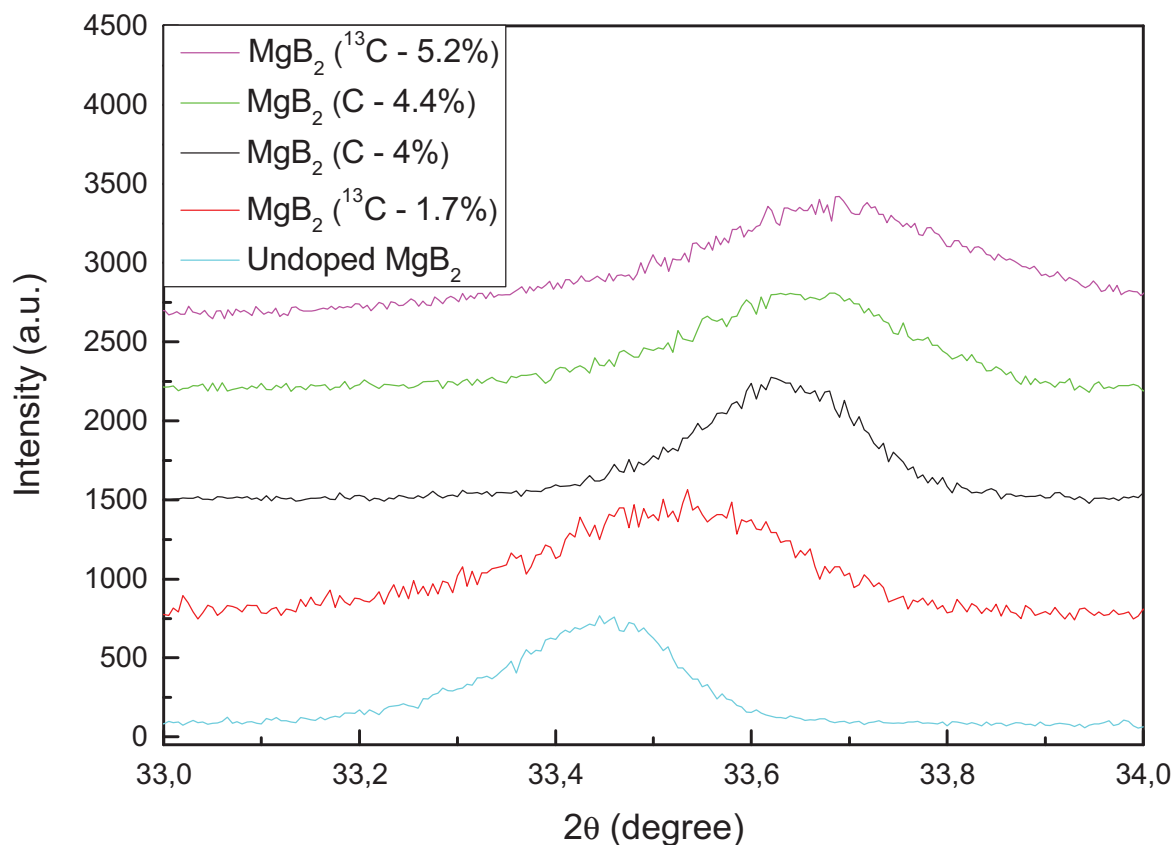


Figure 3.4: Reflection of (100) from XRD of the undoped and C-CVD doped samples with increasing nominal doping percentages of C.

Sample	Nominal doping fraction (%)	Actual doping fraction (%)	Carbon doping temperature ($^\circ\text{C}$)
$\text{MgB}_2(\text{C} - 4\%)$	6.3	4.0	650
$\text{MgB}_2(^{13}\text{C} - 1.7\%)$	4.2	1.7	650
$\text{MgB}_2(^{13}\text{C} - 5.2\%)$	7.5	5.2	650
$\text{MgB}_2(\text{C} - 4.4\%)$	6.4	4.4	900

Tab.3.1. Nominal and actual doping content of $\text{MgB}_2(\text{C} - x\%)$ along with the carbon doping temperature at which the C-CVD process was performed.

In fig.(3.5) the change in the lattice parameter, a , plotted against the nominal percentage of C for the C-CVD MgB_2 powder samples was compared to the literature-reported data for carbon substituted single crystals [75], and B_4C [43], SiC [43] and C-CVD doped bulk samples [40]. In [40] it was shown that full carbon substitution at the nominal doping level was achieved in C-CVD samples as evidenced by the agreement of Δa between these samples and C doped single crystal reported in the literature. In this work, we employed the same C-CVD method, but we focused on preparing samples using smaller powder size (which was 20-100 nm in this study and less than $1\ \mu\text{m}$ in [40]) because we wanted to verify if better structural and superconducting properties can be achieved using nano-sized boron powder. In terms of level of boron substitution by the C content in MgB_2 lattice, our C-CVD MgB_2 powder samples exhibited a shrinkage of the a -axis length, Δa , significantly smaller than that of the carbon substituted single crystals (as did the other C doped MgB_2 samples produced using different sources of carbon doping). The different results obtained in the two $\text{MgB}_2(\text{C} - x\%)$ samples made from C-CVD doped boron could be explained by virtue of the substantially different particle sizes of the boron powder. It is also worth noting that whilst, in the following analysis of the XRD data, the shifting of the (100) peak was calculated using Al_2O_3 peak as a reference, in [40] the (002) peak was used as a reference. This difference in the type of reference used, which provides a better level of approximation, since the (100) peak and the Al_2O_3 peak are comparatively close, could also partially affect the calculated change in the a -axis lattice parameter Δa in [40].

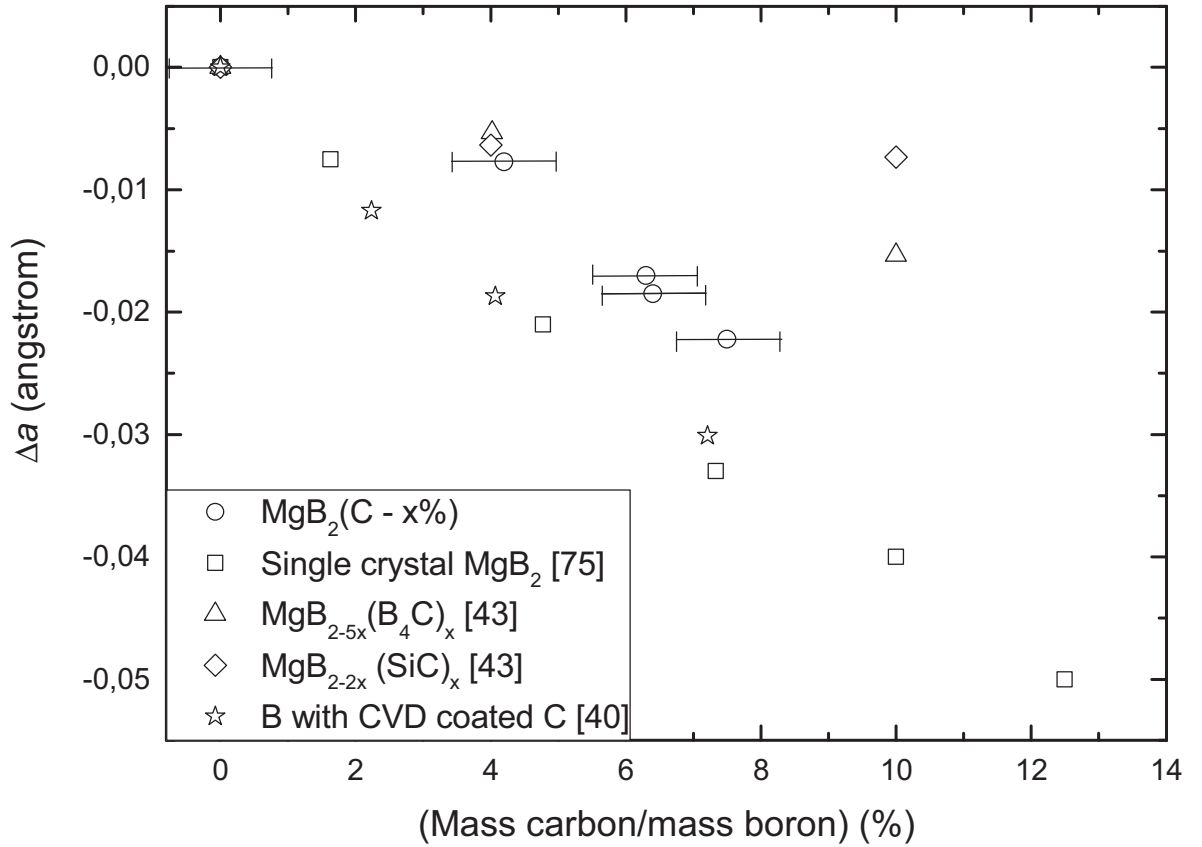


Figure 3.5: The change in the a -axis lattice constant, Δa , against the nominal percentage of C indicated specifying an error bar of $\pm 0.5\%$, for the $\text{Mg}(\text{B}_{1-x}\text{C}_x)_2$ samples, made from C-CVD boron powder, from this work. The data are compared to the literature-reported values for C doped single crystals [75], and doped MgB_2 bulk samples, [40] and [43].

In order to better evaluate the effect of the pre-reaction boron and boron-carbon mixture on the phase homogeneity of reacted carbon-doped magnesium diboride, the temperature dependence of FC (field-cooled) magnetization was studied for the undoped and the C-CVD doped MgB_2 powder samples. In fact, phase homogeneity can be better assessed in powders than in bulk samples, owing to the absence of screening currents which affect magnetic susceptibility measurements. Fig.(3.6)-(3.10) show the temperature-dependent field cooled magnetization curves at 100 Oe, along with those of the respective first derivatives of the magnetization, dM/dT , for undoped MgB_2 , $\text{MgB}_2(^{13}\text{C} - 1.7\%)$, $\text{MgB}_2(\text{C} - 4\%)$, $\text{MgB}_2(\text{C} - 4.4\%)$, and $\text{MgB}_2(^{13}\text{C} - 5.2\%)$, respectively.

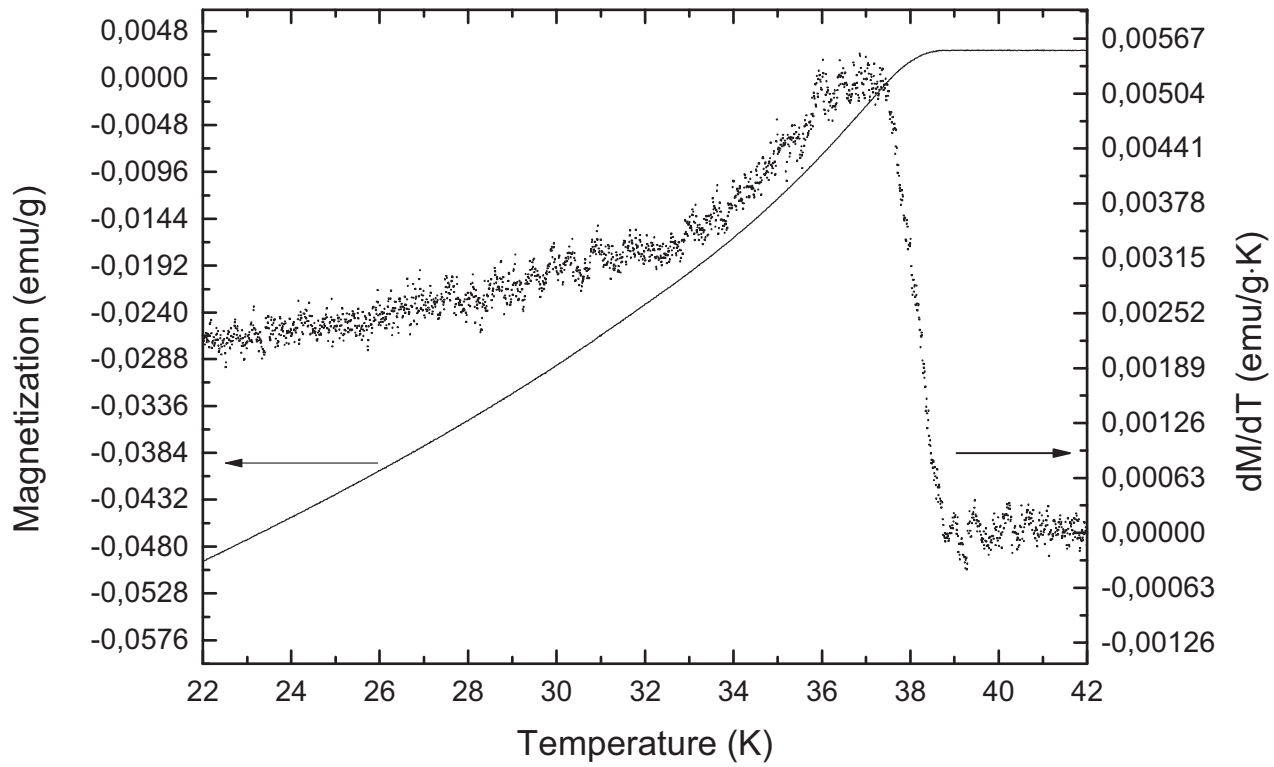


Figure 3.6: Temperature-dependent FC magnetisation (solid line) and dM/dT (filled-in symbols), at 100 Oe, for undoped MgB_2 .

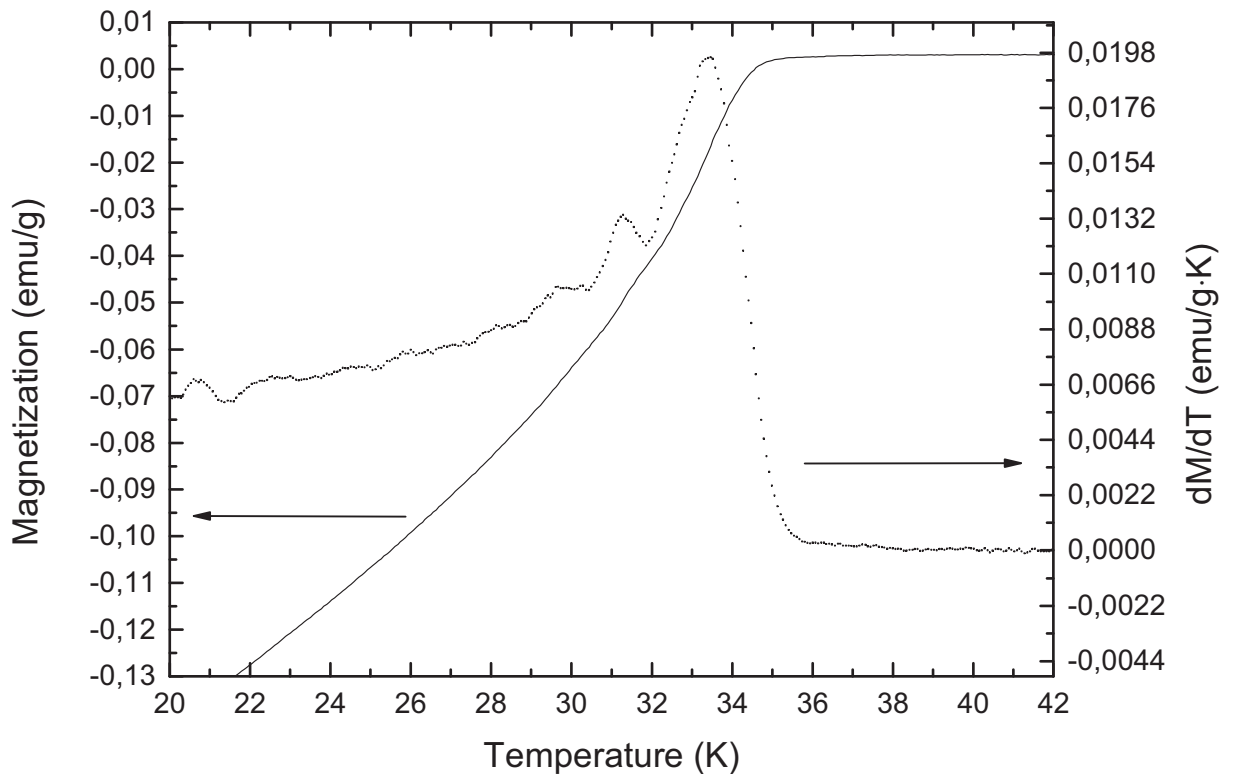


Figure 3.7: Temperature-dependent FC magnetisation (solid line) and dM/dT (filled-in symbols), at 100 Oe, for $MgB_2(^{13}C - 1.7\%)$ doped at $650^\circ C$.

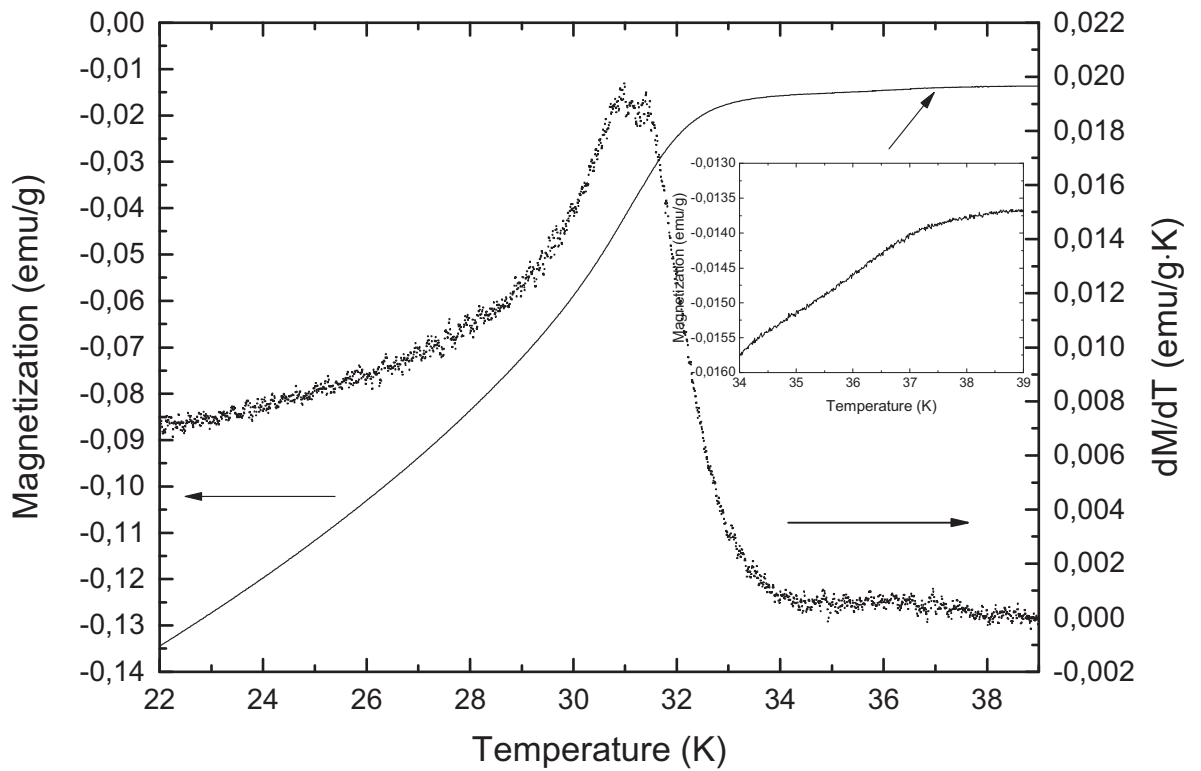


Figure 3.8: Temperature-dependent FC magnetisation (solid line) and dM/dT (filled-in symbols), at 100 Oe, for $MgB_2(C - 4\%)$ doped at $650^\circ C$. The inset shows the enlarged view of the temperature-dependent FC magnetisation in the region of 34-39 K.

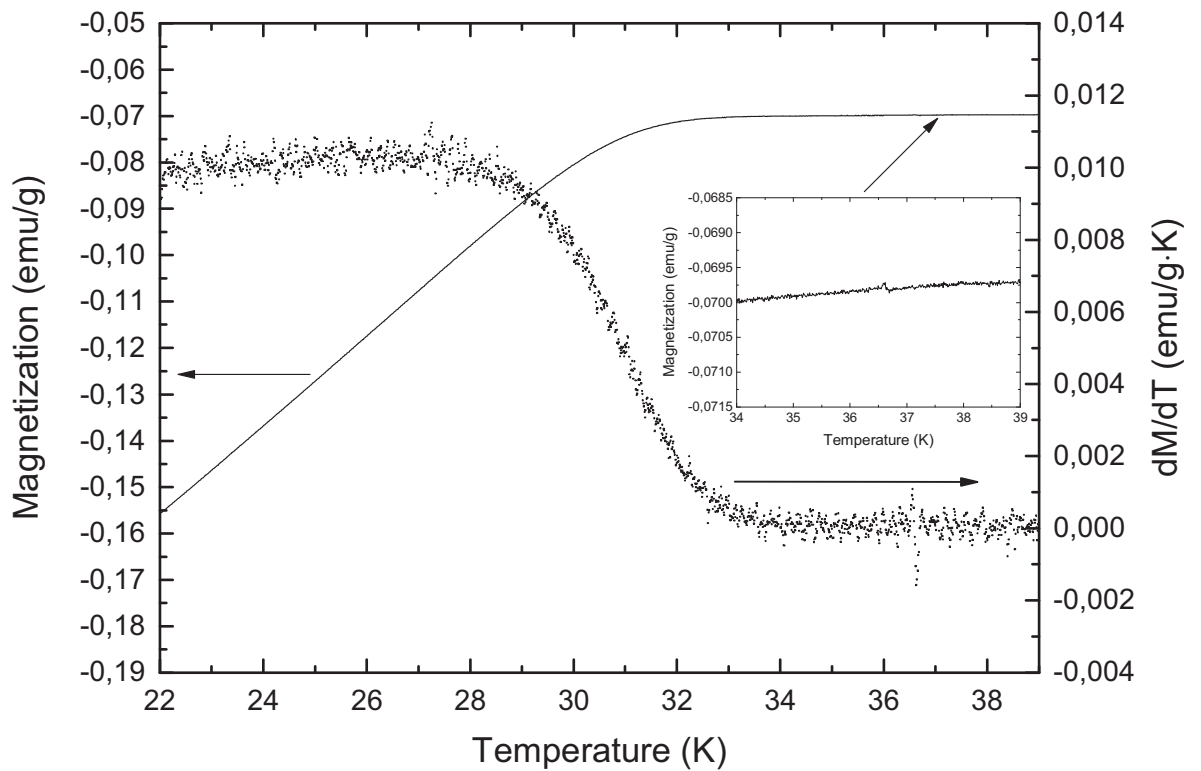


Figure 3.9: Temperature-dependent FC magnetisation (solid line) and dM/dT (filled-in symbols), at 100 Oe, for $MgB_2(C - 4.4\%)$ doped at $900^\circ C$. The inset shows the enlarged view of the temperature-dependent FC magnetisation in the range of 34-39 K.

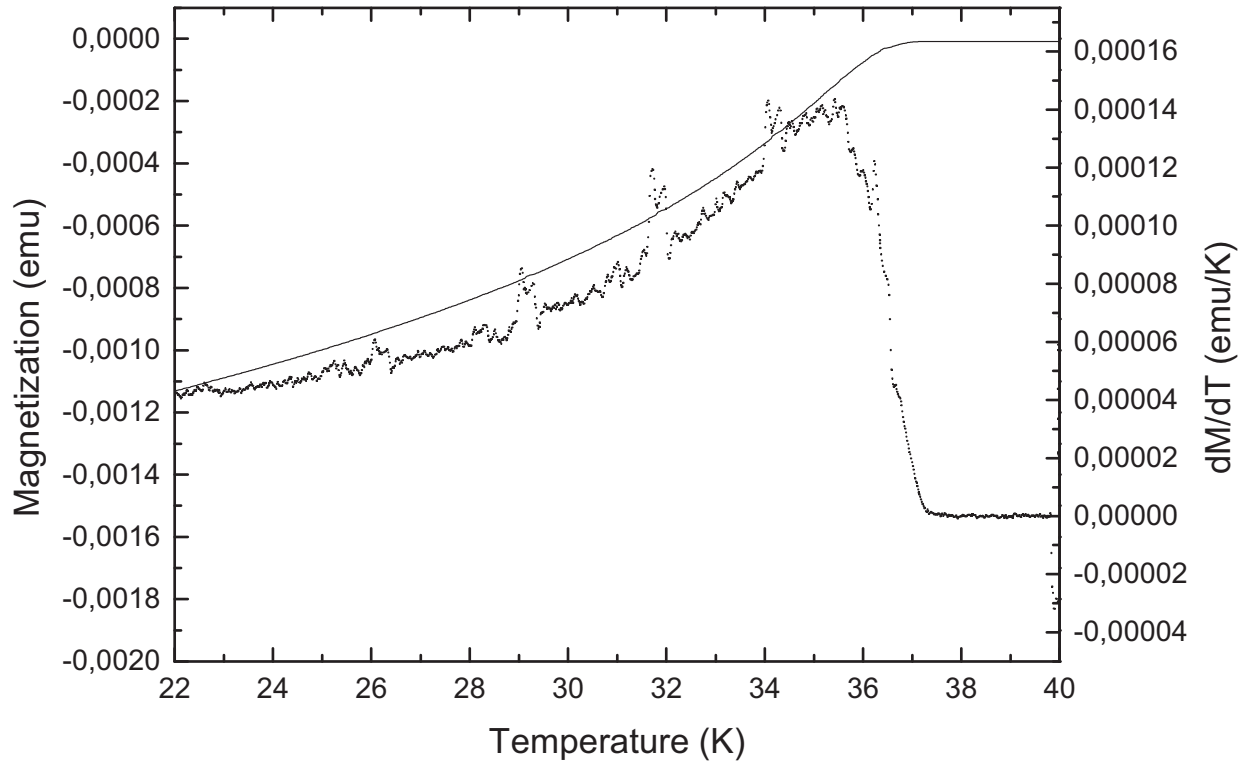


Figure 3.10: Temperature-dependent FC magnetisation (solid line) and dM/dT (filled-in symbols), at 100 Oe, for $MgB_2(^{13}C - 5.2\%)$ doped at $650^\circ C$.

All samples exhibited a broad superconducting transition which suggests the possibility of phase separation. However, whilst the onset T_c was easily determined (taking the interpolated value corresponding to the first significant positive deviation in the dM/dT curve), the transition peak representing to a potential lower T_c cannot be properly resolved. Inductive currents arising from local variations in magnetic field affected the nature of magnetic measurements, preventing us from separating the contribution due to the Meissner effect from that attributable to the presence of demagnetization currents. In fig.(3.11) the onset values of critical temperature have been plotted as a function of Δa (change in the a -axis lattice constant) for the undoped and C-CVD doped MgB_2 samples. In the same graph, the T_c versus Δa (and X) behaviour for C-CVD doped MgB_2 is compared with the literature data relative to the $Mg(B_{1-x}C_x)_2$ samples prepared using carbon black [81] and B_4C doped MgB_2 samples [43], with the $Mg(B_{1-x}C_x)_2$ single crystal sample [75] shown as a reference.

T_c 's (onset) of the C-CVD doped MgB_2 prepared and characterised in this work are comparable to those of single crystal sample, whereas the other two polycrystalline samples from literature exhibited values that are noticeably higher. This behaviour indicates that doping by CVD results in more homogeneous crystalline properties, except for $MgB_2(^{13}C - 5.2\%)$ which exhibited a relatively high T_c . The broad T_c transition and the fact that T_c onset increases again with a higher doping percentage might suggest that there is a distribution of composition within $MgB_2(^{13}C - 5.2\%)$ and the highest T_c value corresponds to the portion of the sample with a lower carbon content. Fig.(3.12) shows the comparative graph of $M/M(22 K)$ vs T for the undoped and doped MgB_2 powder samples.

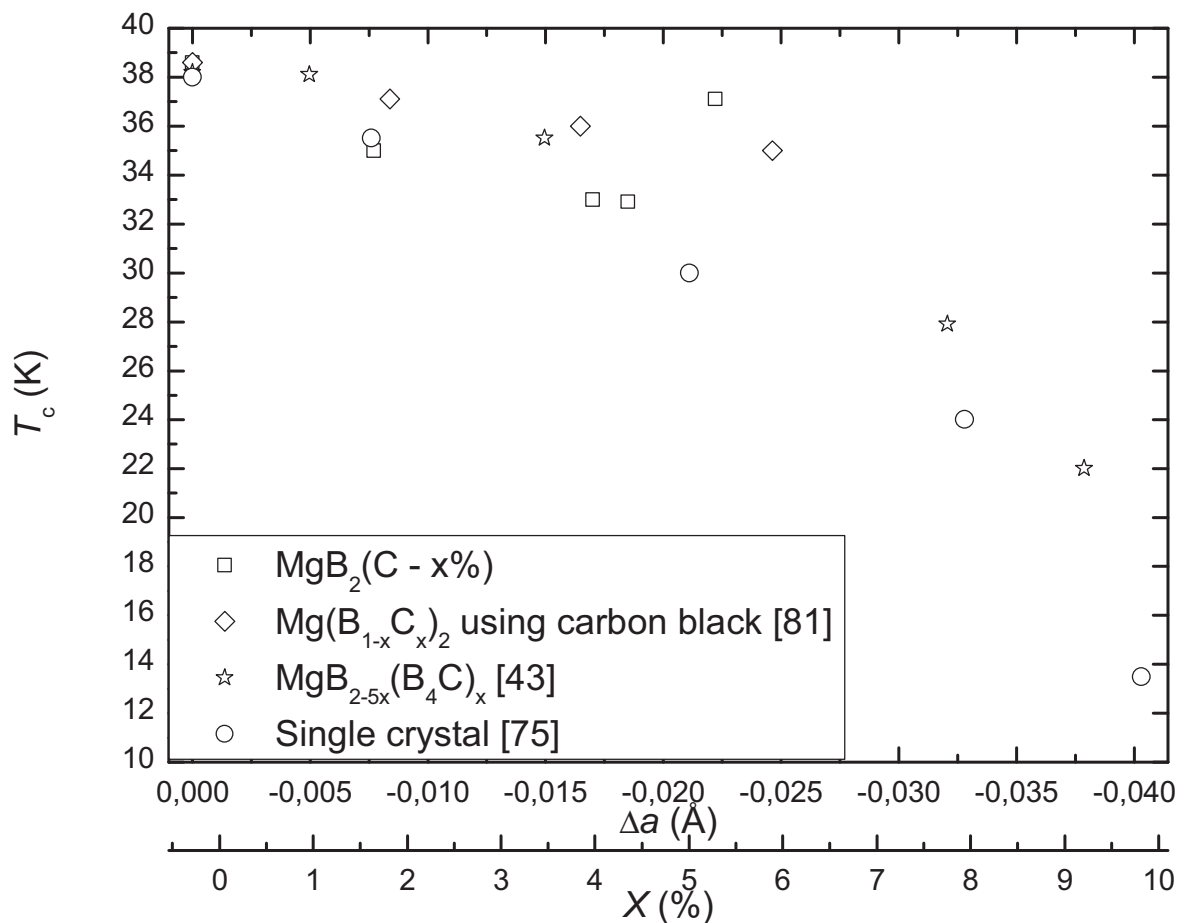


Figure 3.11: Comparison of the critical temperature, T_c , as a function of Δa (and X), between $MgB_2(C - x\%)$ prepared by C-CVD boron powder from this work and $Mg(B_{1-x}C_x)_2$ made using carbon black, B_4C doped MgB_2 samples and $MgB_2(C - x\%)$ single crystal samples.

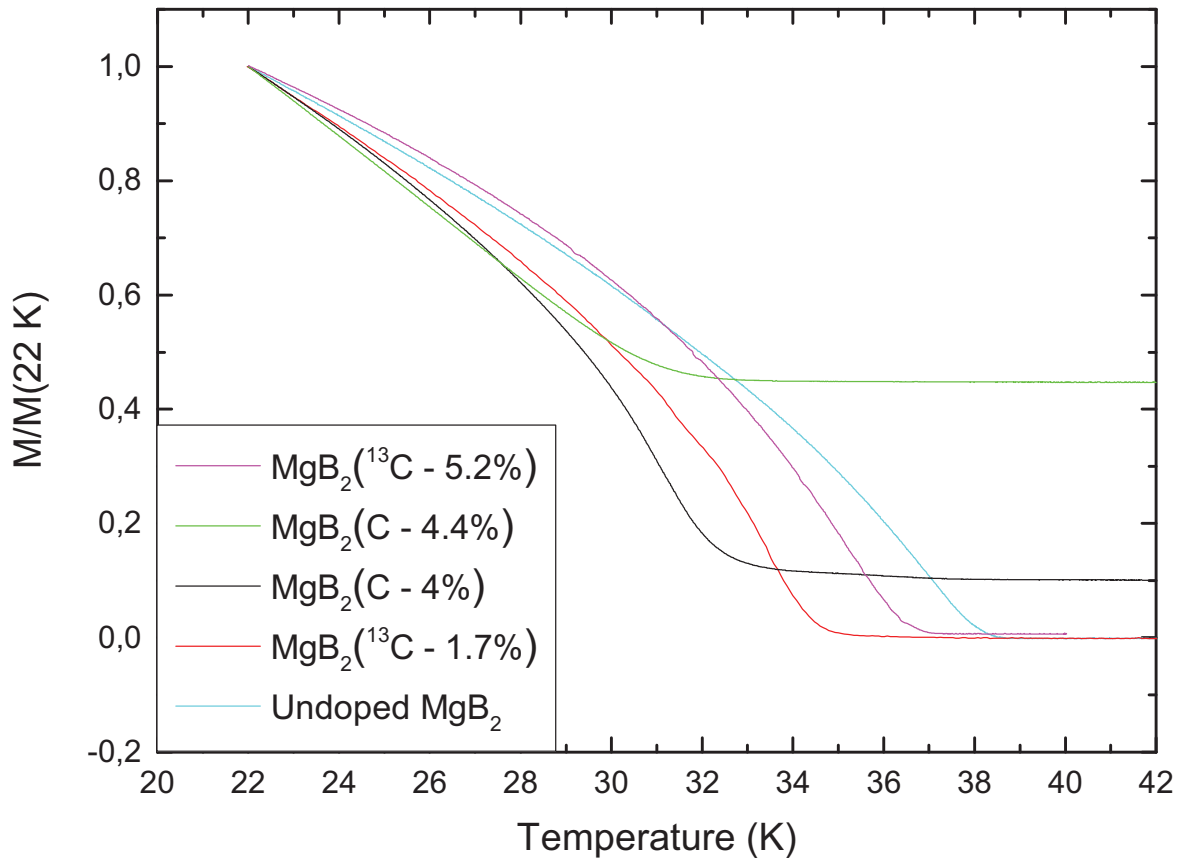


Figure 3.12: Comparative graph of $M/M(22\text{ K})$ vs T for the powder samples listed in Table 3.1.

The distribution of T_c at different carbon doping temperatures was also investigated, by carrying out a comparative analysis of the temperature-dependent field-cooled magnetization curves -see fig.(3.8) and (3.9)- for $\text{MgB}_2(\text{C} - 4\%)$ doped at 650°C and $\text{MgB}_2(\text{C} - 4.4\%)$ doped at 900°C . The comparatively sharp profile of the temperature dependence magnetization graph for the 650°C treatment presented two clear and distinct variations in slope of the curve, one corresponding to about 37 K and the other to 33 K. In contrast, with regard to the C-CVD 900°C MgB_2 , the 37 K step was virtually absent and, furthermore, there was a broad superconducting transition below 33 K indicating a lower homogeneity of carbon doping. The results correlated with the XRD data, showing a wider distribution of T_c with the higher carbon doping temperature.

3.3 TEM image analysis

In order to assess the level of homogeneity within the carbon distribution and check for any correlation between the boron grain size and the amount of deposited carbon, we used the TEM (transmission electron microscopy), the theoretical principles of which were described in the second chapter.

In fig.(3.13(a)-(b)) the TEM images of pure boron powder (a) and carbon-doped boron powder (b) are presented. The thickness of the deposited carbon layer achieved by CVD was observed to be virtually constant, as shown in the TEM images of fig.(3.14) and in the graph of fig.(3.15), where the carbon layer thickness has been plotted as a function of boron particle diameter. The results confirmed that deposited carbon layer remains nearly constant at 5.5 ± 0.7 nm with varying values of particle size. Both the pure boron and the carbon coated boron particles were observed to be hexagon-shaped, however, in order to provide a quantitative estimation of the fractional carbon volume relative to the volume of the boron grain, the particle circled in red dashed line in fig.(3.13(b)) was considered as a parallelepiped, and it was assumed that the length of the boron particle was equal to the width since it simplified the calculation. The value of fractional carbon volume relative to the volume of the boron particle has then been estimated using the following relation:

$$\frac{Volume_{Carbon}}{Volume_{Boron}} = \frac{(l + 2a) \times (w + 2a) \times (t + 2a)}{l \times w \times t} - 1 \quad (3.1)$$

where l is the length, w is the width, t is the thickness of the boron particle, and a is the thickness of the carbon layer. The fractional carbon value, as assessed in terms of volume, was estimated to be approximately 99%. Since the amount of deposited carbon was estimated to be just

under 7 wt% of the boron mass, the density of the carbon layer is about 14 times smaller than that of the boron particle. In order to have a carbon layer with the same density of the boron particle, the layer thickness would have had to be 0.45-0.50 nm, a value less than one tenth of the actual carbon layer thickness. The comparatively small density of the carbon layer suggests that the mass of C deposited was composed predominantly of light compounds of carbon such as carbon black. Carbon black is a fluffy fine powder with a large surface area and is composed essentially of elemental carbon. It is generally manufactured by the controlled vapour-phase pyrolysis and partial combustion of hydrocarbons and it is initially formed as roughly spherical primary particles, which tend to rapidly form aggregates [82]. The aggregate dimension ranges from tens to a few hundred nanometers with a density comprised in the range of 0.02-0.38 g/cm³ when available in the form of fluffy powder, or 0.2-0.68 g/cm³ when compressed into pellets. Comparison of the TEM images of fig.(3.16(a) and (b)) relative, respectively, to undoped MgB₂ and C-CVD doped MgB₂ suggests that there was no appreciable remnant of carbon on the surface. This result contradicts the XRD finding that only partial carbon substitution of the nominal doping content was achieved in these samples via the CVD technique. This contradiction could be explained assuming that the remaining carbon was located at grain boundaries, however the amount present, which was about 2%, was not sufficient to cause an appreciable variation in the mass-thickness contrast in the TEM images.

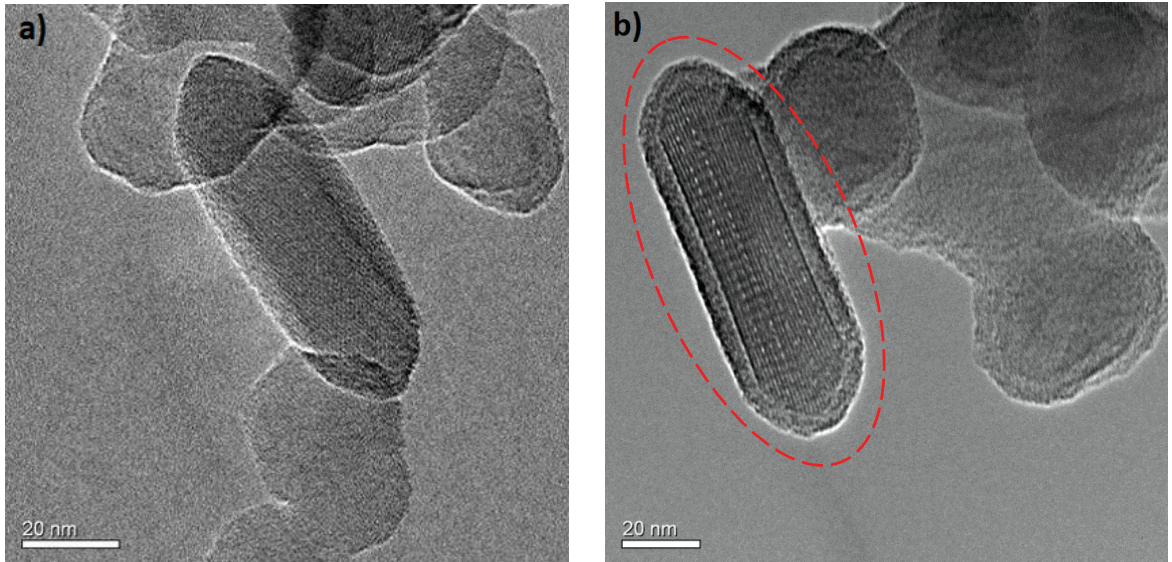


Figure 3.13: TEM images of pure boron powder (a), C-CVD doped boron (b). The boron particle, circled by the red dashed line, was used to estimate the fractional carbon volume by using the eq.(3.1).

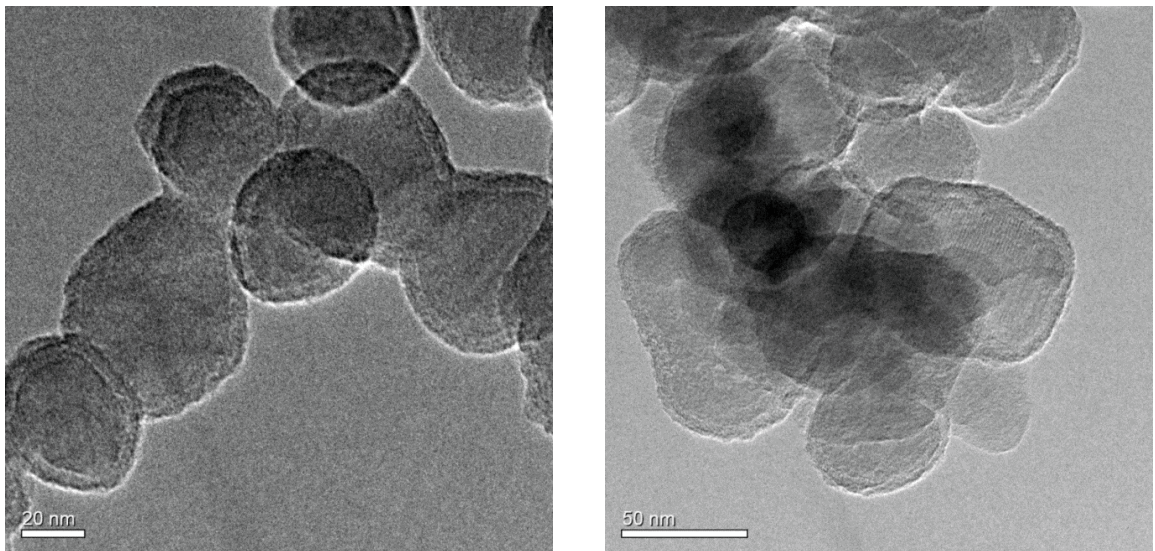


Figure 3.14: TEM images of C-CVD doped boron powder.

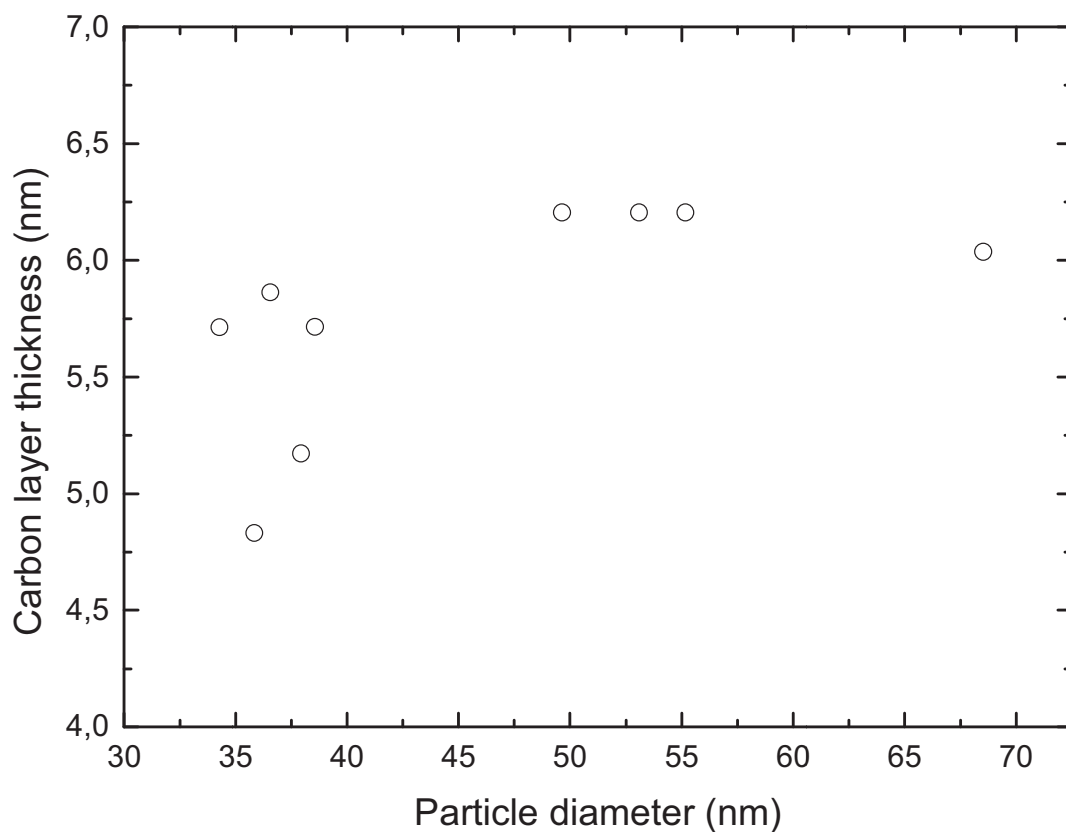


Figure 3.15: Carbon layer thickness plotted as a function of boron particle diameter.

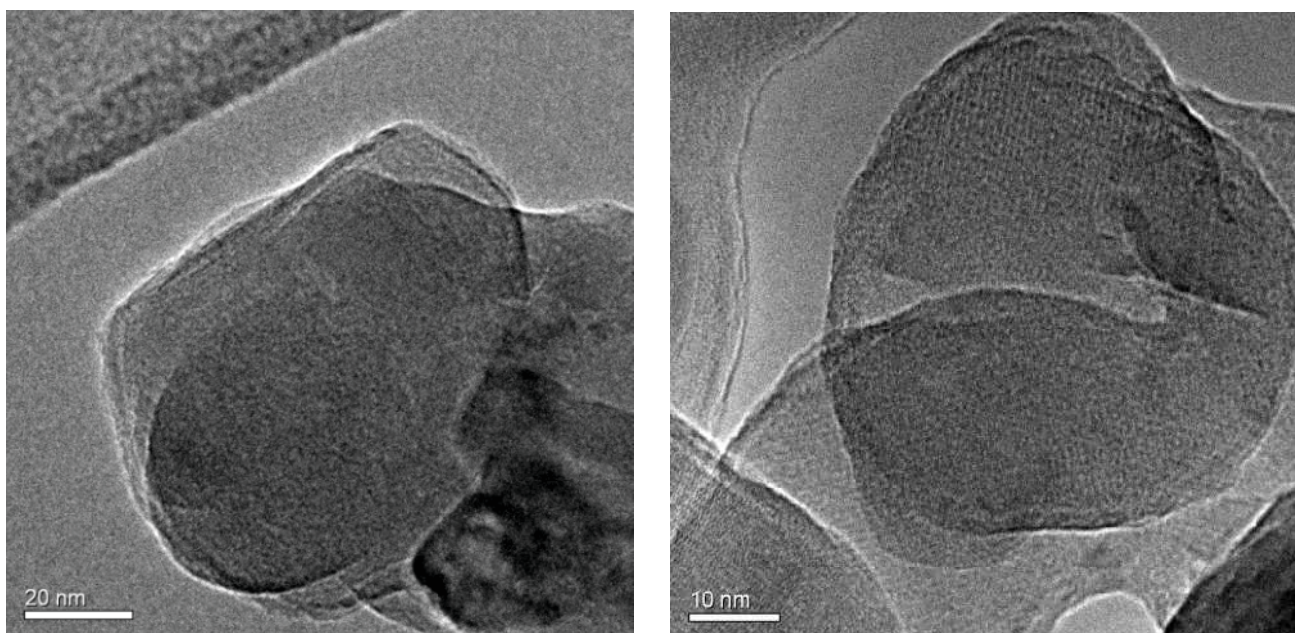


Figure 3.16: TEM images of undoped MgB_2 (left), C-CVD doped MgB_2 (right).

3.4 Conclusion

In this chapter promising results on controlling the carbon doping of MgB₂ powder have been presented. The XRD analysis of the (100) peak has evidenced both an incomplete carbon substitution at the nominal doping level and an inhomogeneous distribution of carbon doping within the MgB₂ lattice. No correlation was seen between the amount of carbon incorporated in the MgB₂ lattice and the FWHM of the XRD peaks, which exhibited noticeably high values for the ¹³C doped samples.

The magnetization data correlated with the findings from the XRD analysis of diffraction patterns: both the decrease of the *a*-axis length and the *T_c* appeared to be due to the actual carbon content. The coexistence of multiple phases, evidenced by the Gaussian analysis of the XRD peaks, could not be resolved using the results of magnetization data, owing to the presence of induced shielding currents. However, the onset *T_c* values plotted as a function of Δa for the C-CVD MgB₂ samples prepared and characterised in this work were found to be comparable to the literature data relative to C doped single crystals. The only significant deviation from single crystal behaviour was observed for MgB₂(¹³C – 5.2%) which exhibited a relatively high *T_c*.

Chemical vapour deposition of carbon was shown by transmission electron microscopy to achieve a constantly thick layer of carbon on each boron powder particle. The layer has also been estimated to be equal to 5.5 ± 0.7 nm, regardless of particle size. The fractional carbon volume relative to the volume of the boron particle has been estimated to be approximately 99%. The resulting significantly low value of the carbon layer density seems to indicate that the mass of C deposited was constituted largely of light carbon compounds such as carbon black.

Chapter 4

Preparation and properties of $\text{MgB}_2(\text{C} - x\%)$ bulk samples using carbon chemical vapour doped boron and SiO_2 coated boron

The purpose of the present research project has been, apart from synthesising the MgB_2 powder samples, the optimization of the preparation process of MgB_2 bulk samples and the characterization of their magnetic and transport properties. In order to enhance their properties, two different doping techniques have been experimented: carbon coating by CVD and silica coating by sol-gel method. The results on the characterisation of undoped and doped MgB_2 bulk samples are presented, discussed and compared with the best data from the literature.

4.1 Methods of preparing MgB_2 bulk samples and related issues

4.1.1 Background to in-situ challenges

Traditionally, the MgB_2 bulk samples are fabricated in two different ways: one is heating and reacting the powder mixture of Mg and B, which is the so-called *in situ* method, and the other is the sintering of commercially available or home-made MgB_2 powders, known as *ex situ* method [35]. The latter method is capable of achieving density values substantially higher than those obtained by the former, with the obvious advantage of enhancing the magnetic and transport properties. However, the *ex situ* method presents the inconvenience that the MgB_2 tends to be brittle and

to form cracks, due to the the weak coupling of MgB_2 crystals. Maintaining the initial content of Mg, which has high chemical reactivity with oxygen and high equilibrium vapour pressure at sintering temperatures, is one of the main issues concerning the *in situ* method. One of the approaches that has been shown to be most effective in this sense is the powder-in-closed-tube (PICT), which is the result of an optimization of the well-known powder-in-tube (PIT) method commonly applied to the manufacture of wires or tapes [35]. This new technology consists of the following steps: first a force is applied to one end of the tube, then after inserting and packing the magnesium and boron powders, the other end of the tube is pressed (this process is illustrated in fig.(4.1)). The central part, in which the powders are placed, is then pressed flat producing a tape-shaped bulk sample, while the ends are folded up and pressed again. In this way it is possible to obtain high quality MgB_2 samples, avoiding the occurrence of losses of Mg, which can result in poor reproducibility of the microstructure as well as the critical current properties.

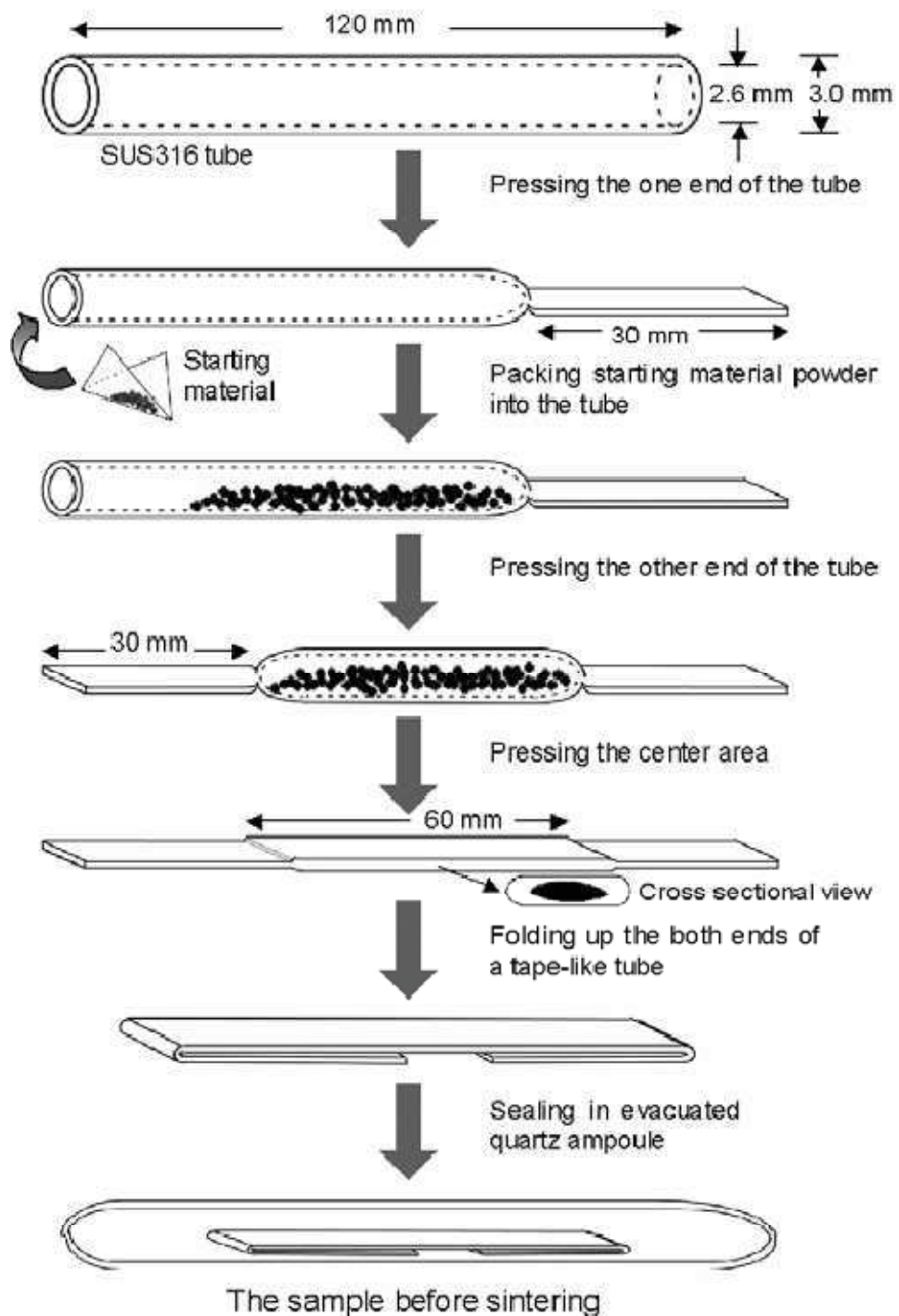


Figure 4.1: Synthesis procedure of the PICT method for MgB_2 bulks [35].

4.1.2 Sample preparation

So as to overcome the issues of fragility and of MgB_2 's tendency to form cracks, some changes to the above described PICT method of preparing the samples have been made. The new preparation assembly and synthesis sequence is illustrated in the flow diagram of fig.(4.2).

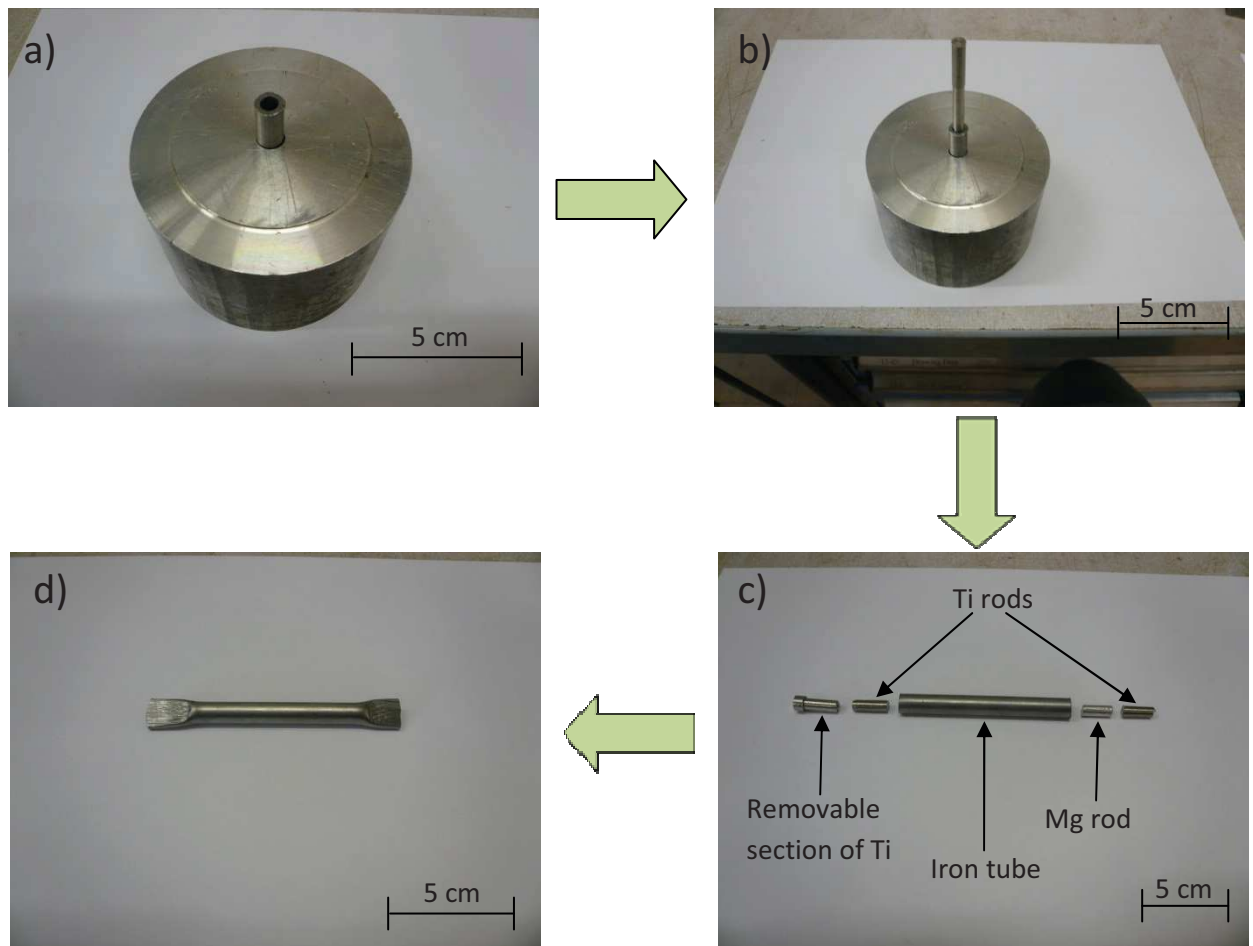


Figure 4.2: Fabrication method of MgB_2 bulk samples: an iron tube was inserted into a purpose-built stainless steel block for boron powder pouring (a); packing of the boron powder (b); exploded view of the rod of Mg, the two rods of Ti, and the removable section of Ti inserted into the iron tube, as indicated in the picture (c); the tube with both ends crimped ready to be heat-treated in the furnace (d).

Boron powder was inserted and packed into an iron tube (5 mm I.D., 8 mm O.D.) between two rods of titanium, and one of magnesium, the mass of which was determined using a super-stoichiometric ratio (20% excess magnesium) with respect to boron. Moreover, a removable section made of titanium was added to one end of the tube where the sample was placed to facilitate clamping. Then the tube was subjected to the same thermal treatment as in the case of the powder samples.

The main difference from the previously described PICT method is that only the two ends of the tube were crimped, while the central part of tube, filled with packed powder, retained its cylindrical shape. Moreover, in place of Mg powder, a Mg rod was placed at one end of the tube.

4.1.3 Study and optimization of preparation process

4.1.3.1 Experimental details

In order to study the parameters affecting the process of reaction and sintering, and the mechanical integrity of final samples, a wide range of experiments in preparing bulk MgB_2 samples, at varying dwell temperatures and temperature ramp rates, have been performed, as detailed in Table 4.1.

Starting materials	Dwell temperature (°C)	Dwell time (h)	Temperature ramp rate (°C)	Boron packing density (%)
Mg rod, B powder	900	6	200	75
Mg rod, B powder	900	6	100	49
Mg rod, B powder	900	6	10	49
Mg rod, B powder	970	6	100	49
Mg rod, B powder, MgB_2 powder	970	6	100	
Mg rod, B powder	850	6	100	41
Mg rod, B powder	775	6	100	36
Mg rod, C doped B powder	850	6	100	33

Table 4.1: Summary table of MgB_2 bulk samples prepared with the dwell temperature, the dwell time, the temperature ramp rate, and the packing density indicated.

In the initial phase, the samples were produced resorting to the PICT (powder-in-closed-tube) method, which has previously been described in the Section 4.1.1, and treated at 900 °C for 6 hours. The only variation to the PICT method was the use of Mg rod (placed at both ends of the tube) in place of Mg powder in order to overcome the problem of the high chemical reactivity of Mg powder with oxygen. However, the results obtained did not prove to be satisfactory in terms of mechanical integrity of sintered samples which, when taken out of the furnace, were found to

be broken into multiple pieces, as shown in fig.(4.3). This was the result of extensive cracking which might be caused by the excessively high value of boron packing density (approximately 75% of the boron density), which hindered the diffusion of Mg into boron during the sintering process. The validity of this hypothesis was also confirmed by the analysis of XRD peaks for the treated sample, fig.(4.4), which revealed the presence of compounds characteristic of a Mg-deficiency.

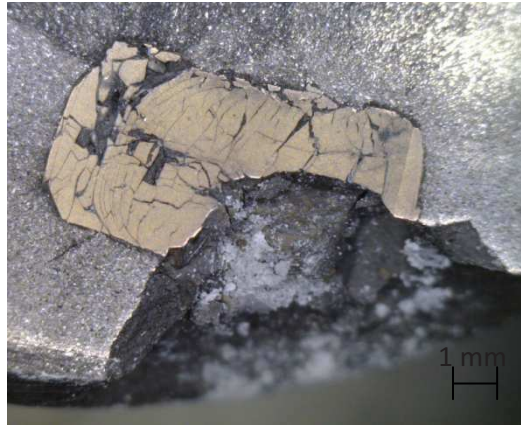


Figure 4.3: Optical microscopy image of undoped MgB_2 synthesized by PICT method and treated at $900^\circ C$.

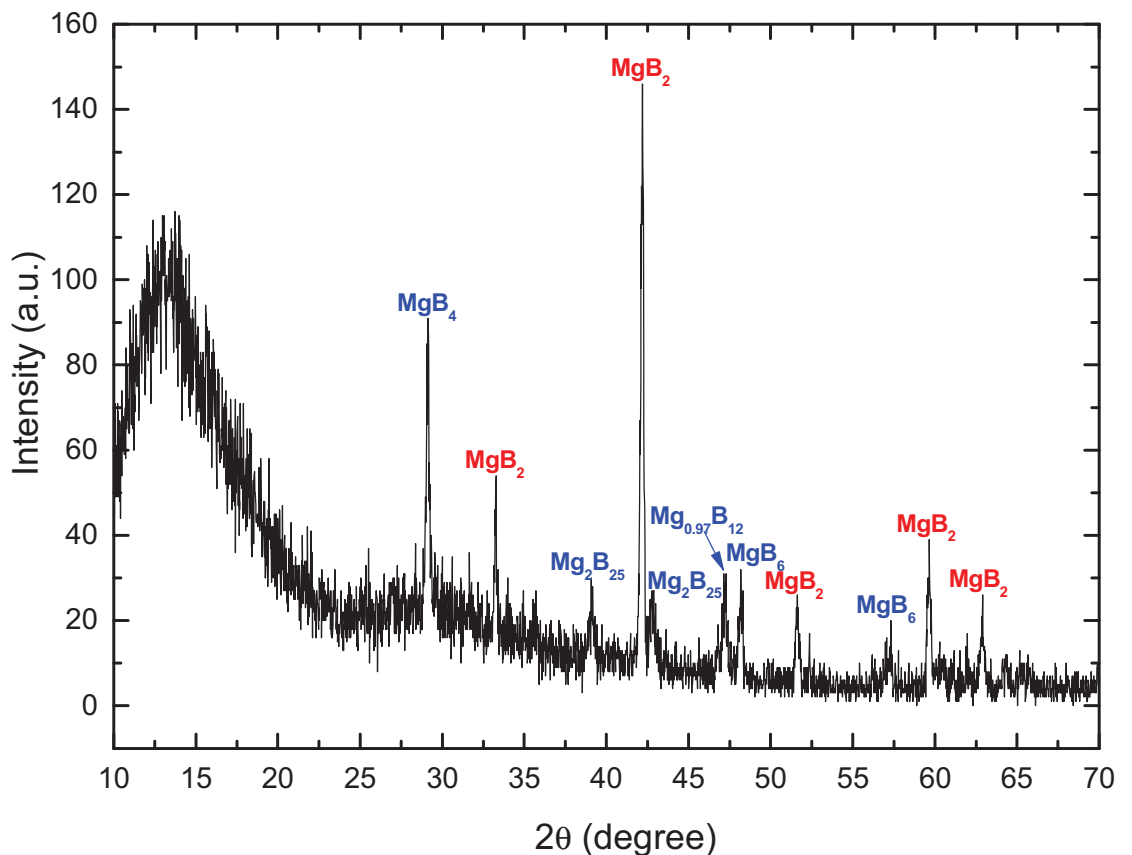


Figure 4.4: XRD pattern for MgB_2 bulk sample with the MgB_2 phases indicated in red, and the Mg-deficient compounds indicated in blue.

The fabrication method and assembly sequence of samples was, then, changed, as described in section 4.1.2 and illustrated in fig.(4.2). These changes to the samples' preparation process allowed the packing density to be reduced to 49% of the boron density. Moreover, the temperature ramp rate was lowered from 200°C/h to 100°C/h and subsequently to 10°C/h. This course of action was undertaken based on the idea that slower heating rate could result in better diffusion of the magnesium, as reported in the literature [83]. The results showed that, whilst the changes improved the compositional homogeneity of the samples (their diffraction patterns, fig.(4.5), are, in fact, devoid of Mg-deficiency compounds except for a minor peak attributable to $Mg_{0.97}B_{12}$), they have not produced significant improvements in the samples' mechanical integrity, as shown in fig.(4.6) and (4.7).

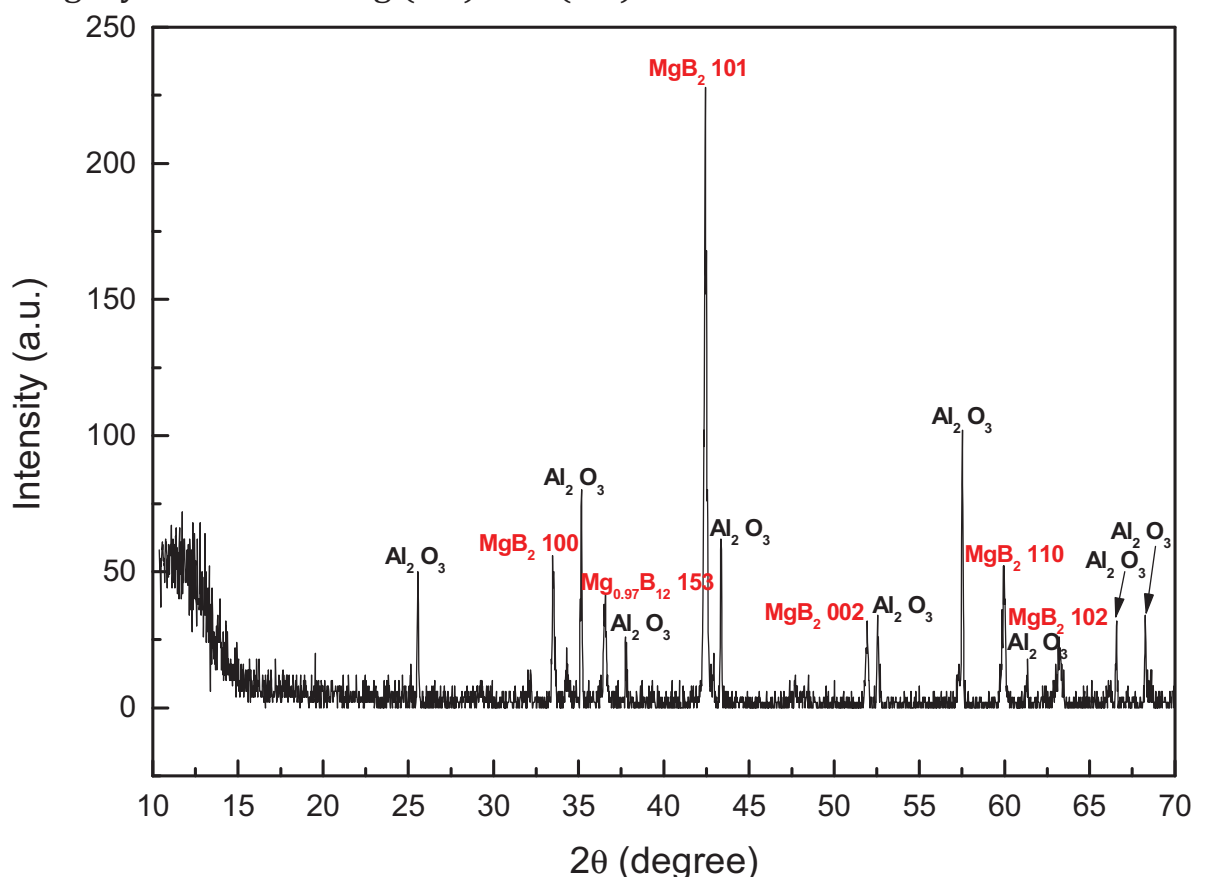


Figure 4.5: XRD pattern for MgB_2 bulk sample sintered at 850°C for 6 hours. A bar-shaped piece of Al_2O_3 has been positioned next to the sample in the sample holder and used as a reference, as explained in Chapter 2.3.

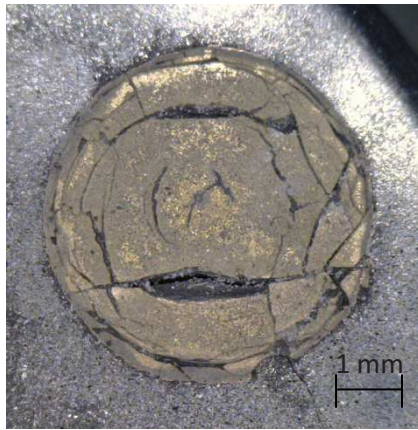


Figure 4.6: MgB₂ bulk sample sintered at 900°C for 6 hours, using a heating rate of 100°C/h.



Figure 4.7: MgB₂ bulk sample sintered at 900°C for 6 hours, using a heating rate of 10°C/h.

At this point, in an attempt to improve the mechanical properties of the samples three different approaches were taken. The first consisted in increasing the dwell temperatures to 970°C, leaving the other parameters unchanged, namely the temperature ramp rate (100°C/h) and dwell time (6 h). This approach made it possible to produce samples which were even more dense than those produced previously. This behaviour can be explained by an increase in the amount of available liquid that permitted the particles to be wetted and favoured interparticle contact. However, the increase in the samples' density did not lead to any significant improvement in the mechanical properties of the samples, which presented random-oriented cracks, as illustrated in fig.(4.8).

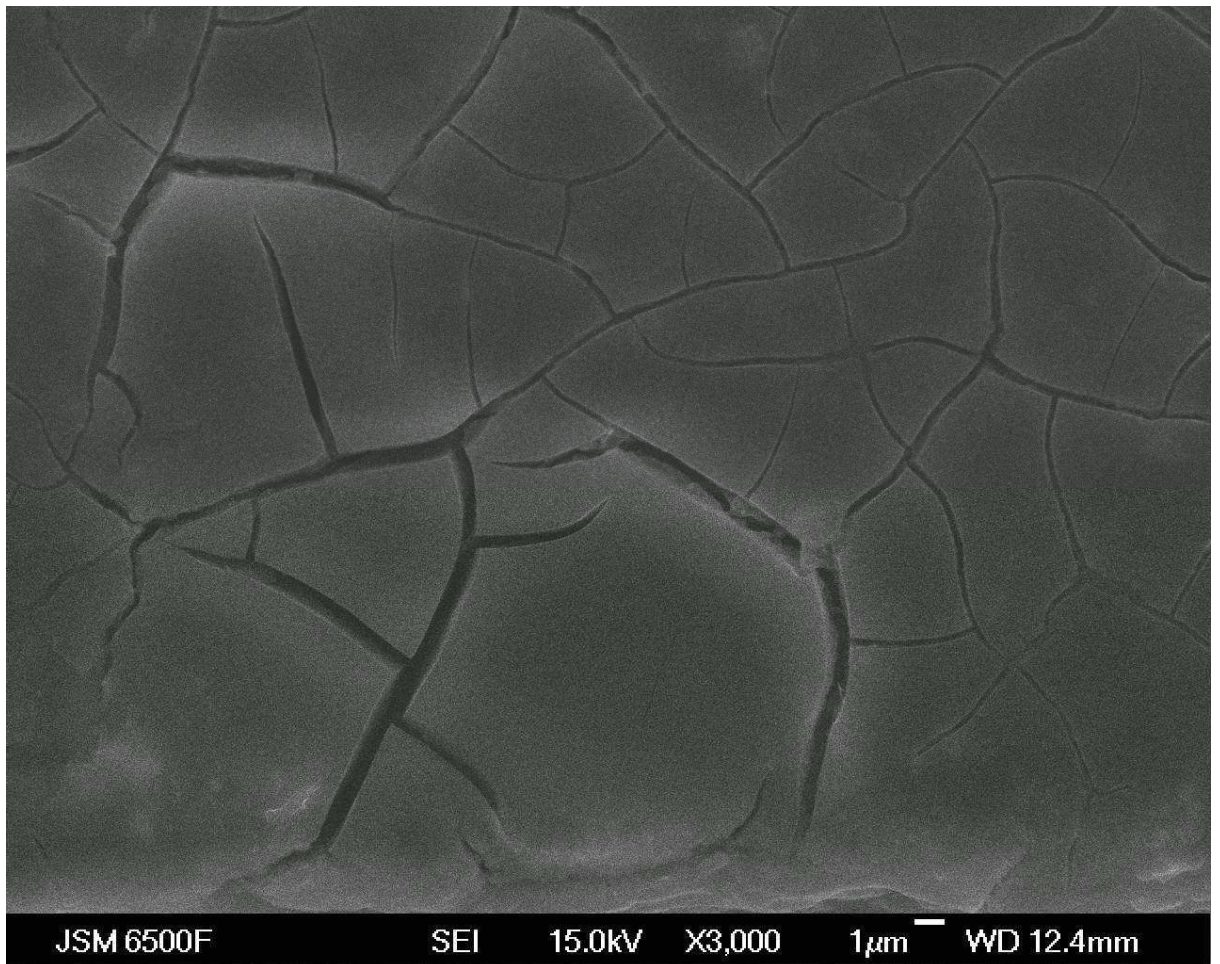


Figure 4.8: SEM image of MgB_2 bulk sample sintered at 970°C for 12 hours.

We have then explored the viability of preparing MgB_2 samples synthesized from a mixture of Mg, B and MgB_2 powder in the molar ratio of $(\text{Mg}+2\text{B}):\text{MgB}_2=1:1$. This approach -defined in the literature as the “premix method” [35], since it is a mixture of MgB_2 , prepared at 900°C for 6 h, and boron powder and then reacted at a temperature of 970°C with a magnesium rod- was attempted to solve the problem of the diffusion of magnesium into the boron particles, by bringing the boron and magnesium powders into intimate contact, which would expect to achieve a well-sintered microstructure devoid of cracks throughout the sample.



Figure 4.9: MgB₂ bulk sample sintered at 970°C for 6 hours starting with a mixture of Mg, B and MgB₂ (molar ratio of (Mg+2B):MgB₂=1:1).

However, samples produced using the “premix method”, when taken out of the furnace, exhibited major cracks orthogonal to their principal axis which caused the samples to fracture into two pieces, although the number and the extension of the cracks were observed to be fewer and less pronounced than in the other samples fabricated using a different method, as shown in fig.(4.9).

The third approach consisted of addressing both the sintering temperature of MgB₂ samples and the boron packing density. In particular, two undoped samples have been produced by lowering the dwell temperature to 850°C and 775°C, respectively, and by reducing their respective boron packing densities to 41% and 36% of the value of boron density. The results obtained showed that progressive reduction of boron packing density and of the sintering temperature caused a significant improvement in the mechanical performance of the material. In fact, the major cracks orthogonal to the sample's principal axis, which were seen to compromise the integrity of the sintered samples, were

observed to be less extensive in the undoped MgB_2 sample treated at 850°C , fig.(4.10), and completely absent in that sintered at 775°C , fig.(4.11). Moreover, as shown in fig.(4.12), the residual small cracks resulting from the hoop stresses, observed in the undoped MgB_2 sample sintered at 775°C , were noticeably smaller than those detected in the higher temperature treated samples. The density was macroscopically measured for the undoped MgB_2 sample sintered at 775°C and was found to be equal to 1.88 g/cm^3 , which is about 73% of the theoretical density of magnesium diboride.

A similar behaviour was observed in the C-CVD doped MgB_2 sample treated at 850°C , fig.(4.13) and (4.14). The sample appeared devoid of major cracks and the resulting microstructure was only marred by the presence of a limited number of voids and microcracks, in the order of a few μm , which was probably the result of the hoop stresses undergone by the specimen.



Figure 4.10: Optical microscopy image of the undoped MgB_2 treated at 850°C .



Figure 4.11: Optical microscopy image of the undoped MgB₂ treated at 775°C.

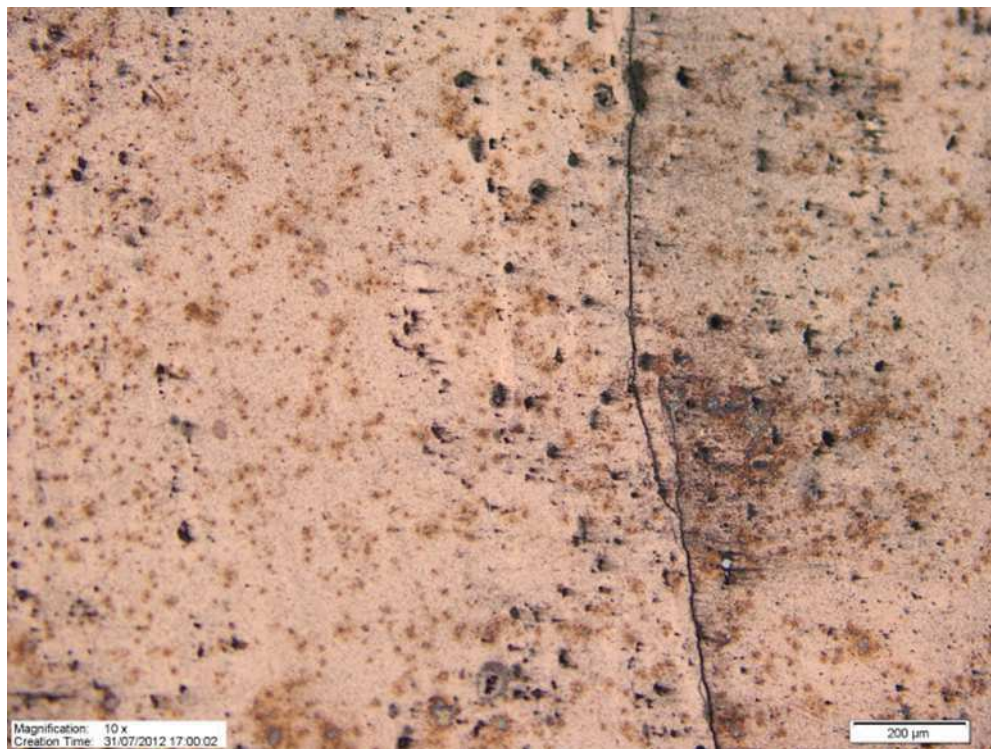


Figure 4.12: Optical microscopy image showing an enlarged view of a section of the undoped MgB₂ treated at 775°C exhibiting comparatively small cracks, which presumably arise from hoop stresses.

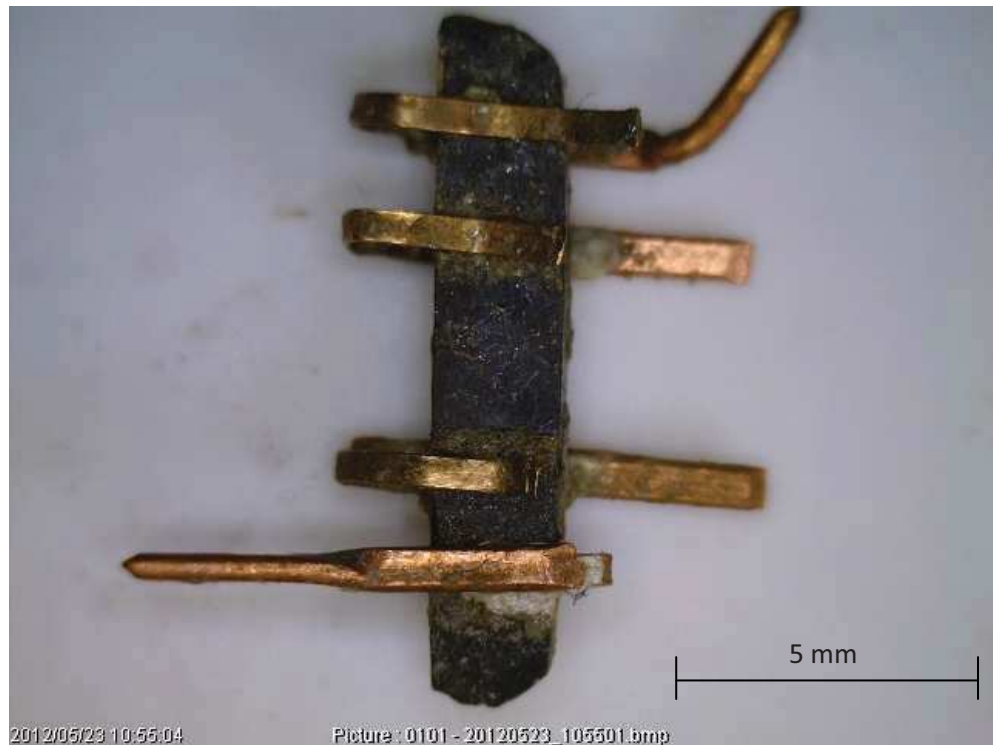


Figure 4.13: Optical microscopy image of C-CVD doped MgB₂ treated at 850°C. The sample was prepared for resistivity measurements in the PPMS.



Figure 4.14: Optical microscopy image of C-CVD doped MgB₂ treated at 850°C.

In order to better study the connectivity of the undoped MgB₂ sample sintered at 775°C and the 3.9% C-CVD doped MgB₂ sample treated at 850°C, resistivity measurements were performed in the Quantum Design PPMS using the four-probe system illustrated in fig.(4.13). The electrical contact was achieved by pressure contacts which were made with custom made, hardened copper clip springs, with one side bonded with silver loaded epoxy for mechanical support and thermal contact. The effective cross section, A_F , was calculated from the temperature dependent resistivity plots of fig.(4.15) by using the following expression:

$$A_F = \frac{1}{F} = \frac{\Delta\rho_{sc}}{\Delta\rho} \quad (4.1)$$

where $\Delta\rho_{sc}$ is the temperature dependent resistivity of the single crystal, i.e. the difference between the resistivity value at room temperature and that at 40 K, whilst $\Delta\rho$ is the change in resistivity between 300 K and 40 K for a polycrystalline bulk sample. The reported values of $\Delta\rho_{sc}$ for undoped and 3.9% C doped single crystal MgB₂ samples are 4.3 $\mu\Omega\text{cm}$ and 4 $\mu\Omega\text{cm}$, respectively [84, 85]. The values of A_F obtained, 0.52 for the undoped MgB₂ sample and 0.25 for the 3.9% C-CVD doped MgB₂ sample, were quite high compared to many polycrystalline samples in the literature which have reported values below 0.2. In particular, the significantly high value calculated for the undoped sample indicates that it exhibited a high density and a low level of porosity. These results confirm that the optimisation of boron packing density, and of synthesis temperature, is capable of achieving a well connected microstructure, characterised by a limited number of cracks and voids within the sintered samples, as evidenced by the analysis of SEM and optical microscopy images. With regard to the undoped sample, the low residual resistivity, ρ_0 , value, (2.5 $\mu\Omega\text{cm}$) is quite close to the values reported for undoped samples produced by using the melt impregnation ($\rho_0=1-2 \mu\Omega\text{cm}$) [86] and single

step methods ($\rho_0=0.55 \mu\Omega\text{cm}$) [87]. C doped sample exhibited a ρ_0 of $10 \mu\Omega\text{cm}$, a significantly low value compared with the literature-reported values of other samples doped with the same actual percentage of C, such as $\text{MgB}_2+\text{C}_4\text{H}_6\text{O}_5$ ($\rho_0=90.2 \mu\Omega\text{cm}$) [88] and MgB_2 doped by high-energy ball milling of C ($\rho_0=95\mu\Omega\text{cm}$) [46]. These results suggest that the manufacturing process of MgB_2 bulk samples, and, in the case of C doped samples, the C-CVD method were capable of producing materials exhibiting high purity as well as high density.

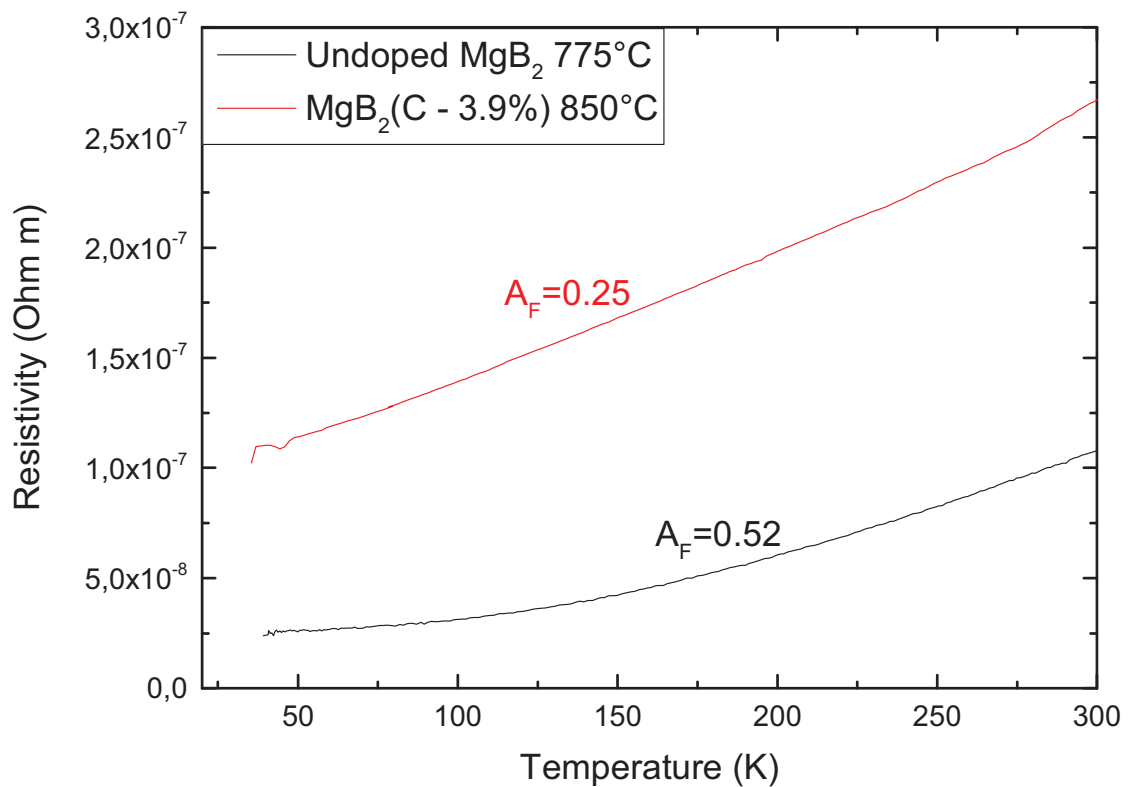


Figure 4.15: Resistivity measurements of the undoped MgB_2 sample sintered at 775°C and the $\text{MgB}_2(\text{C} - 3.9\%)$ sample treated at 850°C . The respective values of A_F , calculated using eq.(4.1), are included in the graph.

4.1.3.2 Crack issue

The study and optimisation of the fabrication method of the bulk MgB_2 samples has suggested that the presence of cracks could be caused by the combination of two distinct phenomena, as described below. A post mechanical analysis of the thermo-mechanical stress behaviour

introduced by the process of sintering has shown that, during the phase of cooling, normal forces (specifically, tensile stress) are produced as a result of shear stresses of friction between the sample and the walls of the iron tube. Mathematically, this may be described by the following relationship:

$$\sigma(x) = -2\alpha(\Delta T)E \quad (4.2)$$

where $\sigma(x)$ is normal stress, ΔT is the temperature difference between the dwell temperature and the room temperature, α is the sample coefficient of thermal expansion and E is the sample Young's module. The above-described analysis shows that the dwell temperature is one of the parameters on which you can act since it affects the thermo-mechanical behaviour of the material. The differences in mechanical behaviour between undoped and C-CVD-doped MgB_2 , when treated at the same dwell temperature, can therefore be explained by virtue of the difference in the coefficients of thermal expansion (along both the a -axis and the c -axis) between the two materials which is reflected in the values of thermo-mechanical stresses in play.

Another possible explanation of the inhomogeneous and incomplete process of sintering and of the consequent phenomenon of cracks might be represented by the difference between the time constant of reaction and the time constant of diffusion. In fact, the magnesium must diffuse into the boron particles in order to react and form magnesium diboride. If the rate of reaction is higher than the rate of diffusion, it could lead to the formation of well-reacted and sintered areas, which are located in the proximity of the original position of the magnesium rod, and of areas which are poorly reacted and sintered, and are predominantly constituted of boron powder, as shown in fig.(4.16). When the poorly reacted and sintered areas finally react and convert to magnesium

diboride, they tend to expand, but this expansion is prevented by the areas that have already reacted and sintered. This phenomenon could result in the formation of cracks compromising the mechanical integrity of the samples, as observed in the Section 4.1.3.1. This behaviour is expected to be more evident when using nanometric boron powder than it is when using coarser boron particles, because both the specific surface area and the packing density are higher than in the case of coarser boron particles. The crucible could not be put in vertical, even though this might have improved the diffusion of Mg in the liquid state, because the length of the iron tubes used, fig.(4.16), was greater than the diameter of the furnace tube.



Figure 4.16: Optical microscopy picture of MgB₂ bulk sample showing the presence of well-reacted and dense areas, which are located in the proximity of the original position of the magnesium rod, and powdery sections of the sample, which are poorly reacted and sintered.

In order to reduce the difference between the rate of reaction and the rate of diffusion, two different approaches were explored: the viability of preparing MgB₂ samples synthesized from a mixture of Mg, B and MgB₂ powder and the progressive reduction of the packing density of boron powder. In particular, the latter method proved to be beneficial to solving the problem of the formation of cracks, in that it favoured the diffusion of

magnesium into boron powder and material rearrangement during the sintering process.

In order to verify which of the two models could explain the formation of cracks within the MgB_2 samples, a very short sample (20 mm) was prepared, using the same method employed to produce the samples discussed in the previous section. The sample was then heat-treated at 750°C for 12 h, cooled to room temperature, and then removed from the iron tube, to be examined under an optical microscope, fig.(4.17a). The sintered sample was then placed between two titanium rods within another iron tube, the two ends of the tube crimped as before, and heat-treated at 950°C for other 12 h. The sample was again removed from the tube and re-examined under the optical microscope, fig.(4.17b). The absence of cracks in both samples, evidenced by the comparison of the two optical microscopy pictures, fig.(4.17a and b), suggested that the difference between the time constant of reaction and the time constant of diffusion was the cause of crack formation. In fact, the well-sintered microstructure which appeared devoid of cracks in the case of the short sample heat-treated at 750°C , indicated that the sintering at comparatively low temperature on a short length scale resulted in a reduction of the gradient between the rate of reaction and that of diffusion. On the other hand, the absence of cracks in the higher temperature treated sample seems to indicate that differential thermo-mechanical stress, which should be enhanced by high sintering temperatures, was not the main mechanism which led to the formation of cracks.

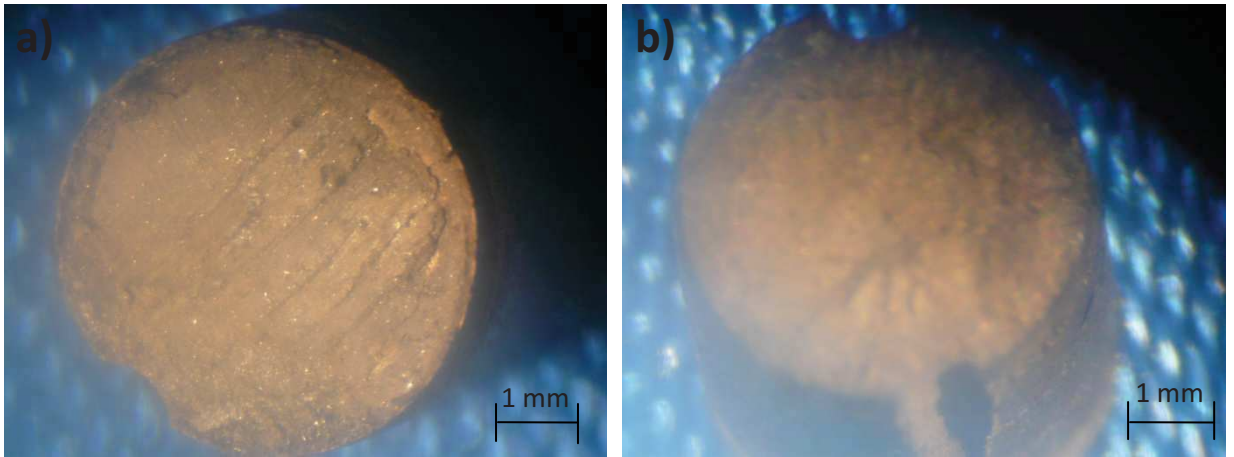


Figure 4.17: Optical microscopy pictures showing an undoped MgB₂ after a first cycle of heating up to 750°C for 12 h and cooling down to room temperature (a), and the same sample after a second cycle of heating up to 950°C for 12 h and cooling down to room temperature (b).

4.2 Characterisation of undoped MgB₂

4.2.1 Experimental details

Using the fabrication method described in the Section 4.1.3.1, three undoped MgB₂ bulk samples, treated at different dwell temperatures as detailed in Table 4.2, have been produced and characterised.

SAMPLE	SINTERING TEMPERATURE (°C)
MgB ₂	850
MgB ₂	775
MgB ₂	740

Table 4.2: Summary table of the undoped MgB₂ bulk samples prepared and characterised in this work, and the respective sintering temperatures.

4.2.2 Structural analysis and critical current density properties

Fig.(4.18) shows the critical current density as a function of magnetic field at 11 K and 22 K for the three undoped MgB₂ samples. The sample treated at 775°C clearly exhibits the best critical current density properties throughout the field range, both at 11 K and 22 K. The J_c value in 0.1 T for this sample is two times higher than that for the 850°C sample at 11 K, and 40% larger at 22 K. The J_c performance of the 740°C sample at low fields is substantially lower than those for the other two higher temperature treated samples. The field dependence of J_c is observed to be comparatively weak in the 850°C sample, whilst it is enhanced in the samples sintered at lower temperatures. This behaviour is even more evident when considering the normalized critical current density, $J_c(B)/J_c(B = 0.1 \text{ T})$, in function of the field B , as shown in fig.(4.19). The $J_c(B)/J_c(B = 0.1 \text{ T})$ curves for the higher temperature treatment fall off more quickly than those for the other two specimens, whilst there is a crossover between the curves of the 740°C sample and

the 775°C sample, corresponding to 2.3 T at 22 K, and 4.3 T at 11 K, respectively.

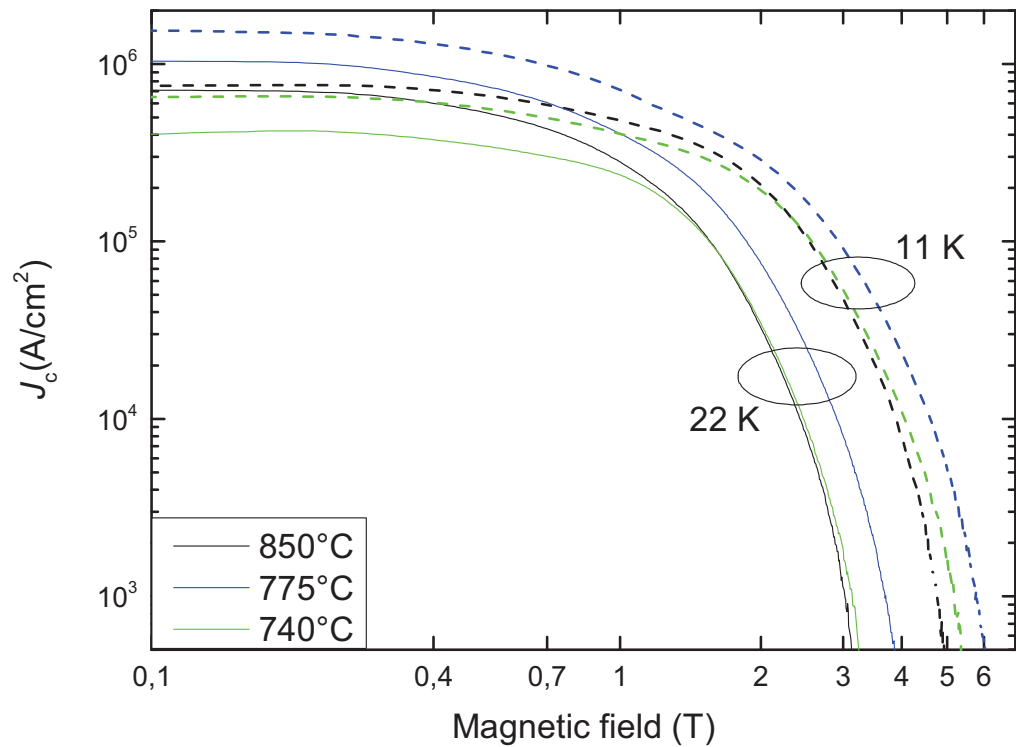


Figure 4.18: Field dependence of the critical current density, $J_c(B)$, at 11 K and 22 K for the undoped MgB_2 samples treated at the specified dwell temperatures.

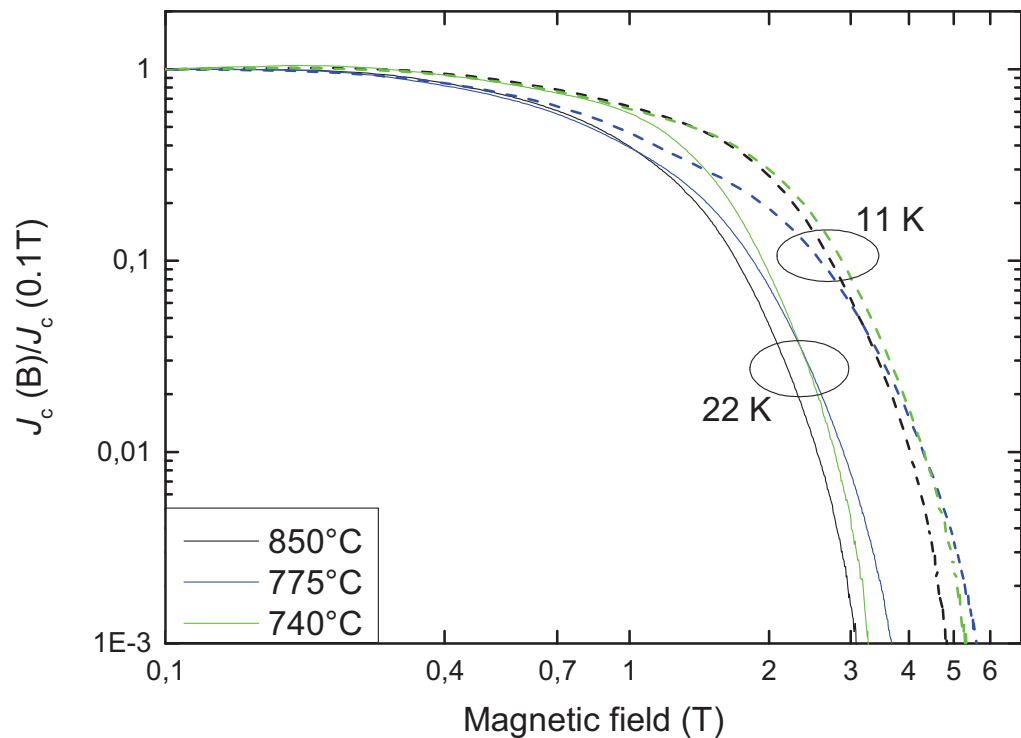


Figure 4.19: Field dependence of the normalized critical current density, $J_c(B)/J_c(B=0.1 \text{ T})$, at 11 K and 22 K for the undoped MgB_2 samples treated at the specified dwell temperatures.

The SEM pictures, fig.(4.20), show that the microstructure of the three undoped samples transitions from spherical shaped grains, mainly grouped into clusters, to well distinguishable, bar/plate shaped grains as sintering temperature is increased. However, the analysis of the SEM images does not provide evidence that there is sufficient difference in the levels of porosity to justify so marked a variation in J_c performance. Therefore, in order to investigate if, and to what extent, the presence of internal cracks affects the J_c properties, magnetisation measurements were performed on the three undoped MgB_2 samples polished at two different levels of thickness. In fact, it can be proved that, by virtue of the Bean critical state model, the J_c value of a sample with a thickness t is not equal to that of another sample composed of two pieces, each one having thickness $t/2$, placed one on top of the other. For a parallelepiped sample with thickness t , length x and width y , J_c is given by:

$$J_c = \frac{20M}{xyt^2} \quad (4.3)$$

whilst the critical current density value for the sample composed of two pieces each having thickness $t/2$ (with the other dimensions x and y unchanged) is equal to:

$$J_c = \frac{40M}{xyt^2} \quad (4.4)$$

Since the model of the two part sample having thickness $t/2$ is equivalent to one sample having a crack in the middle, the equations (4.3) and (4.4) prove that the presence of cracks would change the J_c value.

Fig.(4.21) shows the $J_c(B)$ curves at 10 K for the 775°C sample which has been polished and characterised for thicknesses of 0.33 mm and 0.23 mm. The curves are observed to almost overlap, which is indicative of an absence of, or a low presence of, internal cracks within the sample. In

contrast, $J_c(B)$ curves, fig.(4.22), at 10 K for the 740°C sample show that the sample 0.74 mm thick exhibited higher critical current density properties throughout the field range than the same sample polished to a thickness of 0.39 mm. This result suggests that the 740°C sample presented an inhomogeneous distribution of internal cracks throughout its thickness, and, unfortunately, the non-cracked portion of the sample was polished away, resulting in a reduction of J_c properties for the 0.39 mm thick sample. With regard to 850°C sample, fig.(4.23), there is a nearly identical J_c performance between the 0.28 mm thick and the 0.117 mm thick sample down to 0.7 T, whilst below that magnetic field value, a significant variation in J_c is observed. That variation might be explained by the presence of internal cracks within the thicker sample, which hindered the J_c at the lower field values.

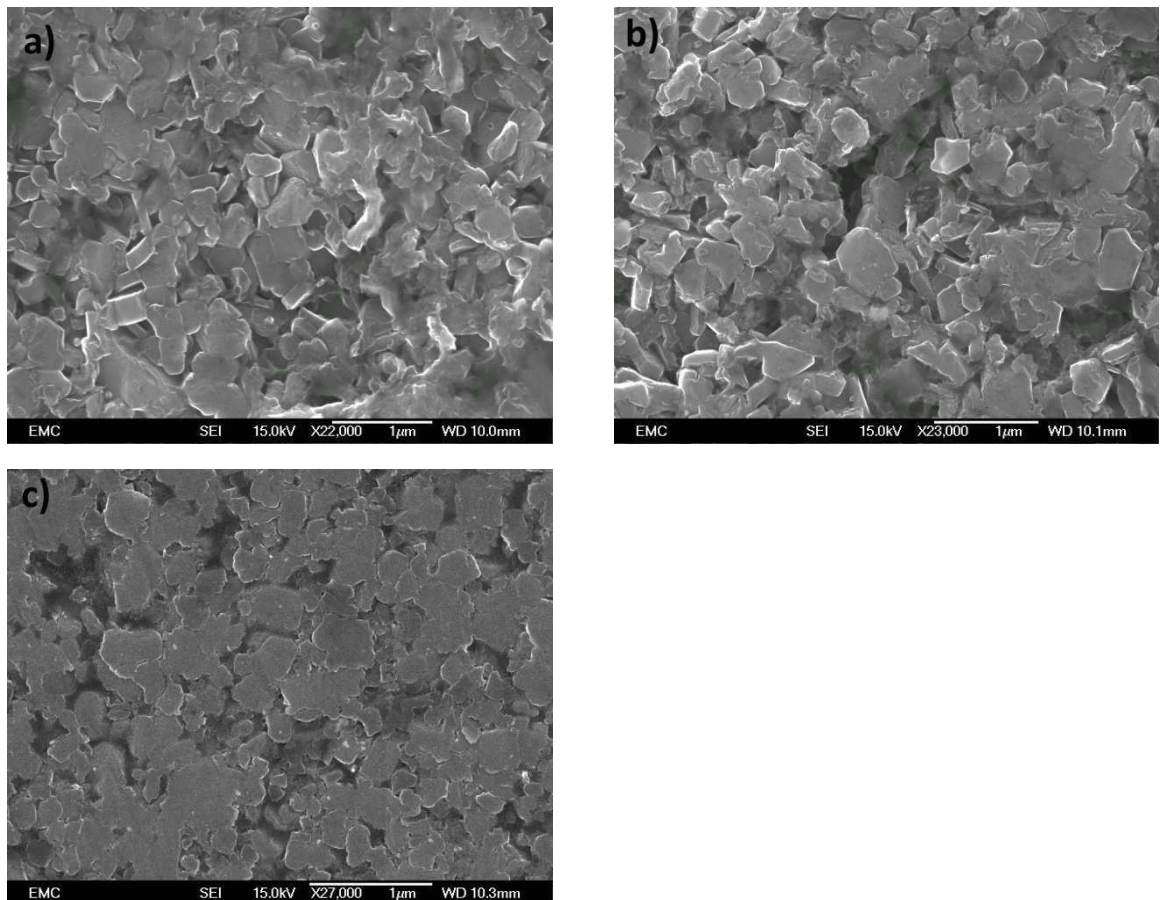


Figure 4.20: SEM images for undoped MgB_2 samples treated at 850°C(a), 775°C (b) and 740°C (c).

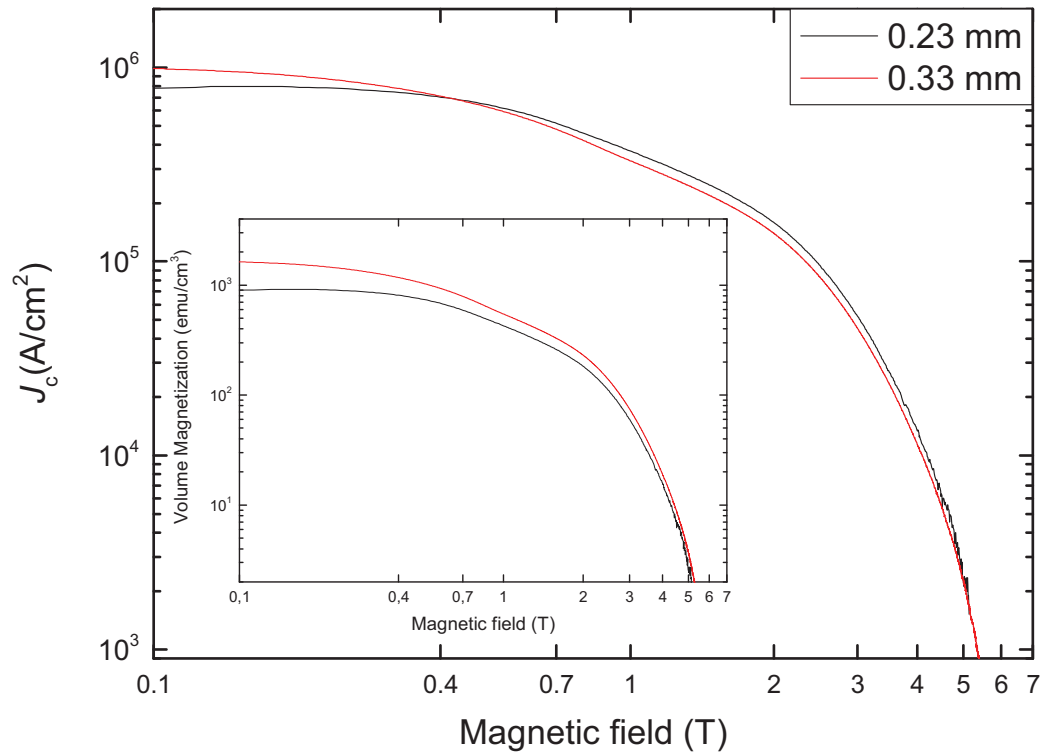


Figure 4.21: Comparison of $J_c(B)$ at 11 K for the 775°C MgB_2 sample, polished and characterised for thicknesses of 0.33 mm and 0.23 mm. The inset shows the magnetisation per unit volume plotted against magnetic field.

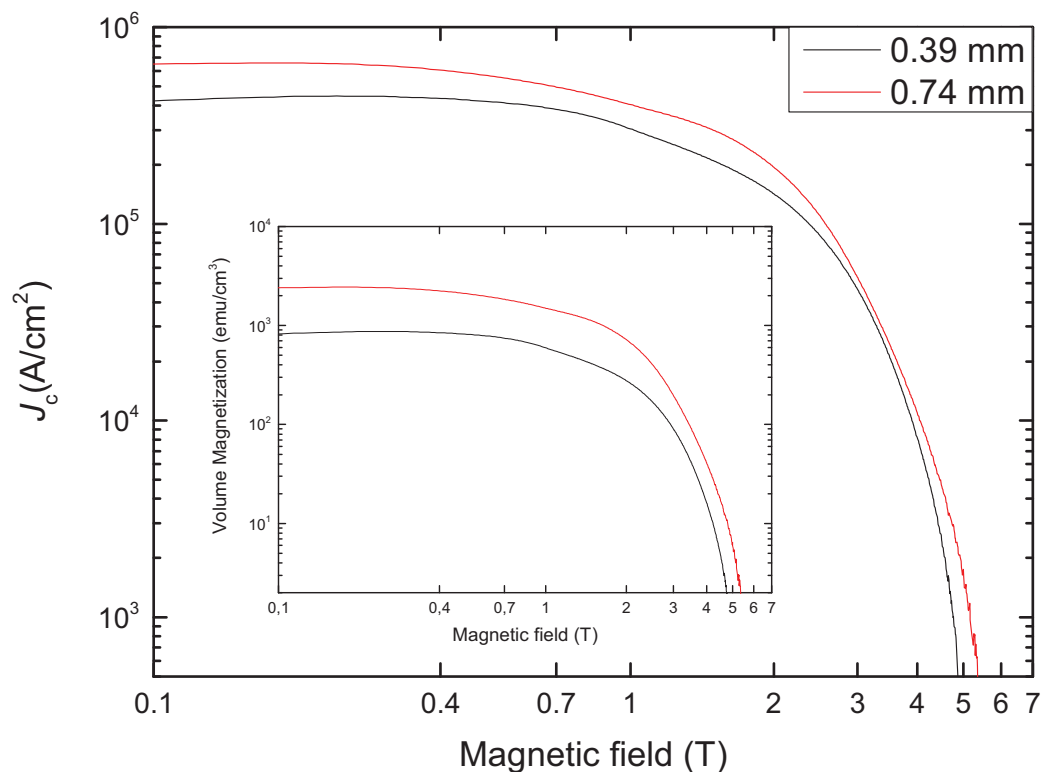


Figure 4.22: Comparison of $J_c(B)$ at 11 K for the 740°C MgB_2 sample, polished and characterised for thicknesses of 0.74 mm and 0.39 mm. The inset shows the magnetisation per unit volume plotted against magnetic field.

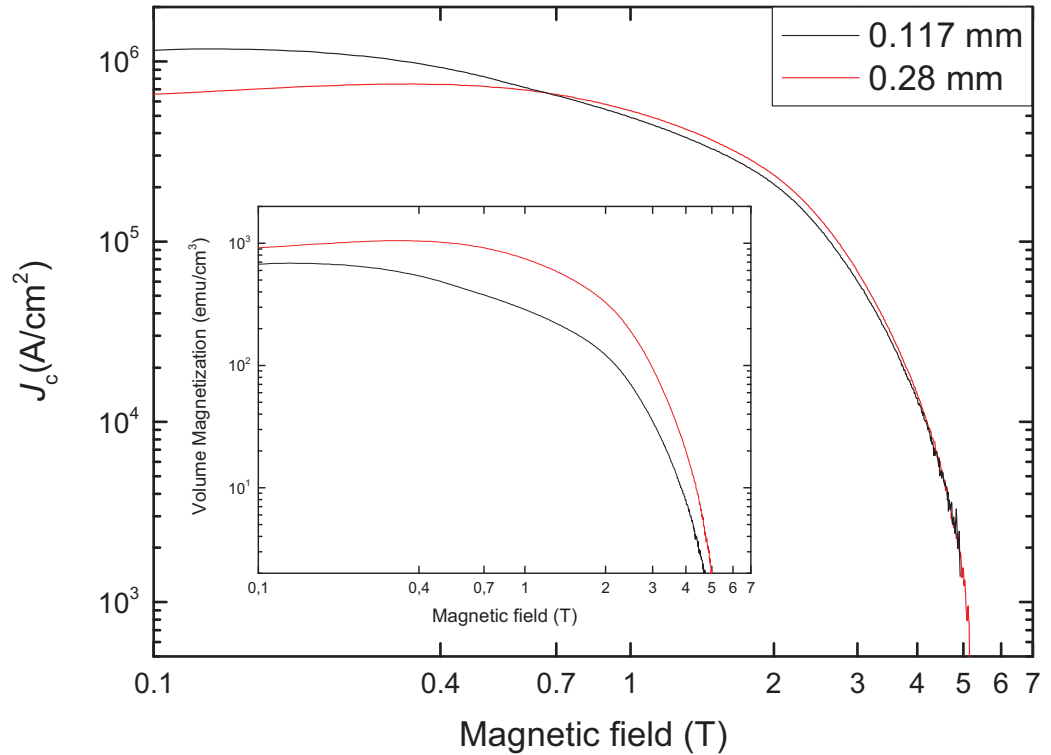


Figure 4.23: Comparison of $J_c(B)$ at 11 K for the 850°C MgB₂ sample, polished and characterised for thicknesses of 0.28 mm and 0.117 mm. The inset shows the magnetisation per unit volume plotted against magnetic field.

The analysis of the XRD patterns has revealed that the full width at half maximum (FWHM) of the (100) peak for the 850°C sample is smaller than that for the lower temperatures sintered samples, as shown in fig.(4.24), passing from 0.1 to 0.17. Therefore, small crystal sizes, evidenced by the broadening of the XRD peaks (higher FWHM values), could be one of the reasons for the enhanced magnetic field dependence of J_c observed in samples processed at low temperatures. In fact, it is reported [43] that the decrease of the crystal size contributes to enhancing the intraband scattering and shortening the electron mean free path l and coherence length ξ . The pinning force at grain boundaries (f_{GB}) is thought to increase with impurity which is inversely proportional to l [89].

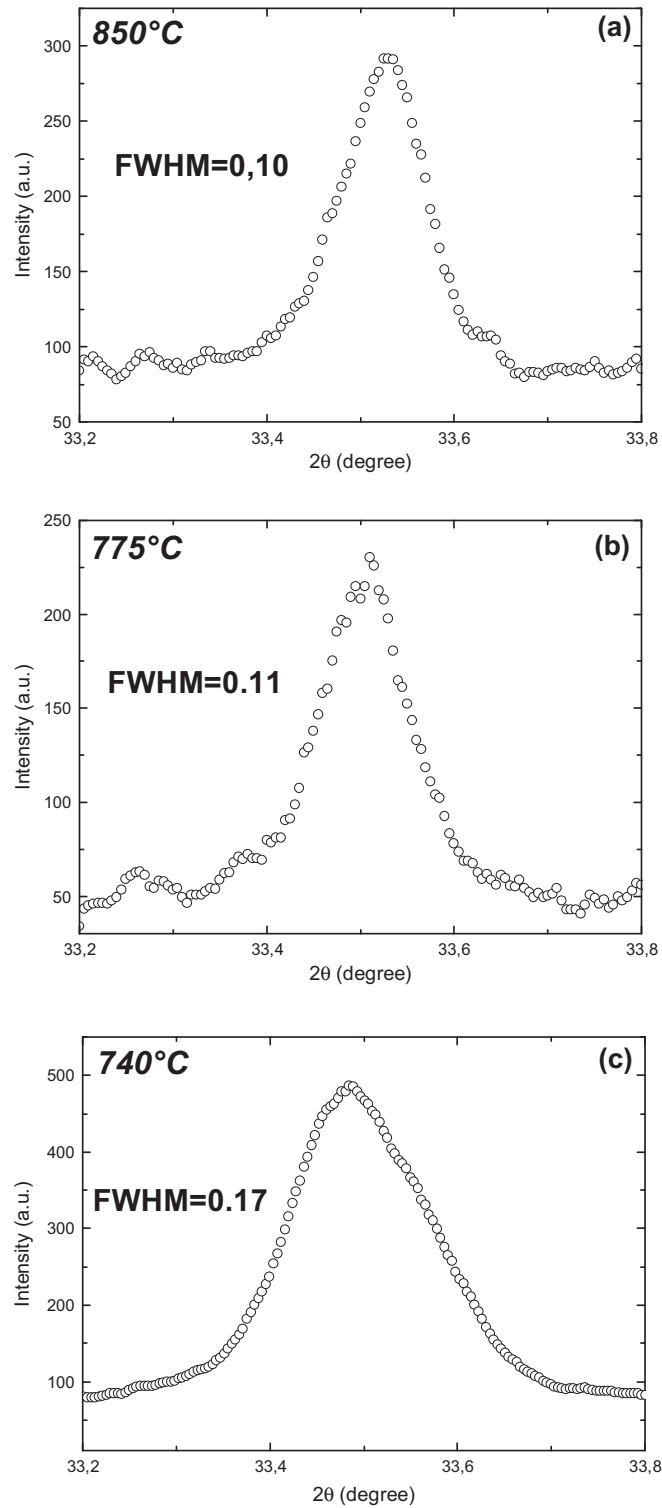


Figure 4.24: XRD patterns of (100) reflection for undoped MgB₂ samples treated at 850°C(a), 775°C (b) and 740°C (c). In the same figures, the full width at half maximum (FWHM) values are indicated.

In order to investigate the pinning mechanisms, we analyzed the pinning force. Fig.(4.25) and (4.26) show the Kramer plots -produced by plotting $F_k = J_c^{0.5} H^{0.25}$ as a function of the applied field H , at 11 K and 22 K- that

have been used to estimate the irreversibility field H_{irr} . [90] Although the plots do not show a linear behaviour in a large range of field, the values of the irreversibility field, $H_{irr} \equiv H_K$, could be estimated by extrapolating the linear part of the Kramer function at high currents to the field axis intercept. These values have then been used to plot the normalized pinning forces, F_p/F_{pmax} where $F_p = J_c H$, as a function of the reduced field H/H_K at 11 K and 22 K, as shown in fig.(4.27) and (4.28). The graphs also include the normalised theoretical curves of pinning forces for grain boundary mechanism, expressed analytically by

$$F_p/F_{pmax} = \left(\frac{H}{H_{irr}}\right)^{0.5} \left(1 - \frac{H}{H_{irr}}\right)^2, \quad (4.5)$$

and point defect mechanism, as reported in [65, 91]. It is evident that no correlation exists between the sintering temperature and the position of the pinning force maximum. In fact, whilst in the case of the sample sintered at 775°C, both at 11 and 22°K, the peak positions are located at values of H/H_K slightly close to 0.2, for both the 850°C and 740°C treatments a shift to a higher angle is observed. The positions of the F_p maxima are virtually coincident at $H/H_K \approx 0.33$ for both samples at 11 K, whereas at 22 K the maximum position tends to approach 0.3 for the 850°C treatment, but it is nearly 0.37 for the sample sintered at 740°C. These results suggest that the predominant pinning mechanism is by grain boundary for the 775°C treatment, whilst in the other two samples (and, in particular, for the 740°C treatment) there is clear evidence of changing of pinning mechanisms to point defects. However, this additional pinning mechanism, which has been found to improve the vortex pinning strength at high field [91], is not capable of producing a significant improvement in J_c in the samples treated at 850°C and 740°C. This is presumably due to the presence of cracks, which, as evidenced by

the analysis of the J_c properties at two different levels of sample thickness, was observed to be more significant than in the sample sintered at 775°C.

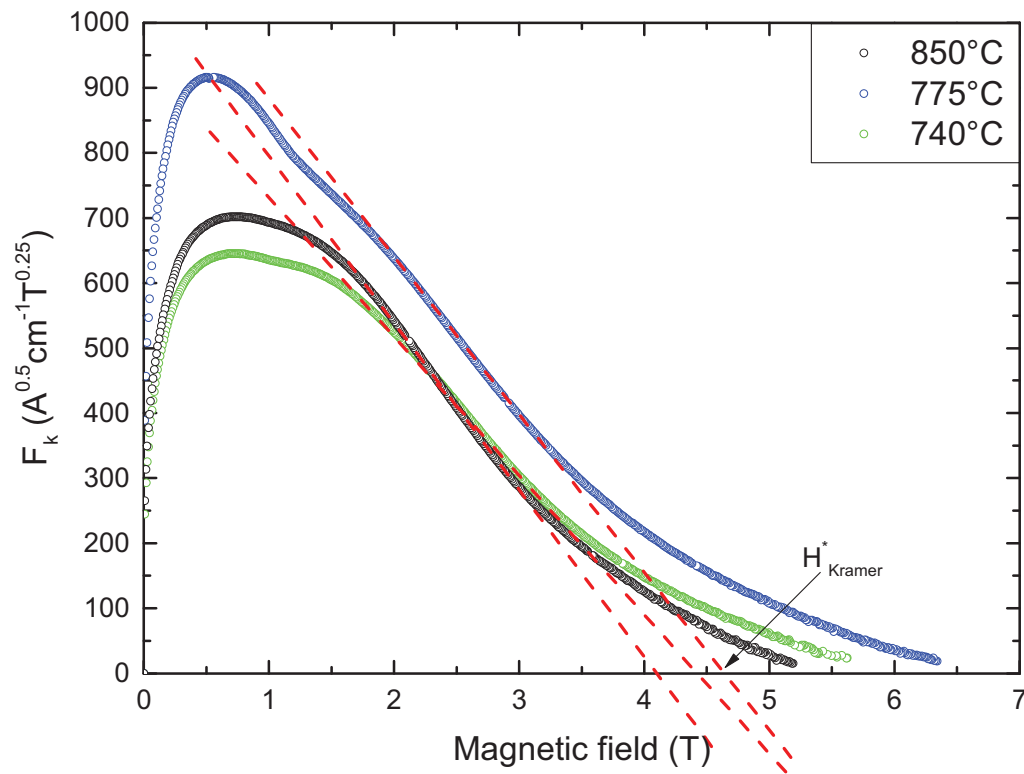


Figure 4.25: Kramer plots as a function of magnetic field at 11 K from the J_c data for undoped MgB_2 samples treated at 850°C (black), 775°C (blue) and 740°C (green).

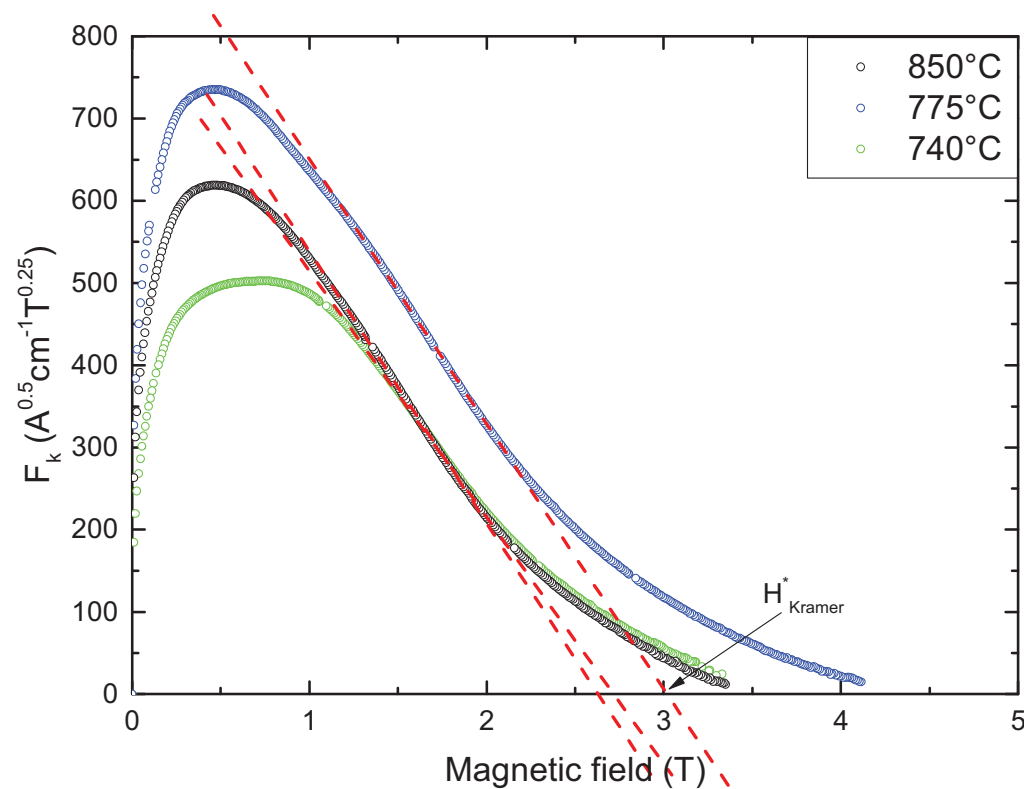


Figure 4.26: Kramer plots as a function of magnetic field at 22 K from the J_c data for undoped MgB_2 samples treated at 850°C (black), 775°C (blue) and 740°C (green).

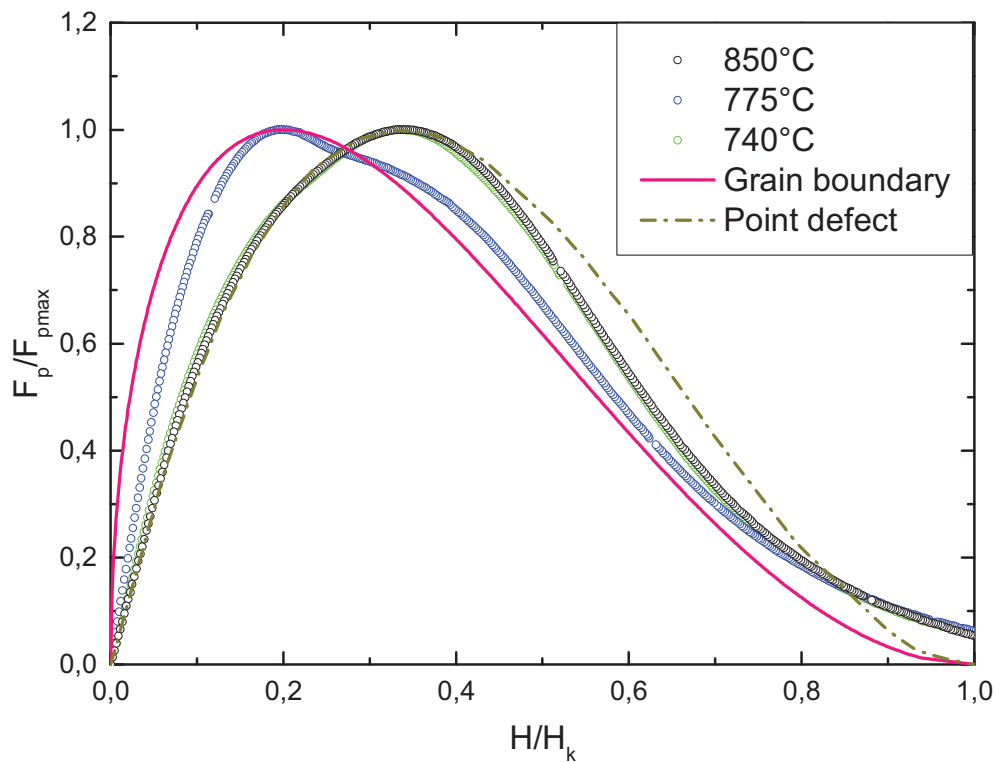


Figure 4.27: Behaviour of the normalised pinning force vs normalised magnetic field at 11 K from the magnetic J_c data for the undoped MgB_2 samples treated at 850°C (black), 775°C (blue) and 740°C (green). Grain boundary pinning, eq.(4.5), and point defect models, [91], are also shown for comparison.

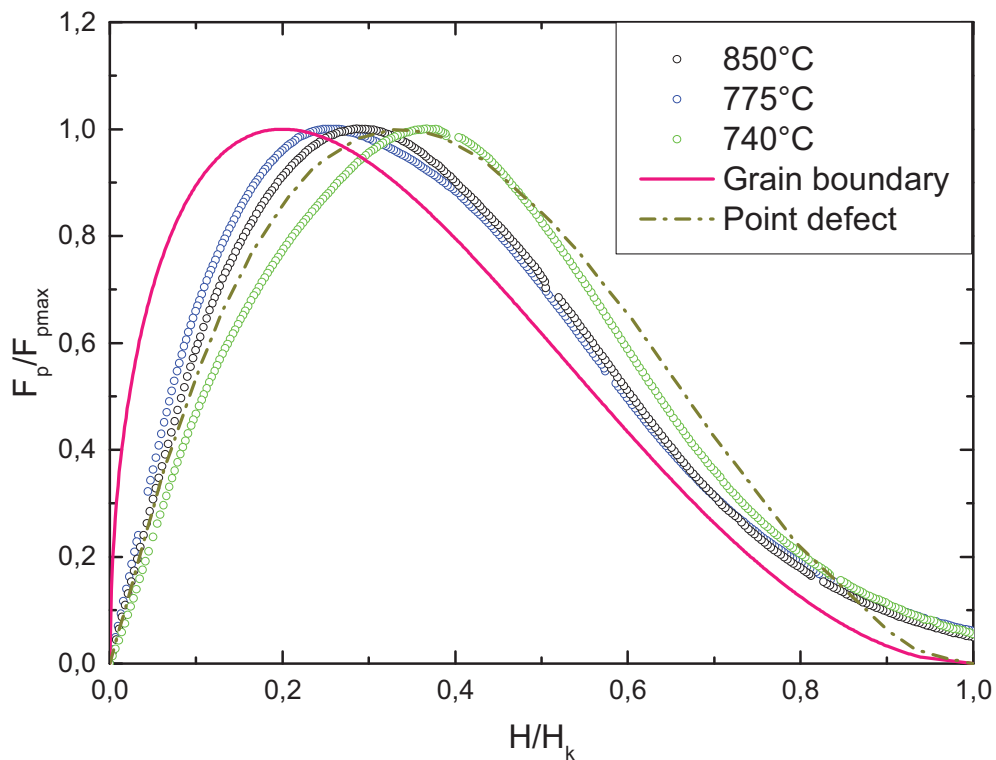


Figure 4.28: Behaviour of the normalised pinning force vs normalised magnetic field at 22 K from the magnetic J_c data for the undoped MgB_2 samples treated at 850°C (black), 775°C (blue) and 740°C (green). Grain boundary pinning, eq.(4.5), and point defect models, [91], are also shown for comparison.

For the 775°C and 850°C samples, the temperature dependence of J_c has also been studied. In the analysis and discussion of the J_c properties, in this chapter, the critical temperature is indicated as T_{irr} since T_c is a reversible property, while the critical current is irreversible. The temperature-dependent critical current density curves at 0.1 T, as shown in fig.(4.29), have been fitted using the equation:

$$J_c(T) = J_c(0) \cdot \left[1 - \frac{T}{T_{irr}} \right]. \quad (4.6)$$

The fitting parameters are $J_c(0) = 3.022 \cdot 10^6$ A/cm² and $T_{irr}=37.5$ K for the 775°C MgB₂ sample, and $J_c(0) = 1.8 \cdot 10^6$ A/cm² and $T_{irr}=37.3$ K for the 850°C MgB₂ sample.

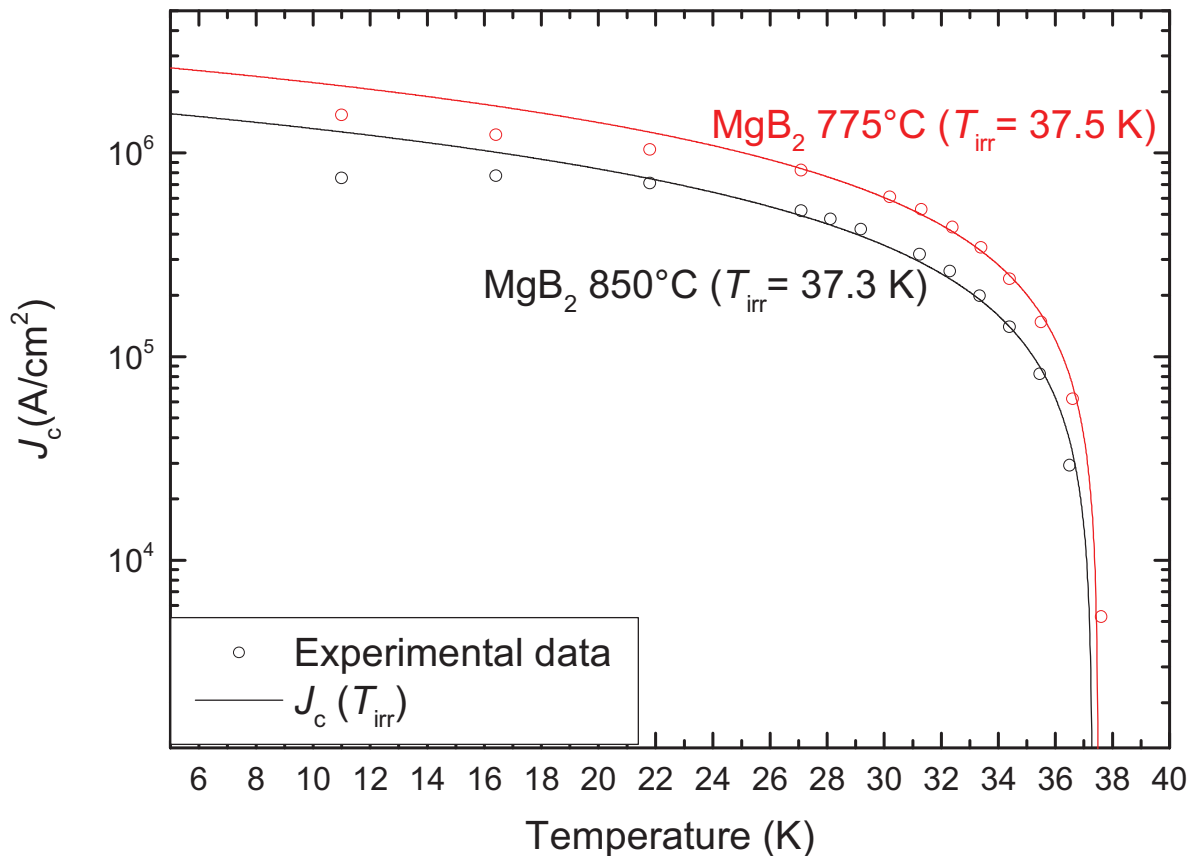


Figure 4.29: Temperature dependence of the critical current density, $J_c(T)$, at 0.1 T for the 775°C MgB₂ (red) and 850°C MgB₂ (black) samples. Circles represent experimental data, whilst solid lines represent fitting curves, described by eq.(4.6).

The linear decrease of J_c with increasing temperatures, which has also been reported in [92, 93] and has been explained by the temperature dependence of the coherence length $\xi(T)$ in $J_c(T)$, was observed to be valid down to 22-24 K. Below that temperature range, the $J_c(T)$ deviated from such behaviour and tends to flatten out.

In order to verify if the flattening off persists at higher magnetic field and study the irreversibility temperature behaviour near the T_{irr} region, the temperature dependence of J_c at 1 T was studied. The temperature-dependent critical current density curves at 1 T, as shown in fig.(4.26) and (4.27), have been plotted and fitted using the following equation:

$$J_c(T) = J_{c_1}(0) \cdot \left[1 - \frac{T_1}{T_{irr_1}}\right] + J_{c_2}(0) \cdot \left[1 - \frac{T_2}{T_{irr_2}}\right] + \dots + J_{c_n}(0) \cdot \left[1 - \frac{T_n}{T_{irr_n}}\right] \quad (4.7)$$

The eq.(4.7) is a linear combination of n eq.(4.6) with different T_{irr} 's and $J_c(0)$'s. In particular, the temperature dependence of J_c of both the undoped MgB₂ samples could be described using two T_{irr} 's, which are 32.7 K and 30.5 K for the 775°C MgB₂ sample, fig.(4.30), and 31.2 K and 29.3 K for the 850°C MgB₂ sample, fig.(4.31). The splitting into two irreversibility temperatures at higher fields could reveal the existence of two current paths having a different pinning strength. The presence of two T_{irr} 's, i.e. two current paths, in the undoped MgB₂ samples can be explained by material inhomogeneities, which are particularly sensitive to the intensity of, and orientation with respect to, the applied magnetic field, as suggested by Eisterer [94]. It is also evident that the flattening off at low temperatures, which was observed in the plot of the temperature-dependent critical current density curves at 0.1 T, fig.(4.29), virtually disappears, which would suggest it is a remnant of the magnetisation measurements due to self field effect.

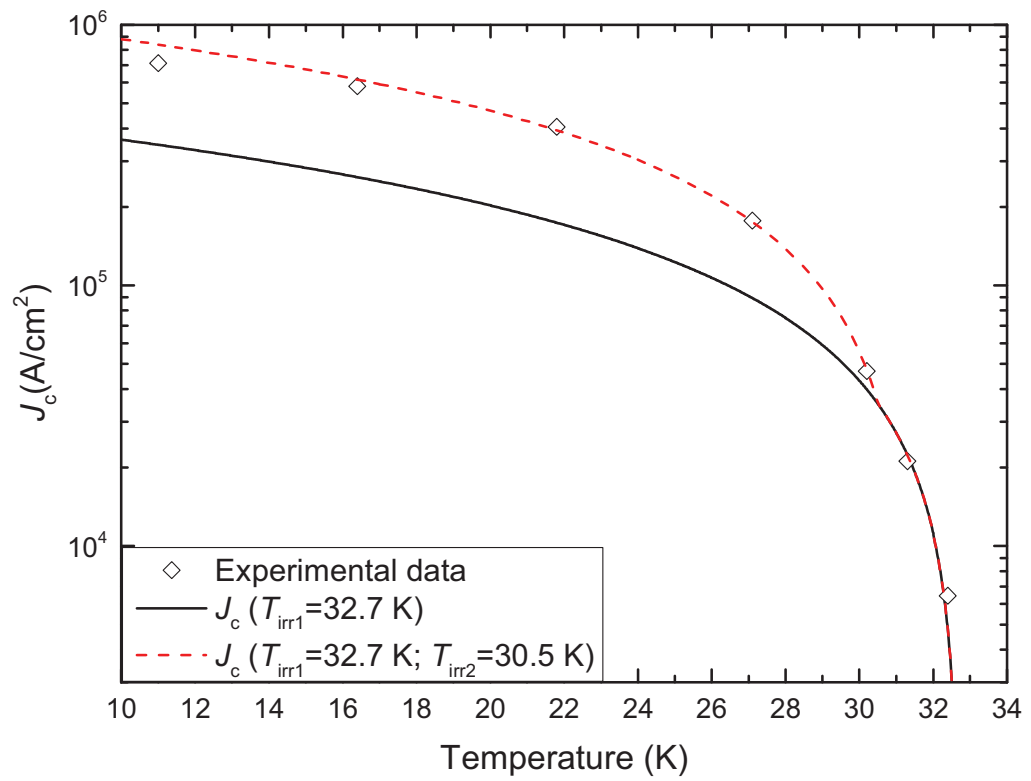


Figure 4.30: Temperature dependence of the critical current density, $J_c(T)$, at 1 T for the MgB₂ sample sintered at 775°C. Circles represent experimental data, whilst solid black line and dashed red line represent respectively the fitting curve defined using one T_{irr} and the cumulative fitting curve defined with two T_{irr} , as described by eq.(4.7).

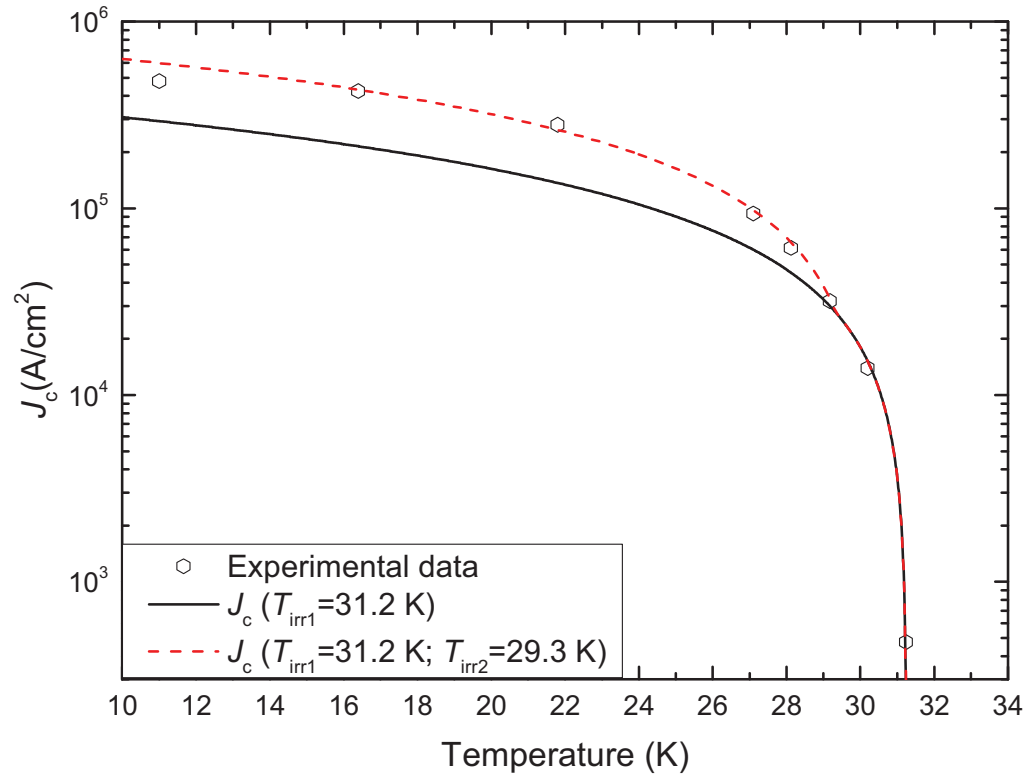


Figure 4.31: Temperature dependence of the critical current density, $J_c(T)$, at 1 T for the MgB₂ sample sintered at 850°C. Circles represent experimental data, whilst solid black line and dashed red line represent respectively the fitting curve defined using one T_{irr} and the cumulative fitting curve defined with two T_{irr} , as described by eq.(4.7).

Another interesting result which could be drawn from the analysis of the temperature dependence of J_c at 1 T is that T_{irr} appears to drop quickly with field. The quick decrease of T_{irr} with field is evident when compared with the literature-reported data [95], [96] for undoped MgB₂ samples characterised using resistivity measurements under the applied magnetic field of 1 T, as detailed in Table 4.3. All the MgB₂ samples exhibited a two-step superconducting transition, however the T_{irr} values estimated from the fitting of the temperature-dependent critical current density curves at 1 T in this work were significantly lower.

SAMPLE (SINTERING TEMPERATURE)	T_{irr1} (K)	T_{irr2} (K)
Bulk (775°C)	32.7	30.5
Bulk (850°C)	31.2	29.3
Wire (725°C) [95]	36.3	35.2
Bulk (750°C) [96]	36.3	35.6

Table 4.3: Comparison between the irreversibility temperature, T_{irr} , values at 1 T for the undoped MgB₂ bulk samples from this work and the literature-reported values [95], [96] for MgB₂ samples characterised by using resistivity measurements.

4.3 Preparation and characterisation of $\text{MgB}_2(\text{C} - x\%)$ using Carbon Chemical Vapour Coated Boron

4.3.1 Experimental details

Two portions of the boron powder were coated with carbon using the CVD technique detailed in Chapter 3. The percentages of C deposited, estimated from the mass gain observed following the process of carbon-doping of the boron powder, were found to be about 6.5% and 19%, respectively. The carbon coated powders were then reacted with magnesium using the *in-situ* process described in Section 4.1.3.1. Three bulk samples were prepared from the two portions of C doped boron powder. Two samples were produced by sintering two portions, respectively, of the 6.5% C doped boron powder and the 19% C doped boron powder at 850°C, whilst the third sample was obtained by first sintering a second portion of the 19% C doped boron powder at 850°C and, then, post-treating it for 24 hours at 1000°C, as detailed in Table 4.4.

4.3.2 Structural analysis and critical current density properties

Fig.(4.22a, b, c and d) shows the (100) reflections for the C-CVD doped MgB_2 samples with the previously discussed undoped MgB_2 treated at 775°C included as a reference. The actual doping fractions have been estimated using the empirical method described in Chapter 2. The nominal and actual doping fractions, along with the sintering temperatures, and any post-treatments are reported in Table 4.4. These results indicate that, for all C-CVD doped MgB_2 samples, only a fraction of the carbon deposited on the boron powder is included in the MgB_2 lattice.

It is worth noting the inconsistency between the nominal and the actual carbon content of the two non-post-treated samples. In fact, the actual doping fraction has been found to be higher in $\text{MgB}_2(\text{C} - 3.9\%)$, although the nominal carbon content estimated from mass gain was much larger in $\text{MgB}_2(\text{C} - 2\%)$, 6.5% compared to 19%, respectively. This result can be explained by supposing that such a high carbon content was not homogeneously distributed within the boron powder. Therefore, the selected portion of C doped boron powder used for preparing $\text{MgB}_2(\text{C} - 2\%)$, was not representative of the average level of carbon content within the boron powder. A Gaussian deconvolution of the (1 0 0) peaks is also shown in fig.(4.32). Two underlying peaks were found in the C doped samples. The $\text{MgB}_2(\text{C} - 3.9\%)$ sample exhibited a major peak at $x=3.7\%$ and a broad secondary peak corresponding to a carbon doping percentage of 5.5%. The $\text{MgB}_2(\text{C} - 2\%)$ sample has one main peak at $x=1.9\%$ with a small secondary peak with a value near 3.4%. With regard to the post-treated sample, the Gaussian deconvolution has shown that the (1 0 0) peak is composed of two reflections with a major peak centered at $x=8.0\%$ and a very small secondary peak at $x=8.5\%$; therefore, the sample can be considered to be formed by a single-phase composition. Moreover, in the XRD pattern of the $\text{MgB}_2(\text{C} - 3.9\%)$ and $\text{MgB}_2(\text{C} - 2\%)$ samples, a second peak was observed. With regard to the latter sample, the presence of two peaks may suggest the existence of two different doping regimes within the sample: the main peak corresponding to a carbon doping level of 2%, whilst the small secondary peak would be consistent with a content of 15.5%. The $\text{MgB}_2(\text{C} - 3.9\%)$ sample also exhibited, along with the major peak at a carbon doping level of 3.9%, a secondary peak centred in correspondence of the reported reflection of boron carbide, B_4C . The post-treatment was observed to not only favour the inclusion of carbon into the magnesium diboride lattice in

MgB₂(C - 8.2%), but also to slightly reduce the broadness of the (100) peak, when compared to the peak for the MgB₂(C - 2%) sample, which is the largest of all the characterised samples.

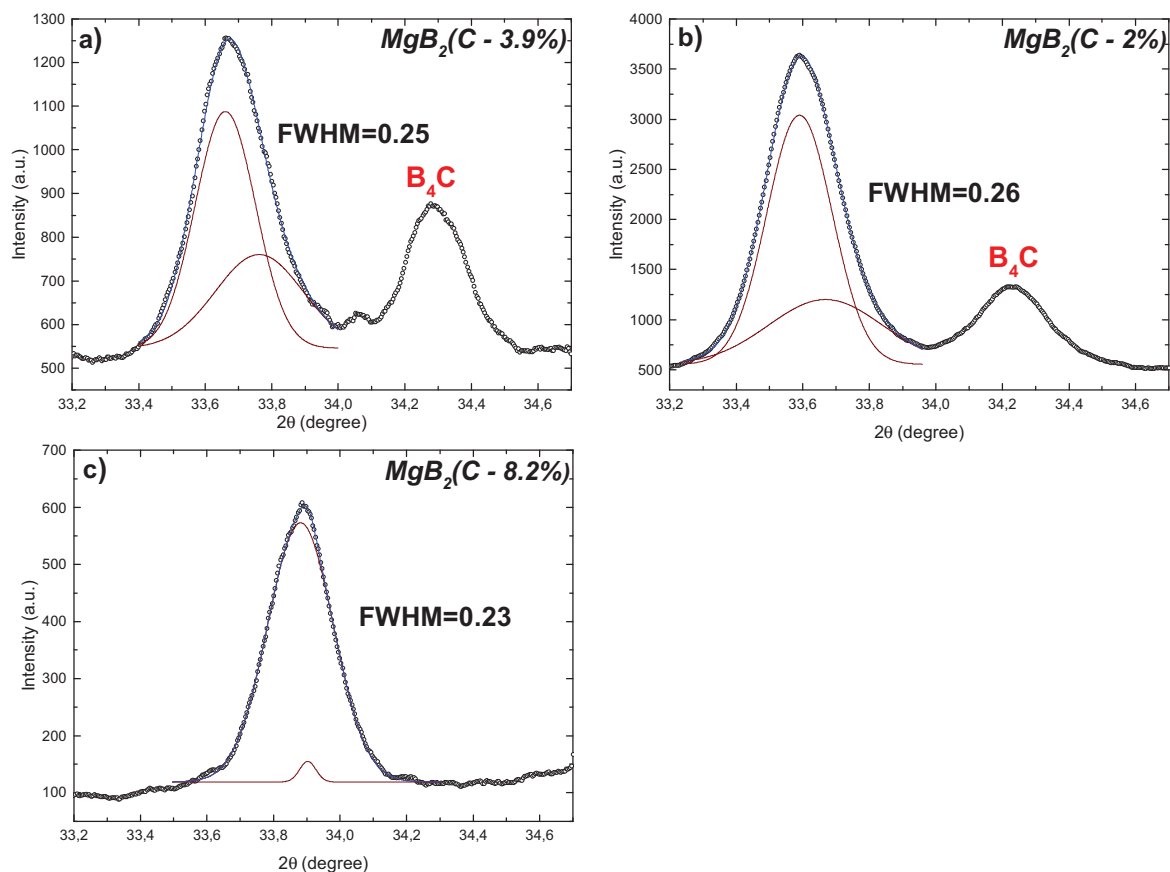


Figure 4.32: XRD patterns (empty circles) of (100) peak for MgB₂(C - 3.9%) (a), MgB₂(C - 2%) (b) and MgB₂(C - 8.2%) (c). In the same graph, the results of the Gaussian deconvolution of the (100) peak are also shown: the deconvolution peaks are plotted with wine line, while Gaussian interpolation with blue line. Any additional secondary phase is indicated in red.

Sample	Nominal carbon content (%)	Actual carbon content (%)	Sintering temperature (°C)	Post-treatment (°C)
MgB ₂ (C - 3.9%)	6.5	3.9	850	none
MgB ₂ (C - 2%)	19	2	850	none
MgB ₂ (C - 8.2%)	19	8.2	850	1000

Table 4.4: Summary table of the C-CVD doped MgB₂ bulk samples. The table lists the estimated nominal and actual doping fractions, the sintering temperatures, and the post-treatment temperatures.

Fig.(4.33) shows the critical current density as a function of magnetic field at 11 K and 22 K for the three C doped MgB₂ samples and the undoped MgB₂ treated at 775°C. Of all the C doped samples, MgB₂(C - 2%) exhibited the best J_c performance throughout the field range, both at 11 K and 22 K. In particular, J_c for this sample reached as high as 4.72×10^4 A/cm² at 11 K in 5 T, over two times as high as the critical current density values for MgB₂(C - 8.2%) and MgB₂(C - 3.9%). At 22 K in 3 T, the J_c value was 2.85×10^4 A/cm² for MgB₂(C - 2%), three times that of MgB₂(C - 8.2%), and almost nine times the MgB₂(C - 3.9%) critical current density value. At low fields (0.1 T), J_c for MgB₂(C - 2%) was 8.52×10^5 A/cm² at 11 K and 5.92×10^5 A/cm² at 22 K, about 40% smaller than the respective values of the undoped MgB₂ samples (at the same temperatures). The J_c value at 11 K was about 20% larger than that for MgB₂(C - 8.2%) and nearly 70% larger than that of MgB₂(C - 3.9%), whilst the critical current density performance of MgB₂(C - 2%) at 22 K was two times as high as the respective values for the other two C doped samples. Magnetic field dependence of J_c was improved by the carbon doping, as evidenced by the fig.(4.34) showing the normalized critical current density, $J_c(B)/J_c(B=0.1 \text{ T})$, in function of the field B. This result indicates that the flux pinning strength under high fields is enhanced by the C-CVD doping. The most significant improvement was observed in the MgB₂(C - 2%) sample, both at 11 K and 22 K. On the other hand, the sensitivity of J_c to magnetic field was considerably decreased also in the post-treated sample, in particular at high fields.

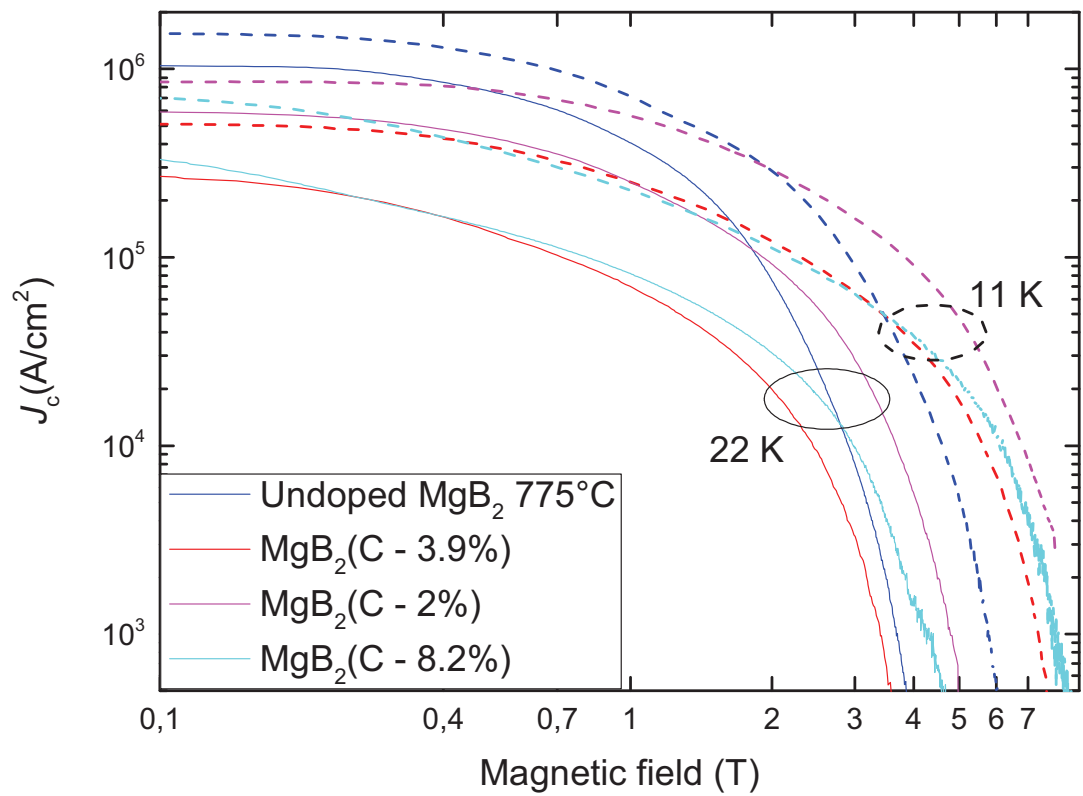


Figure 4.33: Field dependence of the critical current density, $J_c(B)$, at 11 K and 22 K for the C-CVD doped MgB_2 bulk samples listed in Table 4.4 and undoped MgB_2 treated at 775°C.

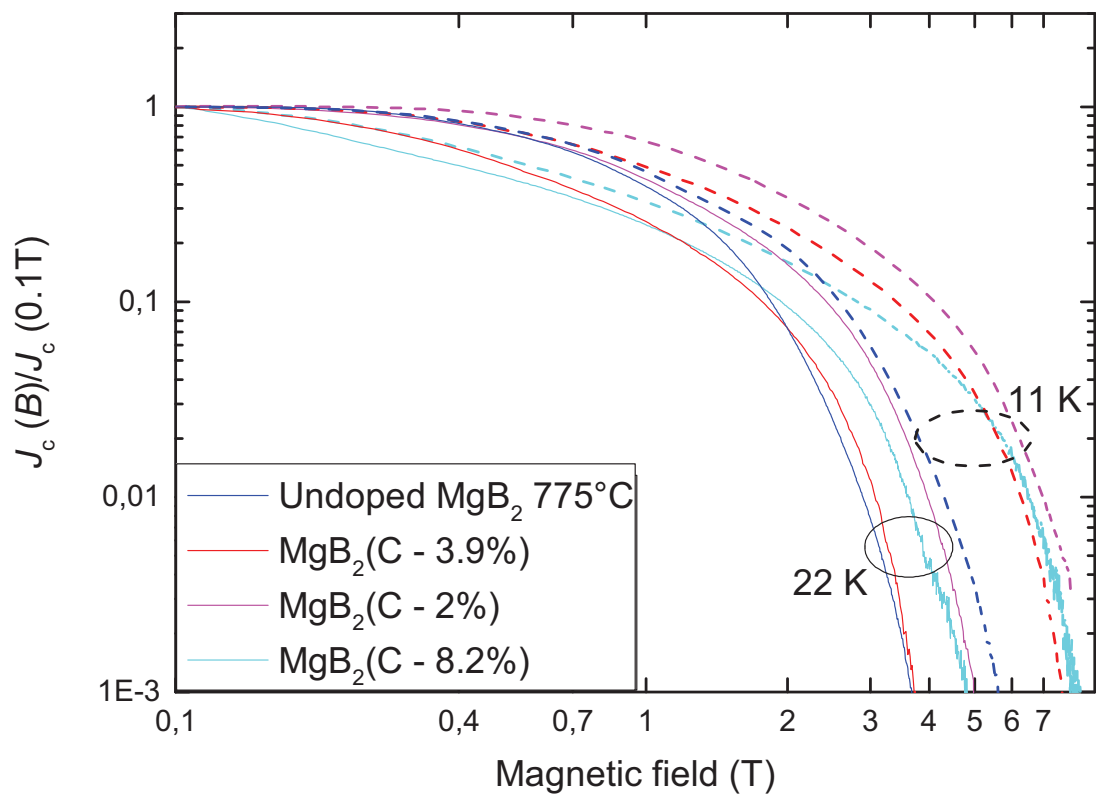


Figure 4.34: Field dependence of the normalized critical current density, $J_c(B)/J_c(B=0.1\text{ T})$, at 11 K and 22 K for the C-CVD doped MgB_2 bulk samples listed in Table 4.4 and undoped MgB_2 treated at 775°C.

In fig.(4.35) and (4.36) the Kramer plots at 11 and 22 K, as extracted from the magnetic J_c , for the three C doped MgB₂ samples are shown. The plots have been employed to evaluate the irreversibility field $H_{irr} \equiv H_K$, as explained in Chapter 4.2. As in the case of the undoped samples, the Kramer functions were not linear throughout the considered field range, but exhibit variations in the slope of the plots. This behaviour has been attributed [63] to percolative paths, which can be quite significant in samples prepared with nanosized boron powders. Considering the linear part of the curve at high current, the H_K values have been extrapolated and employed to plot the normalized pinning forces, F_p/F_{pmax} , as a function of the reduced field H/H_K at 11 K and 22 K, as shown in fig.(4.37) and (4.38). Unlike the undoped samples, which exhibited a varying pinning force maximum with sintering temperature, the predominant pinning mechanism for all the characterised C doped MgB₂ samples is grain boundary, whether or not post-treatment was performed, and regardless of the amount of carbon included. This behaviour is evidenced by the plots, fig.(4.38), which show that the normalized pinning force as a function of reduced field at 22 K almost overlapped the theoretical curve defined by eq.(4.7) for the grain boundary mechanism. At 11 K, as shown in fig.(4.37), while the maxima for all C doped samples were very close to 0.2, the pronounced broadening of the F_p/F_{pmax} curves observed for MgB₂(C - 2%) and, in particular, for MgB₂(C - 8.2%) suggests that a minor contribution from the point defect pinning mechanism should be considered.

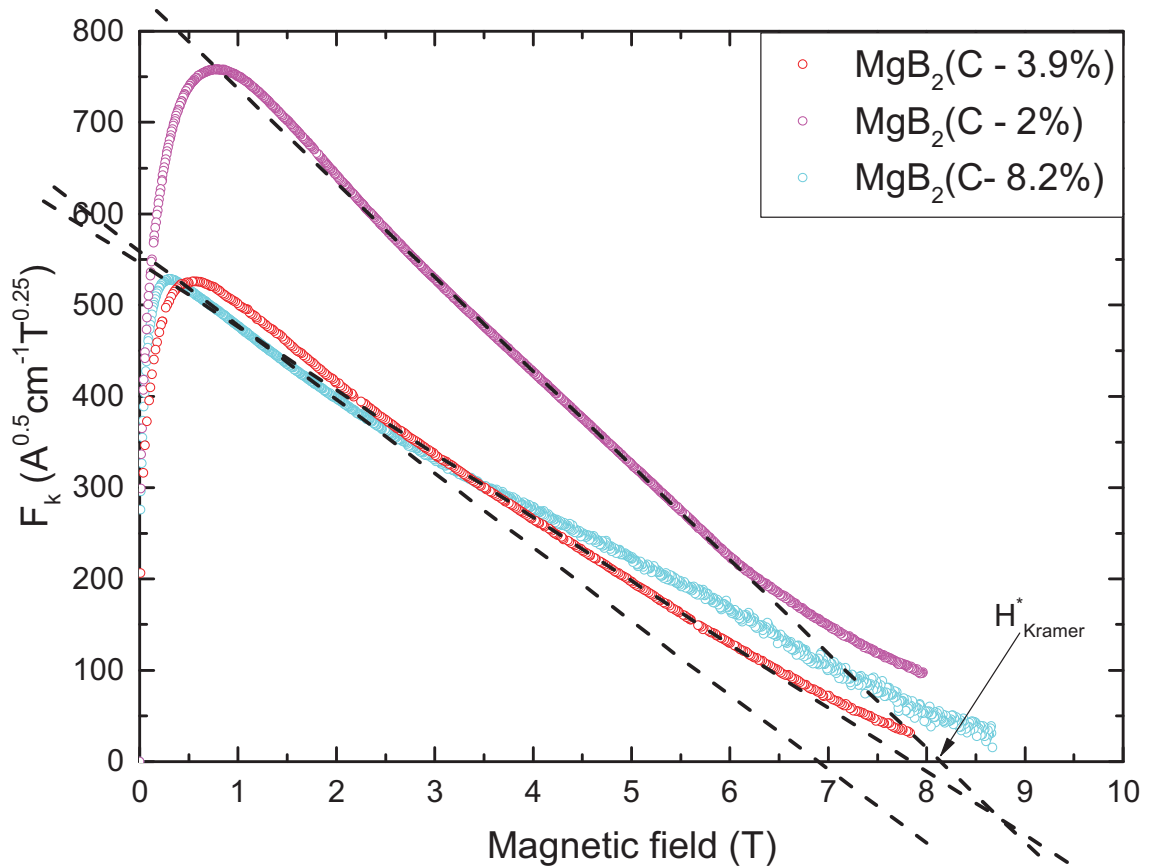


Figure 4.35: Kramer plots as a function of magnetic field at 11 K from the magnetic J_c data for the C-CVD doped MgB_2 bulk samples listed in Table 4.4.

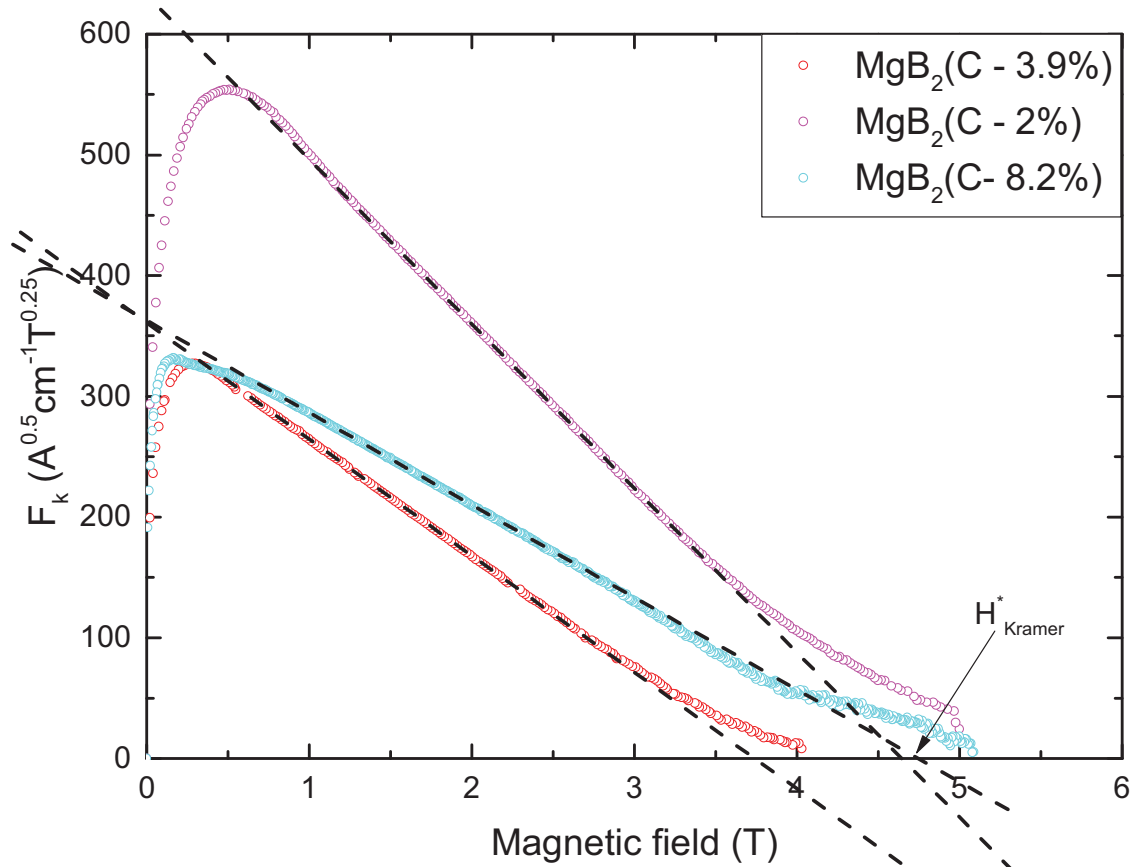


Figure 4.36: Kramer plots as a function of magnetic field at 22 K from the magnetic J_c data for the C-CVD doped MgB_2 bulk samples listed in Table 4.4.

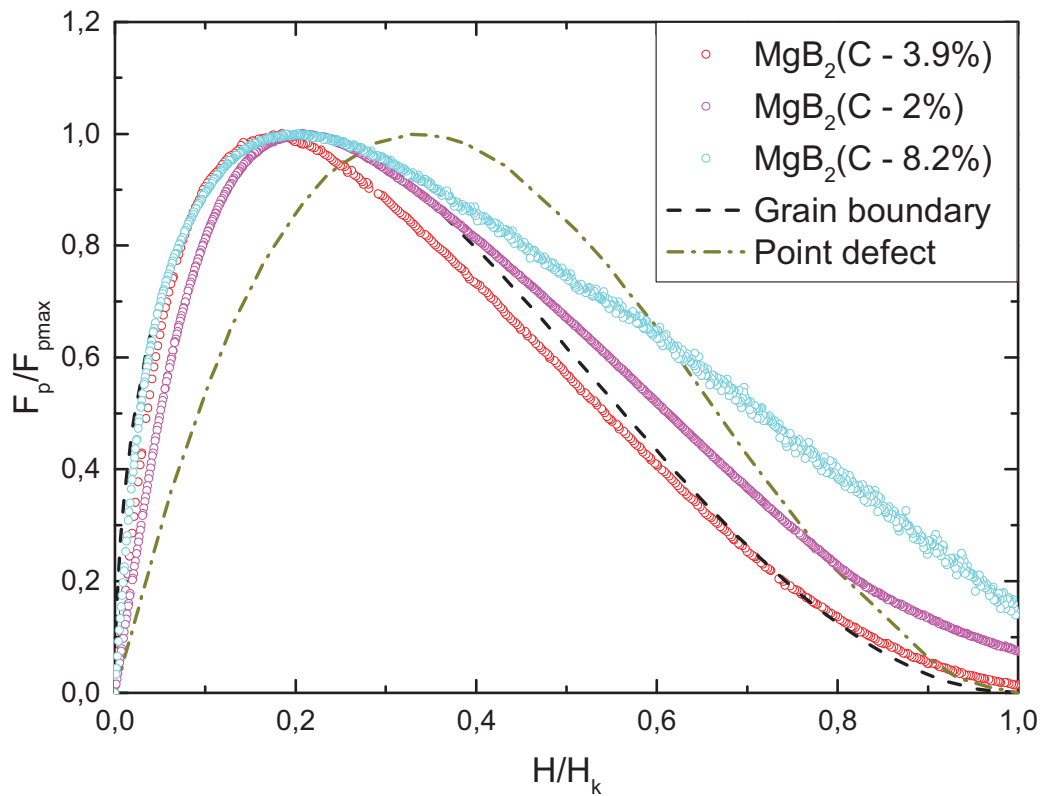


Figure 4.37: Behaviour of the normalised pinning force vs normalised magnetic field at 11 K from the magnetic J_c data for the C doped MgB_2 bulk samples listed in Table 4.4. Grain boundary pinning, eq.(4.5), and point defect models, [91], are also shown for comparison.

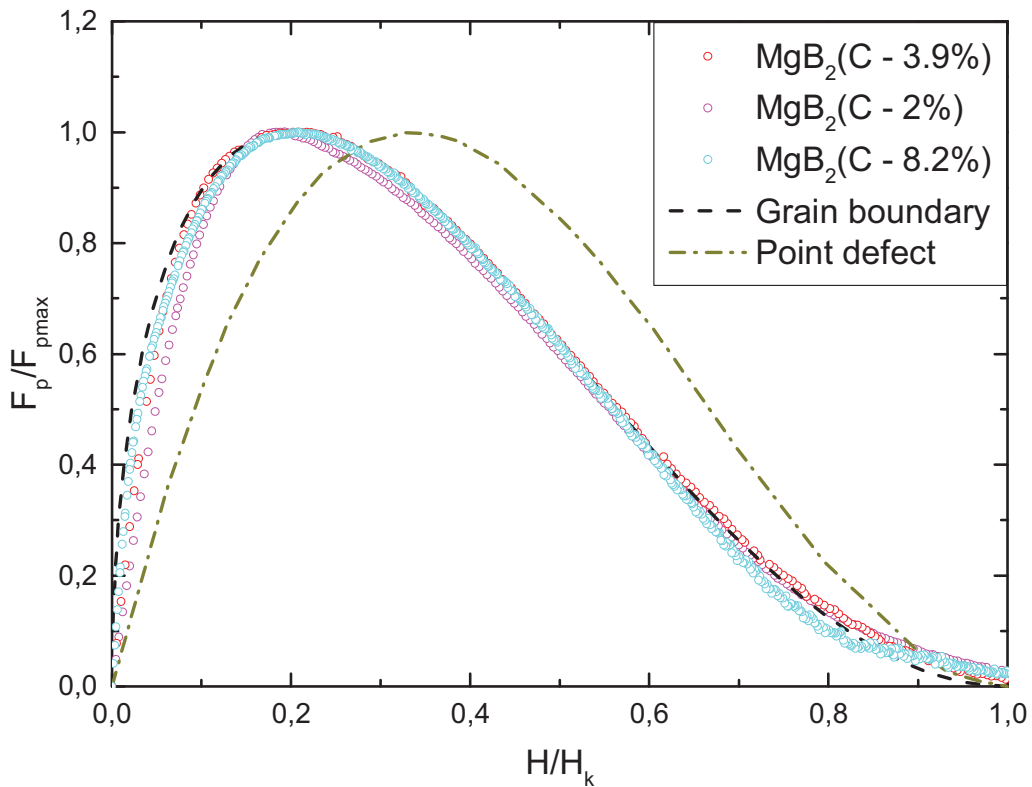


Figure 4.38: Behaviour of the normalised pinning force vs normalised magnetic field at 22 K from the magnetic J_c data for the C doped MgB_2 bulk samples listed in Table 4.4. Grain boundary pinning, eq.(4.5), and point defect models, [91], are also shown for comparison.

In order to further investigate what factors affect the critical current density performances of carbon doped MgB₂ samples, the temperature dependence of J_c has also been studied. The temperature-dependent critical current density curves at 0.1 T, plotted in fig.(4.39)-(4.41), have been fitted using eq.(4.6), which is the fitting equation used to describe the temperature-dependent J_c behaviour for the undoped MgB₂ samples at 1 T in the previous section. The provision of different T_{irr} 's reveals the existence of multiple current paths due to distinct doping regimes within the C doped samples, as suggested also by the XRD analysis. In particular, the temperature dependence of J_c of the MgB₂(C - 3.9%) sample could be described using two T_{irr} 's, which are 32.3 K and 30.7 K, as shown in fig.(4.39). In the case of MgB₂(C - 2%) and MgB₂(C - 8.2%), three T_{irr} 's are needed to fit the $J_c(T)$ curves. They are, respectively, 34.1 K, 32.7 K and 31.3 K for the non-post-treated sample, fig.(4.40), and 32.2 K, 30.2 K and 25 K for the post-treated sample, fig.(4.41). A large amount of carbon substitution, as in the case of the post-treated sample, was observed to cause quite a significant decrease of T_{irr} 's degrading the J_c characteristics, particularly at low fields, as displayed in fig.(4.33) and (4.34). In contrast, the presence of a phase containing a level of carbon of 15.5% was seen not to reduce the T_{irr} 's for MgB₂(C - 2%), and this could explain the significant J_c characteristics at low fields. On the other hand, this phase is thought to improve the magnetic field dependence of J_c , as suggested by the analysis of the normalized field dependent critical current density graph, $J_c(B)/J_c(B=0.1\text{ T})$. It is also worthwhile to notice that there was a significantly wider distribution of T_{irr} 's for the post-treated sample than that for non-post-treated sample. These results contrast with the XRD data that the post-treatment was observed to reduce the FWHM of the (100) peak.

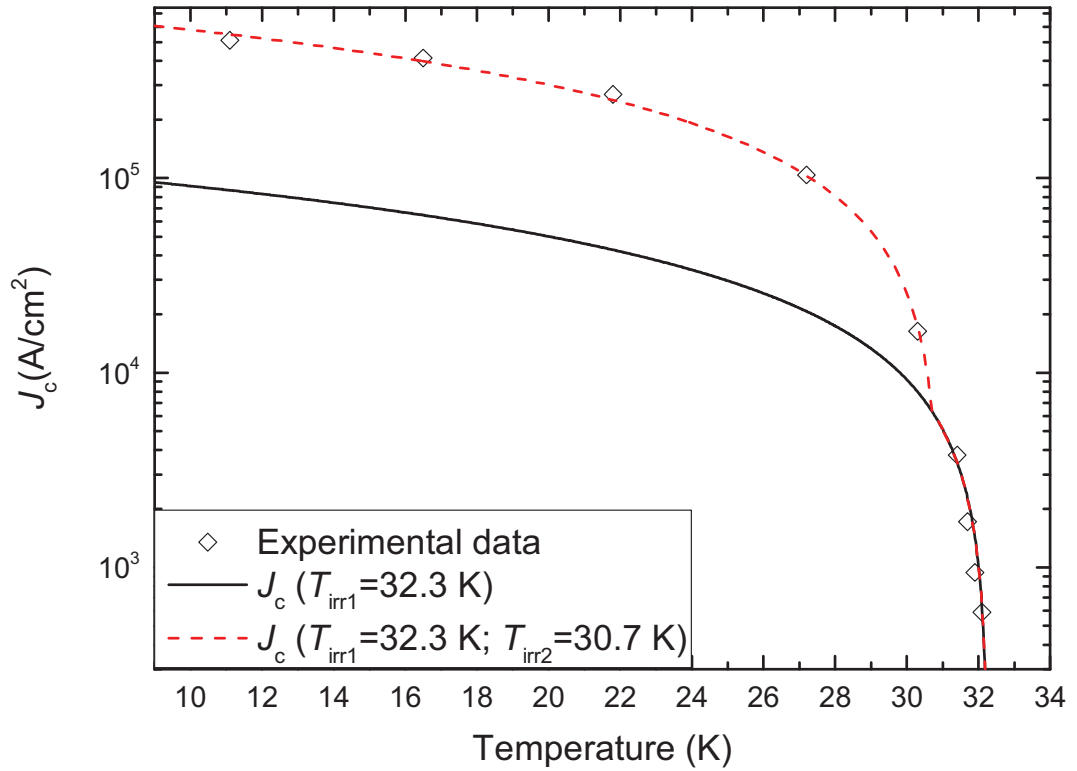


Figure 4.39: Temperature dependence of the critical current density, $J_c(T)$, at 0.1 T for the MgB₂(C - 3.9%) sample. Circles represent experimental data, whilst solid lines represent fitting curves, which are described by eq.(4.6).

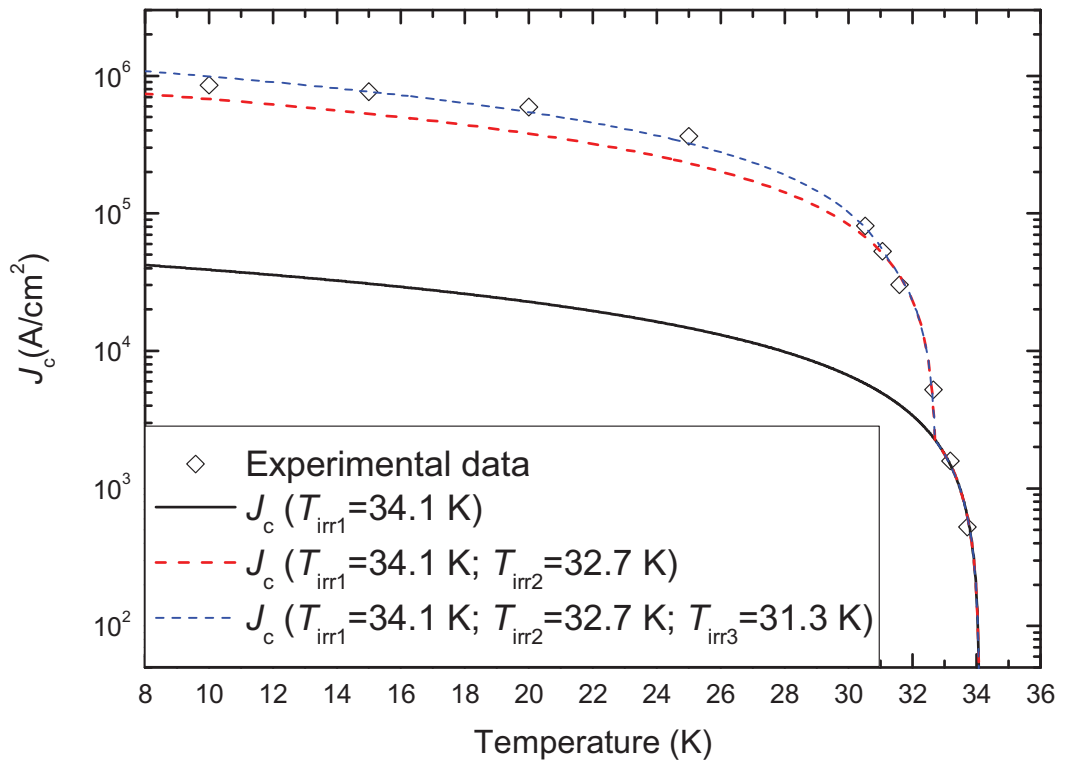


Figure 4.40: Temperature dependence of the critical current density, $J_c(T)$, at 0.1 T for the MgB₂(C - 2%) sample. Circles represent experimental data, whilst solid lines represent fitting curves, which are described by eq.(4.6).

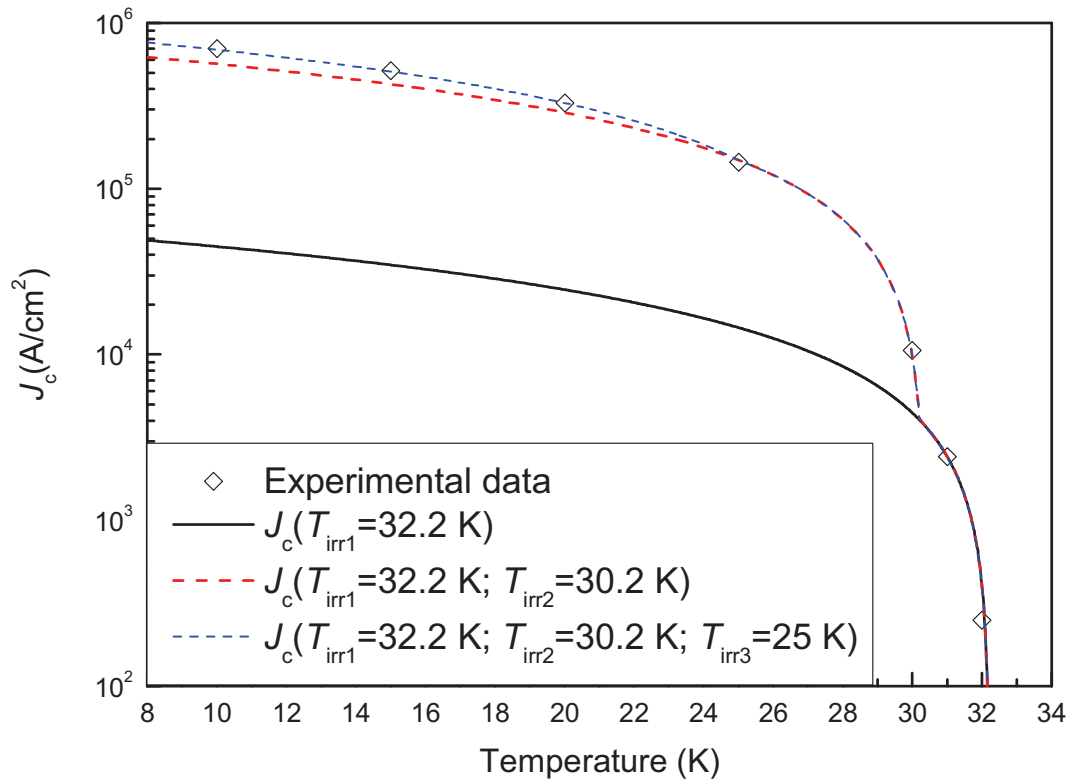


Figure 4.41: Temperature dependence of the critical current density, $J_c(T)$, at 0.1 T for the $\text{MgB}_2(\text{C} - 8.2\%)$ sample. Circles represent experimental data, whilst solid lines represent fitting curves, which are described by eq.(4.6).

In fig.(4.42) the values of critical temperatures, estimated by the fit of the temperature-dependent J_c curves, have been plotted in function of Δa (and X) for the undoped and C-CVD doped MgB_2 bulk samples. Each C doped sample included a phase, corresponding to a respective value of critical temperature, which was comparable to the value reported for single crystals [75]. The same samples exhibited additional critical temperature values, which were observed to lie either above or below those of single crystals. With regard to $\text{MgB}_2(\text{C} - 8.2\%)$, it had two higher T_{irr} 's than would be expected, so the main current path was not through the higher doped region, which was seen in the XRD analysis. In contrast, the $\text{MgB}_2(\text{C} - 3.9\%)$ and $\text{MgB}_2(\text{C} - 2\%)$ samples exhibited, respectively, one T_{irr} and two T_{irr} 's lower than would be expected, therefore the main current path is likely to have been through regions with a carbon content higher than that was estimated from the (100) peak. Therefore, the multiple T_{irr} 's could be interpreted as a result of distinct levels of carbon

doping, with the biggest contribution coming from the middle value (indicated with a red circle in fig.(4.42)), which represents the dominant pinning mechanism, and a weaker one -absent in the case of $\text{MgB}_2(\text{C} - 3.9\%)$ - at higher temperatures. The lower temperature value was difficult to argue as it was quite weak.

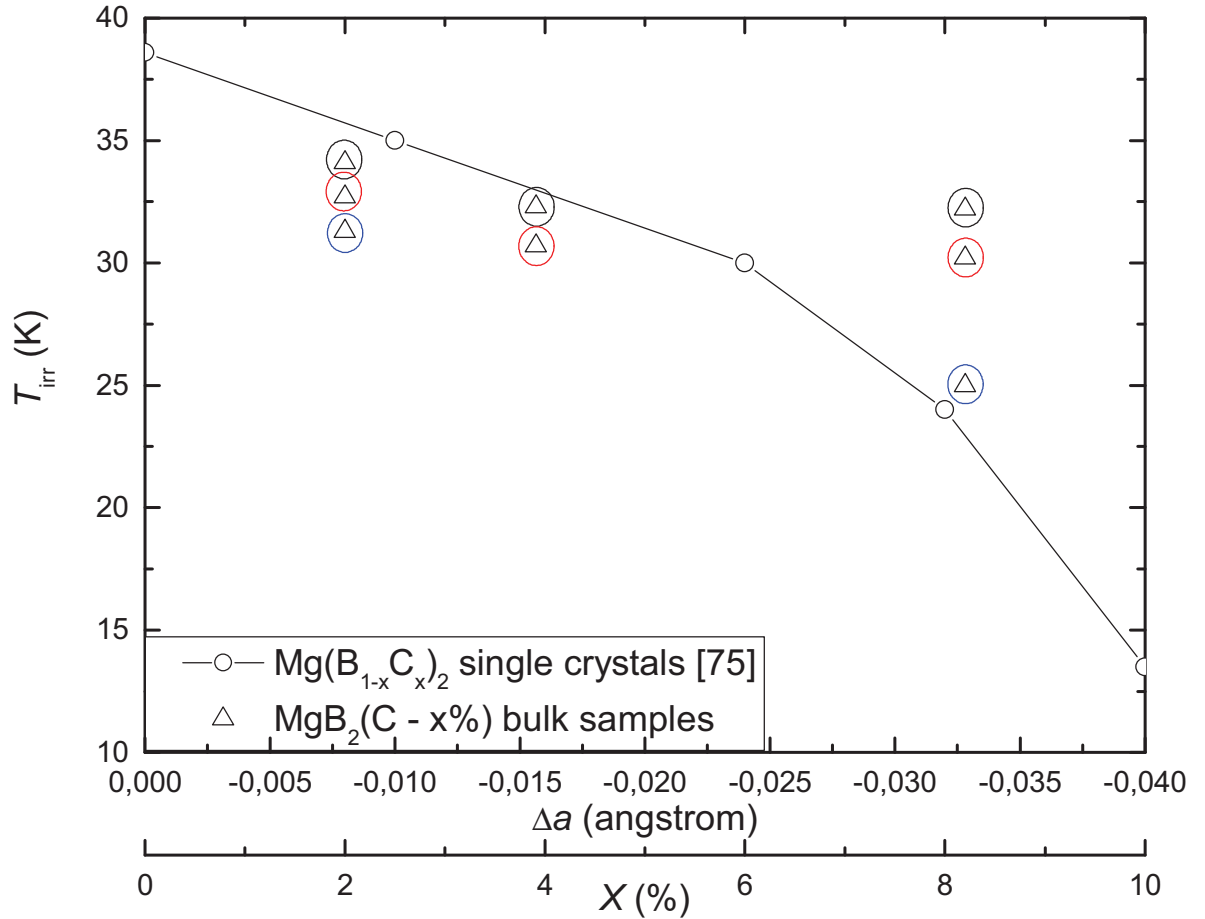


Figure 4.42: Dependence of T_{irr} on Δa (and X) for C-CVD doped MgB_2 bulk samples and C doped MgB_2 single crystals [75]. The circles in black, red and blue around the symbols indicate, respectively, the T_{irr1} , T_{irr2} and T_{irr3} estimated by the fit of the temperature-dependent J_c curves, as shown in fig.(4.25)-(4.27).

The analysis of SEM images, displayed in fig.(4.43a) and (4.43b), revealed that the post-treatment resulted in an increase in the density of the sample through a coalescence of grains and in the growth of the particles, which reached dimensions of 200-300 nm, whilst in the non-post-treated sample, particles with a radius of about 100 nm were observed. These results correlated with the XRD data, fig.(4.23), which showed a decrease in the average FWHM value of the (100) peak for the post-treated sample, compared to those of the non-post-treated samples. The degradation of crystallinity was believed to increase grain boundary pinning improving the field dependence of the critical current density, $J_c(B)$, as observed in the MgB₂(C - 2%) sample.

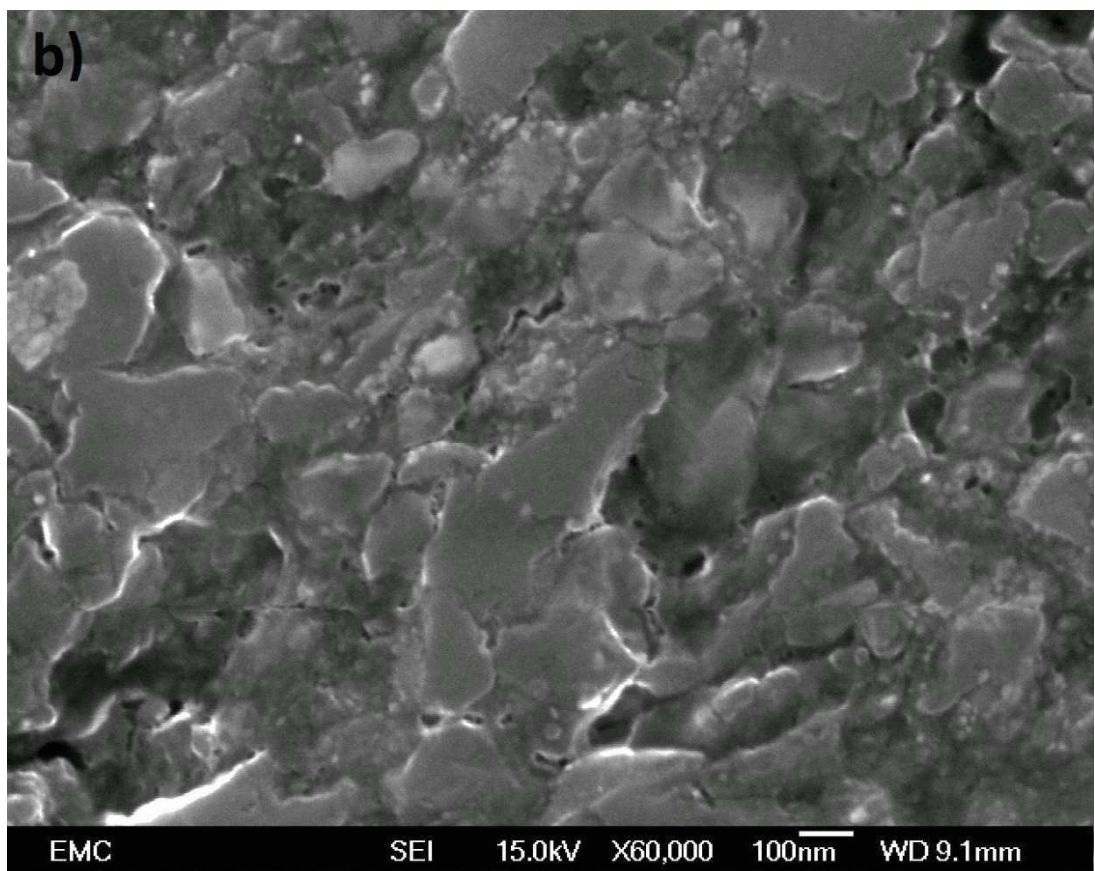
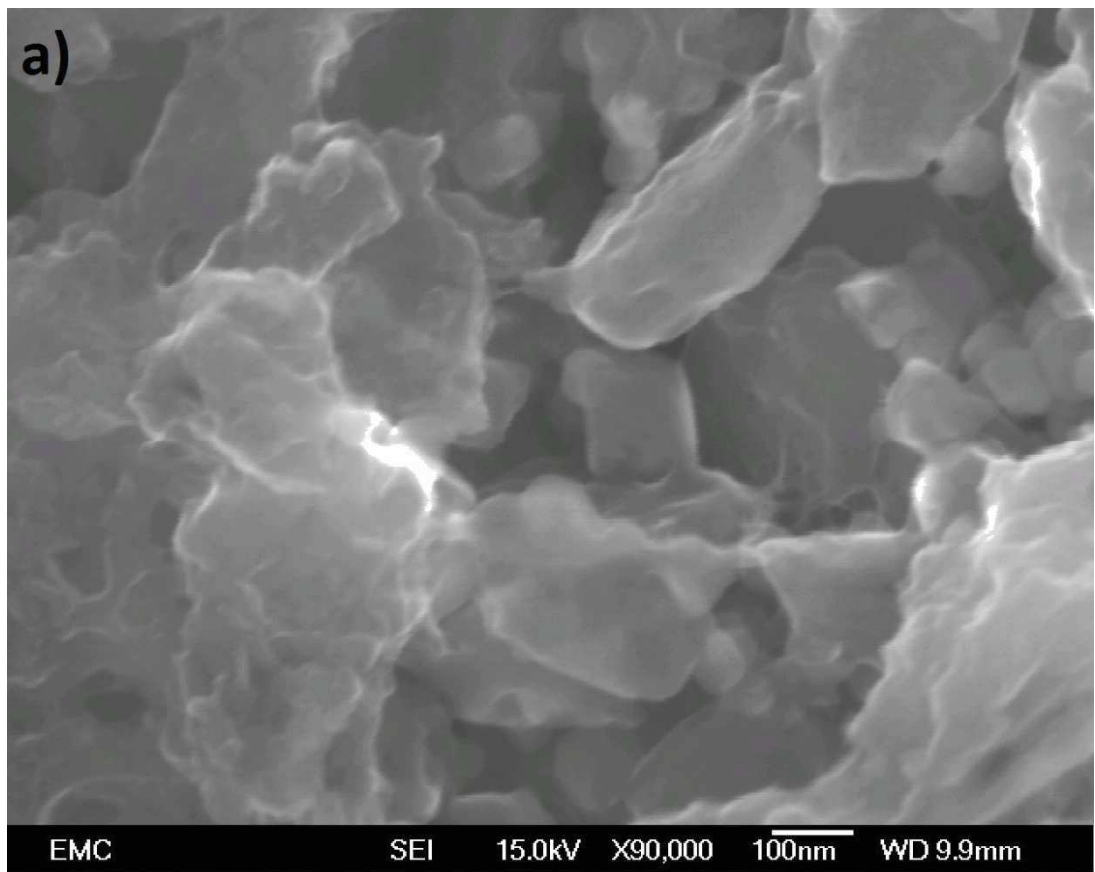


Figure 4.43: SEM images for $\text{MgB}_2(\text{C} - 2\%)$ (a) and $\text{MgB}_2(\text{C} - 8.2\%)$ (b) samples.

4.4 Preparation and characterisation of SiO₂-coated MgB₂(C – x%) using Silica Sol-Gel and Carbon Chemical Vapour Coated Boron

4.4.1 Experimental details

Nano-sized boron powder has been coated with silica by using the sol-gel method, as detailed in Chapter 2. 0.5 g of boron was mixed with 500 cm³ of ethanol and sonicated in ultrasound bath for 5 minutes to achieve good dispersion. 53 cm³ of ethanol, 1.2 cm³ of precursor TEOS, Si(OC₂H₅)₄, and 3.5 cm³ of aqueous NH₃ (catalyst) was slowly added to the suspension of boron at room temperature under vigorous stirring. The solutions were allowed to react for 12 hours under stirring followed by separation of a dark brown precipitate using filtration. The solid sample was thoroughly washed with ethanol, filtered and dried at room temperature. The resultant percentage of silica included into boron powder was 16 wt%. Two portions of the silica-coated boron were also subsequently coated with carbon using the CVD technique detailed in Chapter 2. Two samples with two different levels of carbon doping were produced by varying the dwell temperature of the carbon doping process from 350°C to 550°C. The percentages of C deposited, estimated from the mass gain observed following the process of carbon-doping of the boron powder, were found to be about 2% and 6.1%, respectively. Both silica coated and silica+carbon coated powders were then reacted with magnesium at 850°C using the *in-situ* process described in Chapter 4.1, in order to produce cylinder-shaped bulk samples. The percentage of silica that was coated onto boron powder, any nominal percentages of carbon doping, along with the dwell temperature of the carbon doping process (if

applicable) are indicated in Table 4.5.

Sample	Mass percentage of silica coating (%)	Nominal carbon content (%)	Dwell temperature of carbon doping process (°C)
MgB ₂ +16 wt% SiO ₂	16	None	None
MgB ₂ (C - 2 wt%)+16 wt% SiO ₂	16	2	350
MgB ₂ (C - 6.1 wt%)+16 wt% SiO ₂	16	6.1	550

Table 4.5: Summary table of the SiO₂ coated MgB₂(C - x wt%) samples. The table lists the estimated mass percentage of silica coating and nominal carbon doping fraction, and the carbon doping dwell temperature.

4.4.2 TEM images analysis of SiO₂-coated boron powder and characterisation of the structural and critical current density properties of reacted bulk samples

The silica-coated boron powder was examined by transmission electron microscopy (TEM) in order to assess the distribution and the level of homogeneity of the coating on the boron powder.

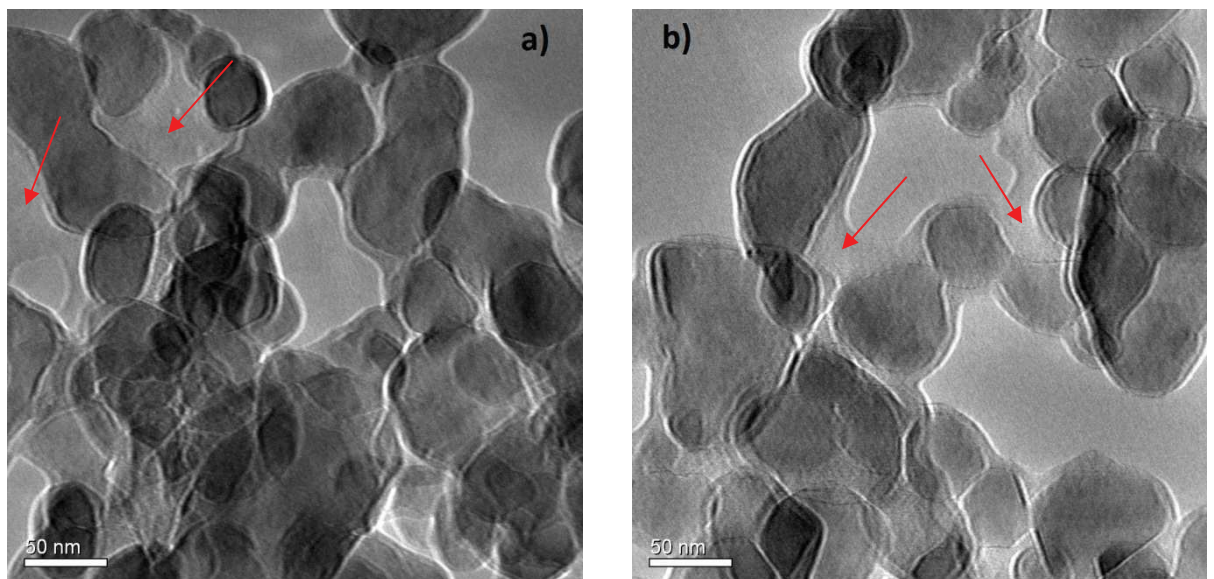


Figure 4.44: TEM images of SiO₂-coated boron powder, (a) and (b). Lumps of silica are indicated with red arrows.

The TEM images, fig.(4.44a) and (4.44b), show that the sol-gel method, differed from the CVD technique in that it was not capable of producing a constant silica-rich layer on each individual boron grain; however, lumps of silica were observed in proximity of some grains.

Fig.(4.45a, b, c and d) shows the wide angular range x-ray diffraction spectra of the undoped MgB_2 sample and the $\text{Mg}(\text{B}_{1-x}\text{C}_x)_2 + \text{SiO}_2$ samples (in the doped samples the positions of the peaks of the crystalline phases were determined by using the Al_2O_3 peak as a reference). The $\text{MgB}_2 + 16 \text{ wt}\% \text{ SiO}_2$ and $\text{MgB}_2(\text{C} - 2 \text{ wt}\%) + 16 \text{ wt}\% \text{ SiO}_2$ samples are composed of nearly single phase of MgB_2 except for a peak of Mg_2SiO_4 , which derives from the reaction $2\text{MgO} + \text{SiO}_2 \rightarrow \text{Mg}_2\text{SiO}_4$, where MgO derives from the reaction $4\text{Mg} + \text{SiO}_2 \rightarrow \text{Mg}_2\text{Si} + 2\text{MgO}$. In contrast, the presence of additional peaks, namely SiC and MgCO_3 (deriving from the reaction $\text{MgO} + 2\text{SiO}_2 + 3\text{C} \rightarrow 2\text{SiC} + \text{MgCO}_3$), was found in the pattern of the $\text{MgB}_2(\text{C} - 6.1 \text{ wt}\%) + 16 \text{ wt}\% \text{ SiO}_2$ sample. In order to elucidate how the presence of those peaks affects the actual percentage of carbon that is incorporated into the lattice of MgB_2 , the peak associated with the (100) reflection was investigated, fig.(4.46a, b, c and d). The Gaussian deconvolution of the (100) peak evidences the presence of three underlying reflections for the higher temperature treated carbon+silica coated MgB_2 sample, as shown in (fig.4.46d). The lowest angle peak corresponds to a percentage of C doping equal to 0.2 at%, the intermediate angle peak to a broad peak centered at 0.5 at%, whilst the highest angle peak approaches 1.3 at%. No appreciable split of the (100) peak was instead observed in relation to the lower temperature treated carbon+silica coated MgB_2 sample, (fig.4.46c), after deconvolution with Gaussian functions and, therefore, it can be considered to be formed by a single-phase composition. Moreover, the percentage of carbon doping in $\text{MgB}_2(\text{C} - 2 \text{ wt}\%) + 16 \text{ wt}\% \text{ SiO}_2$ is not sufficient to determine any shift in

the (100) peak position with respect to the undoped MgB_2 sample, although a broadening of the reflection was observed.

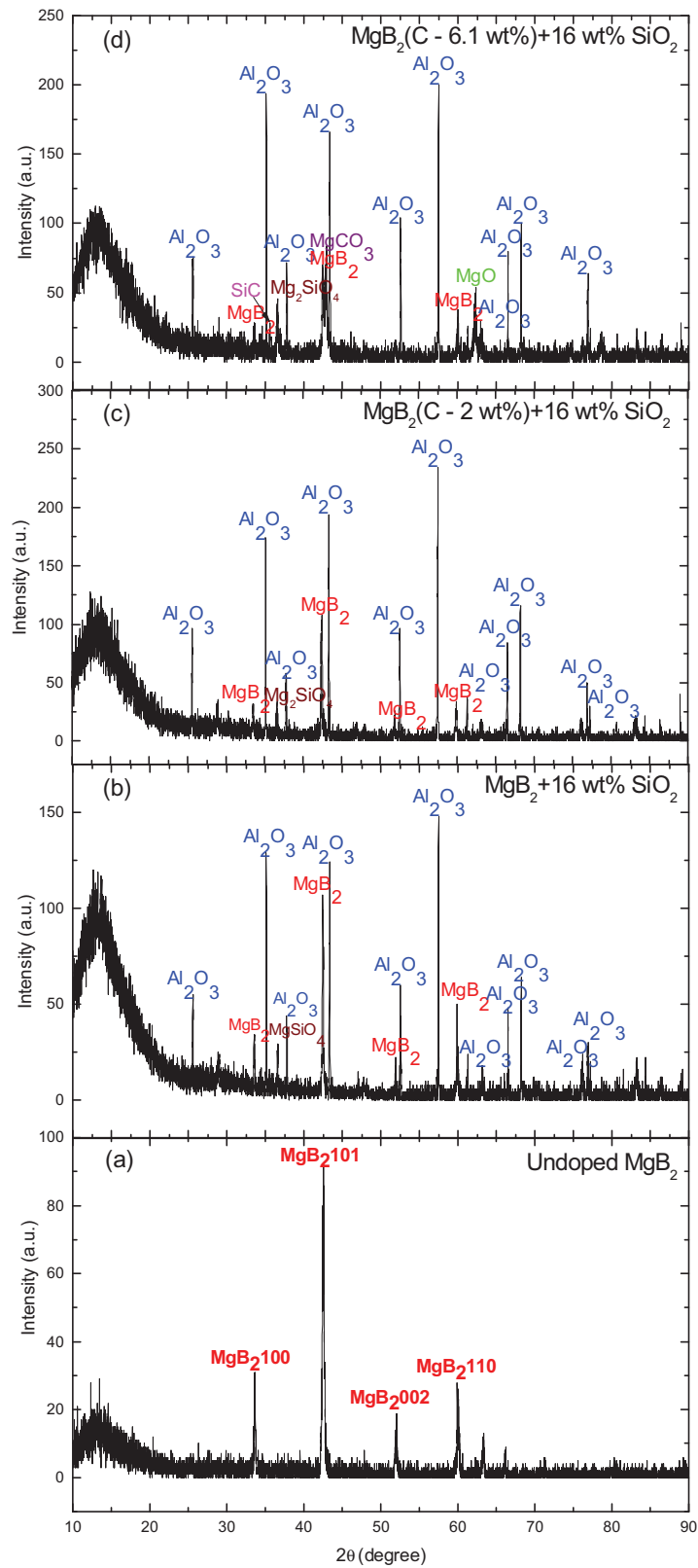


Figure 4.45: Wide angle x-ray diffraction spectra of undoped MgB_2 (a), MgB_2 +16wt% SiO_2 (b), MgB_2 (C - 2 wt%)+16 wt% SiO_2 (c) and MgB_2 (C - 6.1 wt%)+16 wt% SiO_2 (d) samples.

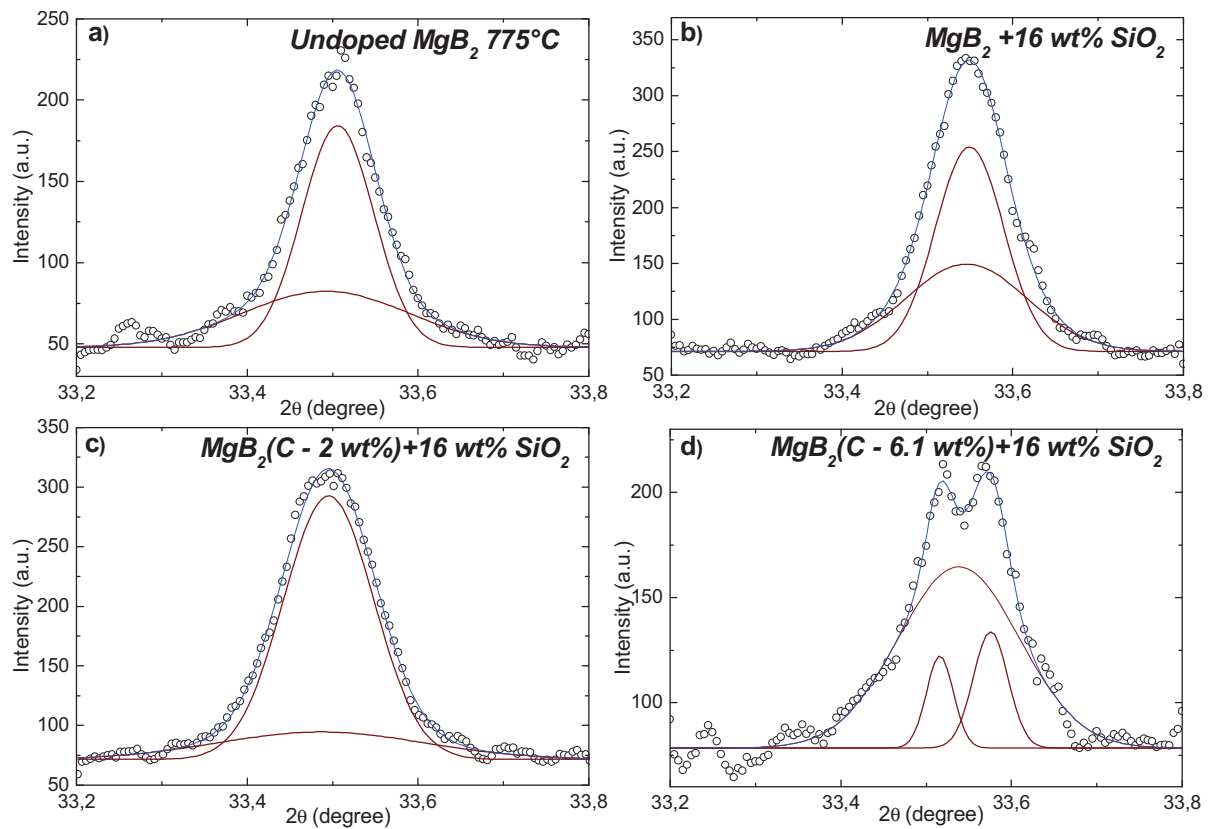


Figure 4.46: XRD patterns (empty circles) of (100) peak for undoped MgB_2 (a), $\text{MgB}_2 + 16 \text{ wt\% SiO}_2$ (b), $\text{MgB}_2(\text{C} - 2 \text{ wt\%}) + 16 \text{ wt\% SiO}_2$ (c) and $\text{MgB}_2(\text{C} - 6.1 \text{ wt\%}) + 16 \text{ wt\% SiO}_2$ (d) samples. In the same graph, the results of the Gaussian interpolation of the (100) peak are also shown, with the solid wine lines representing the deconvoluted peak reflections, whilst the solid blue line represents the cumulative fit peak.

In the case of the $\text{MgB}_2 + 16 \text{ wt\% SiO}_2$ sample, (fig.4.46b), a (100) peak shift to a larger angle was observed whilst the (002) peak position, as shown in (fig.4.47), remained comparatively unchanged. This behaviour contrasts with what has been reported [74], namely, that the addition of SiO_2 does not affect the position of (100) reflection, but it does favour the formation of Mg_2Si , and causes an increase in the c lattice parameter, leading to the (002) angle shifting to lower angles. Our results could be explained, in the absence of carbon, by an excess percentage of magnesium, as suggested by [97], although the shortening of a lattice parameter has generally been observed in samples sintered at temperatures below 850°C .

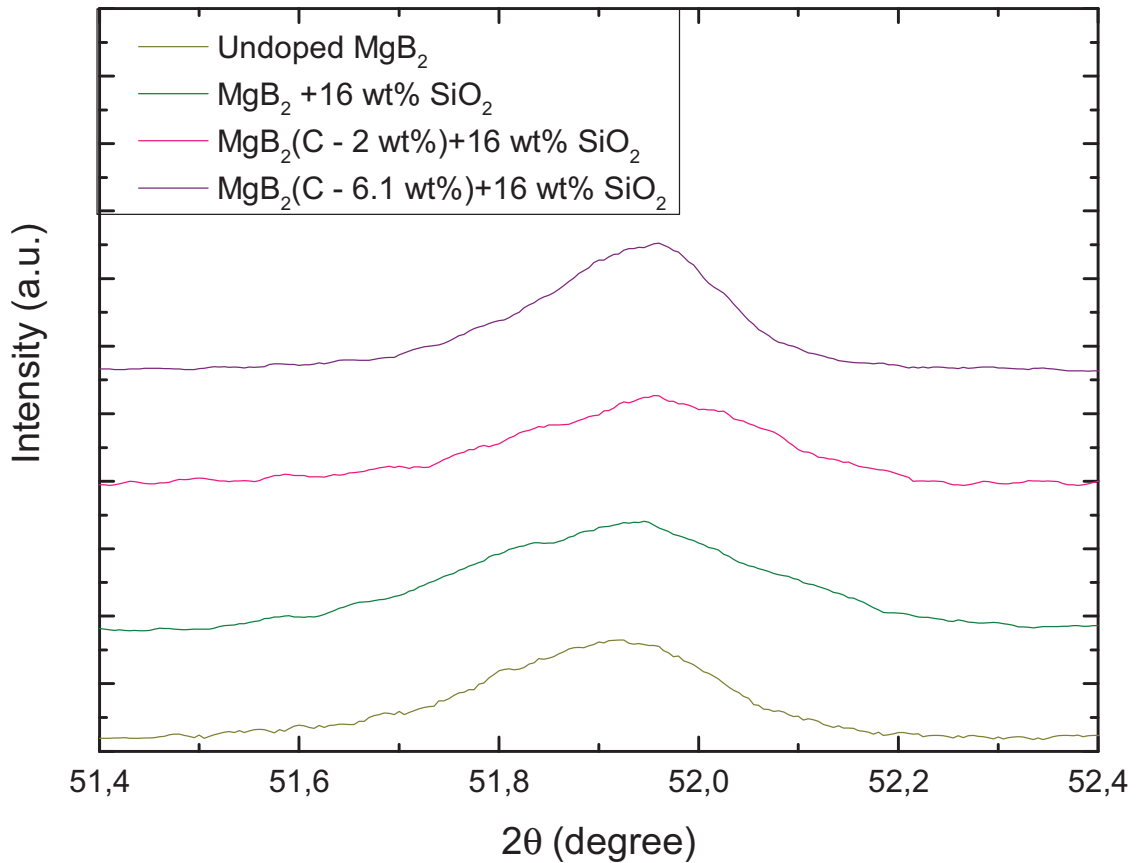


Figure 4.47: XRD reflection of (002) peak for the undoped MgB_2 , $\text{MgB}_2+16 \text{ wt}\% \text{ SiO}_2$, $\text{MgB}_2(\text{C} - 2 \text{ wt}\%)+16 \text{ wt}\% \text{ SiO}_2$ and $\text{MgB}_2(\text{C} - 6.1 \text{ wt}\%)+16 \text{ wt}\% \text{ SiO}_2$ samples.

Fig. 4.48 shows the critical current density as a function of the magnetic field at temperatures at 11 K and 22 K for undoped MgB_2 , $\text{MgB}_2+16 \text{ wt}\% \text{ SiO}_2$, $\text{MgB}_2(\text{C} - 2 \text{ wt}\%)+16 \text{ wt}\% \text{ SiO}_2$, and $\text{MgB}_2(\text{C} - 6.1 \text{ wt}\%)+16 \text{ wt}\% \text{ SiO}_2$. Of all the Si coated samples, $\text{MgB}_2+16 \text{ wt}\% \text{ SiO}_2$ exhibited the best J_c performance throughout the field range, both at 11 K and 22 K. The introduction of carbon into MgB_2 lattice for Si coated samples not only impairs J_c at low fields, but also does not seem to result in any improvement even at high fields. This deterioration in critical current density performance becomes more evident with increasing percentages of C included: J_c for $\text{MgB}_2(\text{C} - 6.1 \text{ wt}\%)+16 \text{ wt}\% \text{ SiO}_2$ was $2.28 \times 10^3 \text{ A/cm}^2$ at 11 K in 3 T, a value which is less than one fifth that for $\text{MgB}_2(\text{C} - 2 \text{ wt}\%)+16 \text{ wt}\% \text{ SiO}_2$ and less than one fifteenth that for $\text{MgB}_2+16 \text{ wt}\% \text{ SiO}_2$. Similar ratios regarding the J_c performances were observed at 22 K in 2 T: the J_c value was $1.2 \times 10^3 \text{ A/cm}^2$ for the $\text{MgB}_2(\text{C} - 6.1 \text{ wt}\%)+16 \text{ wt}\%$

SiO₂ sample, which is as high as one ninth that for lower C doped sample and less than one fifteenth that for MgB₂+16 wt% SiO₂.

The undoped sample clearly exhibited better critical current density properties throughout the field range in comparison to any Si coated sample. On the other hand, the sensitivity of J_c to magnetic field at low fields, both at 11 K and 22 K, for MgB₂+16 wt% SiO₂ is even better than that of the undoped MgB₂ sample, as displayed in fig.(4.49). The presence of the MgCO₃ and MgSiO₄ compounds observed within the MgB₂(C - 6.1 wt%)+16 wt% SiO₂ sample, is thought to impair its critical current density performance and, in particular, its self-field J_c which was found to be significantly reduced as compared to the other characterised samples.

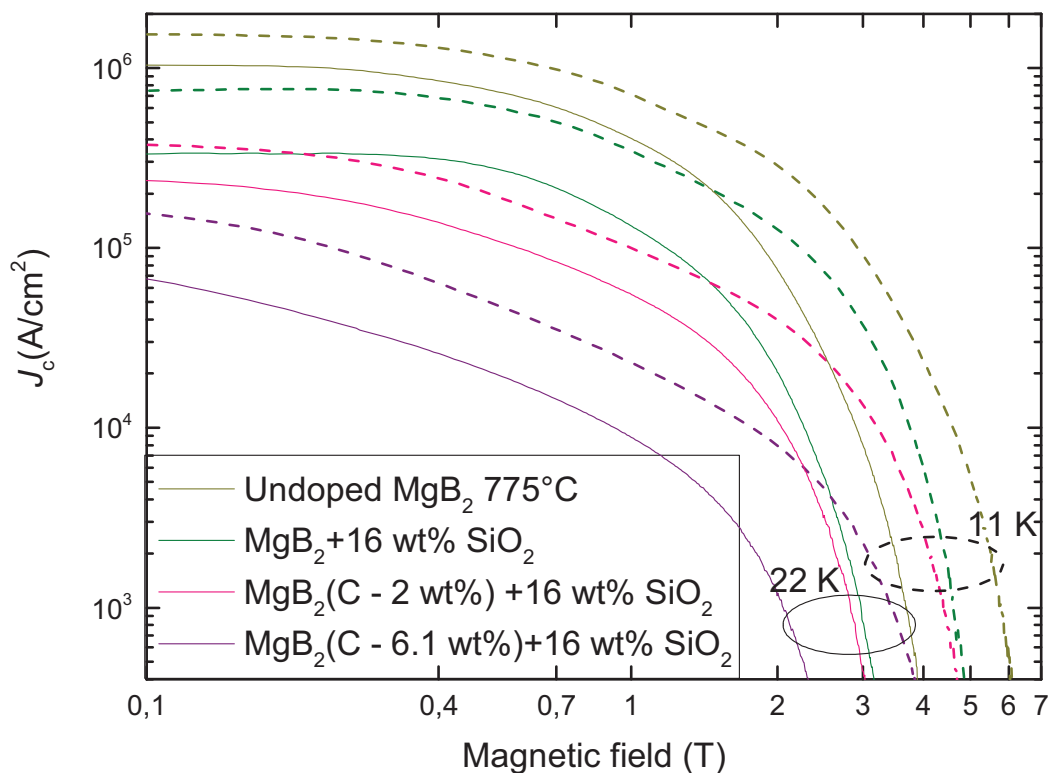


Figure 4.48: Field dependence of the critical current density, $J_c(B)$, at 11 K and 22 K for undoped MgB₂, MgB₂+16 wt% SiO₂, MgB₂(C - 2 wt%)+16 wt% SiO₂ and MgB₂(C - 6.1 wt%)+16 wt% SiO₂ samples.

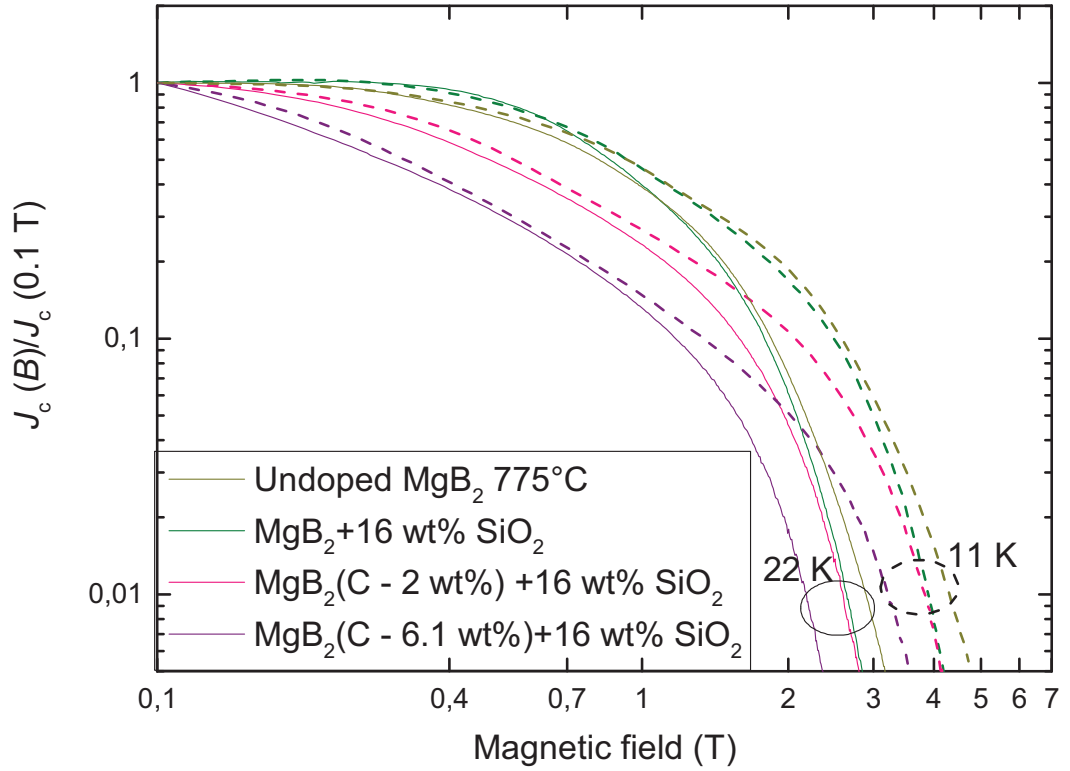


Figure 4.49: Field dependence of the normalized critical current density, $J_c(B)/J_c(B=0.1 \text{ T})$, at 11 K and 22 K for the undoped MgB_2 , $\text{MgB}_2+16 \text{ wt\% SiO}_2$, $\text{MgB}_2(\text{C} - 2 \text{ wt\%}) +16 \text{ wt\% SiO}_2$ and $\text{MgB}_2(\text{C} - 6.1 \text{ wt\%}) +16 \text{ wt\% SiO}_2$ samples.

Fig.(4.50) and (4.51) show the Kramer plots at 11 and 22 K, as extracted from the magnetic J_c , for the three SiO_2 -coated undoped and C-CVD doped MgB_2 samples. The plots have been employed to evaluate the irreversibility field $H_{\text{irr}} \equiv H_K$, by extrapolating the linear part of the Kramer function at high currents to the field axis intercept, as described for the undoped and C-CVD doped MgB_2 samples. Fig.(4.52) and (4.53) show the behaviour of the normalized pinning forces curves as a function of the reduced field H/H_K at 11 K and 22 K, which have been plotted by using these H_K values. The dominant pinning mechanism was observed to be grain boundary at both 11 K and 22 K, actually at 11 K the maximum values of $F_p/F_{p\text{max}}$ was shifted to values lower than 0.2, the typical value for this pinning mechanism as shown by the normalised theoretical curve [65, 91] included in fig.(4.40). It is worth noting that the coating with silica, similar to what was seen for the carbon doping, did not introduce any additional pinning mechanism. Moreover, the best

sample, $\text{MgB}_2+16 \text{ wt}\% \text{ SiO}_2$, achieved maximum pinning force values of $3.55 \times 10^9 \text{ N/m}^3$ at 11 K, and $1.51 \times 10^9 \text{ N/m}^3$ at 22 K, both of which were 40% lower than the respective values for the best C-CVD doped sample, namely $\text{MgB}_2(\text{C} - 2\%)$, while the best undoped sample, the 775°C MgB_2 sample, reached values of $7.19 \times 10^9 \text{ N/m}^3$ at 11 K, and $4.24 \times 10^9 \text{ N/m}^3$ at 22 K. The pronounced broadening of the $F_p/F_{p\text{max}}$ curves observed for $\text{MgB}_2(\text{C} - 6.1 \text{ wt}\%)+16 \text{ wt}\% \text{ SiO}_2$ at 22 K suggests that a minor contribution from the point defect pinning mechanism should be considered. However, the synergic effect of the C doping and the coating with SiO_2 in $\text{MgB}_2(\text{C} - 6.1 \text{ wt}\%)+16 \text{ wt}\% \text{ SiO}_2$ was observed to strongly reduce the maximum pinning force values which were estimated to be an order of magnitude lower than those for $\text{MgB}_2+16 \text{ wt}\% \text{ SiO}_2$, at both 11 K and 22 K.

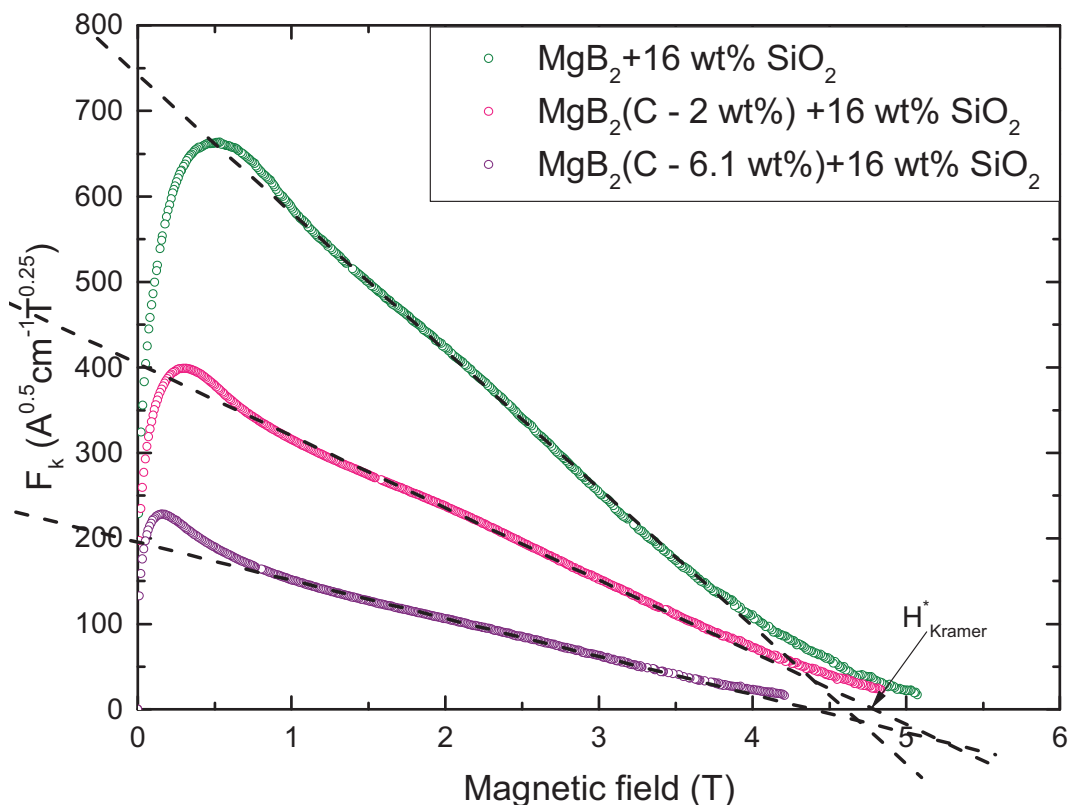


Figure 4.50: Kramer plots as a function of magnetic field at 11 K from the magnetic J_c data for the SiO_2 -coated $\text{MgB}_2(\text{C} - x \text{ wt}\%)$ bulk samples listed in Table 4.5.

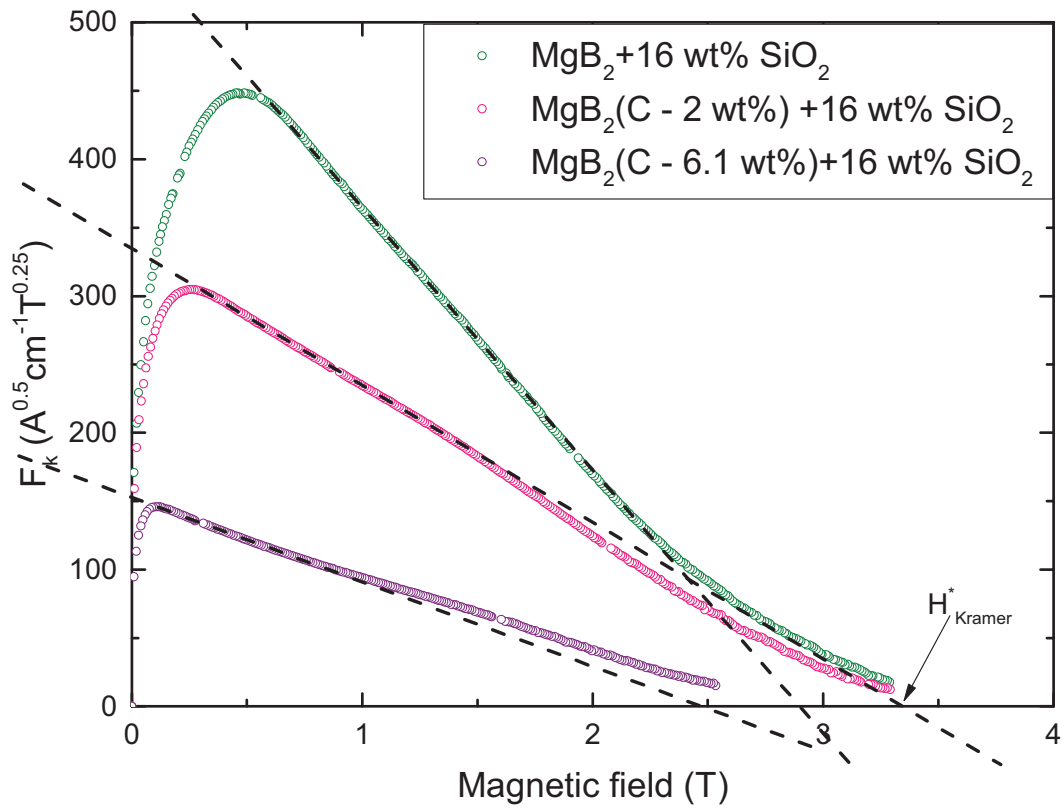


Figure 4.51: Kramer plots as a function of magnetic field at 22 K from the magnetic J_c data for the SiO_2 -coated $MgB_2(C - x wt\%)$ bulk samples listed in Table 4.5.

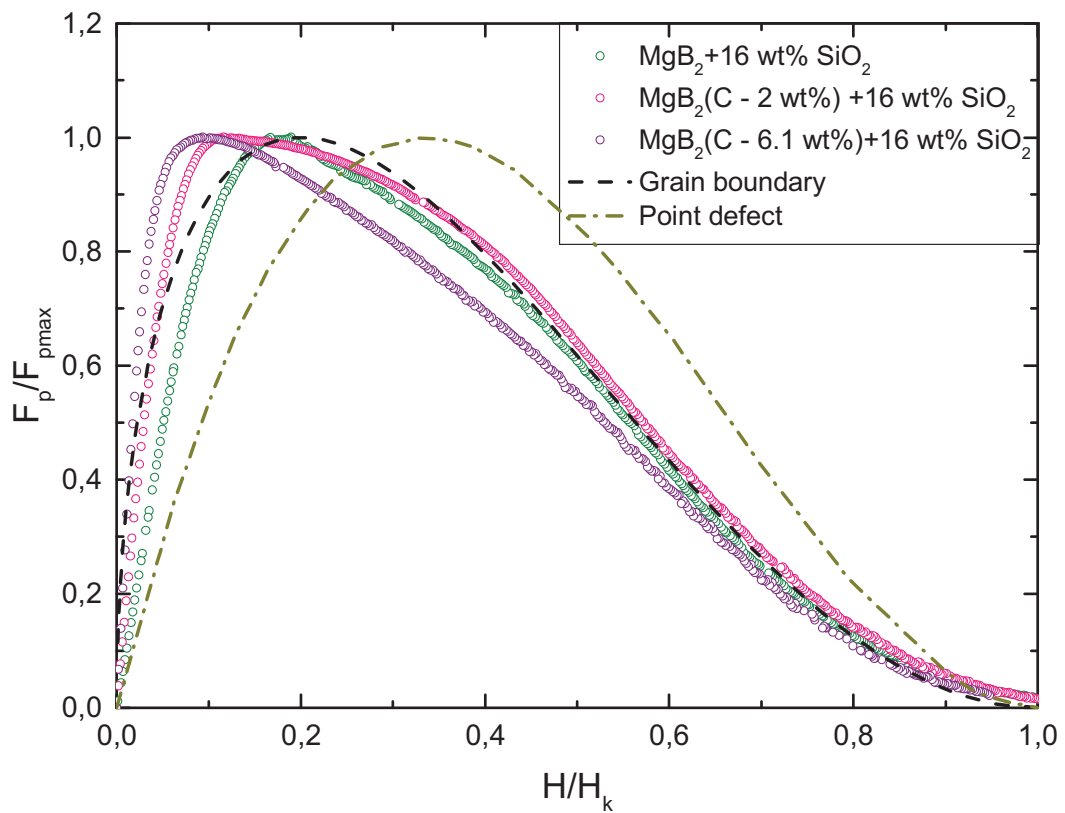


Figure 4.52: Behaviour of the normalised pinning force vs normalised magnetic field at 11 K from the magnetic J_c data for the SiO_2 -coated $MgB_2(C - x wt\%)$ bulk samples listed in Table 4.5. Grain boundary pinning, eq.(4.5), and point defect models, [91], are also shown for comparison.

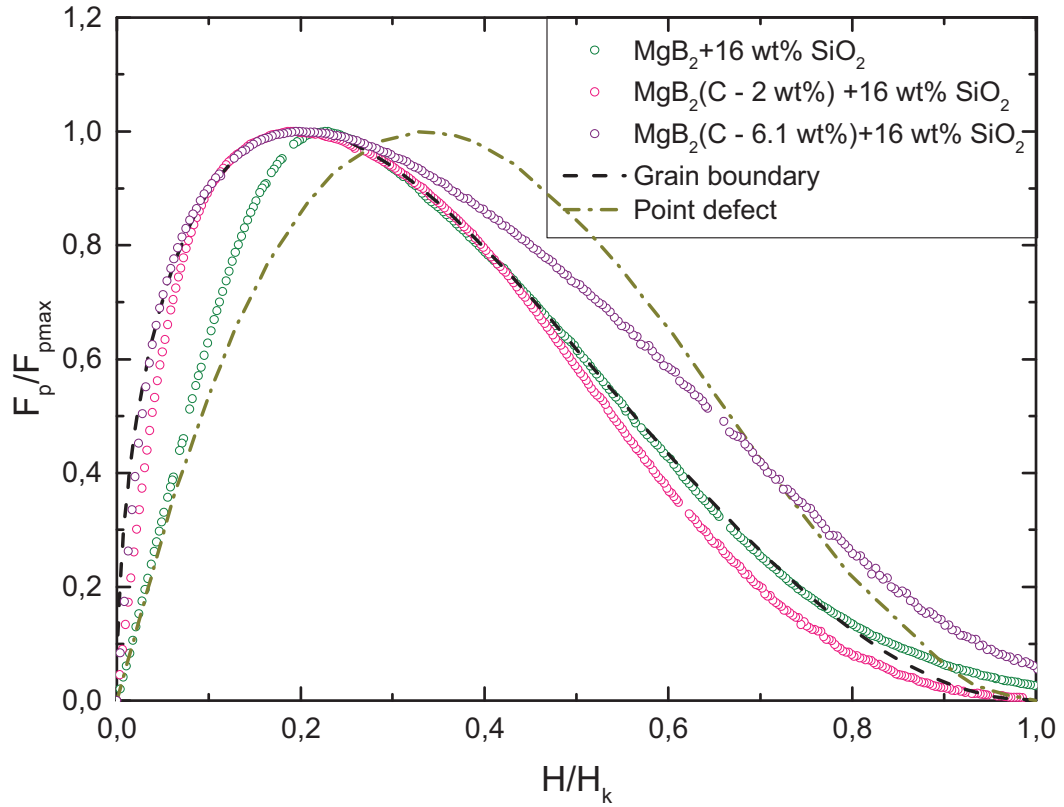


Figure 4.53: Behaviour of the normalised pinning force vs normalised magnetic field at 22 K from the magnetic J_c data for the SiO_2 -coated $\text{MgB}_2(\text{C} - x \text{ wt}\%)$ bulk samples listed in Table 4.5. Grain boundary pinning, eq.(4.5), and point defect models, [91], are also shown for comparison.

Fig.(4.54)-(4.56) show the temperature-dependent critical current density curves in 0.1 T for the three SiO_2 coated $\text{Mg}(\text{B}_{1-x}\text{C}_x)_2$ samples. The curves have been fitted using the equation (4.2). Whilst the temperature dependence of J_c of $\text{MgB}_2+16 \text{ wt}\% \text{ SiO}_2$ and $\text{MgB}_2(\text{C} - 2 \text{ wt}\%)+16 \text{ wt}\% \text{ SiO}_2$ could be described using one T_{irr} , two T_{irr} 's are needed to fit the $J_c(T)$ curves in the case of $\text{MgB}_2(\text{C} - 6.1 \text{ wt}\%)+16 \text{ wt}\% \text{ SiO}_2$. This finding correlates with the results of XRD analysis, showing the existence of two different doping regimes within the higher C doped sample, whilst the other two SiO_2 coated $\text{Mg}(\text{B}_{1-x}\text{C}_x)_2$ samples can be considered to be formed by a single-phase composition. Moreover, the comparatively low values of T_{irr} 's for the $\text{MgB}_2+6.1 \text{ wt}\% \text{ C}+16 \text{ wt}\% \text{ SiO}_2$ sample could explain the degradation of J_c performances particularly at low magnetic fields, as displayed in fig.(4.48) and fig.(4.49).

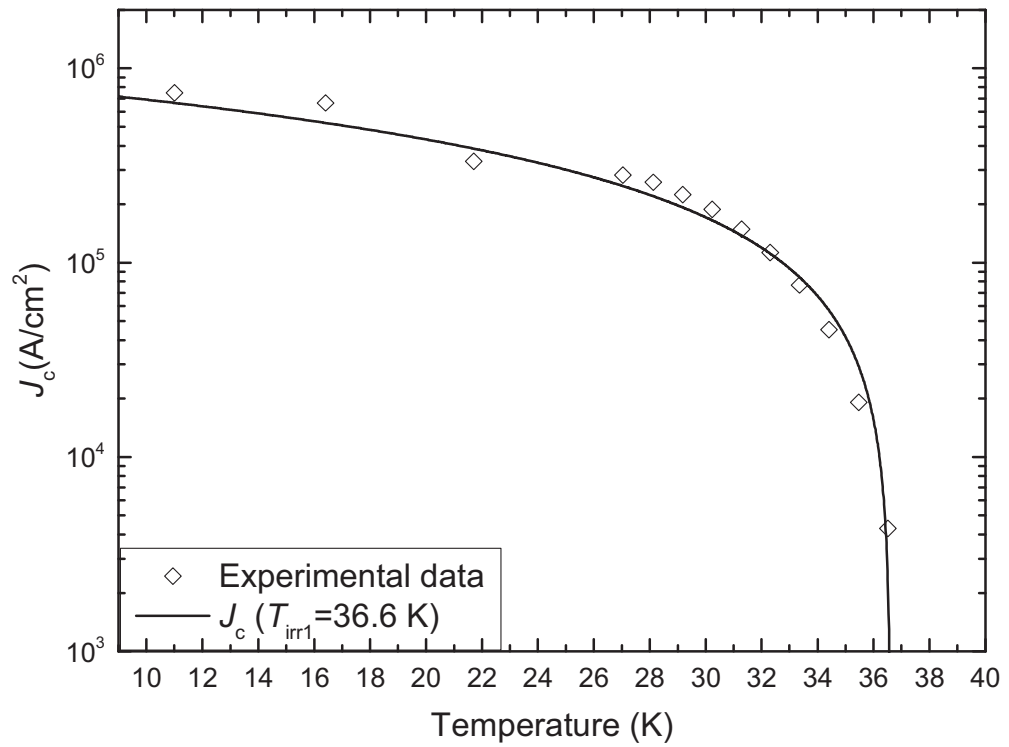


Figure 4.54: Temperature dependence of the critical current density, $J_c(T)$, at 0.1 T, for the MgB₂+16 wt% SiO₂ sample. Circles represent experimental data, whilst solid line represents fitting curve, which is described by eq.(4.6).

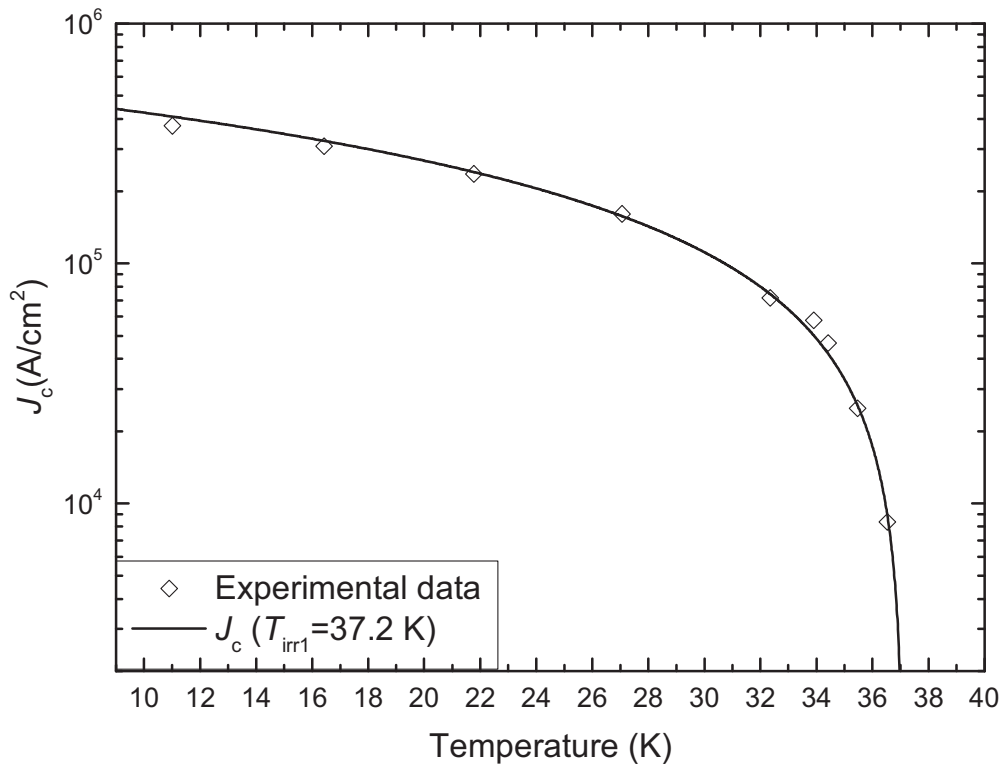


Figure 4.55: Temperature dependence of the critical current density, $J_c(T)$, at 0.1 T, for the MgB₂(C - 2 wt%)+16 wt% SiO₂ sample. Circles represent experimental data, whilst solid line represents fitting curve, which is described by eq.(4.6).

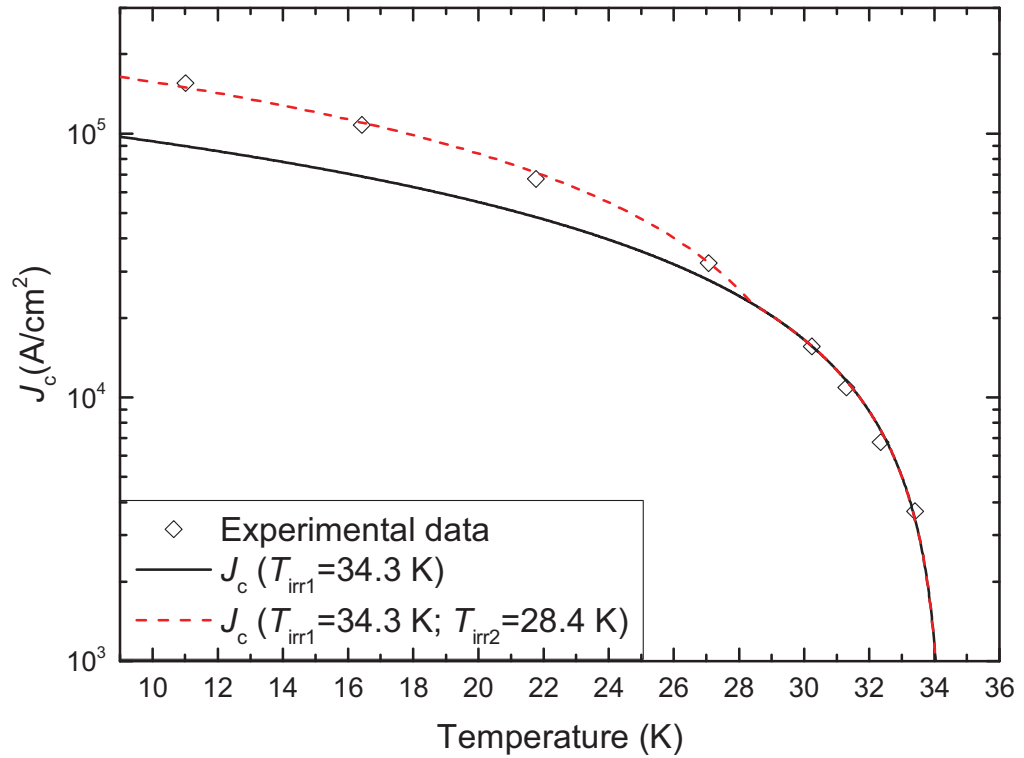


Figure 4.56: Temperature dependence of the critical current density, $J_c(T)$, at 0.1 T, for the $\text{MgB}_2(\text{C} - 6.1 \text{ wt}\%) + 16 \text{ wt}\% \text{ SiO}_2$ sample. Circles represent experimental data, whilst solid line represents fitting curve, which is described by eq.(4.6).

In fig.(4.57) the values of T_{irr} from magnetisation measurements have been plotted in function of Δa (and X) for the SiO_2 -coated $\text{MgB}_2(\text{C} - x \text{ wt}\%)$ samples. The values for the undoped and C-CVD doped MgB_2 samples, which have already been presented in the previous section, are shown for comparison. With regard to the $\text{MgB}_2(\text{C} - 6.1 \text{ wt}\%) + 16 \text{ wt}\% \text{ SiO}_2$ sample, both the values of T_{irr} 's (34.3 K at $X=0.2\%$ and 28.4 K at $X=1.3\%$) are noticeably lower than the respective values for single crystals. This behaviour indicates that the main current path is not through the lower doped regions, as otherwise shown by the XRD analysis, and that the formation of compounds MgCO_3 and MgSiO_4 could have caused a dramatic decrease of T_{irr} , significantly reducing the self-field J_c compared to the other samples. In contrast, the virtual coincidence between the T_{irr} 's of $\text{MgB}_2 + 16 \text{ wt}\% \text{ SiO}_2$ and $\text{MgB}_2(\text{C} - 2 \text{ wt}\%) + 16 \text{ wt}\% \text{ SiO}_2$ and that of undoped MgB_2 on the one hand confirms the virtual absence of carbon incorporated into the MgB_2 lattice for the $\text{MgB}_2(\text{C} - 2 \text{ wt}\%) + 16 \text{ wt}\% \text{ SiO}_2$

sample, as suggested by the XRD data. On the other hand, it suggests that silica behaves differently from carbon, in that it is not substituted in the boron honeycomb layers, hence it does not provide impurity scattering of charge carriers, which leads to a decrease of T_{irr} .

In fig.(4.58) the SEM image of the $MgB_2+16\text{ wt}\% SiO_2$ sample shows the presence of dispersed magnesium silicate inclusions of the order of 50 nm in size, whilst agglomerations were observed at grain boundaries which limit the current path. Optical microscope pictures show that $MgB_2(C - 6.1\text{ wt}\%)+16\text{ wt}\% SiO_2$, fig.(4.59), exhibited a microstructure that appeared quite inhomogeneous, possessing a large number of voids when compared to $MgB_2(C - 2\text{ wt}\%)+16\text{ wt}\% SiO_2$ and $MgB_2+16\text{ wt}\% SiO_2$ (which exhibited a very limited number of voids), fig.(4.60) and (4.61).

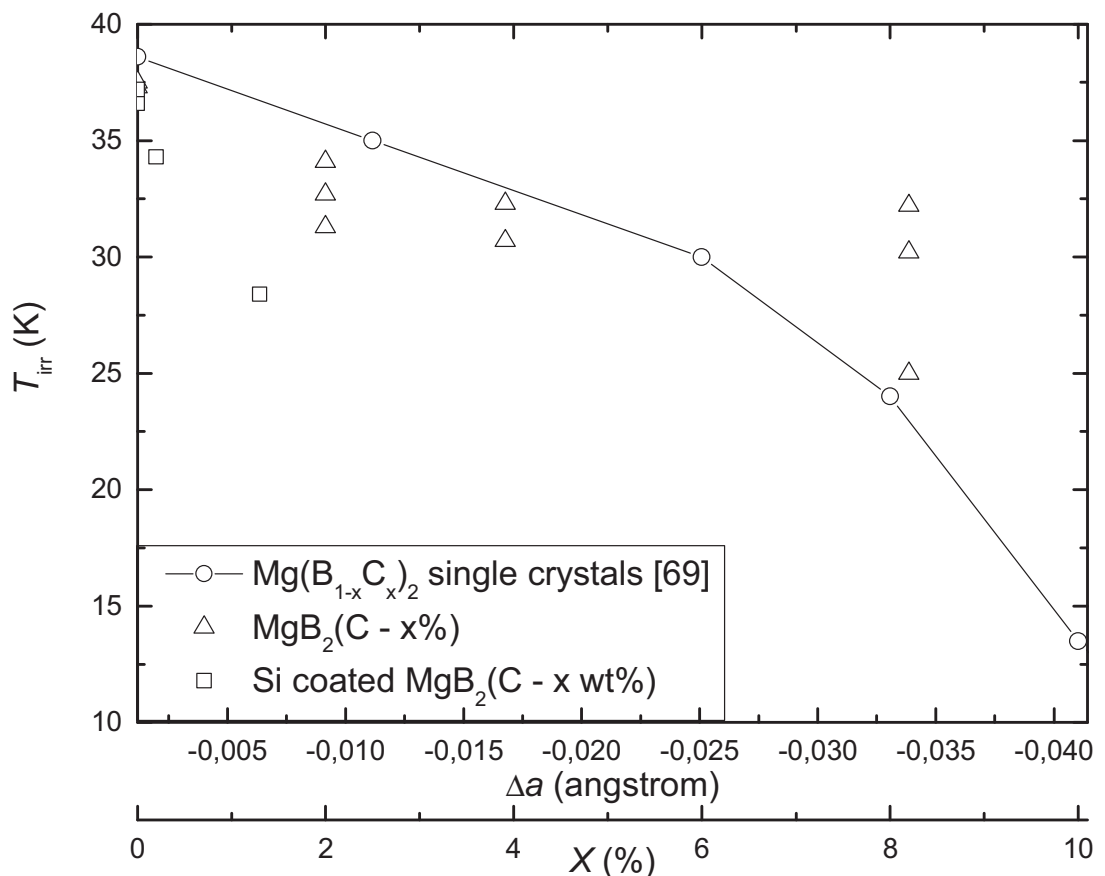


Figure 4.57: Dependence of T_{irr} on Δa (and X) for SiO_2 -coated $MgB_2(C - x\text{ wt}\%)$ samples and $Mg(B_{1-x}C_x)_2$ single crystals [75]. In the same graph the values for the $MgB_2(C - x\%)$ samples are shown for comparison.

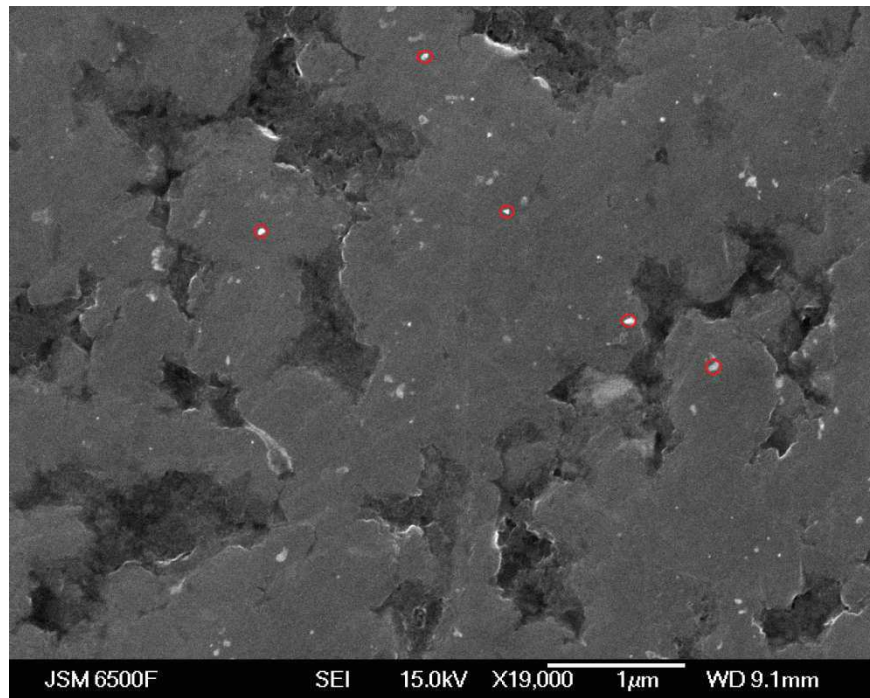


Figure 4.58: SEM image for MgB₂+16 wt% SiO₂. The nano-sized magnesium silicate inclusions are circled in red.



Figure 4.59: Optical microscopy picture of MgB₂(C - 6.1 wt%)+16 wt% SiO₂.



Figure 4.60: Optical microscopy picture of $\text{MgB}_2+2 \text{ wt}\% \text{ C}+16 \text{ wt}\% \text{ SiO}_2$.



Figure 4.61: Optical microscopy picture of $\text{MgB}_2+16 \text{ wt}\% \text{ SiO}_2$.

4.5 Comparison of $J_c(B)$ between $\text{MgB}_2(\text{C} - 2\%)$ and literature-reported data for doped MgB_2 bulk samples, and MgB_2 wires and tapes

4.5.1 Comparison of $J_c(B)$ between $\text{MgB}_2(\text{C} - 2\%)$ and literature-reported data for doped MgB_2 bulk samples

In fig.(4.62), the $J_c(B)$ at 20 K of our best C-CVD sample, $\text{MgB}_2(\text{C} - 2\%)$, is compared with that of the best bulk samples from the literature. The $\text{Mg}(\text{B}_{0.98}\text{C}_{0.02})_2$ sample exhibited critical current density performance as high as $24.8 \times 10^4 \text{ A/cm}^2$ in 1 T, and $5.5 \times 10^3 \text{ A/cm}^2$ in 4 T, which were comparable with the highest values reported for doped MgB_2 bulk samples.

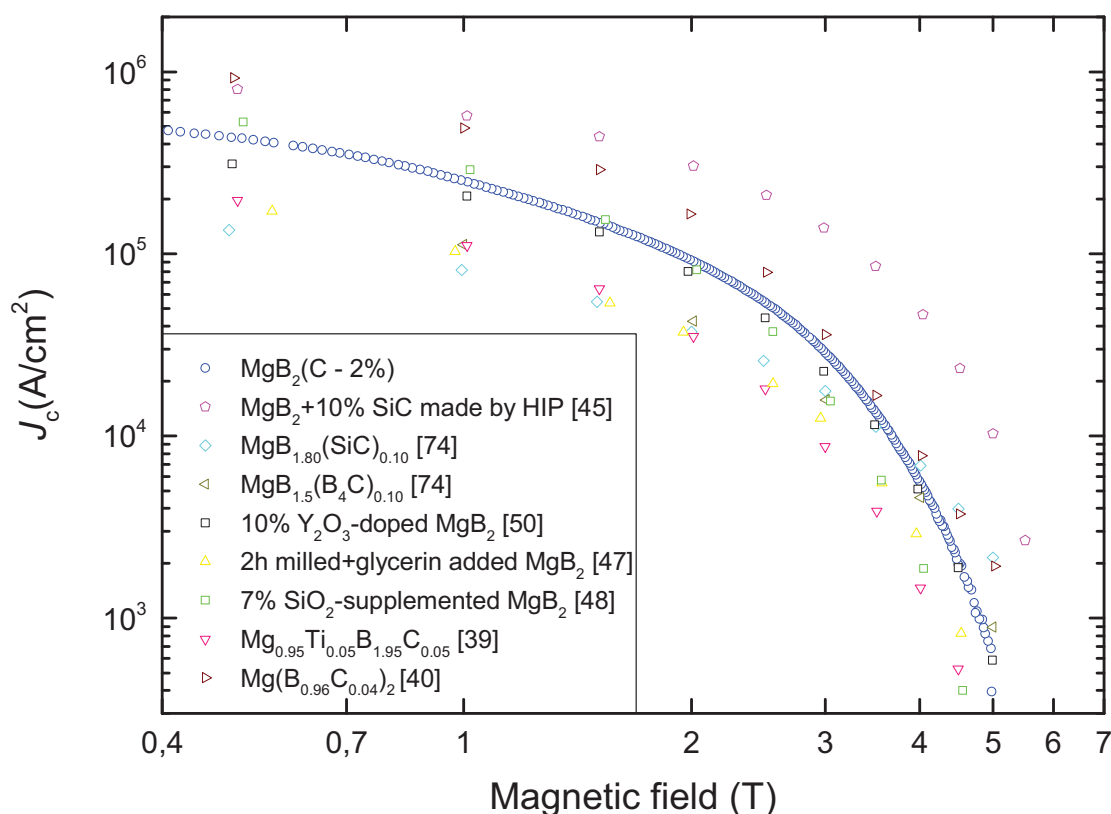


Figure 4.62: Comparison of the field dependence of the critical current density, $J_c(B)$, at 20 K, between $\text{MgB}_2(\text{C} - 2\%)$ and bulk samples data from the literature.

The only sample that was reported to have a better performance throughout the field range is the 10 wt% nano-SiC doped sample prepared using the hot-isostatic pressing (HIP) method [45]. The presumable difference in density between our sample (49% packing dense) and the 10 wt% nano-SiC doped sample (no value has been reported, but the authors specified that the samples were HIPed under 150 MPa at 850°C for 30 min) could explain the difference in J_c , in particular at low fields. As explained in Chapter 4.1, lowering of the packing density is observed to be beneficial to solving the problem of the crack formation. However, it arguably has a limiting effect on the transport properties, although the effective cross section, A_F , estimated from the resistivity for the $MgB_2(C - 3.9\%)$ sample treated at 850°C, was found to be 0.25, which is relatively high when compared to many polycrystalline samples in the literature, which have reported values below 0.2. The difference in the J_c performance between the $Mg(B_{0.98}C_{0.02})_2$ and the 10 wt% nano-SiC doped sample becomes more pronounced with increasing field strength, as evidenced by fig.(4.63), in which the normalized critical current density, $J_c(B)/J_c(B=1\text{ T})$, has been plotted as a function of the magnetic field. Wang *et al.* [45] have observed that the smaller the doping source particles were, the smaller the precipitates formed, and the stronger the flux pinning achieved. Our sample has been prepared by reacting a Mg rod with C-CVD coated boron powder composed of particles sized in the range 30-100 nm, as revealed by TEM images in Chapter 3, whilst the 10 wt% nano-SiC doped samples have been produced from mixing Mg, B with SiC powder which has particle sizes of 20 nm. Therefore, the difference both in the doping method employed and in particle size could be responsible for the increasing gap in the field-dependent J_c performance between the two samples. Another reason could be the processing conditions under which

the two samples have been treated. The $\text{MgB}_2(\text{C} - 2\%)$ sample has been sintered at 850°C for 12 h, whilst the 10 wt% nano-SiC doped sample has been heat-treated at $700\text{--}900^\circ\text{C}$ for 3 min to 1 h. The different processing conditions were likely to produce a degradation of crystallinity in the 10 wt% nano-SiC doped sample, resulting in an enhancement of H_{c2} , H_{irr} and, therefore, J_c . Dou *et al.* have proposed a dual reaction model [44], according to which, as explained in Chapter 1, SiC can provide suitable content of carbon within MgB_2 even through the low-temperature synthesis performed at 600°C , which yields small grain size with poor crystallinity. This result could also explain the significant magnetic field dependence of J_c reported for another SiC-doped sample, the $\text{MgB}_{1.80}(\text{SiC})_{0.10}$ [74], which showed a crossover with that of the $\text{MgB}_2(\text{C} - 2\%)$ sample at 4 T, as evidenced by fig.(4.62).

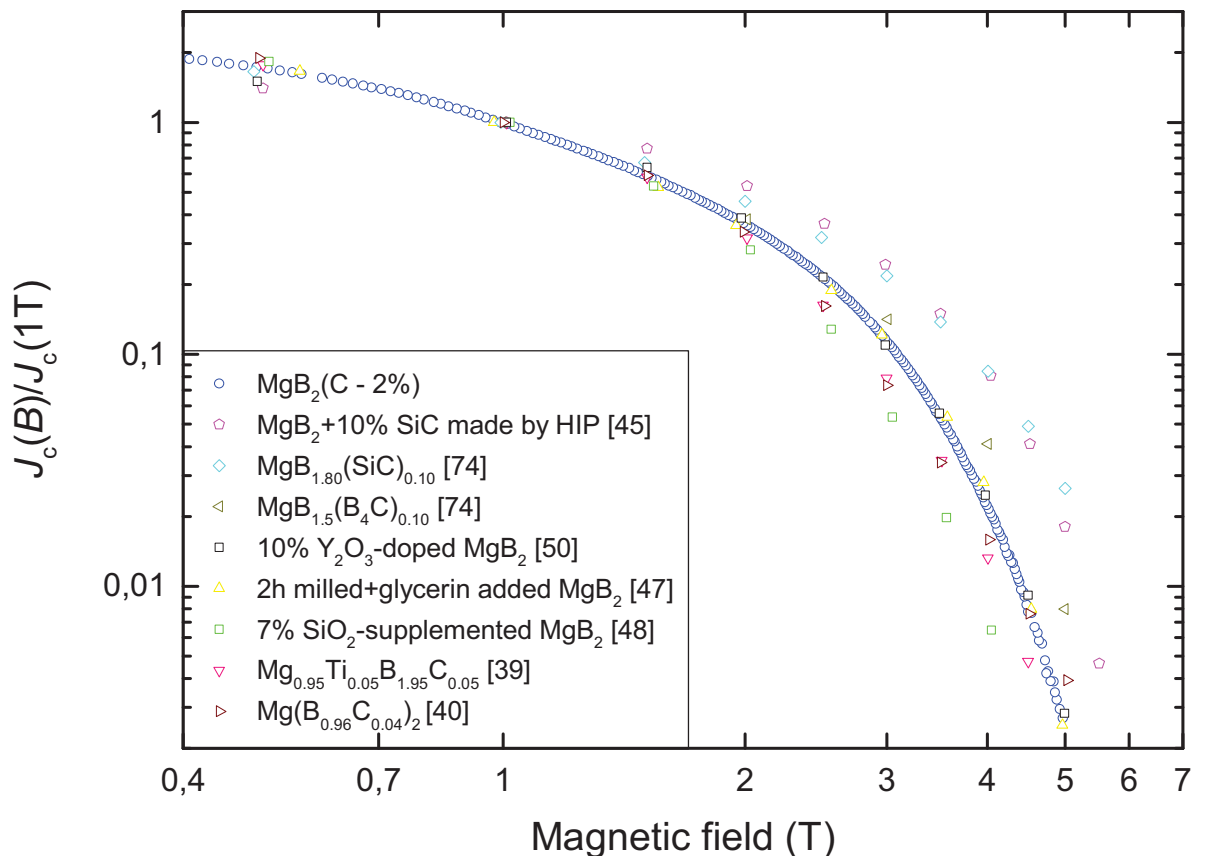


Figure 4.63: Comparison of the field dependence of the normalized critical current density, $J_c(B)/J_c(B=1\text{ T})$, at 20 K, between $\text{MgB}_2(\text{C} - 2\%)$ and bulk samples data from the literature.

It is worth noting that the 7% SiO₂-supplemented MgB₂ sample [48] exhibited the highest J_c performance at low fields among the samples considered (except for the 10 wt% nano-SiC doped sample), whilst its critical current density fell off with increasing field strength. These results confirmed the outcomes on the field dependence of J_c for the SiO₂ doped Mg(B_{1-x}C_x)₂ samples presented in this work.

At 5 K, as shown in fig.(4.64), the MgB₂(C - 2%) sample exhibited J_c performance, which, compared to that of other literature reported bulk samples, was better than that observed at 20 K. Except for the above mentioned 10 wt% nano-SiC doped sample, which exhibited quite an erratic J_c behaviour, only the mechanically alloyed Mg(B_{0.93}C_{0.07})₂ sample [46] had a better performance throughout the field range. The use of the *ex-situ* process (using pre-reacted powder) and the HIP processing at 1000°C for 200 min of the before-sintering-pellets for this sample could partly account for the difference in J_c as compared to our C-CVD MgB₂ sample, particularly at low fields. The gap in J_c at high fields can instead be explained as a result of the difference in the grain size between the mechanically alloyed Mg(B_{0.93}C_{0.07})₂ sample (\approx 50 nm) and the MgB₂(C - 2%) sample (\approx 100 nm, as revealed by the SEM images in Chapter 4.3) rather than of the amount of carbon included into MgB₂ (B. J. Senkowicz *et al.* observed that, for nominal content larger than 0.05, the error bar in the lattice parameter measurement became too large to draw true conclusions).

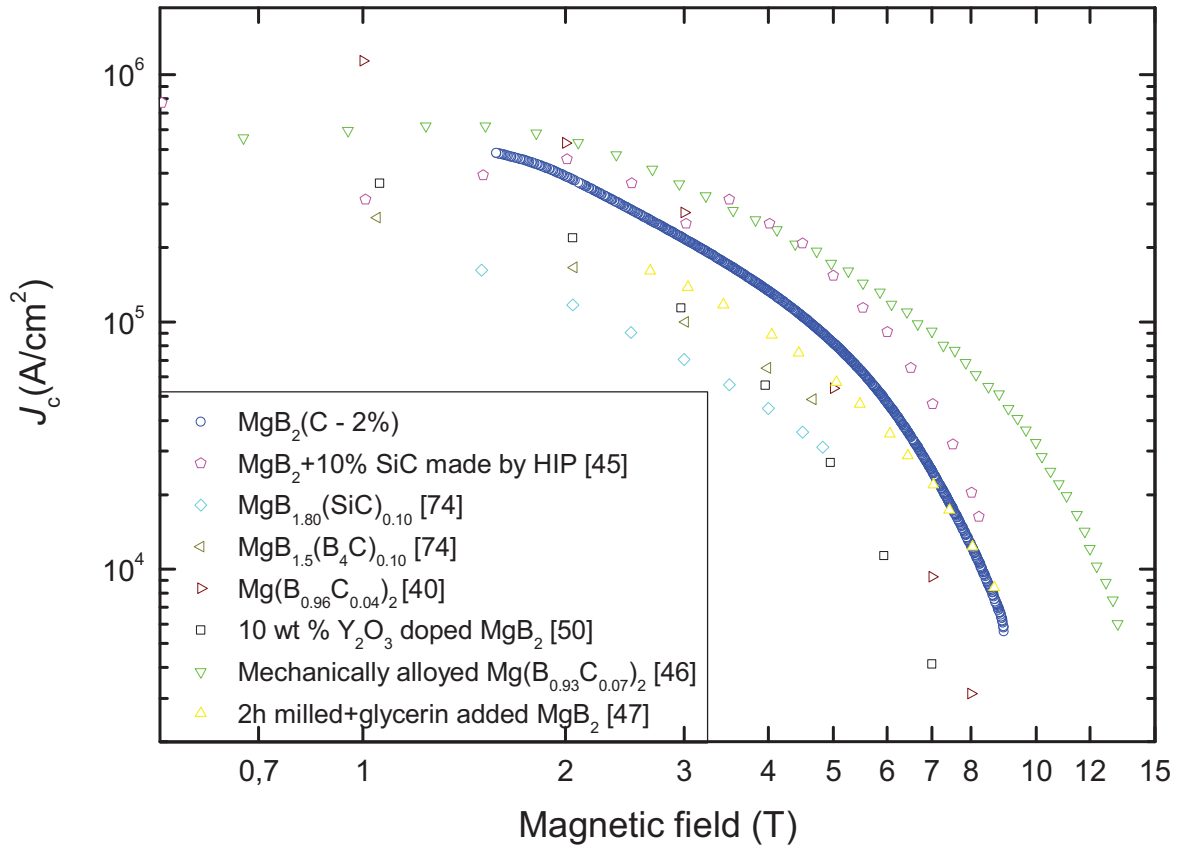


Figure 4.64: Comparison of the field dependence of the critical current density, $J_c(B)$, at 5 K, between $\text{MgB}_2(\text{C} - 2\%)$ and bulk samples data from the literature.

The field dependence of normalized critical current density, $J_c(B)/J_c(B=2 \text{ T})$, graph, fig.(4.65), confirms the significant critical current in field performance for the $\text{MgB}_2(\text{C} - 2\%)$, which was observed to be comparable to the one of the two reported SiC doped samples, $\text{MgB}_{1.80}(\text{SiC})_{0.10}$ [74]. $\text{MgB}_2(\text{C} - 2\%)$ exhibited a better J_c field dependence as compared to that of the other C-CVD sample, $\text{Mg}(\text{B}_{0.96}\text{C}_{0.04})_2$ [40], whilst the J_c values at low fields was lower. Since the carbon doping process was the same for both samples, these results can be accounted for by the difference in the boron particle sizes (Young *et al.* have used boron powder with a grain size of less than $1 \mu\text{m}$).

The pinning force behaviour is well described by the grain boundary based pinning model in all C doped bulk samples, and no additional pinning mechanisms was introduced upon carbon doping.

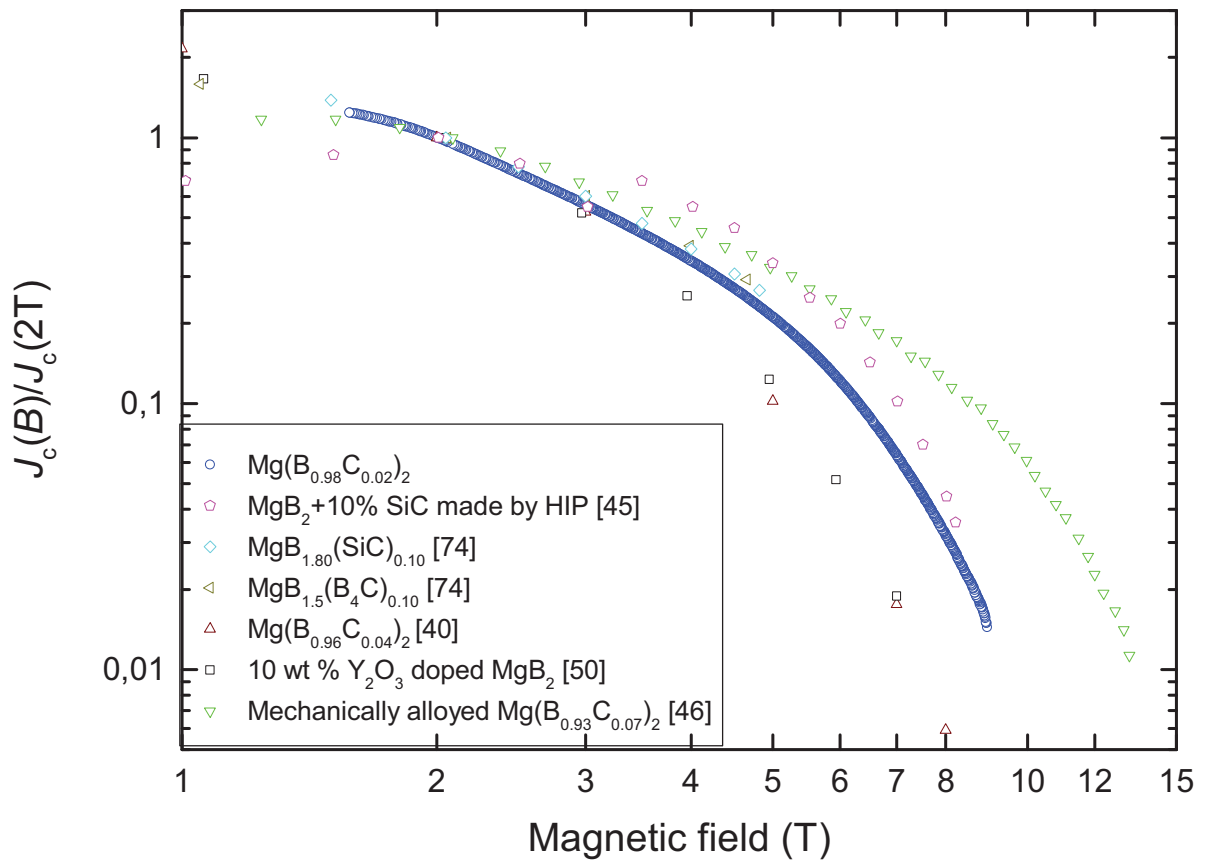


Figure 4.65: Comparison of the field dependence of the normalized critical current density, $J_c(B)/J_c(B=2\text{ T})$, at 5 K, between $\text{Mg}(\text{B}_{0.98}\text{C}_{0.02})_2$ and bulk samples data from the literature.

4.5.2 Comparison of $J_c(B)$ between $\text{MgB}_2(\text{C} - 2\%)$ and literature-reported data for doped MgB_2 wires and tapes

In order to achieve a more complete understanding of the effects of chemical doping process of MgB_2 , the field-dependent J_c properties, at 20 K and 5 K, of our $\text{MgB}_2(\text{C} - 2\%)$ and of the best bulk samples from fig.(4.43) have been plotted, fig.(4.66)-(4.67), along with the best results for doped wires and tapes from the literature, a brief description of which has been provided in Chapter 1.9. Before starting any discussion on the comparison between the properties of these samples, it should be noted that some deviations in the results can be partly attributed to the different types of measuring techniques adopted (the J_c of all the bulk

samples considered has been estimated from magnetic measurement of critical current density, whilst transport measurements of J_c have been performed in the case of the wires and tapes). In particular, magnetic J_c has been shown to depend on the size of the sample [98] and characteristic deviations from transport J_c (upwards at low fields and downwards at higher fields [99]) have been observed. The detailed study by Hovart *et al.* [100] has shown that the field dependence of J_c is actually a contribution of different types of screening. One source, which is prevalent at low fields, is that coming from the screening currents around the cells of MgB₂ between the voids, another is related to currents flowing around the whole of samples giving a dominant contribution to the measured irreversible magnetic moment in the intermediate fields, a third contribution, which dominates at high fields, is that found at the ≈ 1 mm clusters that constitute the MgB₂ crystals. Only the Δm within the intermediate field range should be used in the critical state model to calculate J_c , which has been found to be in good agreement with the transport J_c .

Fig.(4.66) shows that, at 20 K, there are two samples, namely the malic acid-doped MgB₂ [52] and monofilamentary malic acid (C₄H₆O₅) added MgB₂ wires obtained by Cold High Pressure Densification (CHPD) [55], that exhibit in-field J_c performance significantly higher than those of all the other doped samples and, in particular, of the bulk samples. These results have been explained by the respective authors as a result of boron vacancies and the associated stacking faults, which produce an enhancement of the upper critical field in the case of the malic acid-doped MgB₂ wire, and of an increase of the C content in the MgB₂ structure as a consequence of CHPD processing. The comparatively high packing density of the wires (and tapes) with respect to bulk samples, could also explain why in the plot of fig.(4.66), the majority of wire and

tapes J_c values lie above the correspondent values for bulk samples in the high magnetic field range.

Also at 5 K, fig.(4.67), the best J_c performance, in the high field region, is observed, apart from the above-mentioned mechanically alloyed $\text{Mg}(\text{B}_{0.93}\text{C}_{0.07})_2$ bulk sample [46], for MgB_2 wires and tapes. The comparatively high in-field J_c properties could be attributed to the greater density achieved in wires and tapes. The best J_c properties are observed in advanced internal-Mg-diffusion-processed MgB_2 wires [68] attributed to the optimum connectivity and high fill factors achieved, and in MgB_2 tapes studied by W. Häußler *et al.* [68] due to the effective combination of the nanocrystalline precursor powder prepared by mechanical alloying and the doping with nanostructured carbon.

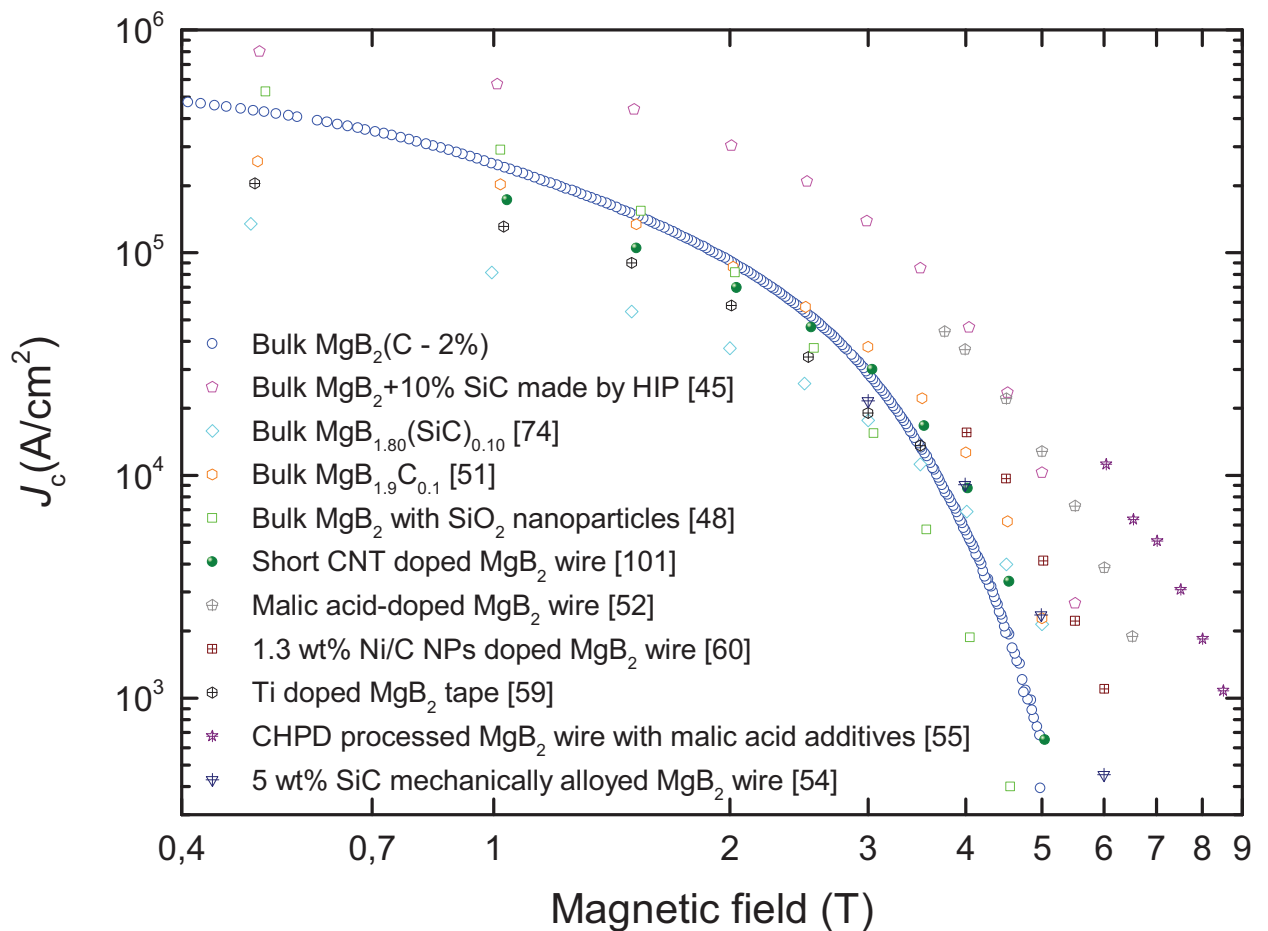


Figure 4.66: Comparison of the field dependence of the critical current density, $J_c(B)$, at 20 K, between $\text{MgB}_2(\text{C} - 2\%)$ and data for doped MgB_2 bulk samples, and wires and tapes from the literature.

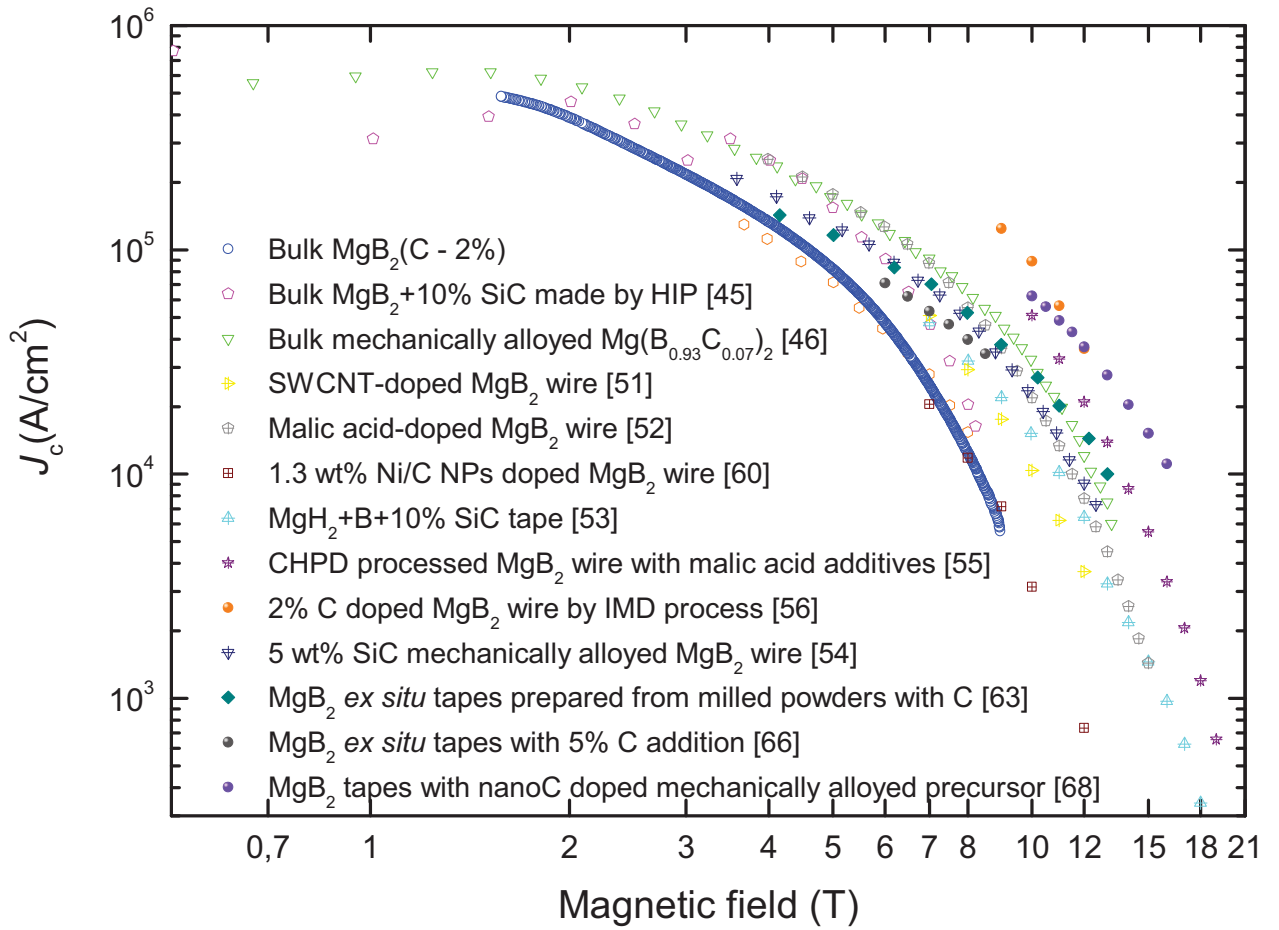


Figure 4.67: Comparison of the field dependence of the critical current density, $J_c(B)$, at 5 K, between MgB₂(C - 2%) and data for doped MgB₂ bulk samples, and wires and tapes from the literature.

Chapter 5

Conclusion and future work

The study of a method of chemical vapour deposition of carbon on to the boron precursor powder has been performed and the effects on the structural and magnetic properties of the sintered $\text{MgB}_2(\text{C} - x\%)$ powder and bulk samples made from the C-CVD doped B and bulk samples have been investigated. In addition, initial results on the physical and critical current density properties of SiO_2 coated $\text{MgB}_2(\text{C} - x\%)$ bulk samples prepared using silica-coated boron via the sol-gel process and C-CVD doped boron were presented.

Chemical carbon deposition of carbon was shown by TEM to achieve an almost constantly thick layer of carbon (5.5 ± 0.7 nm) on each boron powder particle, which was independent of the boron particle sizes. A quantitative estimation of the fractional carbon volume relative to the volume of the boron grain has evidenced that the density of the carbon layer is about 14 times less than that of the boron particle. This result suggested that the mass of C deposited was composed predominantly of light compounds of carbon, and, in particular, the estimated density value was found to be consistent with that of carbon black.

The Gaussian analysis of the (100) peak revealed the coexistence of multiple phases within the sintered $\text{MgB}_2(\text{C} - x\%)$ powder samples, which could not be resolved using the results of the field-cooled magnetisation data, due to the presence of induced shielding currents. The broadness of the superconducting transition, which was a common feature of all the characterised samples, was observed to be significantly pronounced for the higher temperature treatment in carbon-doping. Both the XRD and magnetisation results could be explained by virtue of the uniformity of the carbon layer thickness, as suggested by the analysis of

the TEM images, from the precursor boron particle sizes which resulted in multiple C doping levels in the $\text{MgB}_2(\text{C} - x\%)$ samples.

The study of the preparation process for bulk samples suggested that the cause of the formation of cracks observed in sintered bulk samples could be the difference between the time constant of reaction and the time constant of diffusion. This finding was confirmed by the results performed on a short sample, prepared using a relatively low packing density (36%), which was found to be devoid of cracks after being treated at low temperature (750°C), and then post-treated at higher temperature (950°C).

The XRD analysis of the (100) peak and the fitting of the temperature-dependence of the critical current density confirmed the existence of multiple doping regimes also within the $\text{MgB}_2(\text{C} - x\%)$ bulk samples. In particular, the provision of multiple T_{irr} 's as fitting parameters of the temperature-dependent J_c curves has been interpreted as a result of distinct levels of carbon doping, with the biggest contribution coming from the middle value, which represents the dominant pinning mechanism, and a possible weaker one existing at higher temperatures. The doping with carbon by CVD method was observed to be beneficial to improving the in-field critical current properties, reaching, in the case of the $\text{MgB}_2(\text{C} - 2\%)$ sample, the J_c performance of the best bulk $\text{MgB}_2(\text{C} - x\%)$ bulk samples. The lower packing density value achieved in the preparation process of the bulk samples in order to limit the problem of the crack formation within the sintered samples could, however, explain the gap in J_c performance, in particular at high magnetic fields, with respect to the best literature-reported data for wires and tapes.

The Sol-gel method has been shown by TEM to be a less controllable coating technique as compared to the CVD process, resulting in samples with a non-constant layer of silica on the boron particles. The huge

amount of silica loaded onto the boron powder, which is likely to impair the connectivity of the samples, and the formation of oxygen containing compounds within the sintered microstructure, are thought to impair the J_c properties of silica-coated $\text{MgB}_2(\text{C} - x\%)$ bulk samples. In particular, as observed in the case of the $\text{MgB}_2(\text{C} - 6.1 \text{ wt}\%) + 16 \text{ wt}\% \text{SiO}_2$ sample, the presence of carbonate was believed to have caused a dramatic decrease of T_{irr} , resulting in a significant reduction of the self-field J_c , compared to the undoped sample.

The results presented in this work on the chemical vapour deposition of carbon onto the boron precursor powder are expected to be confirmed by future experiments on samples made by a wider range of carbon dopant conditions. In particular, it would be interesting to prepare samples using boron powder having a narrow range of particle sizes. In that way, it would be possible to achieve an homogeneous carbon-rich layer on each individual boron powder particle, since, as was observed in the analysis of the TEM images, the deposited layer of carbon has a uniform thickness, with varying values of particle sizes. Future work should also address the preparation of long bulk samples devoid of cracks, by attempting to overcome the problems derived from the difference between the time constant of reaction, and the time constant of diffusion in the course of the sintering process. It could be interesting to explore the viability of producing bulk samples using coarser boron particles, since their specific surface area is lower than in the case of nanometric boron powder. This approach could prove to be beneficial to reducing the rate of reaction, although it might negatively affect the critical current density performance, due to the consequent decrease of the grain boundary density.

The results on the SiO_2 -coating of boron by the sol-gel method suggest that it might be beneficial to try to reduce the amount of silica loading on

the precursor powder. That reduction could be expected both to improve the connectivity of the samples, and should hinder the formation of oxygen containing compounds, resulting in a significant improvement of the J_c properties throughout the magnetic field range.

References

- [1] H. K. Onnes, *Leiden Comm.* 120b, 122b, 124c, 1911.
- [2] CHARLES P. POOLE, HORACIO A. FARACH, RICHARD J. CRESWICK, RUSLAN PROZOROV. *Superconductivity*. Academic Press, 2007, pp. 23-430. "Figures reprinted from this book with permission of Elsevier".
- [3] THOMAS P. SHEAHEN. *Introduction to High-Temperature Superconductivity*. Springer, 2002, pp. 15-34.
- [4] CHIA-CHUN CHEN; STEPHEN P KELTY; CHARLES M. LIEBER. *(Rb_xK_{1-x})₃C₆₀ Superconductors: Formation of a Continuous Series of Solid Solutions*. Science, Vol. 253, 1991, pp. 886-888.
- [5] C. KITTEL. *Introduction to Solid-State Physics*, 6th ed, 1986.
- [6] http://shodhganga.inflibnet.ac.in/bitstream/10603/8002/9/09chapter_1.pdf
- [7] G. BLATTER. *Vortex matter*. Physica C 282-287, 1997, pp. 19-26.
- [8] A. A. ABRIKOSOV. *On the Magnetic Properties of Superconductors of the Second Group*. Zh. Eksp. Teor. Fiz. 32, 1442, 1957 [Sov. Phys. JETP 5, 1174, 1957].
- [9] L.V. SHUBNIKOV, V.I. KHOTKEVICH, YU.D. SHEPELEV, AND YU.N. RIABININ. *Magnetic properties of superconducting metals and alloys*. Zh.Eksp. Teor. Fiz. 7, 1937, pp. 221-237.
- [10] G. FUCHS, K.-H. MÜLLER, A. HANDSTEIN, K. NENKOV, V.N. NAROZHNYI, D. ECKERT, M. WOLF, L. SCHULTZ. *Upper critical field and irreversibility line in superconducting MgB₂*. Solid State Communications, Volume 118, Issue 10, 2001, pp. 497-501.
- [11] http://www.qm.phy.cam.ac.uk/teaching/lecture_4_12.pdf
- [12] A. A. ABRIKOSOV. *Fundamentals of the Theory of Metals* (North-Holland, Amsterdam: 1988).
- [13] R. FLUKIGER. *Overview of Superconductivity and Challenges in Applications*. Reviews of Accelerator Science and Technology Vol. 5, 2012, pp. 1-23.

- [14] G. ASCHERMANN, E. FRIEDRICH, E. JUSTI, AND J. KRAMER. *Supraleitfähige Verbindungen mit extrem hohen Sprungtemperaturen (NbH und NbN)*. Phys. Z., 42, 1941, pp. 349–360.
- [15] B. T. MATTHIAS, T. H. GEBALLE, S. GELLER, AND E. CORENZWIT. *Superconductivity of Nb₃Sn*. Phys. Rev. 95, 1954, pp. 1435.
- [16] T.G. BERLINCOURT AND R.R. HAKE. *Pulsed-Magnetic-Field Studies of Superconducting Transition Metal Alloys at High and Low Current Densities*. Bull. Am. Phys. Soc. II 7 408, 1962.
- [17] R] COHN, *Record superconductor at 22.3 K*. Physics Today, vol. 26, issue 10, 1973, pp. 17.
- [18] G. BEDNORZ AND K. A. MULLER. *Possible highT_c superconductivity in the Ba–La–Cu–O system*. Z. Phys. Volume 64, Issue 2 , 1986, pp. 189-193.
- [19] M. K. WU, J. R. ASHBURN, C. J. TORNG, P. H. HOR, R. L. MENG, L. GAO, Z. J. HUANG, Y. Q. WANG, AND C. W. CHU. *Superconductivity at 93 K in a new mixed-phase Y-Ba-Cu-O compound system at ambient pressure*. Z. Phys. Phys. Rev. Lett. 58, Number 9, 1987, pp. 908-910.
- [20] H. MAEDA, Y. TANAKA, M. FUKUTOMI AND T. ASANO. *A new high-r-oxide superconductor without a rare earth element*. Jpn. J. Appl. Phys. 27, 1988, L209-10.
- [21] C. C. TORARDI, M. A. SUBRAMANIAN, J. C. CALABRESE, J. GOPALAKRISHNAN, K. J. MORRISSEY. *Crystal Structure of Tl₂Ba₂Ca₂Cu₃O₁₀, a 125 K Superconductor*. Science. 240(4852), 1988, pp. 631-4.
- [22] D. D. BERKLEY, E. F. SKELTON, N. E. MOULTON, M.S OSOFSKY, W.T. LECHTER, V.M. BROWNING, and D.H. LIENBENBERG. *Pressure dependence of the superconducting transition in single crystals of Tl₂Ba₂Ca₂Cu₃O_{10-x}*. Phys. Rev. B, 47, 1993, pp. 5524-5527.
- [23] L. GAO, Y. Y. XUE, F. CHEN, Q. XIONG, R. L. MENG, D. RAMIREZ, C. W. CHU, J. H. EGGERT, and H. K. MAO. *Superconductivity up to 164 K in HgBa₂Ca_{m-1}Cu_mO_{2m+2+δ} (m=1, 2, and 3) under quasihydrostatic pressures*. Phys. Rev. B 50, 1994, pp. 4260-4263.
- [24] J. NAGAMATSU, N. NAKAGAWA, T. MURANAKA, Y. ZENITANI and J. AKIMTSU, *Superconductivity at 39 K in magnesium diboride*. Nature 410, 2001, pp. 63-64.

- [25] Y. KAMIHARA, T. WATANABE, M. HIRANO AND H. HOSONO. *Iron-Based Layered Superconductor $La[O_{1-x}F_x]FeAs$ ($x=0.05-0.12$) with $T_c=26$ K*. J. Am. Chem. Soc. 130 (11), 2008, pp. 3296-3297.
- [26] CAO WANG, LINJUN LI, SHUN CHI, ZENGWEI ZHU, ZHI REN, YUKE LI, YUETAO WANG, XIAO LIN, YONGKANG LUO, SHUAI JIANG, XIANGFAN XU, GUANGHAN CAO, ZHU'AN XU. *Thorium-doping-induced superconductivity up to 56 K in $Gd_{1-x}Th_xFeAsO$* . Euro. Phys. Lett. 83, Number 6, 2008, pp. 67006-p1 - 67006-p4.
- [27] <https://nationalmaglab.org/magnet-development/applied-superconductivity-center/plots>
- [28] A. XU, J. J. JAROSZYNSKI, F. KAMETANI, Z. CHEN, D. C. LARBALESTIER, Y. L. VIOUCHKOV, Y. CHEN, Y. XIE and V. SELVAMANICKAM. *Angular dependence of J_c for YBCO coated conductors at low temperature and very high magnetic fields*. Supercond. Sci. Technol. 23, 014003, 2010, pp. 1-7.
- [29] ALEX GUREVICH. *To use or not to use cool superconductors?* Nature Materials 10, 2011, pp. 255-259.
- [30] W. SCHAUER AND W. SCHELB, *Improvement of Nb_3Sn high field critical current by a two-stage reaction*. IEEE Transactions on Magnetics VOL. MAG-17, NO. 1, 1981, pp. 374-377.
- [31] V. SELVAMANICKAM AND J. DACKOW. *Progress in SuperPower's 2G HTS wire development and manufacturing*. DOE Advanced Cables & Conductors Peer Review, 2010.
- [32] T. HOLESINGER, L. CIVALE. US DOE Superconductivity for Electric Systems Annual Peer Review, Arlington, VA, 2006.
- [33] L. CIVALE, A. D. MARWICK, T. K. WORTHINGTON, M. A. KIRK, J. R. THOMPSON, L. KRUSIN-ELBAUM, Y. SUN, J. R. CLEM, AND F. HOLTZBERG. *Vortex confinement by columnar defects in $YBa_2Cu_3O_7$ crystals: Enhanced pinning at high fields and temperatures*. Phys. Rev. Lett. 67, pp. 648-651.
- [34] CRISTINA BUZEA AND TSUTOMU YAMASHITA. *Review of the superconducting properties of MgB_2* . Supercond. Sci. Technol. 14, 2001 R115-R146.
- [35] AKIYASU YAMAMOTO, JUN-ICHI SHIMOYAMA, SHINYA UEDA, YUKARI KATSURA, SHIGERU HORII AND KOHJI KISHIO. *Synthesis of high J_c MgB_2 bulks with high reproducibility by a modified powder-in-tube*

method. Supercond. Sci. Technol. 17, 2004, pp. 921–925. “Figures reprinted from this book with permission of the authors”.

[36] V. BRACCINI, A. GUREVICH, J. E. GIENCKE, M. C. JEWELL, C. B. EOM, D. C. LARBALESTIER, A. V. POGREBNYAKOV, Y. CUI, B. T. LIU, Y. F. HU, J. M. REDWING, QI LI, X. X. XI, R. K. SINGH, R. GANDIKOTA, J. KIM, B. WILKENS, N. NEWMANN, J. ROWELL, B. MOECKLY, V. FERRANDO, C. TARANTINI, D. MARRÉ, M. PUTTI, C. FERDEGHINI, R. VAGLIO, AND E. HAANAPPEL. *High-field superconductivity in alloyed MgB₂ thin films*, Phys. Rev. B 71, 2005, pp. 012504-1 - 012504-4.

[37] W. K. YEOH, S. X. DOU. *Enhancement of H_{c2} and J_c by carbon-based chemical doping*, Physica C, 456, 2007, pp. 170–179.

[38] A. GUREVICH. *Enhancement of the upper critical field by nonmagnetic impurities in dirty two-gap superconductors*. Physical Review B 67, 184515, 2003, pp. 1-13.

[39] T. M. SHEN, G. LI, C. H. CHENG AND Y ZHAO. *Doping effects of carbon and titanium on the critical current density of MgB₂*. Superconductor Science and Technology 19.11, 2006, pp. 1219-1224.

[40] E.A. YOUNG AND Y. YANG. *Preparation and properties of Mg(B_{1-x}C_x)₂ using Carbon Chemical Vapor Coated Boron*. IEEE TRANSACTIONS ON APPLIED SUPERCONDUCTIVITY, VOL. 17, NO. 2, 2007, pp. 2794-2797.

[41] W. K. YEOH, J HORVAT, J. H. KIM, X. XU AND S. X. DOU. *Effect of processing temperature on high field critical current density and upper critical field of nanocarbon doped MgB₂*. Appl. Phys. Lett. 90, 122502, 2007, pp. 1–3.

[42] W. K. YEOH, J. H. KIM, J HORVAT, S. X. DOU AND P. MUNROE. *Improving flux pinning of MgB₂ by carbon nanotube doping and ultrasonication*. Supercond. Sci. Technol. 19, 2006, pp. L5–L8.

[43] AKIYASU YAMAMOTO, JUN-ICHI SHIMOYAMA, SHINYA UEDA, ISAO IWAYAMA, SHIGERU HORII AND KOHJI KISHIO. *Effects of B₄C doping on critical current properties of MgB₂ superconductor*. Supercond. Sci. Technol. 18, 2005, pp. 1323-1328.

[44] S.X. DOU, O. SHCHERBAKOVA, W.K. YEOH, J.H. KIM, S. SOLTANIAN, X.L. WANG, C. SENATORE, R. FLUKIGER, M. DHALLE, O. HUSNJAK, E.BABIC. *Mechanism of Enhancement in Electromagnetic Properties of MgB₂ by Nano SiC Doping*. Phys. Rev. Lett. 98, 097002, 2007, pp. 1–4.

- [45] X.L. WANG, S. SOLTANIAN, M. JAMES, M.J. QIN, J. HORVAT, Q.W. YAO, H.K. LIU A, S.X. DOU. *Significant enhancement of critical current density and flux pinning in MgB₂ with nano-SiC, Si, and C doping*. Physica C 408–410, 2004, pp. 63-67.
- [46] B J SENKOWICZ, A POLYANSKII, R J MUNGALL, Y ZHU, J E GIENCKE, P M VOYLES, C B EOM, E E HELLSTROM and D C LARBALESTIER. *Understanding the route to high critical current density in mechanically alloyed Mg(B_{1-x}C_x)₂*. Supercond. Sci. Technol. 20, 2007, pp. 650–657 “Figures reprinted from this book with permission of Elsevier”.
- [47] BYUNG-HYUK JUN, YI-JEONG KIM, KAI SIN TAN AND CHAN-JOONG KIM. *Effective carbon incorporation in MgB₂ by combining mechanical milling and the glycerin treatment of boron powder*. Supercond. Sci. Technol. 21 105006, 2008, pp. 1–5.
- [48] X F RUI, Y ZHAO, Y Y XU, L ZHANG, X F SUN, Y ZWANG AND H ZHANG. *Improved flux pinning behaviour in bulk MgB₂ achieved by nano-SiO₂ addition*. Supercond. Sci. Technol. 17, 2004, pp. 689–691.
- [49] Y. ZHAO, C. H. CHENG, X. F. RUI, H. ZHANG, P. MUNROE, H. M. ZENG, N. KOSHIZUKA, AND M. MURAKAMI. *Improved irreversibility behavior and critical current density in MgB₂-diamond nanocomposites*. Appl. Phys. Lett., 83, 2003, pp. 2916–2918.
- [50] J. WANG, Y. BUGOSLAVSKY, A. BERENOV, L. COWEY, A. D. CAPLIN, L. F. COHEN, J. L. MACMANUS DRISCOLL, L. D. COOLEY, X. SONG, AND D. C. LARBALESTIER. *High critical current density and improved irreversibility field in bulk MgB₂ made by a scalable, nanoparticle addition route*. Appl. Phys. Lett., 81, 2002, pp. 2026–2028.
- [51] J. H. KIM, W. K. YEOH, M. J. QIN, X. XU, S. X. DOU, P. MUNROE, H. KUMAKURA, T. NAKANE, AND C. H. JIANG. *Enhancement of in-field J_c in MgB₂ Fe wire using single- and multiwalled carbon nanotubes*. Appl. Phys. Lett. 89, 122510, 2003, pp. 1–3.
- [52] JUNG HO KIM, SANGJUN OH, YOON-UK HEO, SATOSHI HATA, HIROAKI KUMAKURA, AKIYOSHI MATSUMOTO, MASATOSHI MITSUHARA, SEYONG CHOI, YUSUKE SHIMADA, MINORU MAEDA, JUDITH L MACMANUS-DRISCOLL and SHI XUE DOU. *Microscopic role of carbon on MgB₂ wire for critical current density comparable to NbTi*. NPG Asia Materials 4, 2012, pp. 1–7.

- [53] A. MATSUMOTO, H. KUMAKURA, H. KITAGUCHI and H. HATAKEYAMA. *Effect of SiO₂ and SiC doping on the powder-in-tube processed MgB₂ tapes*. Supercond. Sci. Technol. 16, 2003, pp. 926–930.
- [54] P. KOVAC, T. MELISEK, L. KOPERA, I. HUSEK, M. POLAK AND M. KULICH. *Progress in electrical and mechanical properties of rectangular MgB₂ wires*. Supercond. Sci. Technol. 22, 075026, 2009, pp. 1–8.
- [55] R. FLÜKIGER, M.S.A. HOSSAIN, C. SENATORE, M. RINDFLEISCH. *Improved transport properties and connectivity of in situ MgB₂ wires obtained by Cold High Pressure Densification (CHPD)*. Physica C 471, 2011, pp. 1119–1123.
- [56] G. Z LI, M. D. SUMPTION, M. A. SUSNER, Y. YANG, K. M. REDDY, M. A. RINDFLEISCH, M. J. TOMSIC, C. J. THONG AND E. W. COLLINGS. *The critical current density of advanced internal-Mg-diffusion-processed MgB₂ wires*. Supercond. Sci. Technol. 25, 115023, 2012, pp. 1–8.
- [57] G. Z. LI, M. D. SUMPTION, J. B. ZWAYER, M. A. SUSNER, M. A. RINDFLEISCH, C. J. THONG, M. J. TOMSIC, AND E. W. COLLINGS. *Effects of carbon concentration and filament number on advanced internal Mg infiltration-processed MgB₂ strands*. Superconductor Science and Technology, vol. 26, no. 9, 095007, 2013, pp. 1-9.
- [58] G. GIUNCHI. *High density MgB₂ obtained by reactive liquid Mg infiltration*. Int. J. Mod. Phys. B, 17, 453, 2013, pp. 1–9.
- [59] H. FANG, P. GIJAVANEKAR, Y. X. ZHOU, P. T. PUTMAN, AND K. SALAMA. *Development of Fe-Sheathed MgB₂ Wires and Tapes for Electric Power Applications*. IEEE TRANSACTIONS ON APPLIED SUPERCONDUCTIVITY, VOL. 15, NO. 2, 2005, pp. 1–3.
- [60] N. NOVOSEL, S. GALIC, D. PAJIC, Z. SKOKO, I. LONCAREK, M. MUSTAPIC, K. ZADRO AND E. BABIC. *Enhancement of the critical current density in MgB₂ wires doped with Ni nanoparticles*. Supercond. Sci. Technol. 25, 095018, 2012, pp. 1–9.
- [61] IGOR F. LYUKSYUTOV AND VALERY POKROVSKY. *Magnetization Controlled Superconductivity in a Film with Magnetic Dots*. Phys. Rev. Lett. 81, 1998, pp. 2344–2347.
- [62] J. I. MARTÌN, M. VÉLEZ, J. NOGUÉS, AND IVAN K. SCHULLER. *Flux Pinning in a Superconductor by an Array of Submicrometer Magnetic Dots*. Phys. Rev. Lett. 79, 1997, pp. 1929–1932.

- [63] VALERIA BRACCINI, ANDREA MALAGOLI, ANDREA TUMINO, MAURIZIO VIGNOLO, CRISTINA BERNINI, CARLO FANCIULLI, GENNARO ROMANO, MATTEO TROPEANO, ANTONIO S. SIRI, AND GIOVANNI GRASSO. *Improvement of Magnetic Field Behavior of Ex-Situ Processed Magnesium Diboride Tapes*. IEEE TRANSACTIONS ON APPLIED SUPERCONDUCTIVITY, VOL. 17, NO. 2, 2007, pp. 2766–2769.
- [64] VALERIA BRACCINI, DAVIDE NARDELLI, ROBERTO PENCO, and GIOVANNI GRASSO. *Development of Ex-Situ Processed MgB₂ wires and their application to magnets*. Physica C, vol. 456, 2007, pp. 209–217.
- [65] A. MALAGOLI, V. BRACCINI, M. TROPEANO, M. VIGNOLO, C. BERNINI, C. FANCIULLI, G. ROMANO, M. PUTTI, C. FERDEGHINI, E. MOSSANG, A. POLYANSKII, AND D.C. LARBALESTIER *Effect of grain refinement on enhancing critical current density and upper critical field in undoped MgB₂ ex-situ tapes*. Journal of applied physics, 104, 2008, pp. 103908–1 - 103908–7.
- [66] ANNA KARIO, VADIM GRINENKO, ALEX KAUFFMANN, WOLFGANG HASLER, CHRISTIAN RODIG, PAVOL KOVAČ, TIBOR MELIŠEK, BERNHARD HOLZAPFEL. *Isotropic behavior of critical current for MgB₂ ex situ tapes with 5 wt.% carbon addition*. Physica C 483, 2012, pp. 222–224.
- [67] ANNA KARIO. *High Energy Milled ex situ MgB₂ for Tapes and Wires, Dissertation*. Technical University Dresden, 2011.
- [68] W. HÄßLER, M HERRMANN, C RODIG, M SCHUBERT, K NENKOV AND B HOLZAPFEL. *Further increase of the critical current density of MgB₂ tapes with nanocarbon-doped mechanically alloyed precursor*. Supercond. Sci. Technol. 21, 062001, 2008, pp. 1–3.
- [69] MARKO HERRMANN, WOLFGANG HAESSLER, CHRISTIAN RODIG, WOLFGANG GRUNER, BERNHARD HOLZAPFEL, AND LUDWIG SCHULTZ. *Touching the properties of NbTi by carbon doped tapes with mechanically alloyed MgB₂*. Applied Physics Letters 91, 2007, pp. 082507-1 – 082507-3.
- [70] N J ARCHER. *Chemical vapour deposition*. Phys. Technol. Vol. 10, 1979, pp. 152–161.
- [71] M. NISHIJIMA, J. YOSHINOBU, T. SEKITANI, AND M. ONCHI. *Chemisorption and thermal decomposition of ethylene on Pd(110): Electron energy loss spectroscopy, low-energy electron diffraction, and*

thermal desorption spectroscopy studies. J. Chem. Phys., Vol. 90, No.9, 1989, pp. 5114–5127.

[72] ANDREA ZATTIN. *Tesi di laurea: Oxocluster di zirconio e afnio come precursori di ossidi misti e di materiali ibridi nanocompositi*. 2004, pp. 18–28.

[73] C. J. BRINKER, G. W. SCHERER. *Sol-Gel Science–The Physics and Chemistry of Sol-Gel Processing*, Academic Press, New York, 1990, pp. 1929–1932.

[74] AKIYASU YAMAMOTO, JUN-ICHI SHIMOYAMA, SHINYA UEDA, YUKARI KATSURA, SHIGERU HORII, AND KOHJI KISHIO. *Doping Effects on Critical Current Properties of MgB_2 Bulks Synthesized by Modified Powder-In-Tube Method*. IEEE TRANSACTIONS ON APPLIED SUPERCONDUCTIVITY, VOL. 15, NO. 2, 2005, pp. 3292–3296 “Figures reprinted from this book with permission of the authors”.

[75] S. LEE, T. MASUI, A. YAMAMOTO, H. UCHIYAMA, AND S. TAJIMA. *Carbon substituted MgB_2 single crystals*. Physica C, vol. 397, 2003, pp. 7–13.

[76] ALEKSANDAR GOLUBOVIC, SLOBODANKA NIKOLIC, STEVAN DJURIC AND ANDREJA VALCIC. *The growth of sapphire single crystals*. J.Sehem.Soc. 66(6), 2001, pp. 411–418.

[77] B. J. SENKOWICZ, R. J. MUNGALL, Y. ZHU, J. JIANG, P. M. VOYLES, E. E. HELLSTROM AND D. C. LARBALESTIER. *Nanoscale grains, high irreversibility field and large critical current density as a function of high-energy ball milling time in C-doped magnesium diboride*. Supercond. Sci. Technol. 21, 035009, 2008, pp. 1–10. “Figures reprinted from this book with permission of the authors”.

[78] PETER GOODHEW, JOHN HUMPHREYS, RICHARD BEANLAND. *Electron microscopy and analysis*. Taylor & Francis, pp. 66–168.

[79] Quantum Design. *Vibrating Sample Magnetometer (VSM) Option User’s Manual. Application*. -100, Rev. B0, 2011.

[80] Quantum Design. *Using PPMS Superconducting Magnets at Low Fields*. Application 1070-207, Rev. A0, 2009, pp. 1–11.

[81] T. TAKENOBU, T. ITO, DAM HIEU CHI, K. PRASSIDES, AND Y. IWASA. *Intralayer carbon substitution in the MgB_2 superconductor*. PHYSICAL REVIEW B, VOLUME 64, 134513, pp. 1–3.

- [82] IARC MONOGRAPHS VOLUME *Carbon black*. 2010, pp. 1-63.
- [83] RANDALL M.GERMAN. *Liquid phase sintering*, 2002, pp. 392-397.
- [84] JOHN M ROWELL. *The widely variable resistivity of MgB₂ samples*. Supercond. Sci. Technol. 16, 2003, pp. R17–R27.
- [85] T. MASUI, S. LEE, A. YAMAMOTO, H. UCHIYAMA, S. TAJIMA. *Carbon-substitution effect on superconducting properties in MgB₂ single crystals*. Physica C 412–414, 2004, pp. 303–306.
- [86] E A YOUNG, A KULAK AND Y YANG. *Thermal–electrical transport of high purity, melt impregnated, polycrystalline MgB₂*. Supercond. Sci. Technol. 24, 2011, 085015, pp. 1-5.
- [87] MPUTTI, V BRACCINI, E GALLEANI, F NAPOLI, I PALLECCHI, A S SIRI, P MANFRINETTI AND A PALENZONA. *Two-band effects in the transport properties of MgB₂*. Supercond. Sci. Technol. 16, 2003, pp. 188–192.
- [88] J. H. KIM, S. ZHOU, M. S. A. HOSSAIN, A. V. PAN, AND S. X. DOU. *Carbohydrate doping to enhance electromagnetic properties of MgB₂ superconductors*. APPLIED PHYSICS LETTERS 89, 2006, pp. 142505-1 - 142505-5.
- [89] W. E. YETTER, D. A. THOMAS AND E. J. KRAMER. *Grain-Boundary Flux Pinning by the Electron-Scattering Mechanism*. Physica C Phil. Mag. B, 46, 1982, pp. 523.
- [90] EDWARD J. KRAMER. *Scaling laws for flux pinning in hard superconductors*. J. Appl. Phys., Vol. 44, No.3, 1973, pp. 1360–1370.
- [91] C. TARANTINI, H.U. AEBERSOLD, C. BERNINI , V. BRACCINI, C. FERDEGHINI, U. GAMBARDELLA, E. LEHMANN, P. MANFRINETTI, A. PALENZONA, I. PALLECCHI, M. VIGNOLO, M. PUTTI. *Neutron irradiation on MgB₂*. Physica C 463–465, 2007, pp. 211–215.
- [92] J. R. THOMPSON, M. PARANTHAMAN, D. K. CHRISTEN, K. D. SORGE, H. J. KIM AND J. G. OSSANDON. *High temporal stability of supercurrents in MgB₂ materials*. Supercond. Sci. Technol. 14, 2001, pp. L17–L20.
- [93] I. SHIGETA, T. ABIRU, K. ABE, A. NISHIDA, Y. MATSUMOTO. *Temperature and field dependence of magnetization of MgB₂ polycrystals*. Physica C 392–396, 2003, pp. 359–363.

- [94] M. EISTERER. *Magnetic properties and critical currents of MgB₂*. Supercond. Sci. Technol. 20, 2007, pp. R47–R73.
- [95] S. SOLTANIAN, X. L. WANG, J. HORVAT, S. X. DOU, M. D. SUMPTION, M. BHATIA, E.W. COLLINGS, P. MUNROE AND M. TOMSIC. *High transport critical current density and large H_{c2} and H_{irr} in nanoscale SiC doped MgB₂ wires sintered at low temperature*. Supercond. Sci. Technol. 18, 2005, pp. 658–666.
- [96] ARPITA VAJPAYEE, R. JHA, A. K. SRIVASTAVA, H. KISHAN, M. TROPEANO, C. FERDEGHINI AND V. P. S. AWANA. *The effect of synthesis temperature on the superconducting properties of n-SiC added bulk MgB₂ superconductor*. Supercond. Sci. Technol. 24, 045013, 2011, 045013, pp. 1–11.
- [97] R ZENG, L LU, J LWANG, JHORVAT, W X LI, D Q SHI, S X DOU, M TOMSIC AND M RINDFLEISCH. *Significant improvement in the critical current density of in situ MgB₂ by excess Mg addition*. Supercond. Sci. Technol. 20, 2007, pp. L43–L47.
- [98] J. HORVAT, S. SOLTANIAN, X. L. WANG, AND S. X. DOU. *Effect of sample size on magnetic J_c for MgB₂ superconductor*. Journal of Applied Physics 96, 2004, pp. 4342–4351.
- [99] J HORVAT, W K YEOH, J H KIM AND S X DOU. *Transport and magnetic critical current in superconducting MgB₂ wires*. Supercond. Sci. Technol. 21, 2008, 065003, pp. 1–6.
- [100] J. HORVAT, S. SOLTANIAN, A. V. PAN, AND X. L. WANG. *Superconducting screening on different length scales in high-quality bulk MgB₂ superconductor*. Journal of Applied Physics 96, 2004, pp. 4342–4351.
- [101] J. H. KIM, W. K. YEOH, M. J. QIN, X. XU, AND S. X. DOU. *The doping effect of multiwall carbon nanotube on MgB₂/Fe superconductor wire*. JOURNAL OF APPLIED PHYSICS 100, 013908, 2006, pp. 1–4.

Appendix

List of publications

M. PAOLELLA, D. BAVYKIN, E.A. YOUNG. *Preparation and Properties of Si Doped $Mg(B_{1-x}C_x)_2$ Using Silica Sol-Gel and Carbon Chemical Vapor Coated Boron*. IEEE Transactions on Applied Superconductivity, VOL. 23, NO. 3, 2013.

M. PAOLELLA, A. KULAK AND E.A. YOUNG. *Correlation between Phase Separation and Transport Properties in C-CVD MgB_2* . Physics Procedia vol. 36, 2012, pp. 629-633.

E.A. YOUNG, Y. YANG AND M. PAOLELLA *IV transport critical current and n number of MgB_2 conductors as a function of temperature*. IEEE Transactions on Applied Superconductivity, 23, 3, 8001304, 2013.